“Water Transport in Gas Diffusion Media for PEM Fuel Cells: Experimental and Numerical Investigation”

Von der Fakultät für Ingenieurwissenschaften, Abteilung Maschinenbau und Verfahrenstechnik
der
Universität Duisburg-Essen
zur Erlangung des akademischen Grades
eines
Doktors der Naturwissenschaften
Dr. rer. nat.

genehmigte Dissertation
von

Dipl.-Ing. Chem. (FH)
Jörg Roth
aus
Nürnberg

Gutachter: Univ.-Prof Dr. rer. nat. Angelika Heinzel
Prof. PhD. Iwan Alexander

Tag der mündlichen Prüfung: 20. August 2010

Water Transport in Gas Diffusion Media for PEM Fuel Cells:

Experimental and Numerical Investigation

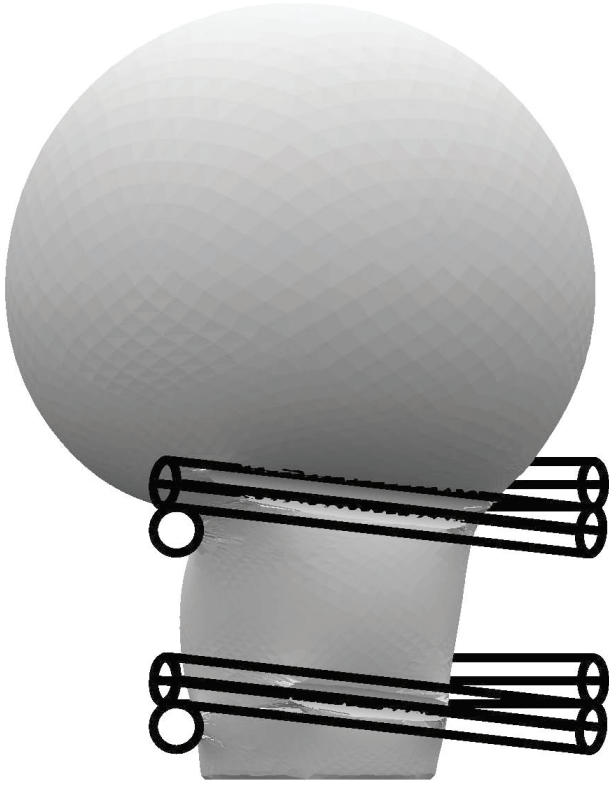

...Et qu'est-ce qu'on brûlera à la place du charbon ?

L'eau, répondit Cyrus Smith.

L'eau, s'écria Pencroff, l'eau pour chauffer les bateaux à vapeur et les locomotives, l'eau pour chauffer l'eau !

« Oui, mais l'eau décomposée en ses éléments constitutifs, répondit Cyrus Smith, et décomposée, sans doute, par l'électricité, qui sera devenue alors une force puissante et maniable, car toutes les grandes découvertes, par une loi inexplicable, semblent concorder et se compléter au même moment. Oui, mes amis, je crois que l'eau sera un jour employée comme combustible, que l'hydrogène et l'oxygène, qui la constituent, utilisés isolément ou simultanément, fourniront une source de chaleur et de lumière inépuisables et d'une intensité que la houille ne saurait avoir. Un jour, les soutes des steamers et les tenders des locomotives, au lieu de charbon, seront chargés de ces deux gaz comprimés, qui brûleront dans les foyers avec une énorme puissance calorifique. Ainsi donc, rien à craindre. Tant que cette terre sera habitée, elle fournira aux besoins de ses habitants, et ils ne manqueront jamais ni de lumière ni de chaleur, pas plus qu'ils ne manqueront des productions des règnes végétal, minéral ou animal. Je crois donc que lorsque les gisements de houille seront épuisés, on chauffera et on se chauffera avec de l'eau. L'eau est le charbon de l'avenir. ... » '

Jules Vernes in «L'Île mystérieuse» (1875) [Ver75]

Preface

This thesis was carried out in the years from 2003 till 2009. The work was embedded deeply in the global industrial automotive fuel cell research program of General Motors in the framework of the international technical development centre of the Adam Opel GmbH in Rüsselsheim. The academic lead was provided by the Institute for Energy and Environmental Protection Technologies, part of the Faculty of Engineering Sciences at Department of Mechanical Engineering of the University Duisburg-Essen, Germany. Major support, for which I would like to express my gratitude, was given by Prof. Dr. rer. nat. Angelika Heinzel from the Institute for Energy and Environmental Protection Technologies at University Duisburg-Essen by advising the thesis and Prof. Dr. Iwan Alexander from the Department of Mechanical and Aerospace Engineering at the Case Western Reserve University, Cleveland (Ohio) as the second reviewer.

Further, essential support was given by my supervisors within the General Motors and Adam Opel GmbH, namely Dr. Udo Winter, whom I would like to express my gratitude posthumous, Dr. Thomas Johnen, Dr. Rittmar von Helmolt, Dr. Stephan Fell, Dr. Mark Mathias and Dr. Josefin Meusinger for the continuous support and the opportunity to work on this interesting topic constantly for all the years. For the general aid given by reflecting many details and questions of all parts in this thesis my thanks goes to Dr. Daniel R. Baker and numerous other colleagues within the GM/Opel consortium. The colleagues from the mechanical and electrical workshop are acknowledged for the straightforward realisation of my numerous requests. The financial support was completely covered by General Motors and Adam Opel GmbH, for which I am very grateful.

My special thanks for the support on the nuclear magnetic resonance part (NMR) of the thesis goes to Dr. Bertram Manz and Dr. Frank Volke from Fraunhofer IBMT in St. Ingbert for the image acquisition and consultancy of the experiment. Many thanks to Stefan Thieme who designed the fuel cell and the fuel cell test station for the NMR experiment as part of his diploma thesis under my guidance. And to my colleague Dr. Stefan Berger for answering the numerous questions on fundamentals of NMR.

I would like to acknowledge my wife Eva Hartmann and my daughter Ragna for the sustaining patience and support throughout the years.

Thank you all!

Trebur, 14. April 2010

Abstract

"Water Transport in Gas Diffusion Media for PEM Fuel Cells:
Experimental and Numerical Investigation"
Jörg Roth

The water flux in partially saturated hydrophobic carbon fibre paper for polymer electrolyte membrane fuel cell applications is investigated and compared with the frequently used constitutive two-phase flow model based on Darcy's law. Further, the first steps towards a math-based material design for gas diffusion media are explored in this thesis.

Two self-developed ex-situ experiments to investigate the liquid water transport are introduced. The first is a newly developed buoyancy-based measurement of the pressure-saturation relationship on thin porous material with an accuracy of 0.5 kPa for the pressure and ± 5 % for the saturation. The second experiment measures the pressure drop in dependence of flow rates down to magnitudes of µL/s across the partially saturated thin porous material. This flow rate is relevant for the fuel cell application.

The liquid water transport through Toray 060 carbon fibre paper, impregnated with 7 % and 10 % PTFE is investigated at wet and dry boundary conditions.

The experiments are also accompanied by analytical and numerical free surface modelling with the consideration of the material morphology and liquid-solid interaction. The imbibing and draining cases of an arrangement of six fibres at varying solid-liquid interaction and boundary conditions are studied with 'Surface Evolver'.

In order to evaluate the findings of ex-situ and modelling work for applicability to water transport in fuel cell operation, the technique of nuclear magnetic resonance (NMR) imaging is assessed. The focus is on the visualisation of 2D and 3D water distribution in the operating fuel cell. The compatibility of the NMR experiment with fuel cell operation in relation to material selection, operating temperature, and current density is addressed. NMR imaging is employed for different current densities, stoichiometries, and fuel cell arrangements. The fuel cell arrangements differ by the cathode diffusion medium. Plain, hydrophobic, and micro porous layered gas diffusion media arrangements were tested. The dynamic aspects of fuel cell operation are addressed by 2D investigation. The achieved spatial resolutions are 625 µm by 313 µm by 20 µm voxel sizes at a temporal resolution of 2 hrs in 3D, while the spatial 2D resolution is 313 µm by 20 µm at a temporal resolution of 1 min.

It is found that the state-of-the-art NMR experiment interferes strongly with fuel cell operation. The operating conditions are limited to near room temperatures ($\leq 50\,^{\circ}\mathrm{C}$), low current densities (≈ 0.1 A/cm^2) and electrically relatively low conductive gas diffusion media (SGL 21AA). Under such conditions, the findings of the 3D visualisation experiment reveals a high water saturation in the cathode diffusion medium close to the interface with the membrane and at the interfaces with the rib. The saturation stays low in the centre of the diffusion medium at the cathode side. Where the cathode diffusion medium faces a channel, the water saturation is high only at the membrane interface. This result, as well as the finding of the dynamic 2D visualisation indicating that the water transport is temporally discontinuous, are in agreement with the major finding of the ex-situ permeation experiment. It is found in the permeation experiment that the conditions of the interfaces of a thin porous material like the gas diffusion medium are more dominant on the liquid water transport than the bulk properties, especially if a dry low-pressure boundary exists. This is also indicated by the free surface modelling.

The work suggests that the classical macroscopic water transport model, based on Darcy's law, is not able to describe water transport in fuel cell gas diffusion media satisfyingly for dry boundary conditions, or in cases where transient phenomena become important.

The numerical free surface modelling has the potential to be a useful tool to describe water transport in thin, hydrophobic, partially saturated fibrous structures, either for math-based material design or the development of an improved constitutive water transport model for fuel cell gas diffusion media and other thin porous materials.

Zusammenfassung

„Wassertransport in Gasdiffusionmedien für PEM Brennstoffzellen:
Experimentelle und Numerische Untersuchungen“
Jörg Roth

Der Transport von flüssigem Wasser in teilgesättigtem, hydrophobem Kohlefaserpapier wird für die Verwendung in Polymerelektrolytbrennstoffzellen untersucht und mit der oft angewandten Zwei-Phasen-Beschreibung, basierend auf Darcys Gesetz, verglichen. Weiterhin werden die ersten Schritte unternommen, die zur modellbasierten Entwicklung von Gasdiffusionsmedien notwendig sind.

Für die experimentelle Untersuchung von Flüssigwassertransport werden zwei selbst entwickelte Ex-situ-Verfahren vorgestellt. Bei dem ersten handelt es sich um eine neu entwickelte, auftriebsbasierte Messung der Druck-Sättigungs-Beziehungen in dünnen porösen Materialien mit einer Genauigkeit von 0.5 kPa für die Druckmessung und ± 5 % für die Bestimmung der Sättigung. Das zweite Verfahren dient zur Bestimmung des Druckverlustes in Abhängigkeit des Wasserflusses unter für Brennstoffzellen relevanten Flussraten im Bereich von µL/s. Sowohl nasse als auch trockene Randbedingungen werden an Toray 060 Kohlefaserpapier, imprägniert mit 7 % und 10 % PTFE, untersucht.

Begleitet werden die Experimente von analytischer und numerischer Simulation. Dabei werden die Materialstruktur und die Flüssig-Feststoff-Phasen-Wechselwirkung aufgelöst. Es werden einströmendes und ausfließendes Verhalten an einer Geometrie, bestehend aus sechs Fasern mit unterschiedlichen Kontaktwinkeln und Randbedingungen, mit der Software „Surface Evolver“ untersucht.

Weiterhin wird bildgebende Kernspinresonanz im Hinblick auf die Anwendbarkeit auf In-situ-Brennstoffzellentests diskutiert. Dies dient zur Bewertung der Ergebnisse der Ex-situ- und Simulationsarbeiten. Hierbei liegt der Schwerpunkt auf der Bildgebung der Flüssigwasserverteilung in einer in Betrieb befindlichen Brennstoffzelle in 2D und 3D. Die Vereinbarkeit von Kernspinresonanzexperiment und Brennstoffzellenexperiment in Bezug auf Materialauswahl, Betriebstemperatur und Stromdichte wird überprüft. Mit der bildgebenden Kernspinresonanz wird die Flüssigwasserverteilung bei unterschiedlichen Stromdichten, Stöchiometrien und Brennstoffzellen untersucht, die mit unbehandelten, hydrophoben und mit mikroporöser Beschichtung ausgestatteten Diffusionsmedien aufgebaut sind. Mit dem 2D-Verfahren werden die dynamischen Aspekte des Verhaltens der Brenn-

stoffzelle betrachtet. Die erreichte räumliche Auflösung sind Blockgrößen von 625 µm x 313 µm x 20 µm bei einer zeitlichen Auflösung von 2 h in 3D; hingegen ist eine räumliche Auflösung von 313 µm x 20 µm bei einer zeitlichen Auflösung von 1 min beim 2D-Verfahren möglich.

Es wird eine starke Beeinflussung der Kernspinresonanz-Verfahren nach Stand der Technik mit dem Brennstoffzellenbetrieb beobachtet. Nur bei einem Betrieb der Brennstoffzelle nahe Raumtemperatur ($\leq 50\,^{\circ}\mathrm{C}$), kleinen Stromdichten ($\approx 0{,}1$ A/cm^2) und Diffusionsmedien mit vergleichsweise geringer elektrischer Leitfähigkeit (SGL 21AA) kann mit der Kernspinresonanz flüssiges Wasser sichtbar gemacht werden. Unter solchen Bedingungen zeigt die 3D-Bildgebung eine große Wassersättigung nahe der Grenzfläche zur Membran sowie nahe des Steges in der Gasverteilerstruktur auf der Kathodenseite. Im Inneren des Diffusionsmediums auf der Kathode ist die Wassersättigung gering. In der Nähe und an der Kontaktzone zwischen dem Diffusionsmedium auf der Kathodenseite sowie dem Gaskanal ist die Sättigung gering und nur nahe der Membran hoch. Sowohl dieses Ergebnis als auch das Resultat der dynamischen 2D-Untersuchung, die ein pulsierendes Wassertransportverhalten anzeigt, sind in Übereinstimmung mit den Ergebnissen der Ex-situ-Permeationsuntersuchung. Dabei kommt zu Tage, dass die Bedingungen, die an der Materialgrenzfläche eines dünnen, porösen Materials, wie dem Diffusionsmedium, eine größere Rolle spielen als die Materialeigenschaften im Inneren. Diese Beobachtung wird auch durch die Freie-Oberflächen-Simulation gestützt.

Die Untersuchungen zeigen an, dass die klassische, auf Darcys Gesetz beruhende Beschreibung des Wassertransports nicht in der Lage ist, den Wassertransport in Diffusionsmedien für Brennstoffzellen bei trockenen Randbedingungen oder in Fällen, in denen dynamische Aspekte von Bedeutung sind, zu beschreiben.

Es hat sich gezeigt, dass die numerische Simulation das Potential besitzt, sowohl die Entwicklung von Diffusionsmedien als auch die Entwicklung einer verbesserten Konstitutivbeziehung zur Beschreibung des Wassertransports in Brennstoffzellen zu unterstützen.

Contents

Appendices

Abbreviations and Symbols

Abbreviations

AFC	Alkaline Fuel Cell
CFD	Computational fluid dynamics
DI	Deionised
DM	Diffusion medium
HOR	Hydrogen oxidation reaction
IUPAC	International Union of Pure and Applied Chemistry
MCFC	Molten carbonate fuel cell
MEA	Membrane electrode assembly
MPL	Micro porous layer
NMR	Nuclear magnetic resonance
ORR	Oxygen reduction reaction
PAFC	Phosphoric acid fuel cell
PBI	Polybenzimidazole
PEMFC	Polymer electrolyte membrane fuel cell
PFSA	Polyfluoro-sulfonic acid
PMMA	Polymethyl-metacrylate
PTFE	Polyfluoro-ethylene
REV	Representative equivalent volume
SOFC	Solid oxide fuel cell
SPE	Solid polymer electrolyte
TP	Test point
TEM	Transmission electron microscopy

Units

A	Ampere	Current
J	Joule	Energy
K	Kelvin	Temperature
g	Gram	Mass
L	Litre (10^{-3}m^3)	Volume
m	Meter	Length
mol	Mol	Amount of substance
Pa	Pascal	Pressure
s	Second	Time
V	Volt	Electrical potential

Physical Constants

$\hbar$	$1.05457 \cdot 10^{-34}$	Js	Planck constant
k_B	$1.38066 \cdot 10^{-23}$	J/K	Boltzmann constant
$\Re$	8.31451	J/mol/K	Ideal gas constant
N_A	$6.022 \cdot 10^{23}$	1/mol	Avogadro constant
ϵ_0	$8.854187 \cdot 10^{-12}$	As/V/m	Electric field constant in vacuum
c^*	$2.997924 \cdot 10^8$	m/s	Speed of light in vacuum
F	96485	As/mol	Faraday constant
g	9.81	m/s^2	Gravity constant
π	3.14159	-	Circle Constant

Prefix

p	10^{-12}	Pico
n	10^{-9}	Nano
µ	10^{-6}	Micro
m	10^{-3}	Milli
c	10^{-2}	Centi
k	10^3	Kilo

Greek letters and operators

α	°	Angle
β	-	Pressure drop factor
Γ	J	Surface energy
γ	N/m	Interfacial tension
γ^*	As/kg	Gyromangetic ratio
δ	m	Layer thickness
Δ	-	Difference
ε	-	Porosity
η	-	Efficiency
θ	°	Contact angle
ι	-	Exponent in relative permeability calculation
κ	-	Molar ratio
λ	-	Stoichiomety
Λ	-	Tortuosity exponent
μ	Pa s	Viscosity
ν	1/s	Frequency
ν^*	-	Stoichiometric number
ξ	-	Van Genuchten porosity coefficient
ϖ		Spatial gradient or relative expression of a physical property
Π		Physical property
ρ	mol/m^3 or kg/m^3	Density
σ	N/m	Surface tension
σ^*	A/V/m	Specific conductivity
τ	-	Tortuosity
ϕ	V	Over potential
χ	-	Brooks-Corey porosity coefficient
ψ	-	Kinetic transfer coefficient
ω	-	Pore size distribution function
∇	-	Spatial differential
∂	-	Partial differential

Latin letters

A	m^2	Area
a	m	Vertical fibre distance
Bo	-	Bond number
b	m	Horizontal fibre distance
C	-	Context related, not closer defined constant
Ca	-	Capillary number
c	mol/m^3	Concentration
c_p	J/mol/K	Heat capacity
D	m^2/s	Diffusion coefficient
d	-	Difference
Ev	-	Eötvös number
f	-	Mathematical function
G	J/mol	Gibbs free energy
g	-	Mathematical function
$\mathcal{H}$	kJ/mol	Enthalpy
H	A/m	Strength of magnetic field
h	m	Height
$\mathcal{I}$	-	Spin quantum number
I	A	Current
i	A/cm^2	Current density
J	-	J-function
$\mathbf{K}$		Proportionality tensor
k	m^2	Darcy permeability (as scalar for 1D)
$\mathbf{k}$	m^2	Darcy permeability (as tensor for 2D and 3D)
L	-	Location
l	m	Thickness, length
$<l>$	m	Diffusion length
$\mathcal{M}$	A/m	Magnetisation
M	g/mol	Molar mass
m	g	Mass
m^*	-	Number of electrode reaction steps before the rate determining step
n	mol	Amount of substance
$<n>$	-	Number
Oh	-	Ohnesorge number
P	Watt	Power
p	Pa	Pressure
Q	-	Mobility in Multi-Phase Mixture Model
q	-	Number for branching
R	Ω/m^2	Resistivity
Re	-	Reynolds number
RH	-	Relative humidity
r	m	Radius
$<r>$	m	Mean radius
S	J/mol/K	Entropy
s	-	Saturation
Su	-	Suratman number
T	K	Temperature
T_1	s	Spin-lattice relaxation time
T_2	s	Spin-spin relaxation time
T_2^*	s	Spin-spin relaxation time
t	s	Time
U	V	Electrical potential
u	m/s	Velocity

Latin letters cont.

V	m^3	Volume
v	-	Exponent for capillary pressure curve
v^*	-	Archie's exponent for porosity
W	m	Width
We	-	Weber number
w	-	Exponent for capillary pressure curve
w^*	-	Archie's exponent for saturation dependent tortouosity / porosity
x	m	Spatial coordinate
Y	m	Constant in permeability model
y	m	Spatial coordinate
z	m	Spatial coordinate
z^*	-	Number of electrons in reaction

Indices

1-15	Index of constant C or functional group in various formulae
0	Condition at t = 0, baseline condition
A..D	Locations A..D
ad	Adsorbed
b	Material constant
Bl	Lower boundary
Bu	Upper boundary
buoy	Buoyancy
cap	Capillary pressure
DM	Diffusion medium
diff	Diffusion
e	Effective
el	Electrical
end	Final
f	Formation
fil	Filament
fluid	Fluid
g	Gas phase
geo	Geometrical
i	Index to differentiate species or properties
in	Inlet
int	Interface
inv	Invisible
liq	Liquid phase
kin	Kinetic
mem	Membrane
mol	Molar
nw	Non wetting
p	Percolation
prod	Product
r	Residual
R	Reaction
rel	Relative
sol	Solid
sub	Submerged
w	Wetting

Chapter 1

Background

1.1 Introduction

Being born in the oil era, we are challenged with the task to develop technology that enables to maintain or even increase the prosperity we have today. The amenities of modern life style are based on the availability of cheap exergy (energy to do work with). According to the International Energy Agency in 2007 the exergy was sourced from fossil resources by 82.7 %, and nuclear sources by 10.6 % the remaining part of 6.7 % was gained from renewable sources (hydro power, solar, bio gas, tidal, wind, geothermal, and waste combustion) on global average [IEA08].

Since the fossil fuels are limited in their supply, the price for exergy is increasing. Hubbert [Hub49] published a paper in 1949 on fossil fuel based energy and development of human population, touching shortly on the possible contribution of water power. Therein, he presented a model how to estimate the temporal range of non-renewable exergy carriers. In 1956, he fed his model with data and predicted the oil and gas production peak for the United States by 1965 and 1970 respectively. As it turned out later, he was not far off, the oil production peaked in 1972, and the gas production in 1971 [EIA07].

Although the oil reserves on a global scale are not known and under debate between the different interest groups, this example shows that the predictive capability and the estimation of the resources are good enough to give early warnings. The global peak in oil production is projected between the year 2005 and 2020 [Rif02, Leg06]. Due to economic

fluctuations, the exact year cannot be identified but this is only of academic interest. The key message is that we live at the turning point today.

The exploration of oil deposits harder to tap, like oil sands, is already in progress, as well as the desperate attempts to increase the recovery rate from already depleted oil fields. Not only shortage due to natural limitation, also political and economic reasons contribute to a rise in cost of exergy and therefore a decrease in prosperity, currently experienced by many people due to the economic situation. Other fuel stock, like gas, uranium, and coal are also subject to the Hubbert characteristic and will be depleted in the near future. The Energy Information Administration projects an increase in coal consumption as gas and oil deplete [EIA08].

This is certainly one strong argument to reduce the dependency on fossil energy carriers. Another argument is the devastating effect of carbon dioxide, released by the oxidation of fossil fuels, on global warming. This effect is considered for a long time, like by Arrhenius in 1903 [AS03], Callendar in 1938 [Cal38] or by Revelle and Suess [RS57] in 1957. The global warming may result in dramatic changes of the climatic conditions on earth, such as sea level rise and shortage on fresh water due to extended melting of snow and ice in mountain area [IPC07]. Leggett came to the conclusion that mankind cannot afford to burn the remaining fossil fuels without putting the prosperity into severe risk due to climate changes [Leg06]. The only way out of this is the fast reduction of the dependency on fossil fuels, either by tapping the renewable exergy to a major extent or by mastering the nuclear fusion reaction. Reducing the energy consumption will buy time to mankind to make the transition happen but will not solve the problem as such. Both pathways, renewable sources and nuclear fusion will result in provision of electrical or chemical energy (like methane, or hydrogen) which needs to be stored for further use in mobile applications. This can be done either by accumulators like the lithium ion cell, or, if a quick refuelling time is required, by fuel cell systems.

Fuel cells are not an invention of today but the first poof of principle of the reversibility of the electrolysis of water was given in 1838 by Christian Friedrich Schönbein [Sch39] and Sir William Grove [Gro39]. Yet, the progress in material science during the past four to five decades makes possible what early visionaries of this technological pathway like Jules Vernes in «L'Île mystérieuse» [Ver75] (see cover page) and J.B.S Haldene envisioned.

Haldene wrote in "Daedalus or Science and the Future" in the year 1924 [Hal24]:

"... Water-power is not, I think, a probable substitute, on account of its small quantity, seasonal fluctuation, and sporadic distribution. ...
Ultimately we shall have to tap those intermittent but inexhaustible sources of power, the wind and the sunlight. The problem is simply one of storing their energy in a form as convenient as coal or petrol. ...
Even tomorrow a cheap, foolproof, and durable storage battery may be invented, which will enable us to transform the intermittent energy of the wind into continuous electric power. Personally, I think that four hundred years hence the power question in England may be solved somewhat as follows: The country will be covered with rows of metallic windmills working electric motors which in their turn supply current at a very high voltage to great electric mains. At suitable distances, there will be great power stations where during windy weather the surplus power will be used for the electrolytic decomposition of water into oxygen and hydrogen. These gasses will be liquefied, and stored in vast vacuum jacketed reservoirs, probably sunk in the ground. ...
In times of calm, the gasses will be recombined in explosion motors working dynamos which produce electrical energy once more, or more probably in oxidation cells. ...
The initial costs will be very considerable, but the running expenses less than those of our present system. Among its more obvious advantages will be the fact that energy will be as cheap in one part of the country as another, so that industry will be greatly decentralised; and that no smoke or ash will be produced..."

As Haldene pointed out, one characteristic of the renewable power sources like wind or solar energy is the discontinuity of energy release, and efficient energy storage systems are needed. Rifkin [Rif02] e.g. promotes the hydrogen economy based on a network of hydrogen and electricity as the primary energy carriers. The device chain of electrolyser, hydrogen storage and fuel cell could serve as such a storage system, though there are technical challenges to master.

A lot of public and industrial attention is devoted to the transportation sector in terms of reducing the dependency on fossil fuels. The advantage of hydrogen-electric based

mobility is the absence of hazardous exhausts and the increased efficiency in comparison to the internal combustion engine. For long-range mobility, the hydrogen-electric drive system, in comparison to available accumulator-electrical drive systems has a much shorter refuelling time and high energy storage density. Linde claimed to have the technology to refuel within 3 min [Lin09]. This is much shorter than the recharging time of any state-of-the-art accumulator system which has a characteristic charge time of three to four hours [Buc01]. Just recently, a group at MIT claimed to have identified materials that would allow to recharge lithium ion accumulators with a one to two order of magnitude reduced recharging time [KC09]. Time will tell if this concept will work out. Meanwhile, the two systems keep competing in one application and supplementing in others.

On the mobility sector, the polymer electrolyte membrane fuel cell (PEMFC) system is favourable due to its operating temperature range that enables sub 0 °C start-ups within seconds to 100 °C continuous operations (for a comparison of the different fuel cell systems see also Section 1.2.1 on page 6). The operating temperature range, being an advantage for the application, presents a challenge for the fuel cell engineering. Since water is the exhaust of the hydrogen-air fuel cell system, the stated temperature range covers two phase changes of the water which makes process engineering demanding. The challenges, currently preventing the large-scale application of PEMFC are the costs associated with the precious metal catalyst (platinum) and the durability due to material degradation. Both limitations touch on the presence of liquid water since liquid water hinders the gas transport to the catalytic reactive zone. This requires excessive catalytic loading and reactant feeds. The state-of-the-art fuel cell systems could be more efficient, more reliable and less expensive if the liquid water handling was improved.

Basically all the components the fuel cell consist of (flow field, gas diffusion media (DM), catalyst layer and membrane) have the potential for fine tuning with regard to liquid water handling but the focus of this work is on the DM. Here, a link between material design and water handling properties is missing. The field of hydrology is leading in characterisation, understanding and describing two-phase transport in porous media [Bea88]. Yet, the length scales in hydrology are three to six orders of magnitude larger than for fuel cell components which requires careful revision and eventually a modification of the models and concepts in light of the application to fuel cell gas diffusion media. The

aim of this work is detailed experimental and numerical investigation of isothermal water transport within the porous fibre structure of the gas diffusion media by assessing the two-phase transport models based on Darcy's law. Further, a link between mathematical mass transport description and material design will be established. The modelling of fuel cell performance as such is beyond the scope of this work.

1.2 Polymer Electrolyte Membrane Fuel Cell

1.2.1 The Principle

Fuel cells belong to the group of primary electrochemical cells like Zn/C battery. But unlike the batteries, educts and products of the chemical reaction are provided and removed continuously by external devices. The advantage is a continuously working power supply compared to a secondary cell (accumulator) or a battery which has to be recharged or replaced once the educts are exhausted.

The key feature of any electrochemical cell is a spatial separation between the oxidation (electron discharge, anode) and reduction (electron consumption, cathode) reaction. This requires an active layer where the electron transfers can take place (catalytic layer) and separate ways of transport. One mode of transport is required for the electrons (electrodes) and the other for the oxidised or reduced species to the reduced or oxidised counterpart (ion conducting separator). The latter is used as a distinctive feature of fuel cells. The different kinds and their major properties of fuel cells are listed in Table 1.1. Due to the operating temperature and simplicity of the system, the Polymer Electrolyte Membrane Fuel Cell (PEMFC) is regarded as well suited to power automotive and other mobile applications. Detailed properties and a description of the polymer electrolyte membranes are introduced in Section 1.2.3 on page 16ff. Since the focus of this work is on the PEMFC, the specifics of the other kind of fuel cells are not described here and the reader is referred to the literature e.g. [VLG03].

Table 1.1: Types and key characterisics of fuel cells

Type	Separator	Operating Temperature	Feed	
			Anode	Cathode
Alkaline Fuel Cell (AFC) [CK03]	Potassium hydroxide solution	50 °C - 200 °C	Hydrogen	Oxygen
Solid Oxide Fuel Cell (SOFC) [HS03]	Ceramic	700 °C - 850 °C	Hydrocarbons, Hydrogen	Oxygen, Air
Phosphoric Acid Fuel Cell (PAFC) [KK03]	Phosphoric acid	80 °C - 200 °C	Hydrogen, Methanol	Oxygen, Air
Molten Carbonate Fuel Cell (MCFC) [Mug03]	Molten carbonates	580 °C - 700 °C	Hydrogen, Methanol	Oxygen Air
Polymer Electrolyte Membrane Fuel Cell (PEMFC) [DR03]	Proton conducting polymer	$\leq$ 30 °C - 120 °C	Hydrogen, Methanol	Oxygen Air

The reaction in the fuel cell takes place on the catalytic layer which forms a continuous surface on the separator (more details on the catalyst layer are given in Section 1.2.4 on

page 18ff.). This implies that the reaction is surface-based in contrast to a volume-based reaction, like non-electrochemical reactions in the fluid phase. In order to transfer the educts to the catalytic layer, several structural features are employed. Educts are fed to the fuel cell by a single pipe and flow field structure, similar to heat exchanger geometries, to dispense the feed stream on a large area. Since the flow field also serves as the current collector, electrical contact between the flow field and the catalytic layer is required. If the flow field is in direct contact to the catalyst layer, the utilisation of the catalyst will be poor (more details on flow fields are given in Section 1.2.6 on page 24ff.). The regions of contact are not accessible by the gaseous educts, therefore, no reaction can occur. This is mitigated by the gas diffusion medium (DM), sandwiched between the flow field and the catalyst layer. Figure 1.1 shows the cross section through a PEMFC.

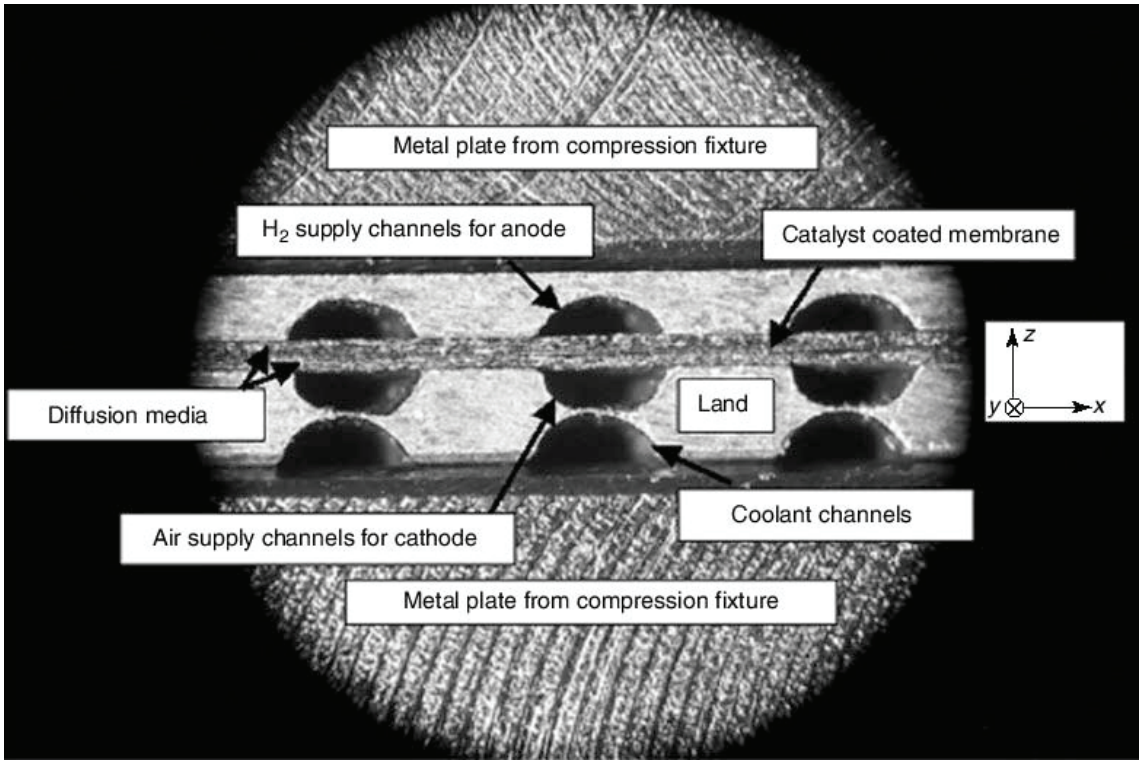

Figure 1.1: Cross section through a PEMFC (image from [MRFL03]).

The DM has to fulfil many requirements like conduction of heat and electricity as well as allowing gas and liquid transport to the catalyst layer and away from it. The varieties and details of DM will be explained in Section 1.2.5 on page 21ff.

The thermodynamic aspects and the components of a PEMFC with regard to their function and material is explained in the following. The mathematical descriptions of the components are only briefly touched in the comming sections with exception of the two-phase transport in the DM (Section 1.3 on page 28ff.) which is in the main focus of this work. A comprehensive overview on modelling of all fuel cell components can be found in the review articles like the one from Weber and Newman [WN04].

1.2.2 Thermodynamics

The electrochemical reaction in the PEMFC is the conversion of hydrogen, hydrogen rich gas, or methanol and oxygen or oxygen rich gas (like air), to water, electricity and, in certain fuel cell systems, carbon dioxide. The electrochemical reactions in the PEMFC are limited by the ability of the catalyst to maintain the corresponding reaction at the maximum operating temperature range up to 120 °C. Beside of hydrogen oxidation, only few organic oxidation reactions like methanol oxidation are possible. Hydrogen or methanol oxidation on platinum or platinum/ruthenium catalysts are technically the most relevant reactions. Nevertheless, research on other reaction systems in the PEMFC are ongoing but not in the scope of this work. The focus of this work is on the hydrogen/air reaction [HV81]:

$$\begin{array}{rcrcll} & & \mathrm{H_2} & \rightleftharpoons & 2\mathrm{H^+} + 2\mathrm{e^-} & \\ \frac{1}{2}\mathrm{O_2} & + & 2\mathrm{e^-} & \rightleftharpoons & \mathrm{O^{2-}} & \\ \hline \frac{1}{2}\mathrm{O_2} & + & \mathrm{H_2} & \rightleftharpoons & \mathrm{H_2O_{liq}} & \Delta_f G^\circ = -237.1 \text{ kJ/mol} \end{array} \tag{1.1}$$

The open cell potential U_0 is

$$U_0 = -\frac{\Delta G}{z^* F} = -\frac{\Delta_f G^\circ}{2\ F} = 1.23 \text{ V} \tag{1.2}$$

z^* represents the number of electrons in reaction, F denotes as the Faraday constant, ΔG the Gibbs free energy and $\Delta_f G^\circ$ relates to the formation at 298.15 K and 100 kPa (standard condition). The mechanistic details for the anodic and cathodic reaction can be found in [HV81]. It is believed that the anodic reaction (hydrogen oxidation HOR) and the cathodic reaction (oxygen reduction ORR) consists of several steps. The hydrogen oxidation to protons is associated with less losses since the heat of adsorption on Pt

surfaces accounts for the energy required to break the H–H bond. The sequence of the anodic reaction is assumed as follows:

$$\begin{aligned} &H_2 \rightleftharpoons H_{2,ad} \\ &H_{2,ad} \rightleftharpoons 2H_{ad} \\ &H_{ad} + H_2O \rightleftharpoons H_3O^+ + e^- \end{aligned} \tag{1.3}$$

or

$$H_{2,ad} + H_2O \rightleftharpoons [H_{ad} \cdot H_3O]^+ + e^- \rightleftharpoons H_{ad} + H_3O^+ + e^- \tag{1.4}$$

H_{ad} denotes as the hydrogen, adsorbed on the surface.

On the cathode side, the situation is more complicated since the O–O bond is stronger than the H–H bond. There are two different reaction mechanisms hypothesised depending on the adsorption site on the catalyst

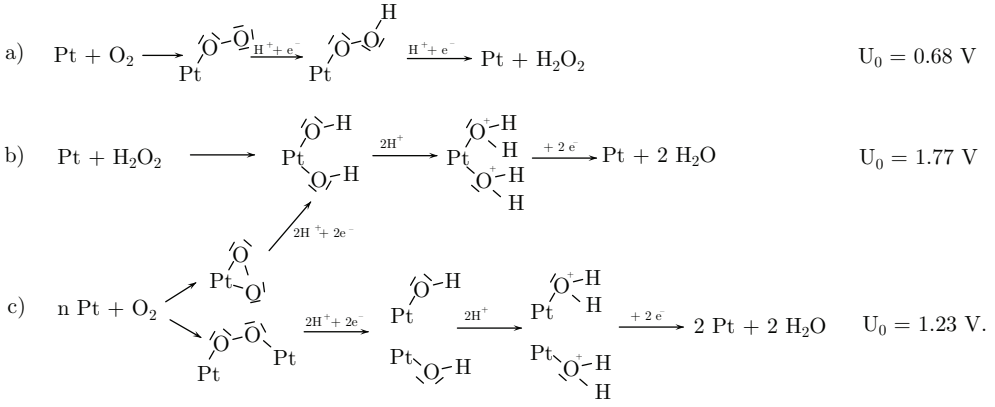

(1.5)

The formation of hydrogen peroxide has a potential of 0.68 V, the oxidation of hydrogen peroxide has a potential of 1.77 V, and the direct oxidation of hydrogen has one of 1.23 V. Since all the processes take place at the electrode simultaneously, a mixed potential is measured. This is the reason why the theoretical open cell potential of 1.23 V is not seen on hydrogen-oxygen (air) fuel cells.

The temperature dependence of the open cell potential is calculated from the Gibbs free energy

$$\Delta G_R(T) \quad = \quad \Delta \mathcal{H}_R(T) - T\ \Delta S_R(T). \tag{1.6}$$

The enthalpies $\Delta\mathcal{H}_{\mathrm{R}}(T)$ and entropies $\Delta S_{\mathrm{R}}(T)$ of the reactions are calculated according to Equation 1.7 and Equation 1.8:

$$\Delta\mathcal{H}_{\mathrm{R}}(T) = \sum \nu_i^* \left[\mathcal{H}_i^\circ + c_{p,i}\ \Delta T\right] \tag{1.7}$$

$$\Delta S_{\mathrm{R}}(T) = \sum \nu_i^* \left[S_i^\circ + c_{p,i}\ \ln\left(\frac{T}{T_0}\right)\right] \tag{1.8}$$

The temperature dependence of the three reactions is plotted in Figure 1.2, based on the values shown in Table 1.2, calculated according to Equation 1.2, while $G_{\mathrm{R}}(T)$ replaces $\Delta_f G^\circ$.

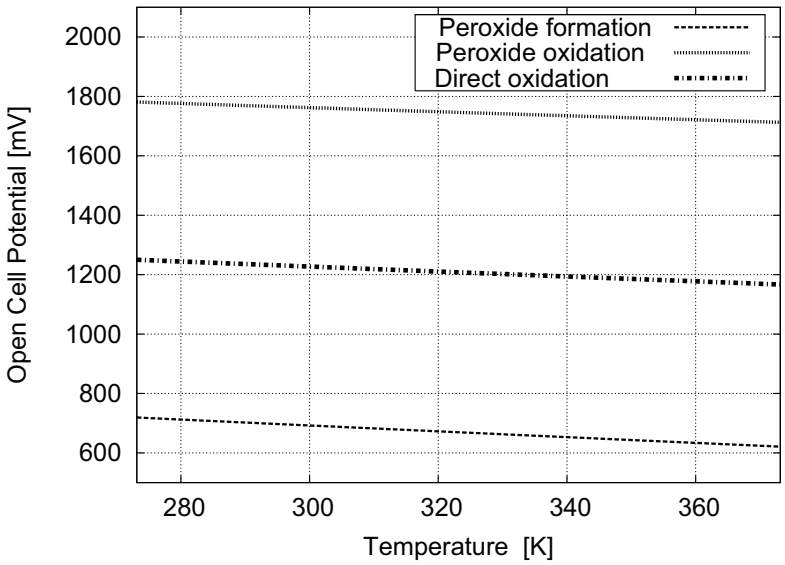

Figure 1.2: Temperature dependent equilibrium potential for the different paths of the oxygen reduction reaction from 293 K to 373 K (Equation 1.5).

The pressure dependence of the equilibrium potential is calculated according to Nernst equation:

$$U(p) = U_0 - \frac{\Re\ T}{z^*\ F}\ \sum \nu_{\mathrm{i,g}}^* \ln\frac{p}{p_0} \tag{1.9}$$

$\Re$ represents universal gas constant while $\nu_{\mathrm{i,g}}^*$ denotes as stoichiometric coefficient of the gaseous species. For the formation of hydrogen peroxide (reaction a) in Equation 1.5 the number of electrons $z^* = -2$; for the oxidation of hydrogen peroxide (reaction b) in Equation 1.5 $z^* = -1$. For the direct water formation (reaction c) in Equation 1.5

Table 1.2: Thermodynamic Data ‡

Species i	$\Delta_f\mathcal{H}^\circ$ kJ/mol	$\Delta_f S^\circ$ J/mol/K	c_p J/mol/K	ν_i^* [Eq. 1.5] a)	b)	c)
O_2	0	205.2	29.4	-1	0	-0.5
H_2	0	130.7	28.8	-1	-1	-1
H_2O(liq)	-285.8	70.0	75.3	0	2	1
H_2O_2(aq)	-191.17*	143.9 *	89.1**	1	-1	0

‡ Data from [Lin96] at 298.15 K besides of * data from [Hoa85]; ** data for H_2O_2(liq) assumed.

$z^* = -1.5$ is found [HV81]. The pressure dependence from 100 kPa to 1000 kPa (relative to $p_0 = 101.3$ kPa) of the equilibrium potential of the three reactions at 298 K is depicted in Figure 1.3.

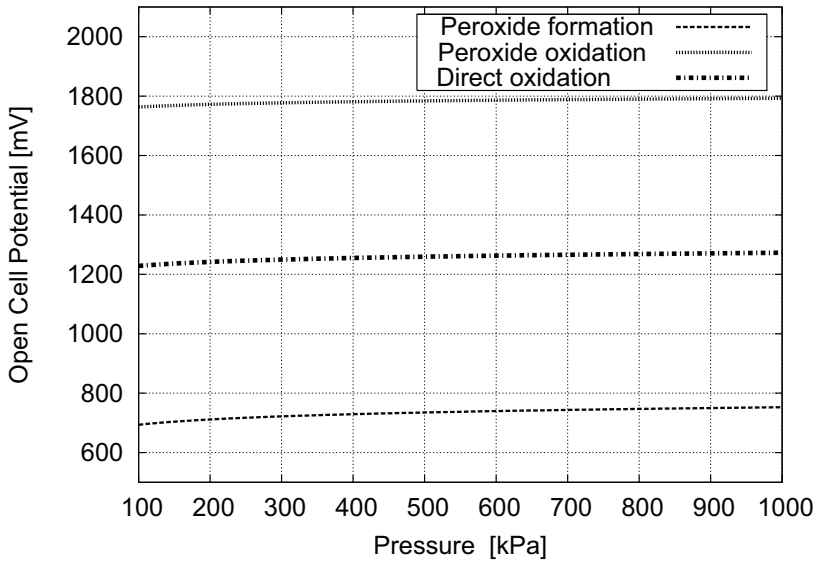

Figure 1.3: Pressure dependent equilibrium potential for the different paths of the oxygen reduction reaction at 298 K for pressures ranging from 100 kPa to 1000 kPa relative to $p_0 = 101.3$ kPa (Equation 1.9).

Based on the equilibrium potential, a low operating temperature and a high pressure is desirable, but based on the kinetics and system requirements (dissipation of excess heat), high temperatures are preferred. The aim is the suppression of the hydrogen peroxide formation for three reasons:

- The decomposition of the peroxide at about 0.7 V decreases the cell potential by creating a mixed potential.
- The mobility of the hydrogen peroxide is a concern, since it can diffuse away from the electrode and might not serve as an educt for the desired electrochemical reaction.
- The diffused hydrogen peroxide can damage the membrane and carbon components like catalyst support.

Depending on the quality and purity of the electrode, the potential on the electrode is always less than the theoretical potential for the direct formation of water from hydrogen and air due to different reaction mechanisms. This situation is not getting better when current is drawn from the fuel cell, as will be discussed next.

The efficiency of an electrochemical device (η_{el}) is expressed by the ratio of the produced power $P_{\text{el}} = UI$ and the theoretical power $P_0 = U_0 I$ with U as the potential and U_0 as the theoretical rest potential, I denotes as the electric current:

$$\eta_{\text{el}} = \frac{P_{\text{el}}}{P_0} = \frac{UI}{U_0 I} = \frac{U}{U_0} \tag{1.10}$$

The efficiency of the fuel cell is a function of the drawn current. The potential-current density characteristic (Figure 1.4) is the most important parameter for fuel cell assessment.

The potential-current density characteristic is dominated by three loss mechanisms which overlap but are most dominant at distinct regions of current density. Each of the individual regions is associated with specific components and operating conditions, to be discussed in the component section, but an overview of the governing equations will be given here.

The mechanisms at the catalyst are rate determining and the major source of losses at low current densities. According to the Butler-Volmer Equation

$$i(\phi) = i_0 \left[\exp\left(\frac{(m^* + \psi)\, z^* F \phi}{\Re T} \right) - \exp\left(-\frac{(m^* + 1 - \psi)\, z^* F \phi}{\Re T} \right) \right], \tag{1.11}$$

expressed for a multi-step reaction, the current is a function of the potential difference (over potential ϕ) between the actual potential and the theoretical potential [BR73]. i denotes

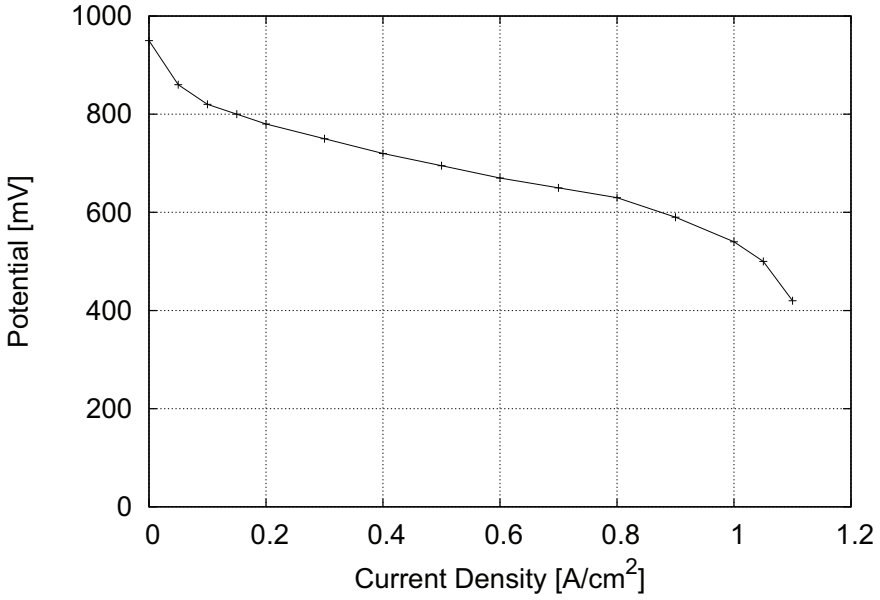

Figure 1.4: Potential-current density characteristic of a hydrogen-air fuel cell.
Conditions: 353 K, constant gas flows, sufficient for 2 A/cm^2 (stoic 1). Anode humidity: 80 % RH, cathode humidity 7 % RH.

as the current density, i_0 as the exchange current density (temperature dependent), m^* the number of electrode reaction steps before the rate determining step, ψ transfer coefficient, a property of the catalyst, z^* the total number of involved electrons. The Butler-Volmer equation is only valid near the equilibrium and both anodic and cathodic part of the half reaction are considered. In the fuel cell only one of the two parts is relevant for each half reaction. Therefore, the potential of the cathode (oxygen reaction) and the anode (hydrogen reaction) can be written as

$$\phi_{\mathrm{kin,O_2}} = -\frac{\Re T\left(\ln\ i - \ln\ i_{0,\mathrm{O_2}}\right)}{\left(m^*_{\mathrm{O_2}} + 1 - \psi_{\mathrm{O_2}}\right) z^* F} \tag{1.12}$$

and

$$\phi_{\mathrm{kin,H_2}} = \frac{\Re T\left(\ln\ i - \ln\ i_{0,\mathrm{H_2}}\right)}{\left(m^*_{\mathrm{H_2}} + \psi_{\mathrm{H_2}}\right) z^* F} \tag{1.13}$$

respectively. The kinetic potential losses become less severe at increased current density but the proton resistance of the membrane becomes dominant and the potential decreases

linearly with the current density (Ohm's law)

$$\phi_{\text{mem}} = R_{\text{mem}}\, i. \tag{1.14}$$

The resistance of the ion conductor is humidity and temperature dependent and represented by R_{mem}.

A third potential loss dominates the performance at high current densities when the mass transport rate of the reactants to the catalyst becomes the rate limiting step. By combining Fick's law of diffusion with the concentration dependent cell potential (Nernst's law), a description of the diffusion dominated potential loss is obtained:

$$\phi_{\text{diff}} = \frac{\Re T}{z^* F} \ln\left[1 - \frac{|i|\delta}{z^* F D c}\right] \tag{1.15}$$

D denotes as Fick's diffusion constant, δ as the thickness of the transfer layer, and c as the concentration of the educt (O_2 or H_2). The potential is the difference of the open circuit potential U_0 from the sum of the kinetic and diffusive losses on anode and cathode ϕ_{kin} and ϕ_{diff}, as well as the loss caused by the membrane

$$U = U_0 - \phi_{\text{kin,O}_2} - \phi_{\text{kin,H}_2} - \phi_{\text{mem}} - \phi_{\text{diff, H}_2} - \phi_{\text{diff, O}_2}\ . \tag{1.16}$$

If Equation 1.16 is normalised by the open cell potential U_0, the efficiency will be obtained, while by multiplication with the current density the power density is calculated. For better illustration of the individual contribution, the individual over-potentials and the resulting efficiency/power-current density plot is depicted in Figure 1.5. The parameters are chosen arbitrarily and just for illustration. The mechanisms of potential losses and the key parameters to minimise the losses are subject of the next section.

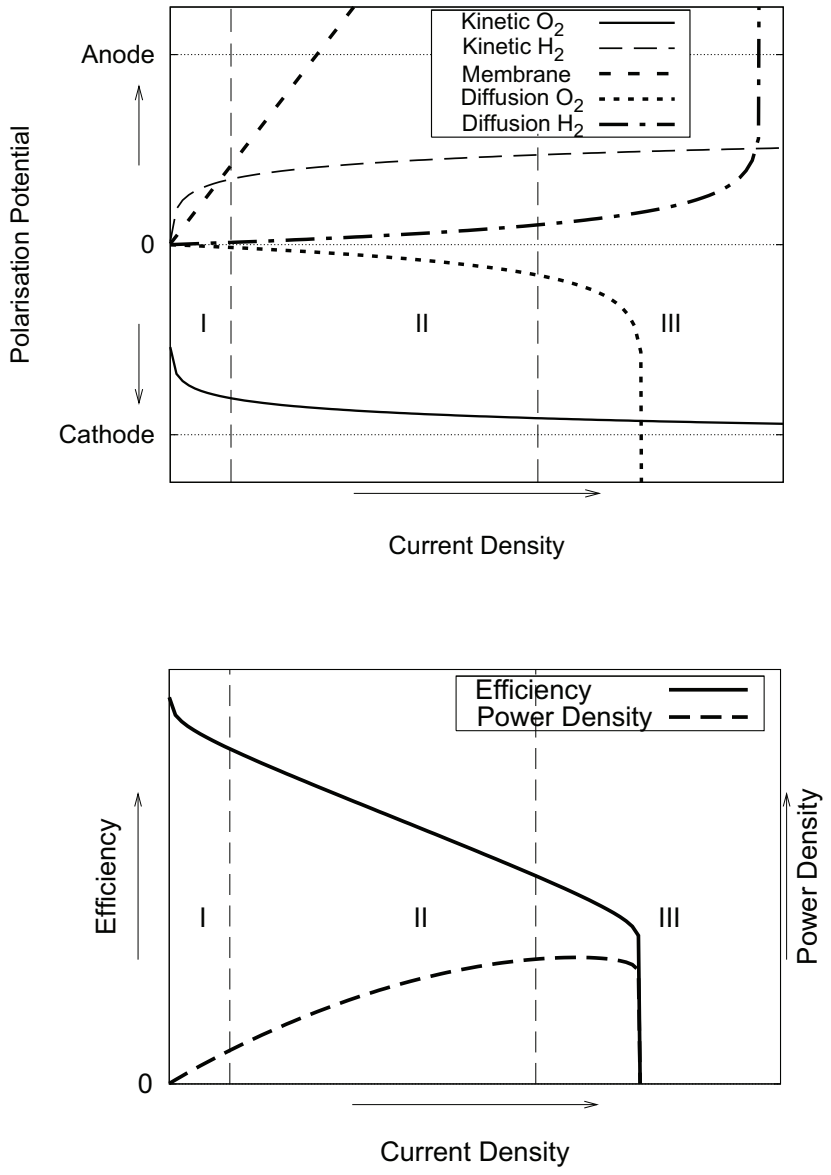

Figure 1.5: Top: Polarisation potential-current density characteristic for processes on cathode, membrane, and anode. Bottom: Efficiency and power density as a function of current density. I: kinetic region, II: electrolyte region, III: mass transport region.

1.2.3 Membrane

The polymer electrolyte membrane is the central compontent of the PEMFC. Four requirements are to be fulfilled by a PEMFC membrane:

- Gas impermeability,
- Chemical and electrochemical stability,
- Ion (Proton) conductivity,
- Electrical insulation.

Ion conducting polymers (ionomer) fulfil these requirements. Nafion®, a ionomer with a fluorinated backbone and sulfonated side chains (PFSA) produced by DuPont (structure see Figure 1.6), primarily used for chloro-alkali electrolysis, is the most prominent example. Although invented in the 1970's [Gro72], this material is still widely used in PEM fuel cells but due to the high costs, the limited operating temperature, the humidity requirements, and the environmental issues associated with fluorine chemistry there is an intense search for alternatives. The major challenge is the long-term stability of alternative hydrocarbon membranes due to the instability against hydrogen peroxide formed on the cathode (see Section 1.2.2 on page 8ff.) [YYX$^+$02, HR98]. The proton conductivity in the ionomer establishes when water interacts with the acidic (sulfonic) groups. With increasing water content the hydrophilic side chains and the hydrophobic backbone begin to establish a phase separation, resulting in water filled channels where the proton conduction takes place [CJTD06]. Two conduction mechanisms are assumed, the fast proton transfer from one hydronium ion to the next water molecule (Grotthuss mechanism [DG06], see also right sketch in Figure 1.6) and the slower electro-osmotic drag of hydronium ions.

The more water is adsorbed in the polymer the better the proton conductivity becomes, but with an increasing number of acidic groups, the solubility of the polymer in water increases. A trade-off between mechanical stability and proton conductivity is necessary. The ratio of the molar mass of the polymer repeat unit divided by the molar mass of water, called equivalent weight, serves as the parameter of comparison to characterise the ionomers with regard to ion conduction and water uptake. The proton conductivity as a function of water content in the membrane is depicted in Figure 1.7.

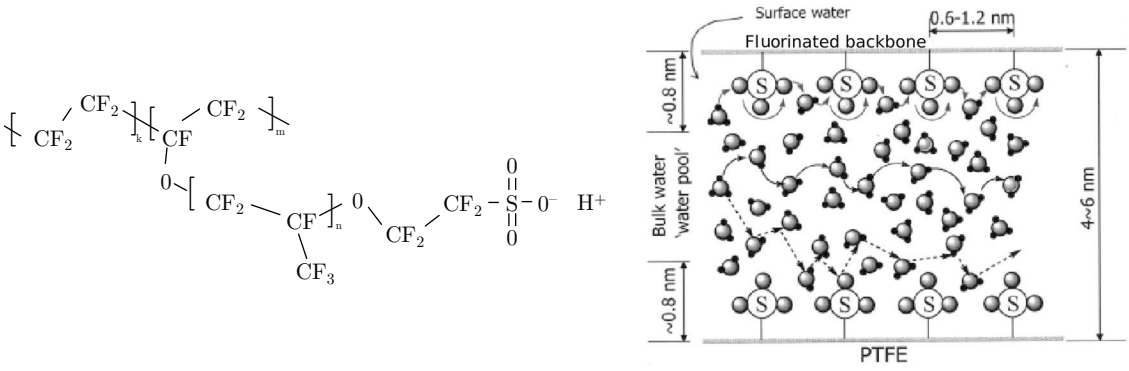

Figure 1.6: Left: Structural formula of Nafion®. Right: Conduction mechanism (figure taken from [CJTD06]).

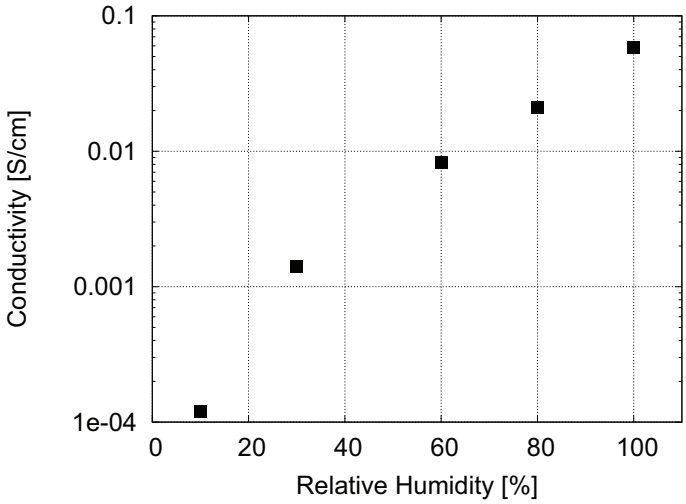

Figure 1.7: Conductivity of Nafion® 1100 as a function of humidity [ASC+03].

Considering the kinetic effects of the oxygen reduction reaction and the fuel cell system requirements, an operating temperature as high as possible is desired, but since the sulfonation reaction is reversible, the ionomers based on sulfonic groups cannot sustain temperatures above 120 °C [DR03] for a time long enough to operate a fuel cell system. Alternatives are membranes relying on phosphoric acid like doped polybenzimidazole (PBI) [WWW+95].

An empirical mathematical description of the ionic conductivity of the membrane was published by Springer and Zawodinsiki [SZG91] in 1991. On a more fundamental basis, molecular modelling with a variety of different approaches to simplify quantum chemistry

is in progress. This approach targets the design of new polymer membranes rather than to predict the overall fuel cell performance. A comprehensive review on this topic can be found by Kreuer et al. [KPSS04].

The membrane models, either based on molecular or phenomenological approach, shall describe the conductivity as a function of humidification. Nafion® exhibits the particular behaviour that the equilibrium water concentration in the membrane is different when the membrane is equilibrating with liquid water (22 molecules of water per sulfonic acid group) or saturated water vapour (14 molecules of water per sulfonic acid group). This so-called 'Schröder's paradox' (Schröder studied the swelling behaviour of gelatin and found an increased water vapour pressure of gelatin, equilibrated with liquid water previously [Sch03]). This property of Nafion® represents a challenge for the numerical modelling of PEM fuel cells since the proton conductivity jumps discontinuously once liquid water appears. Different macroscopic approaches like Weber and Newman's [WN03] had been suggested to overcome this challenge by assuming diffusive water and proton transport in the vapour equilibrated region and hydraulic transport in the liquid equilibrated zone, including weighting factors to handle the transition. As a summary, there are several more or less empirical macroscopic models in use. With increasing computing power, the fundamental models on molecular level are getting towards domain sizes big enough to analyse the interaction of the non-functional backbone with the functional side chains. This allows for studying the phase segregation like Jang and Goddard [JG07] did.

1.2.4 Catalyst

The hydrogen oxidation, as well as the oxygen reduction reaction in the PEM fuel cell is heterogeneous since the educts are in gas phase (O_2 and H_2), and in liquid and ionomer dissolved (H_3O^+), while the product is generated on a solid catalyst in quasi-liquid environment (electrolyte). In order to engineer such a reaction, three requirements on the catalyst have to be fulfilled:

- Gas access to the catalyst,
- Proton access to the catalyst,
- Electrical connection to the catalyst.

The electrical connection is granted by the connectivity of neighbouring catalyst particles or the support structure. The gas has access to the exposed catalyst surfaces. Finally, the protones reach the reaction zone due to the contact between the catalyst and the electrolyte. This results in the requirement of a three-phase zone, since the solubility and migration rate of oxygen and hydrogen in water and the common electrolytes are not sufficient to enable the desired current densities. The situation at the catalyst is sketched in Figure 1.8.

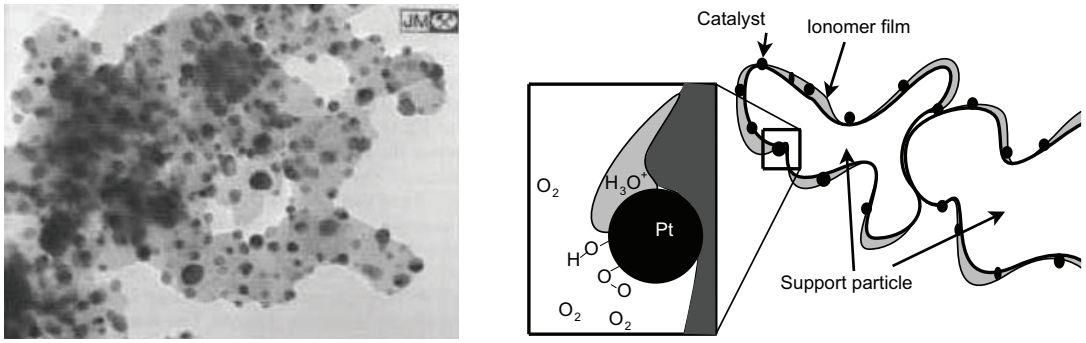

Figure 1.8: Left: TEM image of Pt/Cr structure on XC72R carbon black, scale: x 530 000 (image taken from [Tho03]). Right: Sketched situation at the three-phase zone.

The challenge in the area of the catalysts is the oxygen reduction reaction as indicated in the previous section. Common catalyst systems are noble metals of the platinum group (Pt/Ru ...), depending on the fuel composition like pure hydrogen, reformat (hydrogen rich gas mixture) or methanol. The anode catalyst contains pure platinum or a mixture of platinum/ruthenium for hydrogen, reformat or methanol oxidation. On the cathode, pure platinum or a platinum alloy is used. The kinetic losses on the anode, especially in applications where pure hydrogen is used, are small. The main challenge is the oxygen reduction reaction on the cathode due to the competing reactions (hydrogen peroxide formation) and the low exchange current density. The latter can be mitigated by a high catalyst loading (0.5 mg/cm^2 based on membrane surface area [SH01]), but this is not desired for economic reasons.

The catalyst utilisation is a topic of great importance and the application of pure and fine dispersed catalyst is replaced by supported catalysts where the catalytic active material is deposited with a thickness of several atom layers on a support structure like carbon

black. The long-term stability of such systems presents a challenge for this approach since the catalyst loses surface area due to migration of individual atoms to locations of lower energy driven by electrical potential cycling [Ant03, YTA+06], as well as due to corrosion mechanisms on the support structure driven by various mechanisms like hydrogen starvation [YGM+06, PD06]. Temperature-induced surface area loss due to sintering seems not to be a problem for the PEM fuel cell due to the comparatively low operating temperature [Ant03].

For mitigation of degradation and to design the catalyst layer, first a fundamental understanding of the chemical and physical processes is necessary which are condensed in a mathematical description of the system to get access to properties not accessible by measurements. These properties are further used to assess sensitive parameters and predict the influence of design modifications. The mathematical description of the catalyst layer is rather complex since all the mechanisms are coupled and depend on boundary conditions resulting from other models (membrane and DM). The processes involved are the proton and oxygen/hydrogen transport in the ionomer dependent upon humidity, temperature, pressure, heterogeneous catalytic reaction, and two-phase mass transport. The structural parameters of this system, like connectivity of the particles and ionomer distribution are rather difficult to get by experiments. This is reflected by the models which are mostly phenomenological, as the one introduced by Eikerling [Eik06]. The basic idea of this model is to use a catalyst utilisation factor obtained by the following approach: The different components of the catalytic layer (carbon particles with platinum sites and ionomer) are represented by a coagulation of spheres with different properties and based on a Lennard-Jones kind of interaction. The morphological appearance of such a system is calculated. For the obtained morphology the usual constitutive relations for two-phase transport are determined. The result is a catalyst utilisation dependent on temperature, stochiometry, current density and structural parameters. Other authors focus on degradation mechanisms like Franco and Mathias [FG08]. These are the first steps towards a quantitative description of the processes in the catalyst layer.

1.2.5 Diffusion Medium

The gas diffusion medium (DM) is sandwiched between the flow field (coarse reactant distribution) and the catalyst layer (gas consumption). Its main function is the fine distribution of the reactant all over the electrochemically active area. Associated with this function are other requirements deduced from the location of the DM in the fuel cell sandwich. These requirements are:

- Electrical and thermal conductivity,
- Corrosion robustness,
- Gas and liquid permeability,
- Mechanical stability.

The material type, the DM can be made from, is determined by the electrical and thermal conductivity. Usually metal-based or carbon-based materials are chosen. Most commonly carbon is used due to its corrosion resistance (historically, the DM development started with the phosphoric acid fuel cell where metal corrosion is an issue). The requirement of gas and liquid permeability sets the structure. Open porosity is required to allow the mass transport. Sintered metal, metal screens, carbon fibre cloth, and non-woven fibre structures are employed (see Figure 1.9).

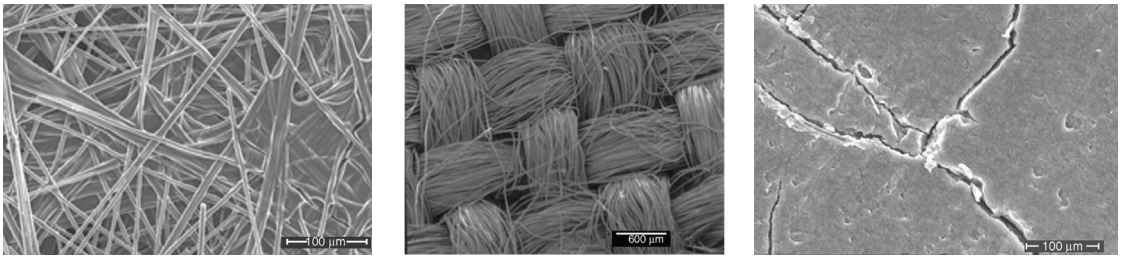

Non-woven Cloth Micro porous layer

Figure 1.9: Micrographs of DM substrate structures and micro porous layer (images taken from [MRFL03]).

The structure is closely related to the mechanical properties. In order to ensure good thermal and electrical conductivity between catalyst layer and the DM, as well between the DM and the flow field, sufficient stiffness is required. A soft DM can help to even

out its own thickness tolerances and the one of the flow field, but also bulges into the gas channels and restricts the gas flow. A detailed study on compression effects was done by Nitta [Nit08]. The DM plays a key role to set the mechanical parameters for stack assembly and mechanical integrity during operation (vibration resistance). It is desirable for manufacturing to have the freedom to roll the DM. This is the area of tension, a trade-off has to be made with regard to the brittleness.

The fluid properties provide a similar dilemma. Gas has to be transferred in one direction towards the catalyst layer, while water in vapour and liquid phase has to be transferred in the opposite direction. On the other hand, the transport must not be too effective, otherwise membrane and ionomer in the catalyst layer dry out. Figure 1.10 shows the influence of humidity on the current characteristic of a fuel cell at a potential of 600 mV [MRFL03]. Starting at dry conditions and becoming more humid, the current increases at constant voltage until the climax with optimal humidity is reached. Then the current drops due to flooding events.

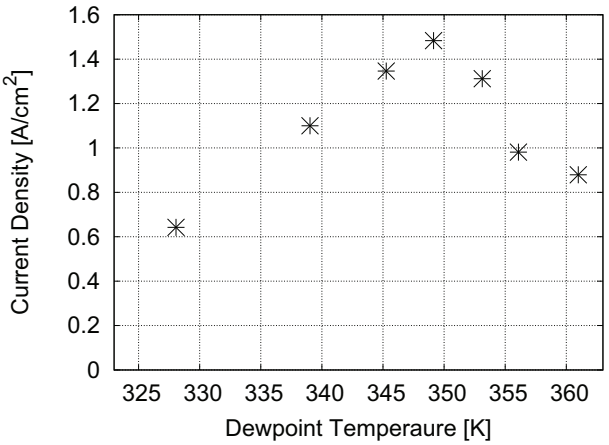

Figure 1.10: Humidification effect on current density: Current density development with increasing temperature of the humidifiers on anode and cathode (symmetrical humidification); cell temperature 353 K; potential 600 mV (data taken from [MRFL03]).

To find a fine balance for water management properties under wet and dry conditions, functional coatings are applied to the base substrate. In order to prevent the liquid water from being soaked into the porous structure resulting in a complete blocking of the gas access, a hydrophobic coating, like PTFE is applied by e.g. a dipping process with a following sintering step. Depending upon the sintering conditions, the distribution

of the PTFE varies [MRFL03]. This treatment forces the water into the largest pores and a positive pressure is required to penetrate the pore space. A second type coating is applied on the interface between the DM substrate and the catalyst layer, referred as micro porous layer (MPL). The layer has a pore diameter in the range of 10 nm to 1 µm [KKL$^+$02, PSL$^+$01] (measured with mercury porosimetry) and provides a transition region between the pores in the catalyst layer and the substrate. The layer is composed of a mixture of carbon powder and PTFE and coated on the DM substrate. Since the carbon support of the catalyst and the carbon in the MPL are similar or even identical, the pore structure is similar and the MPL ensures an intimate contact between the catalyst layer and the DM substrate. A micro graph of the surface of the MPL is shown in Figure 1.9 (right).

According to the IUPAC nomenclature [MLE01], the term 'micro porous' does not apply since the pores are too large but, nevertheless, this expression is widely used in the fuel cell community. The micro porous layer definitely helps to increase the performance of the fuel cell under wet operating conditions [AKP$^+$07], but the exact mechanism is still not yet identified. One hypothesis is the increased thermal resistance which allows for higher temperature at the catalyst layer. In combination with the strong hydrophobicity this results in the assumption that the water permeates in vapour phase only [Wie01]. Another hypothesis is that the liquid water pressure inside the MPL is huge compared to the pressure in the substrate and thus, a driving force exists to move the liquid water away from the catalyst layer. By this mode of operation, mud cracks and other defects would help for the selective saturation of the MPL. The mathematical description of the processes in the DM follows the laws of conservation, most commonly by the application of constitutive relations. These have the advantage of less computational effort in comparison to structure resolved calculations. The main challenge is the accurate representation of liquid water transport in the mostly hydrophobic structure. The physical understanding of this component regarding the two-phase transport characteristic is not highly developed and still under investigation. The most state-of-the-art models for the DM are macroscopic and with respect to the two-phase transport, these models were taken from the field of soil science. Few semi-microscopic models have been presented, representing the DM as a network of interconnected capillaries [NK03, SW08] and some models treat the DM on

a really microscopic level, like the morphological model from [SMB+06]. More on water transport in porous systems will be discussed in Section 1.3 on page 28ff. and farther back.

1.2.6 Flow Field

Also the flow field, like the DM, has to serve several partly contradicting requirements which can be grouped into two blocks.

1. Fluid mechanical requirements:
    - Gas distribution with low pressure drop requirements,
    - Liquid water handling capability,
    - Coolant distribution.
2. Material related requirements:
    - Electrical conductivity,
    - Heat conductivity,
    - Corrosion resistance,
    - Mechanical stability,
    - Producibility.

It is not to forget the usual requirements of cheap manufacture and low material costs. The group of the fluid mechanical requirements are fully covered by the geometry of the plate. There are several ways to distribute the gas uniformly across the active area. In fuel cell systems using pure hydrogen and oxygen at elevated temperatures, the flow field can consist simply of dimples or just be a porous plate. But if air is used as cathode feed, those simple structures are no longer appropriate, even on the anode, since nitrogen can permeate to the anode side during certain system operation modes (dead-ended or recycling the anode stream). The reason is that in multi-component feed streams the reactant has lower partial pressure and, therefore, an increased transport resistance towards the reaction zone. Depletion zones are likely to be formed in the simple structure. To avoid depletion, the feed streams are directed in a single meandering channel or several channels either straight or meandering, with a trade-off between pressure drop

and distribution control. Basic design rules for manifolds can be found in [Wag01]. The flow field design can also show a combination of the different types. Flow fields with the highest pressure drops have non-continuous channels (interdigitated) to force the feed streams into the gas diffusion layer. A review of the different flow field geometries was presented by Li and Sabir in 2004 [LS04]. The representation of the different concepts is depicted in Figure 1.11.

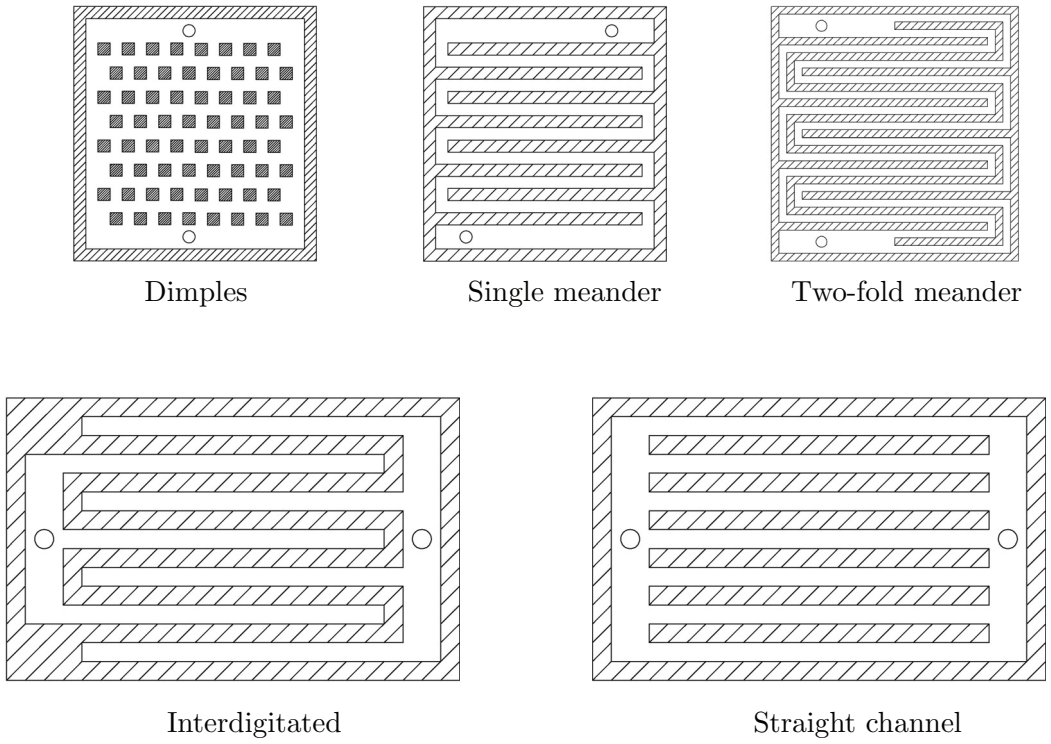

Figure 1.11: Common flow field geometries.

The key to the liquid water handling capability lies in the profile of the channel in connection with the surface energy of the channel walls. The combination of the two parameters dictates whether the liquid water forms a bead or a film. In cases of acute angled corners and hydrophilic walls, the water accumulates preferentially in the corners if the Concus-Finn condition is fulfilled [CF69]. The freedom to design the channel cross section is limited by the manufacturing technology of the bipolar plate like stamping, milling, injection moulding, etching and others. The typical cross sections are depicted in Figure 1.12. Characteristic parameters are the flank angle α, the width W and the height

h. Typical dimensions are 0.5 mm $\leq W \leq$ 2 mm, 0.5 mm $\leq h \leq$ 2 mm, $45° \leq \alpha \leq 90°$ [WV03]. Since it is unlikely that all the material requirements like forming, electrical and thermal conductivity, as well as inexpensiveness and corrosion resistance can be fulfilled all by the material itself, coatings are applied to cover the corrosion and wetting properties. Open literature on coatings like [WSKB02] is rare, since this is key technology for the fuel cell stack manufacturers.

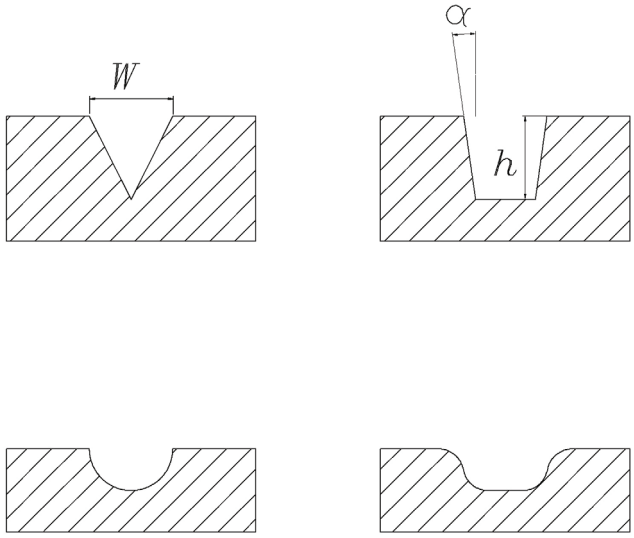

Figure 1.12: Various channel cross sections.

The former said applies to single cells for small power applications and lab cells, as well as for fuel cell stacks for more power demanding applications. The fuel cell stack consists of many single cells connected electrically in serial mode, but in parallel mode with regard to the feed streams. This sets the requirements for the thermal control of the fuel cell stack, being another function the bipolar plate has to fulfil.

For fuel cell stacks, anode and cathode flow field are on the two opposite sides of the flow distribution plate (bipolar plate). Depending on the cooling concept, bipolar plates consist either of a single sheet of material with the flow fields on both sides or of two sheets of material bonded together with a coolant flow field in-between. For the first type, separate coolant plates inserted regularly between the electrochemically active cells, are necessary. This leads to non-uniform temperature distribution from plate to plate. The

second approach enables a more uniform temperature distribution from cell to cell, but is more demanding with regard to plate design. The latter concept is very common for automotive application and will be discussed in detail next.

In order to get a high volumetric power density, it is advantageous to design the anode and cathode flow field in such a way that the coolant flow field is formed by the back sides of anode and cathode plate (nested concept for stamped sheet metal bipolar plates [Goe09]). If carbon composite or graphite are the materials of choice, this concept is difficult to use due to brittleness of the material. For such materials, the coolant flow channels are incorporated in the back side of the cathode plate, since heat is released by the oxygen reduction reaction on the cathode.

Standard fluid mechanic concepts are employed to calculate pressure drop of the flow field [BD01a], the uniformity of the flow distribution [Pha05], and the liquid water behaviour [RRF08, JZQ06a, JZQ06b]. But nevertheless, there is still work to be done to fit two-phase channel flow into the macroscopic descriptions by constitutive relations.

1.3 Momentum Transfer in Porous Systems

1.3.1 Different Model Depths

The aim of this section is to explain the theoretical background of two-phase momentum transport in order to set the experimental work of the thesis in relation to the state-of-the-art description of simultaneous water and gas transport in porous media. The analytical and empirical aspects of the state of the art theory is discussed.

All descriptions of physical phenomena (model) can be done at different levels of complexity. Depending on the question that has to be answered by the model, the proper level has to be chosen to get the best answer in shortest time. The simplest model gives the fastest and computationally cheapest answer. In case of water and gas transport in porous systems, this is based on constitutive relations like Darcy's law (Equation 1.30 on page 37). Here, the individual motion and momentum of the involved molecules are not resolved, but the resulting net effect of the combined motion and momentum exchange is described. Furthermore, the structural features within the fluid domain are not resolved and are treated as a net resistance to the flow. The model complexity is increased by resolving the structural features and the interface between liquid and gas phase like the approach of Lattice-Boltzmann or free surface models (for details of these models see e.g. [CD98] and [SZS99]). These models are statistical ones with respect to the molecules of the fluid phases, but the solid phase is represented in a detailed manner. While the most complex models resolve also the motion of individual molecules like the Monte Carlo simulation or molecular modelling (details of these models can be found by e.g. [HT78] and [FS02]). The constitutive relations and the property constants can be derived either from the detailed models with the aid of statistical methods from a theoretical point of view, or by empirical curve fitting of experimentally measured data from an applied point of view. Typically, the latter approach limits the range of applicability of the model to the system that was used to obtain empirical data on the constitutive and transport property constants. The required level of model complexity for a given situation depends upon the size of the system and the required accuracy. Dimensionless numbers (e.g. Bond number Bo, see Section 1.3.6 on page 52ff.) are used to guide the decision. The most challenging situations are the cases that require higher model complexity in one region of the

control volume and allow for simpler physical representation in other regions (multi-scale modelling). Also, cases where the scale of the characteristic dimensionless numbers are such that the effects in comparison are similarly important (transition region between two scales).

The most general and simplest definition is a conservation equation describing the temporal change of a property Π by a linear function of the spatial gradient of that property or a related property ϖ, like momentum, heat, and species:

$$\begin{aligned} \begin{pmatrix} \left(\frac{d\varpi}{dt}\right)_x \\ \left(\frac{d\varpi}{dt}\right)_y \\ \left(\frac{d\varpi}{dt}\right)_z \end{pmatrix} &= \mathbf{K} \begin{pmatrix} \frac{d\Pi}{dx} \\ \frac{d\Pi}{dy} \\ \frac{d\Pi}{dz} \end{pmatrix} \\ \frac{d\varpi}{dt} &= \mathbf{K}\, \nabla \Pi, \end{aligned} \tag{1.17}$$

where $\mathbf{K}$ represents a general proportionality constant and is a tensor in the most general case, ϖ corresponds to scalar variables (e.g. saturation, velocity components, species, et.) and Π corresponds to associated variables (scalars such as pressure, species, but also vectors, such as diffusive fluxes).

The diffusion-type equations apply to species transport as in gas diffusion, electronic conduction, as well as on transport of properties like energy, as in heat and momentum transport. The equation is macroscopic since it describes the behaviour of all particles and their properties in the control volume in a statistical manner.

The description of gas-phase transport in the DM is based on a macroscopic point of view for the most cases. This is due to the fact, that the number of gas molecules in the DM with a footprint of 1 cm^2 is in the order of 10^{16}, and the pore length scale in the substrate is several times larger than the mean free path length (exceptions for this can be found in the catalyst layer and the micro porous layer). The macroscopic view implies that the details of the sample are not resolved and it is believed that the sample volume is sufficiently large to average the local inhomogeneities. The smallest sample volume complying with this criterion is called representative equivalent volume (REV) [Bea88]. The size of the REV depends upon the micro structure of the matrix and the property of interest. It is found by measuring the property of interest, e.g. the permeability on

different matrix volumes. When the value of the measured property, normalised by the sample size, remains constant within the experimental errors, the REV is found. So far, no detailed study of the REV for relevant properties on DM has been published.

The definition of the relevant macroscopic properties like saturation, capillary pressure, porosity, and tortuosity and relative properties will be given in the coming section. This is followed by the description of the absolute pressure-driven kind of flow in single-phase and two-phase situation (Section 1.3.3 on page 36ff.) and the multi-phase mixture formulation. Finally, the description of liquid water flow in porous environment with resolved structure topology is discussed (Section 1.3.6 on page 52ff.).

1.3.2 Macroscopic Properties

Saturation and pressure are important properties in the context of multi-phase related questions in PEMFCs. The species and phases of interest are water in liquid or vapour phase and hydrogen and nitrogen at the anode or oxygen and nitrogen (air) at the cathode side in gas phase. The phases differ with respect to their viscosity, density, and wetting behaviour. Since the characteristic length scale of the DM is in the order of 0.1 mm to 10 µm, the density effects, resulting in small pressure gradients can be neglected. Also the velocities are small, thus the inertia and viscous effects are of minor significance. This makes the wetting behaviour, expressed by the surface tension and contact angle the dominating property. Further details on the importance of the different effects will be given by comparing various dimensionless numbers in Section 1.3.6 on page 52ff.

Different definitions of the two-fluid phase interaction, depending upon the application, are common in the literature. The most general phase distinction would be ‘wetting’ (contact angle smaller 90°, subscript ‘w’) and ‘non-wetting’ (contact angle larger 90°, subscript ‘nw’) or, not as general, ‘liquid’ (subscript ‘liq’) and ‘gas’ phase (subscript ‘g’). The ‘wetting’, ‘non-wetting’ terminology is used in geological publications since these deal mostly with two liquid phases (oil and water). In this work, the DM is in focus and therefore, the gas phase is considered as the wetting phase while, due to PTFE treatment, the DM is water-repellent; water is the non-wetting phase. This definition shall be valid in further explanations unless explicitly stated differently.

The two fluid phases share the same pore space in the solid matrix and therefore, they cannot move within the matrix independently. In terms of the constitutive description of multi-phase transport, a key property is the saturation s_i of phase i. It is defined as the volume ratio of the fluid of interest V_i and the total non-solid volume:

$$s_i = \frac{V_i}{\sum_{i=1}^{n} V_i} \tag{1.18}$$

with i = liq for liquid and g for gas phase, resp. w for wetting and nw for non-wetting case. The saturation of $s_i = 0$ and $s_i = 1$ are found in real systems only under special conditions, when either the porous material had not been in contact with one of the two individual phases before or the fluid has been removed by evaporation. In all other cases, a small saturation of one of the phases resides in the porous matrix even if the system is not exposed to any external pressure gradients. To give an example, in hydrology a column of soil is completely saturated with water and then drained by gravity excluding vapourisation. The saturation found at equilibrium is defined as the residual saturation s_r. This concept applies to both phases.

Since the residual saturation $s_{\mathrm{r,i}}$ is an offset to the saturation, it increases the complexity of the equations using the saturation. To mitigate this, the normalisation of the saturation by the residual saturation is introduced and called 'effective saturation' $s_{\mathrm{e,i}}$ [BC64]:

$$s_{\mathrm{e,w}} = \frac{s_\mathrm{w} - s_{\mathrm{r,w}}}{(1 - s_{\mathrm{r,w}})} \tag{1.19}$$

$$s_{\mathrm{e,nw}} = \frac{s_\mathrm{nw} - s_{\mathrm{r,nw}}}{(1 - s_{\mathrm{r,nw}})} \tag{1.20}$$

The interpretation of s_r depends on the problem of interest, since the draining mechanism is not limited to gravity. Any pressure difference between the invading and the draining fluid acts as a draining mechanism. In this case, the residual saturation depends on the maximum pressure difference applied to equilibrate the system.

The interaction of the solid surface with the fluid is different for the individual fluid due to different surface tensions of the fluids. This is manifested by a pressure, required to push the non-wetting phase into or to suck the wetting phase out of the porous matrix.

This pressure depends also upon saturation. Commonly, the Young-Laplace Equation is used to calculate the pressure:

$$p(s_{\mathrm{liq}}) = -\frac{2}{r(s_{\mathrm{liq}})}\,\sigma\cos\theta \tag{1.21}$$

The pore radius, filled with liquid, is represented by $r(s_{\mathrm{liq}})$, σ denotes as the surface tension of the liquid and θ as the contact angle between the liquid and the porous matrix. The formulation given here only holds for a spherical liquid-gas interface, found in cylindrical pore systems. The model conception behind this is a bundle of straight tubes with different diameters. The contact angle exceeds 90° in a non-wetting situation and the cosine is negative. This notation defines that the pressure of the non-wetting phase has to be positive to invade the matrix. The difference of the pressures of each phase is also called capillary pressure [Bea88]. The surface tension induced pressure of the gas phase on the interfaces is nonexistent for ideal gasses and, compared to the pressure of the liquid phase, negligible small for real gases, thus, the surface tension induced gas phase pressure is ignored. The capillary pressure is given by

$$p_{\mathrm{cap}}(s) = -\frac{2}{r(s_{\mathrm{liq}})}\,\sigma_{\mathrm{liq}}\,\cos\theta = p_{\mathrm{nw}} - p_{\mathrm{w}} \approx p_{\mathrm{nw}} = p_{\mathrm{liq}}. \tag{1.22}$$

The only parameter representing the geometry of the porous matrix is the 'pore radius' r which is subject of numerous studies, each using certain model systems. The relation between the radius and the saturation will serve as the basis for the following discussion on two-phase transport. It is to notice that the original literature stems from hydrology, where the height of the water column above an arbitrary datum level is used as reference pressure. Therefore, the pressure is often noted positive in wetting situations. Nevertheless, from the point of the discussion here, the subject is easier to understand if the pressure in a wetting situation is noted negative since it acts as a suction tension.

One of the most cited theoretical work on the pressure-saturation relationship was done by M.C. Leverett [Lev41]. He found that the pressure-saturation relationship of different sands can be represented by one curve if the pressure is normalised by the interfacial tension $\sigma\cdot\cos\theta$, the porosity ε and the absolute permeability k. He suggested a normalised

representation of the pressure-saturation relationship, known as J-Function. There, a third-order polynomial, suggested by Udell [Ude85], is frequently used to express $J(s_{\mathrm{e,w}})$

$$\frac{p}{\sigma \ \cos\theta} \sqrt{\frac{k}{\varepsilon}} = J(s_{\mathrm{e,w}}) \tag{1.23}$$

with

$$J(s_{\mathrm{e,w}}) = C_1 \ (1 - s_{\mathrm{e,w}})^3 + C_2 \ (1 - s_{\mathrm{e,w}})^2 + C_3 \ (1 - s_{\mathrm{e,w}}) + C_4 \tag{1.24}$$

while

$$C_1 = 1.263 \ \ C_2 = -2.120 \ \ C_3 = 1.417 \ \ C_4 = 0.$$

C_1 - C_4 are constants, dependent on the porous material. These values are frequently employed in fuel cell models like by Wang [WB93]. The nature of the J-function depends upon the geometrical morphology of the porous matrix. Many researchers suggested different fit functions for the capillary pressure function by studying experimentally found pressure data in dependence of saturation. Others, like Corey [BC64], concluded from empirical fits on experimental saturation dependent permeability data to the capillary-pressure function. Corey suggested that the relationship between pressure and saturation for the substrates he investigated (sand stone, soil, glass beads), is of the kind

$$s_{\mathrm{e,nw}} = 1 - \left(\frac{p_{\mathrm{b}}}{p}\right)^2, \tag{1.25}$$

formulated for the non-wetting fluid. Where p_{b} is a material constant, which can be interpreted as the pressure that is required to start the displacement of the wetting fluid by the non-wetting fluid. The exponent '2' in Equation 1.25 depends upon the pore size distribution and is highly sample dependent. Brooks and Corey extended the equation by treating the exponent as a material dependent property. They suggested the following equation [BC64]:

$$s_{\mathrm{e,nw}} = 1 - \left(\frac{p_{\mathrm{b}}}{p}\right)^{\chi} \text{ for } p > p_{\mathrm{b}} \tag{1.26}$$

An example plot of this function is shown in Figure 1.13.

Brooks and Corey found that their mathematical model of the pressure-saturation relation deviates from measured data for anisotropic porous media. Furthermore, the fact

that a threshold pressure has to be overcome to get a saturation is a reasonable feature with regard to hydrophobic DM for fuel cell application. Yet, it causes numerical difficulties since the function is not continuously differentiable. The term dp/ds is important in the two-phase flow formulation of Darcy's law, as discussed in Section 1.3.4 on page 43ff. Van Genuchten [VG80] suggested Equation 1.27 as an alternative for describing the pressure-saturation relationship, which is continuously differentiable:

$$s_{\mathrm{e,nw}}(p) = 1 - \left[\frac{1}{1+(\xi p)^v}\right]^w \tag{1.27}$$

The parameters ξ, v and w have to be determined experimentally. Two example plots of this function, as well as the a third-order polynomial and the Brooks Corey's formulation, are also shown in Figure 1.13. The reason for showing two plots of the Van Genuchten function is based on the fact that these will be used later to discuss the relative permeability relationships (see Section 1.3.4 on page 43ff.). Table 1.3 shows the equations of comparison.

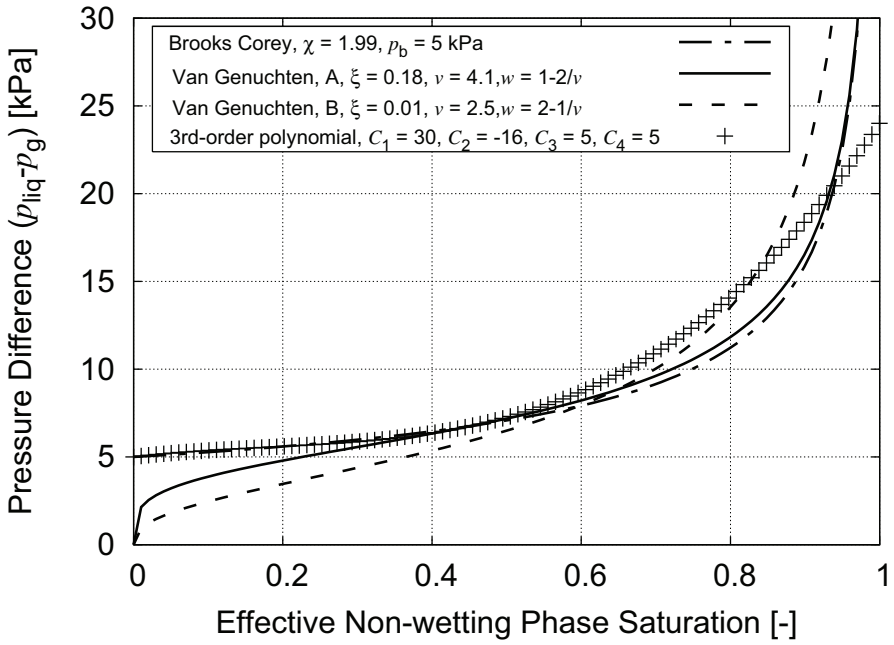

Figure 1.13: Examples of frequently used pressure-saturation functions. The constants in the equations are chosen in a way that the functions look as similar as possible and serve only for illustration.

The discussion is based on the effective saturation of the non-wetting fluid ($s_{\mathrm{e,nw}}$) since

Table 1.3: Frequently used pressure-saturation functions

$s_{\mathrm{e,nw}}(p)$ or $p(s_{\mathrm{e,nw}})$	Equation
Brooks-Corey [BC64]	$s_{\mathrm{e,nw}}(p) = 1 - \left(\frac{p_{\mathrm{b}}}{p}\right)^{\chi}$ Corey: $\chi = 2$
Van Genuchten [VG80]	$s_{\mathrm{e,nw}}(p) = 1 - \left[\frac{1}{1+(\xi p)^{v}}\right]^{w}$
Udell [Ude85]	$p(s_{\mathrm{nw}}) = \sqrt{\frac{\varepsilon}{k}}\sigma\cos\Theta\left[C_1\ (s_{\mathrm{nw}})^3 + C_2\ (s_{\mathrm{nw}})^2 + C_3\ (s_{\mathrm{nw}}) + C_4\right]$

it is more illustrative with regard to fuel cells. In geological literature, the discussions are based on the effective wetting fluid saturation, but since they are related by $s_{\mathrm{nw}} = (1 - s_{\mathrm{w}})$, they can be interchanged easily. To summarise, the three mathematical formulations of the pressure-saturation relationship frequently used in fuel cell models by e.g. Berning [Ber02], Nam and Kaviany [NK03], and others, are based upon fit functions to experiments with mostly hydrophilic sands.

Porosity and tortuosity are additional parameters, required in the description of porous media. The porosity ε is defined by the volumetric ratio of the fluid volume V_{fluid} to the volume calculated from the other dimensions of the sample V_{geo}. The general definition is

$$\begin{aligned} \varepsilon &= \frac{V_{\mathrm{fluid}}}{V_{\mathrm{geo}}} \\ \varepsilon &= \frac{V_{\mathrm{liq}} + V_{\mathrm{g}}}{V_{\mathrm{liq}} + V_{\mathrm{g}} + V_{\mathrm{sol}}} \end{aligned} \tag{1.28}$$

The second geometrical structure property in this context is the tortuosity

$$\tau = \frac{l}{l_{\mathrm{geo}}}. \tag{1.29}$$

The simplest and most intuitive definition of this property is the ratio of the real path length l between two locations (L_1 and L_2) within a porous medium and the length l_{geo}, the thickness of the porous material (see Figure 1.14). The tortuosity can be a three-dimensional tensor in anisotropic porous media.

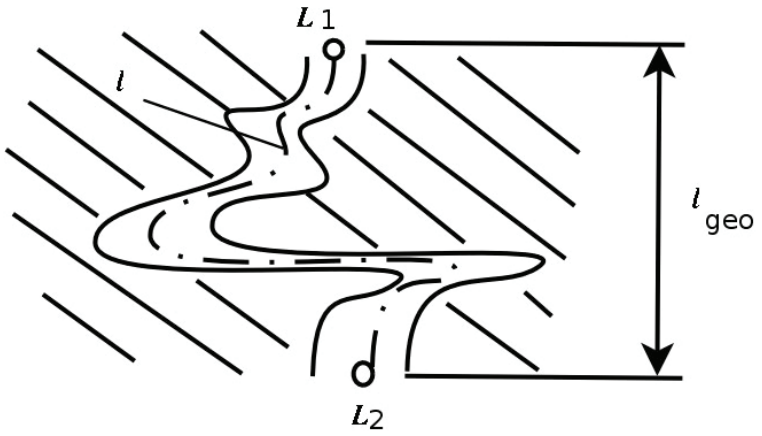

Figure 1.14: Cross section through a pore to illustrate the tortuosity factor.

As a side note, the tortuosity enters the equations for diffusion-driven and pressure-driven flow quadratically. This is caused by the fact that the gradient strength of pressure and also the partial pressure gradient depend upon the length as well as the velocity of the molecules [Eps89]. The literature is not consistent with the definition of tortuosity. Many authors define the square of the given definition as tortuosity, e.g. [BC64]. In the following the definition given in Equation 1.29 is used.

1.3.3 Total Pressure Gradient

The gas transport, driven by the total pressure gradient (convective gas transport) in the DM, is anisotropic and the discussion of this transport mode will reflect this.

In the through-plane direction of the DM (flow is perpendicular to the surface) the pressure difference between catalyst layer and flow field exists only for a short time. At open circuit potential the gas composition and the pressure at both locations is identical. When a certain current is drawn, the oxygen will be consumed and – in case of conditions where the product water condensates – the pressure at the catalyst layer starts to drop. This causes a gas flow from the channel towards the catalyst layer, where just the oxygen is consumed and nitrogen is accumulated. After a while, the pressure difference between the catalyst layer and the flow field vanishes because of the accumulation of nitrogen and only diffusion remains as transport mechanism. In case of conditions where the water

stays in vapour phase, the pressure at the catalyst layer increases since each consumed oxygen molecule produces two molecules of water. A pressure-driven gas flow from the catalyst layer to the flow field takes place until all the oxygen near the catalyst layer is consumed. The oxygen has to diffuse against a pressure-driven flow in order to reach the catalyst layer. Both mechanism last only for a short time after start-up; later only diffusion remains as the transport mechanism for oxygen in the through-plane direction of the DM, as assumed in the model by Springer et al. [SZG91].

In the in-plane direction (flow is parallel to the surface of the DM) the flow field geometry determines whether pressure driven gas flow takes place or not. In extreme cases, the pressure drop can reach the order of several kPa; this is estimated for the pressure drop between two channels connected by a U-turn. A detailed discussion on that subject can be found by Baker and Darling [BD01a]. In a straight channel geometry, the gas flow in the plane direction of the DM might become important in situations where parts of the flow field are blocked by water droplets. For the convection, Darcy [Dar56] proposed a linear relationship between the pure fluid velocity and the pressure gradient:

$$\begin{aligned} \mathbf{u}_i &= -\frac{\mathbf{k}_i}{\mu} \nabla p_i \\ \begin{pmatrix} u_{ix} \\ u_{iy} \\ u_{iz} \end{pmatrix} &= -\frac{1}{\mu} \begin{pmatrix} k_{ixx} & k_{ixy} & k_{ixz} \\ k_{iyx} & k_{iyy} & k_{iyz} \\ k_{izx} & k_{izy} & k_{izz} \end{pmatrix} \begin{pmatrix} \frac{dp_i}{dx} \\ \frac{dp_i}{dy} \\ \frac{dp_i}{dz} \end{pmatrix} \end{aligned} \tag{1.30}$$

$\mathbf{u}_i$ denotes as velocity and μ as the molar viscosity. It also becomes clear that the permeability $\mathbf{k}_i$ is not a scalar, but a tensor which becomes important in case of an anisotropic porous medium. Furthermore, $\mathbf{k}_i$ is also a function of saturation and often scaled by the relative permeability (see Section 1.3.4 on page 43). In order to focus on the main idea, the anisotropy is ignored at this point. Therefore, $\mathbf{k}_i$ is treated as a scalar.

The relationship between volumetric flow dV/dt and pressure drop is analogous to the Hagen-Poiseuille law, describing the pressure drop for laminar flow in a cylindrical capillary:

$$\frac{dV}{dt} = -\frac{\pi <r>^4 <n>}{8\mu} \frac{dp}{dl} \tag{1.31}$$

The geometry-dependent term corresponds to the Darcy permeability constant k. Reformulated for the velocity, Equation 1.31 becomes:

$$u = \frac{1}{<n> \pi <r>^2} \frac{dV}{dt} = -\frac{<r>^2}{8\mu} \frac{dp}{dl} \tag{1.32}$$

The number of openings with mean radius $<r>$ is represented by $<n>$. This assumes a model where the DM consists of a bundle of straight capillaries.

To account for the obvious deviation of the real DM from this model, the tortuosity τ and the porosity ε (non-solid volume divided by total volume) can be introduced (see Section 1.3.2 on page 35). Also the mean square radius is an apparent radius since the pressure drop related with deflection of the flow is not considered in Equation 1.31. With Equation 1.28 and Equation 1.29, Equation 1.32 becomes:

$$u = \frac{1}{\varepsilon A_{\text{geo}}} \frac{dV}{dt} = -\frac{<r>^2}{8\mu \tau^2 l_{\text{geo}}} \Delta p. \tag{1.33}$$

The motivation to introduce the porosity arises from the fact that in a macroscopic sample only the non-solid parts of the volume can contribute to flow, and therefore, the cross sectional area of the macroscopic sample has to be reduced. The tortuosity accounts for the meandering of the flow path in the real substrate. The area A_{geo} in Equation 1.33 refers to the geometrical area since it describes a macroscopic property. With that, the permeability constant k can be expressed as

$$k = \frac{<r>^2 \varepsilon}{8\tau^2}. \tag{1.34}$$

Both, porosity and tortuosity are matrix properties and not independent from each other. Several suggestions for correlation exist, as discussed in Section 1.3.4 on page 39ff.

From the analogy between the laws of Darcy and Hagen-Poiseuille, it becomes clear that Darcy's law is valid for laminar flow within the porous medium, where the energy is mainly dispersed by viscosity. The validity of Darcy's law is discussed by Bear [Bea88]. As in pipes, it is suggested that the flow stays laminar only up to a certain flow rate, and,

in analogy to pipe flow, a Reynolds number for porous media is defined:

$$\mathrm{Re} = u\frac{l\rho}{\mu} \tag{1.35}$$

with ρ as the fluid density. The characteristic length l is not commonly defined.
It has been suggested to take a certain grain diameter in a packing of grains where the grain fraction exceeds 10 % or 50 % wt. of the grain diameter distribution.

If $l = \sqrt{k}$ is taken for the characteristic length, the ideal gas law used to calculate the density and the velocity u follows Darcy's law (Equation 1.30), and the Reynolds number can be calculated according to

$$\mathrm{Re} = \frac{k^{3/2}\ M\ p}{\mu(T)^2\ \Re\ T}\frac{dp}{dl}. \tag{1.36}$$

The largest Reynolds numbers appear for in-plane gas flow (since the in-plane permeability is larger than the through-plane permeability). With the assumptions listed in Table 1.4, the Reynolds number is in the range between one and two, meaning that Darcy's law can be applied for gas, unless one of the parameters changes by two orders of magnitude. Experimentally it was found that the pressure drop starts to deviate from Darcy's law if Re is between 10 and 100 [Bea88].
In case of liquid flow, the viscosity is three orders of magnitude larger, yet the density is increased by three orders of magnitude also.

Table 1.4: Boundary conditions for estimating the Reynolds number for gas in DM

Parameter	Value	Unit	Comment
k	$10 \cdot 10^{-12}$	m^2	In-plane permeability
p	150	kPa	Absolute gas pressure
dp	10	kPa	Pressure difference between adjacent channels
M	29	g/mol	Molar mass of air
μ	$20 \cdot 10^{-6}$	Pa s	Viscosity at 353 K
T	273 – 373	K	Temperature
dl	$10 \cdot 10^{-3}$	m	Distance between adjacent channels
Re	1 - 3		Reynolds number for in-plane gas flow in DM

1.3.4 Relative Properties

Relative porosity and tortuosity are commonly chosen when saturation comes into play. By definition, the relative property Π_{rel} is the quotient of the actual property $\Pi_i(s_i)$ and the theoretical or measured property $\Pi(s_i = 1)$ at complete saturation

$$\Pi_{\text{rel}} = \frac{\Pi(s_i)}{\Pi(s_i = 1)}. \tag{1.37}$$

This is of importance for absolute pressure gradient driven flow (discussed in Section 1.3.3 on page 36ff.) and for the diffusive transport. For the latter, the ratio of porosity over tortuosity is used as a relative property for the free gas diffusion coefficient to get an estimate for the effective diffusion coefficient.

The tortuosity is difficult to measure, but based upon the consideration that the porosity and tortuosity are defined by the same solid matrix, the two structural parameters are related. Several relations between tortuosity and porosity had been suggested. For a start, the saturation dependency of the tortuosity itself is ignored, only the porosity dependence on saturation is considered. The porosity is related to the gas phase volume as a function of saturation:

$$\varepsilon(s) = \frac{V_{\text{fluid}}}{V_{\text{geo}}} \left[1 - s_{\text{liq}}\right] \tag{1.38}$$

This procedure is by no means exact since the distribution of the phases influences the tortuosity significantly. In case of film formation, this attempt would result in complete failure. Nevertheless, this practice is common for fuel cell models, see e.g, Berning and Djilali [BD01b].

For the ratio of porosity over tortuosity Bruggeman [Bru35] suggested, based on the work of Rayleigh for spherical particles and dry conditions, the following relation:

$$\Pi_{\text{e}} = \varepsilon^{1.5}\ \Pi \tag{1.39}$$

with Π_{e} as any effective property Π.

Originally, Bruggeman's focus was on dielectrics and electrical conductivity constants. He considered a model of regular lattice of spheres where a small fraction of the total volume is replaced by spheres of same size but with different property Π. Equation 1.39

represents the limiting case of replaced spheres with a property value of zero (e.g. non conductive material). Bruggeman suggested different relations based on different shapes of particles. But, the one given in Equation 1.39 is frequently used in fuel cell literature.

The suggestion of Bruggeman was experimentally tested by De La Rue and Tobias [DLRT59] by measuring the conductivity of electrolytes containing glass beads, sand, and polystyrene cylinders. Good experimental agreement was found only for the spherical particles (which the model was originally derived for). The extension of this relationship to anisotropic porous media was made by Nader [NN76] and finally used for fuel cell related work by Berning [Ber02] and others. Mezedur [MKM02] suggested the relationship:

$$\frac{\varepsilon}{\tau^2} = 1 - (1-\varepsilon)^{0.64} \tag{1.40}$$

The saturation dependence of the tortuosity is considered in hydrology. Burdine [Bur53], e.g. found based on permeability experiments that the tortuosity can be approximated with a linear saturation dependence:

$$\tau = C_5 \; s_{\text{liq}} + C_6 \tag{1.41}$$

C_5 and C_6 represent structure dependent constants.

Tomadakis and Sotirchos [TS91] suggested based upon Monte Carlo simulations the following equation:

$$\tau^2 = \tau_0^2 \left(\frac{\varepsilon_0 - \varepsilon_\text{p}}{\varepsilon(s) - \varepsilon_\text{p}} \right)^\Lambda \tag{1.42}$$

The interesting feature in their relation is the introduction of a percolation threshold. Below a certain (percolation) porosity ε_p with ($\varepsilon(s) \ll \varepsilon_\text{p}$) the ratio τ is not defined, but as the porosity gets larger than the percolation porosity, the tortuosity starts at an infinite large number and approaches the dry value as the porosity increases.
ε_0 and τ_0 represent the dry porosity and tortuosity values. This is especially of interest in cases where liquid water is present and, therefore, the porosity is a function of saturation. The percolation porosity ε_p and the coefficient Λ are empirical parameters. For DM like fibre-based porous structures, $\varepsilon_\text{p} = 0.11$ and $\Lambda = 0.521$ for the in-plane and $\Lambda = 0.785$ for the through-plane direction have been suggested by Tomadakis and Sotirchos [TS93].

Equation 1.42 suggested by Tomadakis and Sotirchos can be reformulated to give the ratio ε/τ^2:

$$\frac{\varepsilon}{\tau^2} = \varepsilon \left(\frac{\varepsilon - \varepsilon_\mathrm{p}}{1 - \varepsilon_\mathrm{p}}\right)^\Lambda \tag{1.43}$$

A comparison between the three relationships (Equations 1.40,1.42, and 1.43), based on a pore network model was done by Nam and Kaviany [NK03] and they recommend Equation 1.43. Furthermore, Nam and Kaviany extended the relation by introducing another term to account for saturation dependency:

$$\frac{\varepsilon}{\tau^2} = \varepsilon_0 \left(\frac{\varepsilon_0 - \varepsilon_\mathrm{p}}{1 - \varepsilon_\mathrm{p}}\right)^\Lambda (1 - s_\mathrm{liq})^2 \tag{1.44}$$

There are more suggestions for the saturation dependency of this ratio available in literature. Archie [Arc42] compared different experimentally found saturation-resistivity plots $R_\mathrm{e}(s)$ for sands and came up with the following expression:

$$R_\mathrm{e}(s) = R(s = 1)s^{-w^*} \tag{1.45}$$

Together with his first law

$$R_\mathrm{e} = R(\varepsilon = 1)\varepsilon^{-v^*}, \tag{1.46}$$

which he obtained by studying the resistivity of saturated sands of different kind,

$$R_\mathrm{e} = R(\varepsilon = 1)\varepsilon^{-v^*}s^{-w^*}, \tag{1.47}$$

called Archies second law, is obtained. w^* and v^* denote as constants to be found experimentally.

Since the nature of electrical conduction by ionic transport in an electrolyte and gas diffusion are both diffusion-type processes, Equation 1.47 is reformulated for describing gas diffusion:

$$\frac{\varepsilon}{\tau^2} = \varepsilon^{v^*}(1 - s_\mathrm{liq})^{w^*} \tag{1.48}$$

It has to be noticed, that Archie worked with water as the conducting fluid, in case of the DM this would be the gas phase and the saturation is replaced by $1 - s_\mathrm{liq}$.

This relationship, with regard to diffusion, was numerically tested with Lattice - Bolzmann methods by Marty [Mar99] on overlapping and non-overlapping sphere geometries. Marty found a good agreement between Archie's equation and his results for $v^* = w^*$, in cases where the saturation of the phase of interest is much higher than the limiting saturation. Below the limiting saturation the phase becomes discontinuous. Applied to the DM, this means that the dependence of gas diffusion appears to be expressible by Archie's equation for low water saturation. The difficult part is the determination of the exponents v^* and w^* in Equation 1.48. The state-of-the-art fuel cell models do not use Archies equation, probably because of a lack of data regarding the exponents, especially w^*. The justification for this is the fact that the porosity is linearly affected by the saturation. A method for the experimental validation on real DM was suggested by Kramer et al. [KFF+08].

There is less analytical background than empirical work behind the common equations describing the ratio ε/τ^2. A summary of frequently used formulations of the ratio porosity over tortuosity can be found in Table 1.5.

Table 1.5: Frequently used formulations for ε/τ^2

ε/τ^2	Equation	Comment
Bruggeman [Bru35]	$\varepsilon^{1.5}$	Historically the first formulation
Mezedur [MKM02]	$1-(1-\varepsilon)^{0.64}$	
Tomadakis [TS91]	$\varepsilon\left(\frac{\varepsilon-\varepsilon_\mathrm{p}}{1-\varepsilon_\mathrm{p}}\right)^{\Lambda}$ with $\Lambda = 0.785$	Good agreement with pore network model (single phase)
Nam and Kaviany [NK03]	$\varepsilon_0\left(\frac{\varepsilon_0-\varepsilon_\mathrm{p}}{1-\varepsilon_\mathrm{p}}\right)^{\Lambda}(1-s_\mathrm{liq})^2$ with $\Lambda = 0.785$	See previous, but for two-phase cases
Archie [Arc42]	$\varepsilon^{v^*}(1-s_\mathrm{liq})^{w^*}$ with $1.3 \leq v^* \leq 2$ and w^* 0.5	Tested with Lattice-Bolzmann, good agreement for spheres

For comparison, the different functions are plotted in Figure 1.15. It can be seen that the difference between the models from Archie, Nam and Kaviany or Tomadakis is not pronounced, and the use of any saturation dependent model would give more realistic results than just ignoring the sensitivity to saturation. Yet, it remains uncertain whether the equations can be used for fibrous structures as found in DM, since they had been

obtained and tested on more or less spherical particle arrangements with the exception of Tomadakis.

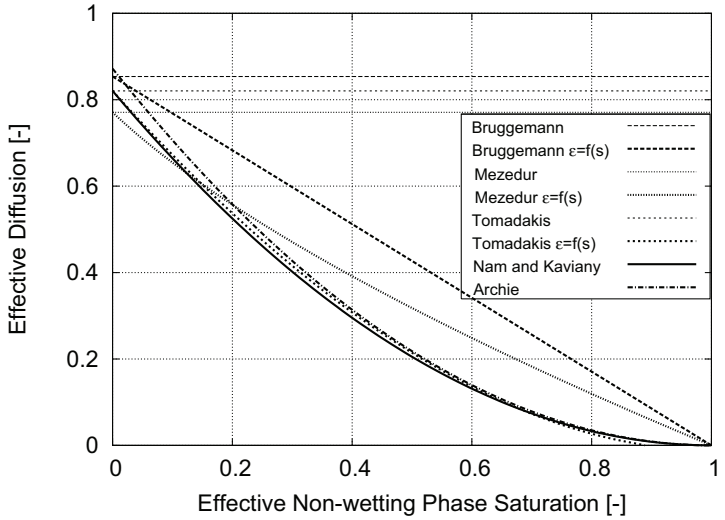

Figure 1.15: Plots of effective gas diffusion versus saturation for different models, see Table 1.5. The dry porosity was chosen to be 0.9, the percolation porosity was set to 0.1.

Relative permeability

$$\mathbf{k}_i(s) = \mathbf{k}\ k_{\mathrm{rel},i}(s_i) \tag{1.49}$$

is widely used to describe the saturation dependency of the permeability and is defined between 0 and 1. Finding the function for $k_{\mathrm{rel},i}(s_i)$ is a challenging task and various concepts for deriving such a function have been proposed in the past and some of them will be introduced here to impart the level of empirical and analytical background. This section is a discussion of geological literature, hence, the relative properties are related to the wetting phase saturation (gas phase) $s_{\mathrm{e,g}}$ mostly.

Wyllie and Gardener [WG58] derived an expression for $k_{\mathrm{rel},i}(s_{\mathrm{g}})$ starting from fundamental equations like Hagen-Poiseuille's law and probability assumptions upon the pore interconnection. By combining the hydraulic radius of cylindrical pores of their model with the capillary pressure (p_{cap}) and the saturation, they derived the following equations for the wetting fluid (gas):

$$k_{\mathrm{rel,g}}(s_{\mathrm{e,g}}) = (s_{\mathrm{e,g}})^2 \; \frac{\int_0^{s_{\mathrm{e,g}}} \frac{ds_{\mathrm{e,g}}}{p_{\mathrm{cap}}^2}}{\int_0^1 \frac{ds_{\mathrm{e,g}}}{p_{\mathrm{cap}}^2}} \tag{1.50}$$

For the non-wetting fluid, Equation 1.50 becomes

$$k_{\mathrm{rel,l}}(s_{\mathrm{e,g}}) = (1 - s_{\mathrm{e,g}})^2 \; \frac{\int_{s_{\mathrm{e,g}}}^1 \frac{ds_{\mathrm{e,g}}}{p_{\mathrm{cap}}^2}}{\int_0^1 \frac{ds_{\mathrm{e,g}}}{p_{\mathrm{cap}}^2}}. \tag{1.51}$$

Here, the concept of 'effective saturation'

$$s_{\mathrm{e,g}} = \frac{s_{\mathrm{e,g}} - s_{\mathrm{r}}}{s_{\mathrm{c}} - s_{\mathrm{r}}} \tag{1.52}$$

introduced by Corey [BC64] is used (see also Section 1.3.2 on page 31). The two equations are known as Burdine's equations. The details of their derivation are shown in the Appendix A on page 171ff.

The assumptions made for deriving the equations are debatable, but the experimental studies of Wyllie and Gardner [WG58] and others did confirm these equations and they are generally accepted. The practical use of these equations is limited since the value of the integrals is only accessible by experiments or expensive numerical simulations. Numerous studies had been executed to measure the saturation-pressure relationship of various soils, rocks, and bead beds. Mualem [Mua76] used 45 of those measurements in his study and derived a relationship of permeability in dependence of saturation based on probability methods and very general assumptions. The probability of overlapping pores in neighbouring regions in a porous matrix was calculated in dependence of the radii of the pores in contact, similar as Wyllie and Gardener did. Further it was assumed that the correlation factors, required for this approach, are power functions of the saturation. The resulting relation

$$k_{\mathrm{rel,g}}(s_{\mathrm{e,g}}) = {s_{\mathrm{e,g}}}^{\iota} \left[\frac{\int_0^{s_{\mathrm{e,g}}} \frac{ds_{\mathrm{e,g}}}{p_{\mathrm{cap}}}}{\int_0^1 \frac{ds_{\mathrm{e,g}}}{p_{\mathrm{cap}}}} \right]^2 \tag{1.53}$$

is not too different from Burdine's equation. The major differences are the variability of the exponent ι (in Burdine's case '2') and the square of the integrals which is a direct result of the probability of overlapping pores of two neighbouring porous surfaces. The exponent is treated as a variable to tune the accuracy of the model in relation to experimental results. The permeability as a function of saturation can be expressed also as a function of pressure by applying the relationships introduced on page 33ff. Mualem used the method of the least square root on experimental data to find the exponent to be $\frac{1}{2}$ by looking at numerous permeability measurements. In order to do so, he required the saturation-pressure relationship and used the one that was suggested by Brooks and Corey (Equation 1.26 on page 33). There are two different suggestions for the relative permeability and two different suggestions to describe the pressure-saturation relationship. This results in four different equations for the relative permeability as a function of pressure and four different equations for the saturation dependency. Thereby, certain assumptions regarding the exponents in the capillary-pressure relation are necessary in order to perform the integrations analytically. This means that the different exponents are not treated as independent parameters anymore. The different equations can be found in Table 1.6.

The Van Genuchten relation for the pressure-saturation relationship represents a challenge for numerical integration when used in Mualem's or Burdine's equation. The only way to allow for analytical integration is making the exponents w and v dependent by $w = 1 - \frac{2}{v}$ for Burdine's equation and $w = 2 - \frac{1}{v}$ for Mualem's equation. This results in two different parameter sets for the capillary pressure function (see Figure 1.13 on page 34). The Van Genuchten relation for the pressure-saturation relationship allows for multiple solutions if integrated within Mualem's or Burdine's equation and here only one possibility is presented.

Table 1.6: Frequently used formulations for k_{rel}

		Van Genuchten		Brooks Corey	
		Gas	Water	Gas	Water
$k_{\mathrm{rel}}(s_{\mathrm{e,g}})$	Burdine	$s_{\mathrm{e,g}}^2 \left[1-\left(1-s_{\mathrm{e,g}}^{\frac{1}{w}}\right)^w\right]$	$(1-s_{\mathrm{e,g}})^2 \left(1-s_{\mathrm{e,g}}^{\frac{1}{w}}\right)^w$	$s_{\mathrm{e,g}}^{\frac{2+3\chi}{\chi}}$	$(1-s_{\mathrm{e,g}})^2\left(1-s_{\mathrm{e,g}}^{\frac{2+\chi}{\chi}}\right)$
	Mualem	$s_{\mathrm{e,g}}^{\frac{1}{2}} \left[1-\left(1-s_{\mathrm{e,g}}^{\frac{1}{w}}\right)^w\right]^2$	$(1-s_{\mathrm{e,g}})^{\frac{1}{2}} \left[1-s_{\mathrm{e,g}}^{\frac{1}{w}}\right]^{2w}$	$s_{\mathrm{e,g}}^{\frac{5}{2}+\frac{2}{\chi}}$	$(1-s_{\mathrm{e,g}})^{\frac{1}{2}}\left(1-s_{\mathrm{e,g}}^{1+\frac{1}{\chi}}\right)^2$
$k_{\mathrm{rel}}(p_{\mathrm{cap}})$	Burdine	$\frac{1-(\xi\ p_{\mathrm{cap}})^{v-2}\left[1+(\xi\ p_{\mathrm{cap}})^v\right]^{-w}}{\left[1+(\xi\ p_{\mathrm{cap}})^v\right]^{2w}}$ with $w=1-\frac{2}{v}$	$\left[1-(1+(\xi p)^v)^{-w}\right]^2 \left(\frac{(\xi p)^v}{1+(\xi\ p_{\mathrm{cap}})^v}\right)^w$ with $w=1-\frac{2}{v}$	$\left(\frac{p_b}{p_{\mathrm{cap}}}\right)^{2+3\chi}$	$\left[1-\left(\frac{p_b}{p_{\mathrm{cap}}}\right)^{\chi}\right]^2\left[1-\left(\frac{p_b}{p_{\mathrm{cap}}}\right)^{2+\chi}\right]$
	Mualem	$\frac{\left[1-(\xi\ p_{\mathrm{cap}})^{v-1}\left[1+(\xi\ p_{\mathrm{cap}})^v\right]^{-w}\right]^2}{\left[1+(\xi\ p_{\mathrm{cap}})^v\right]^{\frac{w}{2}}}$ with $w=1-\frac{1}{v}$	$\left[1-(1+(\xi\ p_{\mathrm{cap}})^v)^{-w}\right]^{\frac{1}{2}} \left(\frac{(\xi\ p_{\mathrm{cap}})^v}{1+(\xi\ p_{\mathrm{cap}})^v}\right)^{2w}$ with $w=1-\frac{1}{v}$	$\left(\frac{p_b}{p_{\mathrm{cap}}}\right)^{\frac{5\chi+4}{2}}$	$\left[1-\left(\frac{p_b}{p_{\mathrm{cap}}}\right)^{\chi}\right]^{\frac{1}{2}}\left[1-\left(\frac{p_b}{p_{\mathrm{cap}}}\right)^{\chi+1}\right]^2$

The two capillary pressure relationships with the two models for relative permeability result in functions which deviate significantly from each other. This fact stresses the importance of proper descriptions for DM substrates. Figure 1.16 shows the relative permeability as a function of saturation for Burdine's and Mualem's model with the capillary pressure function according to Brooks Corey (top) and Van Genuchten (bottom). In general, Burdine's model gives lower relative permeability for the non-wetting phase compared to Mualem's formulation. Especially in combination with Van Genuchten's capillary pressure function, the difference between Mualem and Burdine is significant. It also appears that the difference between Van Genuchten and Brooks Corey is marginal if Burdine's equation is used (which seems to be logical since the capillary pressure functions are chosen to be similar), but when based on Mualem's equation, the difference is significant.

To summarise, it is by no means sufficient to measure the capillary pressure relationship only since the different relative permeability models differ significantly and there exists no theoretically motivated method to decide which model is to apply. The description of the permeability function and the pressure-saturation relationship is more driven by empiricism than by theoretical analysis of the physics of fluids in porous systems, even in the soil science area where experimental data are available. This becomes explicitly obvious when the procedure of integration is considered. Hydrological formulations are often used when dealing with porous flow systems that are not typical of soil science and hydrology. In these cases the accuracy (of even applicability) of the description of such systems decreases as the morphological differences or the scales in focus between these systems and their counterparts in soil science or hydrology increases.

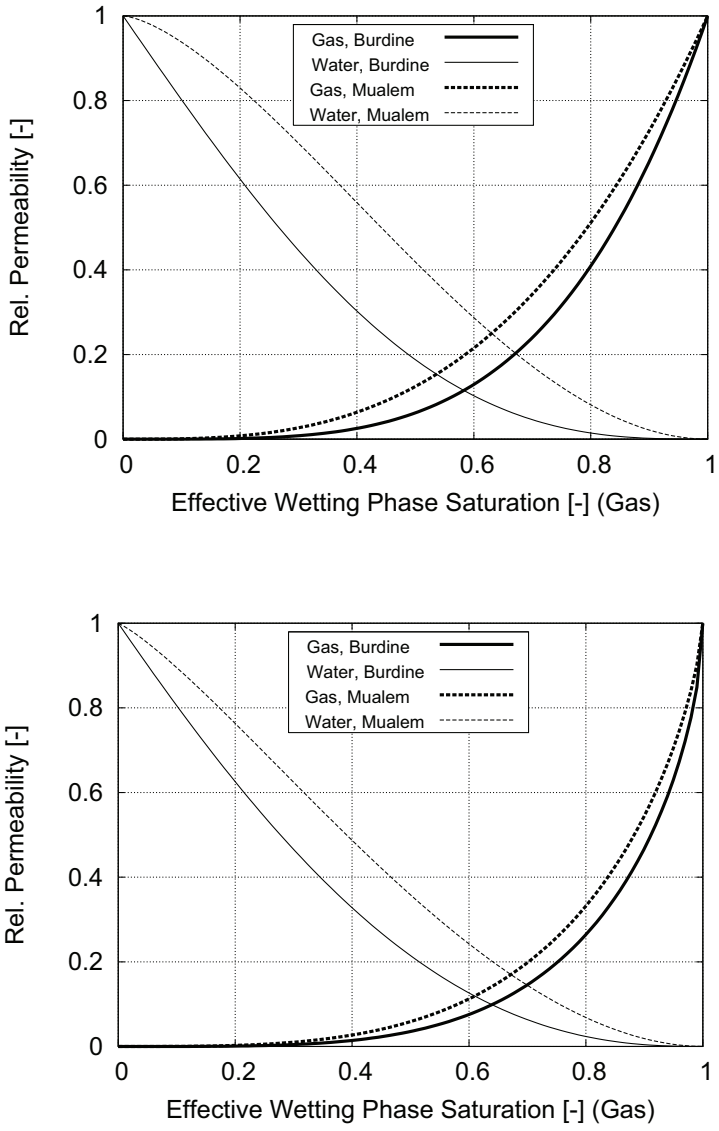

Figure 1.16: Top: Relative permeability according to Mualem [Mua76] and Burdine [Bur53] with capillary pressure functions according to Brooks and Corey [BC64]. Bottom: Relative permeability according to Mualem [Mua76] and Burdine [Bur53] with capillary pressure functions according to Van Genuchtens model [VG80]. Based on the equations listed in Table 1.6.

1.3.5 Multi-Phase Mixture Model

The multi-phase mixture model, suggested by Chavent [Cha76], is a variation of the common two-phase models based on conservation equations of mass and momentum. In order to reduce the numerical effort of calculation, the two phases are replaced by a virtual fluid with a set of effective properties of the original fluids. The saturation serves as a weighting factor.

Chavent started from a set of equations for immiscible two-phase systems and proved mathematically that the transport equations for miscible two-component systems are equal to the formulation for miscible two-phase systems. He compared the equation for slow miscible displacement

$$2\varepsilon\frac{dc}{dt} - \sum_{i=1}^{n}\left[\frac{\partial}{\partial x_i}\left(2D_i\frac{dc}{dx_i}\right)\right] - \sum_{i=1}^{n}\left[\frac{k_i}{\mu(c)}\frac{dp}{dx_i}\frac{\partial}{\partial x_i}\left(2c-1\right)\right] = 0 \tag{1.54}$$

with an equation he derived starting from the multi-phase formulation of Darcy's law (Equation 1.30 on page 37). The concentration 'c' is used in this equation rather than the saturation since it describes the miscible case, dx_i denotes the spatial derivative. Chavent published Equation 1.54 as presented here but it looks different from other publications like in [PRJ62] because of the factor '2' in concentration and the diffusion term. The factor '$2c-1$' in the permeation term can be further differentiated and '$2c$' remains, which allows to reduce the equation. In a more familiar notation, Equation 1.54 becomes

$$\varepsilon\frac{dc}{dt} - D\nabla^2 c - \frac{k}{\mu(c)}c\nabla p = 0, \tag{1.55}$$

as Peaceman and Rachford [PRJ62] suggested.

In order to describe the total flow velocity in the immiscible two-phase case, the Darcy terms for each flow are added up and Chavent formulates a substitute for the two terms:

$$\mathbf{u}(s) = \mathbf{u}_{\mathrm{nw}}(s) + \mathbf{u}_{\mathrm{w}}(s) = \frac{\mathbf{k}_{\mathrm{nw}}(s)}{\mu_{\mathrm{nw}}}\nabla p_{\mathrm{nw}} + \frac{\mathbf{k}_{\mathrm{w}}(s)}{\mu_{\mathrm{w}}}\nabla p_{\mathrm{w}} \equiv \mathbf{k}(s=1)\ Q(s)\ \nabla p(s) \tag{1.56}$$

This is the basic idea in order to derive the multi-phase mixture model. The parameter $Q(s)$ and the pressure p are called 'global mobility' and 'global pressure', respectively.

These two parameters are defined as follows:

$$Q(s) = \frac{k_{\mathrm{rel,nw}}(s)}{\mu_{\mathrm{l}}} + \frac{k_{\mathrm{rel,\ w}}(s)}{\mu_{\mathrm{w}}} \tag{1.57}$$

$$p(s) = \frac{p_{\mathrm{nw}} + p_{\mathrm{w}}}{2} + \frac{g(s) + g(s=0)}{2} \tag{1.58}$$

The function $g(s)$ compensates the average pressure between the two phases for the saturation dependent capillary pressure component and has the following definition:

$$g(s) = \int_{s_{\mathrm{a}}}^{s} \left(\frac{k_{\mathrm{rel,nw}}(s)}{\mu_{\mathrm{nw}} Q(s)} - \frac{k_{\mathrm{rel,\ w}}(s)}{\mu_{\mathrm{w}} Q(s)} \right) \frac{dp_{\mathrm{cap}}(s)}{ds} ds \tag{1.59}$$

with s_{a} as an arbitrary saturation at the inlet boundary at the beginning (t = 0 s). These definitions are necessary to make Equation 1.56 hold true. The differential transport equations for the two-phase case, coming from the mass balance, are:

$$\begin{aligned} \varepsilon \frac{ds_{\mathrm{nw}}}{dt} - \nabla \cdot \left[\frac{k_{\mathrm{nw}}}{\mu_{\mathrm{nw}}} \nabla p_{\mathrm{nw}} \right] &= 0 \\ \varepsilon \frac{d(1 - s_{\mathrm{nw}})}{dt} - \nabla \cdot \left[\frac{k_{\mathrm{w}}}{\mu_{\mathrm{w}}} \nabla p_{\mathrm{w}} \right] &= 0 \end{aligned} \tag{1.60}$$

By subtracting the two equations (Equation 1.60) the transport equation for the immiscible case is obtained:

$$2\varepsilon \frac{ds_{\mathrm{nw}}}{dt} - \nabla \cdot \left[\frac{k_{\mathrm{nw}}}{\mu_{\mathrm{nw}}} \nabla p_{\mathrm{nw}} \right] + \nabla \cdot \left[\frac{k_{\mathrm{w}}}{\mu_{\mathrm{w}}} \nabla p_{\mathrm{w}} \right] = 0 \tag{1.61}$$

With the definition of the global pressure and the mobility, the permeability dependent terms of Equation 1.61 can be reshaped leading to a diffusion term and a permeation term

$$\varepsilon \frac{ds_{\mathrm{nw}}}{dt} - \nabla \cdot \left[k \frac{k_{\mathrm{rel,nw}}\ k_{\mathrm{rel,w}}}{\mu_{\mathrm{nw}}\ \mu_{\mathrm{w}}\ Q} \frac{dp_{\mathrm{cap}}}{ds_{\mathrm{nw}}} \nabla S_{\mathrm{nw}} \right] - \nabla \cdot \left[\left(\frac{k_{\mathrm{rel,nw}}}{\mu_{\mathrm{nw}}} - \frac{k_{\mathrm{rel,w}}}{\mu_{\mathrm{w}}} \right)\ \frac{k}{2} \nabla p \right] = 0, \tag{1.62}$$

like in Equation 1.54 for the miscible case. The details of the transformation can be found in Appendix B on page 175ff. With k as the saturated permeability. In order to be consistent with the previous notation, the wetting fluid (index 'w') denotes the gas phase

and the non-wetting fluid (index 'nw') the liquid phase. Hence, Equation 1.62 becomes:

$$\varepsilon \frac{ds_{\mathrm{liq}}}{dt} - \nabla \cdot \left[k \frac{k_{\mathrm{rel,liq}}\ k_{\mathrm{rel,g}}}{\mu_{\mathrm{liq}}\ \mu_{\mathrm{g}}\ Q} \frac{dp_{\mathrm{cap}}}{ds_{\mathrm{l}}} \nabla s_{\mathrm{liq}} \right] - \nabla \cdot \left[\left(\frac{k_{\mathrm{rel,liq}}}{\mu_{\mathrm{liq}}} - \frac{k_{\mathrm{rel,g}}}{\mu_{\mathrm{g}}} \right)\ \frac{k}{2} \nabla p \right] = 0 \qquad (1.63)$$

The multi-phase mixture model contains all the variables and parameters of the conventional macroscopic description. The reliability of fuel cell models depends upon the quality of these parameters and the validity of Darcy's law. Traditionally, the parameters used in the geologic models are transferred since the measurement of relative permeability and capillary pressure in real anisotropic gas diffusion media is challenging. During the course of this work an experimental method is developed for measuring this parameter (see Chapter 2 on page 59), also methods and results were just recently presented (e.g. by Nguyen et al. [NLOW06] or Gostick et al. [GFI06, GIFP08]).

1.3.6 Models of Increased Complexity

Dimensionless numbers are essential tools to prioritise the multiple physical effects within a problem, like surface tension, inertia, gravity, friction and so forth.

When the two-phase boundary region is resolved in the model, a completely different point of view is taken compared to the previously explained macroscopic approach. This is a computational challenge since it requires a resolution below the fibre diameter of the DM in order to calculate the menisci and the interface pressure correctly. Due to the complex geometry, any attempt to approach this problem analytically will be limited to extremely simplified cases. The characteristic fibre distance in the DM is in the order of 20 µm and with a thickness of 200 µm the number of fibre layers which have to be considered are in the order of ten layers. This is a number that keeps the number of discrete elements for CFD calculations in a range that allows a computation in affordable time in 2D [RRF08] on the one hand, and puts a question mark on the phenomenological approach on the other hand. Since it assumes that the model domain is sufficiently large to average the properties (see discussion of REV on page 29). With an approach that resolves the interfaces, it is possible to drive material design based on well defined surface and geometrical properties which can be directly manipulated by manufacturing processes. This is impossible with the constitutive approach.

It is essential for any model system that all the relevant physical effects of the real system are represented sufficiently well. In most cases, the underlying physics of the real system is reduced to first and sometimes second order effects in the model system to keep it usable. In order to discuss the details of the different kind of models, it is necessary to get an overview of the dominating physical effects on the length scale of DM.

The physics of fluids on sub-millimetre length scales deviate significantly from fluid behaviour on more familiar length scales, such as a glass of water. The effects of surface tension are insignificant in the centimetre range, but dominate the physics in sub-millimetre scales. In order to describe the behaviour of fluids correctly, a set of equations needs to be selected according to the length scale. Dimensionless numbers had been introduced to guide the decision. A comprehensive overview of common dimensionless numbers is given by Boucher [BA59, BA63]. To this end, the different relevant forces acting on a volume of fluid are related with the force caused by the interfacial tension. These are the inertial force, the gravity force, and the friction force. The corresponding dimensionless numbers are called Weber number (We) for inertia, Eötvös or Bond number (Ev, Bo) for gravity, and capillary number (Ca) for friction. Furthermore, the Suratman and Ohnesorge number (Su, Oh) for a combined ratio between surface, inertia, and frictional forces are defined (the two numbers can be transformed into each other). Except for the Suratman number, all dimensionless numbers discussed here have the property that that when surface tension is dominant, the number is small and surface tension effects can be ignored when the number is large. If the number is of the order of one, the surface tension is comparable to the other force that characterises the number. The dimensionless numbers are of importance if the shape of a fluid volume in presence of another fluid is of interest like in mist flow and spraying problems. When a third phase is present, like fibres of a DM or a channel wall, these numbers do not allow to predict the behaviour of the interaction since the force involved in the solid-fluid interaction is not considered.

To predict the influence of gravity on a droplet of water in or on a DM, the interfacial tension between the fibres and the water has to be included and for this special case a dimensionless pressure (the ratio between hydrostatic and capillary pressure) is suggested here. For a contact angle of 0° and a water height of two times the characteristic radius this pressure becomes equal with the Eötvös number. An overview of the definition and a

rough estimate of the number for the DM can be found in Table 1.7.

Table 1.7: Dimensionless numbers for two-phase-flow

Force	Dimensionless Number	Symbol	Definition	Value in DM ‡
Gravity	Eötvös / Bond	Ev / Bo	$\frac{\Delta\rho g r^2}{\sigma}$	10^{-7}
Viscous	Capillary	Ca	$\frac{\mu\ u}{\sigma}$	10^{-12}
Inertia	Weber	We	$\frac{\rho r u^2}{\sigma}$	10^{-17}
Inertia and viscous	Suratman	Su	$\frac{\rho\sigma r}{\mu^2}$	10^{4}
	Ohnesorge	Oh	$\frac{1}{\sqrt{\text{Su}}}$	10^{-2}
Gravity, Fibres	Dimensionless Pressure		$\frac{\Delta\rho g h r}{2\ \sigma\ \cos\theta}$	10^{-3}

‡Parameters: Characteristic length $r = 50$ µm, viscosity of water at 353 K $\mu = 354.4$ µPa s, water velocity in DM $u = 9.3 \cdot 10^{-10}$ m/s for 1 A/cm^2, water surface tension $\sigma = 62.67$ mN/m at 353 K, water density $\rho = 1000$ kg/m^3, height of DM $h = 200$ µm, contact angle water/fibre $\theta = 120°$, gravity constant $g = 9.81$ m/s^2.

As it can be seen, the surface tension is the dominating effect due to small length scales and velocities. The Bond number is the key to familiarise with the capillary dominated physics. Since the Bond number scales with gravity, a low-gravity environment could provide insight into the physics on a much larger scale that is much easier to access experimentally. Experiments in drop towers, parabolic flights, and even in space had been performed to understand the physics. Especially for fluid management in space applications like fuel handling on spaceships, this knowledge is vitally important since the liquid behaviour is capillary driven (even in a large pipe or tank with dimensions of centimetres). The design of liquid-gas separators for spacecraft application has to consider this fact. This is one of the reasons why scientists at space agencies are most knowledgeable in this field.

Two major kinds of model approaches are taken to handle the microscopic details. The network model is more traditional and easier to handle. Thereby, the porous material is represented by a two or three dimensional network of capillaries with different diameters and contact angles as well as different numbers of capillaries meeting at an intersection (coordination number). This model type is based on statistical assumptions

on the structure, while the other kind of models are based on the real micro structure as computational domain and compute the transport and species distribution with the aid of Monte-Carlo techniques, Lagrange techniques, Lattice-Boltzmann or volume of fluid techniques to minimise the surface film energies. To provide the computational domain is the difficult part for the latter kind of models.

Network models of porous media attempt to represent both permeability and pressure-saturation relationship by applying a network structure with a set of more or less distributed properties. In detail, such a model is based on capillaries of a certain length, diameter, and contact angle with the fluid, connected by nodes with certain coordination numbers. For illustration, Figure 1.17 shows a network with a coordination number of 3 and different distances between the nodes.

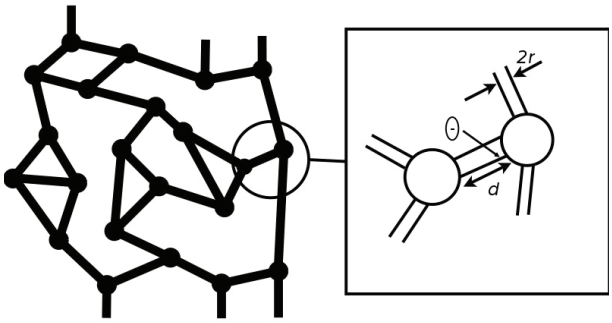

Figure 1.17: Left: 2D network model with a coordination number of 3. Right: Illustration of model parameters like distance between nodes (d), diameter of capillaries ($2r$) and contact angle (θ).

These kinds of models are used to explore fingering phenomena to be compared with the flow pattern on etched structures of similar shape. Lenormand, Touboul, and Zarcone [LTZ88] employed such a model where they used five parameters to describe the pore network: The mean pore and node diameter, the distribution width of the diameters, and the distance between the nodes. In these models the entry pressure for each connecting capillary on a node is calculated and the capillary with the least entry pressure is filled until the next node is reached. Thereby, the displacement pattern and the pressure-saturation relationship is obtained. For fuel cell modelling, e.g. Nam and Kaviany [NK03] or Sinha and Wang [SW08] used the pore network approach.

Network models are fairly easy to handle by computers, but have the disadvantage that

the network, except for etched structures, differs significantly from most porous materials, especially the DM. Furthermore, it is necessary to choose a property, like permeability, to calibrate the model to match with the real structure. The network model is not a good representation of the real structure. But it is fairly close to the constitutive models. The free surface models are more meaningful to investigate water transport and displacement in DM on a fundamental base.

Numerical free surface models are the most costly models with regard to computer resources and processing time, but they represent the real situation as close as possible. The starting point for these models is the geometrical structure in a computer processable format which can be obtained from pictures, tomographs or computer simulations. Both methods, the imaging of real material as well as the computer simulated geometries, have their advantage. While the first method helps to understand the physics of water transport, the latter can be used to tailor the DM by varying geometrical features virtually without going through real manufacturing steps. An early attempt to use such a three-dimensional representation for a drainage and permeation calculation was done at the Fraunhofer Institut für Techno- und Wirtschaftsmathematik (ITWM) by Schulz et al. [SKWS05] and followed by Becker et al. [BIS+06] from the same institute. Their approach is called 'Pore Morphology Method' and analyses the pore structure in such a way that a contact angle between the solid and the invading fluid is assumed and the fluid invades the structure from one side, similar to a displacement experiment. Thereby, the shape of the meniscus and the connection to the 'reservoir' are tracked. For a given curvature of the liquid phase boundary invading the solid structure, the saturation can be assigned to a pressure. At this point the morphology of the partially saturated structure is given and traditional computational fluid dynamic (CFD) tools can be applied to calculate effective properties like the diffusion coefficient and the permeability. Due to the large computer power required to do such calculations on domain sizes that might represent an REV, this method is fairly new and results are rarely published like by Schulz et al. [SKWS05].

Before computers had the required performance, analytical approaches to that matter had been taken a long time ago like by Plateau in 1873 [Pla73]. As indicated above, the fluid management at low gravity is an applied free surface problem and, therefore, a fair

amount of literature on analytical solutions is available ([MBK+86], [SA03] and others). The principle of the analytical solution is based on the search for the interface contact line with the smallest amount of energy. From a mathematical point of view, the problem boils down to find the minimum of a function of the three space variables x, y, and z describing the contact surface, while x, y, and z are linked with each other via the volume of the liquid. In Figure 1.18 a drop on a surface illustrates the dependency.

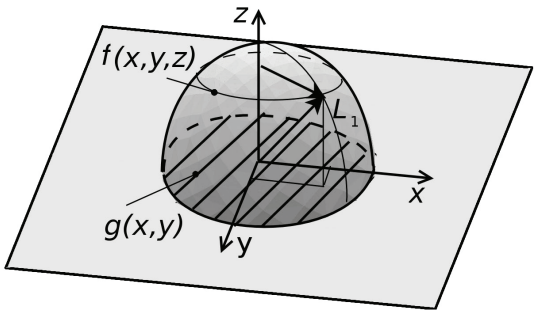

Figure 1.18: Drop on a surface to illustrate the mathematical description of free surface problems. L_1 locates an arbitrary position on the surface described by the function $f(x, y, z)$.

In this case, the drop will adopt the shape with the lowest possible surface energy by minimising the contact area at the interface bottom surface and the liquid as well as the interface between gas and liquid. The drop interface with gas is described by a function $f(x, y, z)$ and the interface with the bottom by a function $g(x, y)$. The total surface energy can be expressed in mathematical terms according to

$$\Gamma = \gamma_{\text{sol, liq}} \int g(x,y)dx + \sigma \int f(x,y,z)dx, \tag{1.64}$$

with $\gamma_{\text{sol, liq}}$ as the interfacial tension between solid and liquid and σ as the surface tension. For the mathematical problem of finding the minimum value of a function of multiple variables, the Euler-Lagrange equation

$$\begin{aligned} \frac{\partial f}{\partial y} - \frac{d}{dx}\frac{\partial f}{\partial \frac{dy}{dx}} &= 0 \\ f &= f\left(x, y, \frac{dy}{dx}\right) \end{aligned} \tag{1.65}$$

is used. With f being the first derivative with regard to x of the function the extreme value is being looked for, in this case the total surface energy Γ.

This approach makes the least assumptions of fluid dynamic aspects in capillary dominated environment (see Section 1.3.6 on page 52ff.), but the nature of the problem finding the geometry with the lowest surface energy is not limited to a unique solution. In more complicated situations than the drop on a surface, there might be several different geometries with the same surface energy and the actual shape of the interface is history dependent and subject of hysteresis (see Slobozhanin, Alexander and Patel [SAP02]). Furthermore, analytical calculations are only feasible for very simple cases. Therefore, free surface problems in more difficult geometries are often approached numerically (see, e.g. Slobozhanin, Alexander et al. [SACG06]).

Chapter 2

Ex-situ Experiments

2.1 Concept

In this section, the pressure dependent saturation and the relative permeability of Toray 060 with hydrophobic impregnation is investigated experimentally. First, a method to measure the pressure dependent saturation on gas diffusion media is introduced. Later, measurements of relative permeability are presented and finally discussed in light of the different permeability models already introduced in Section 1.3.4 on page 43ff.

2.2 Water Saturation

2.2.1 Setup

Traditionally, the saturation-pressure relationship is obtained by drainage experiments of a fully saturated porous sample [BC64, Bea88]. The wetting phase is usually the denser phase and the head pressure across a fairly large sample is the driving force for the outflow of the wetting fluid. The pressure gradient is associated with a local saturation, which is determined either gravimetrically or by other techniques. For the gas diffusion medium this approach is not applicable since one sheet of DM is between 150 µm and 300 µm thin and the head pressure gradient is negligible compared to the entry pressure (5 kPa, in comparison to 3 Pa, see page 73). Furthermore, the local saturation is not measurable if only one sheet of material is investigated. Another important limitation is the fact that

the DM of interest is rendered hydrophobic to a large extent. Therefore, the techniques traditionally applied by hydrologists fail.

For materials like DM the pore size distribution in connection with the Young-Laplace equation is used to calculate the saturation-pressure relationship [GFI06, KSM07]. The saturation dependent notation of the Young-Laplace equation

$$p_{\mathrm{cap}}(s) = \frac{2\sigma \cos\theta}{r(s)} \tag{2.1}$$

contains the pore radius r as a function of the saturation s. Thereby, it is assumed that the contact angle θ between the solid and the liquid is a constant for the pores in the sample. The pore size distribution can be obtained by mercury porosimetry, capillary porosimetry, standard porosimetry, or by other methods. Gostick et al. [GFI06] made a comparison between pressure-saturation functions based on pore size distributions coming from standard and mercury porosimetry on SGL and Toray DM materials. Different approaches not relying on any assumptions with regard to the contact angle were suggested by Koido et al. [KFMT06], Nguyen et al. [NLOW06], and Gostick at al. [GIFP08], using partly volumetric and gravimetric techniques to measure the saturation at an applied liquid pressure or pressure difference.

An alternative way to measure the pressure dependent saturation relationship for a non-wetting fluid, like water in DM, was developed and will be presented here. This method is also not restricted to the assumption of a uniform contact angle since it is a direct measurement of the saturation at a given liquid pressure. The measurement principle is based on the saturation dependent change of the buoyancy of a partially saturated sample, immersed into water. The buoyancy of the sample is majorly caused by the large volume of air inside the sample. The buoyancy of the sample as a function of saturation is obtained by the following equation:

$$m_{\mathrm{buoy}} = V_{\mathrm{geo}} \left[\varepsilon \left(1 - s\right) \rho_{\mathrm{g}} + \left(1 - \varepsilon\right) \rho_{\mathrm{sub}} + \left(s - 1\right) \rho_{\mathrm{liq}}\right] \tag{2.2}$$

The effective mass of the partially saturated and submerged media is represented by m_{buoy}, V_{geo} denotes as the volume of the sample based on the outer dimensions, ε the porosity,

s the saturation, ρ_{liq}, ρ_{g}, and ρ_{sub} are densities of the liquid, the gas and the substrate, respectively. The sample is saturated by exposing it to different water pressures under immersion. It is important that the sample is kept surrounded by water between the saturation and the measurement procedure in order to sustain the equilibrium. The non-water-wetting material expels the water when the surrounding pressure decreases and gas enters the pore space.

When the DM is submerged into water at a pressure exceeding the entry pressure, the air in the porous system is compressed by the entering water. The buoyancy changes since the saturation increases. But the increased gas pressure inside the DM is not desirable for two reasons:

- The buoyancy measurement has to take place in a pressurised environment to ensure a constant saturation during the measurement.
- The pressure inside the sample is not known and has to be calculated based on saturation data afterwards.

These drawbacks can be avoided by performing the saturation in the following way (see also Figure 2.1):

1. The sample is placed in the upper part of a sealed container, partially filled with water (Pos. I in Figure 2.1). The water is not in contact with the sample.
2. The gas pressure in the container is lowered to the desired pressure difference, causing the gas pressure inside the sample to decrease as well (Pos. II in Figure 2.1).
3. The sample is submerged into the water (Pos. III in Figure 2.1).
4. The environmental pressure is re-established. Thereby, the air in the sample contracts and the water around the sample starts to invade the pores (Pos. IV in Figure 2.1).

It is convenient to measure the saturation with a surface balance, like the Krüss K12, used in this work. A sketch of the procedure is represented in Figure 2.2.

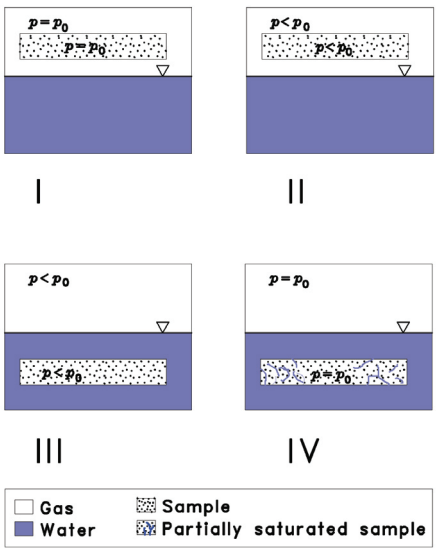

Figure 2.1: Saturation procedure for DM. Conditions in the sample compartment at stage I: Environmental pressure in gas phase and DM. II: Reduced pressure in gas phase and DM. III: Reduced pressure in gas phase and DM, but DM submerged in water. IV: Environmental pressure in gas phase, reduced pressure in DM, water invades the pore space.

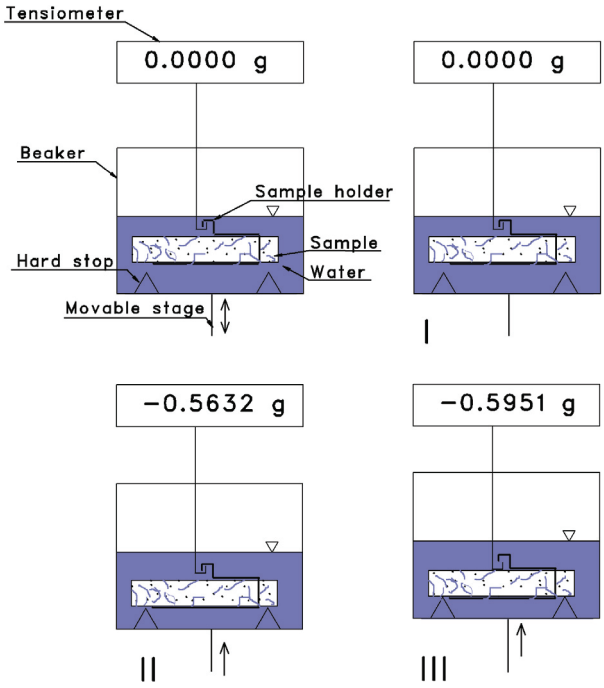

Figure 2.2: Measurement procedure for partially saturated DM. I: Surface balance is tared. II: Stage is risen, sample gradually touches the hard stop. II: DM rests on the hard stop. III: No connection between sample holder and load cell.

The surface balance consists of a load cell, mounted above a vertically moving stage. The sample is placed on a sample holder connected to the load cell by a thin wire. During the whole experiment, the sample stays submerged in water all the time to avoid an uncontrolled change of the saturation. The balance is tared and the stage is moved upwards (see Pos. I in Figure 2.2). The load, indicated by the balance, is the sum of the weight of the wire, the sample, the entrapped air, reduced by the buoyancy of the named components. As the stage moves upwards, the sample will eventually rest on a hard stop position where the sample loses the connection to the load cell (Pos. III in Figure 2.2). The release of the connection between the load cell and the sample is ensured by a hook.

The raw data of this measurement are depicted in Figure 2.3. The roman numeral in the plot correspond to the previously described steps. The transition region II is caused by the alignment of the sample. If the sample is not in a strictly horizontal position, the sample contacts the hard stop not instantly but gradually. This causes a step-wise reduction of the force on the balance. The difference in force between the taring and the final position gives the total effective buoyant mass. Since the porosity of the DM is in the order of $70\,\% - 90\,\%$, the samples tend to float at low saturation. To avoid this, a wire bracket (sample holder) surrounds the sample and establishes the connection to the wire coming from the load cell.

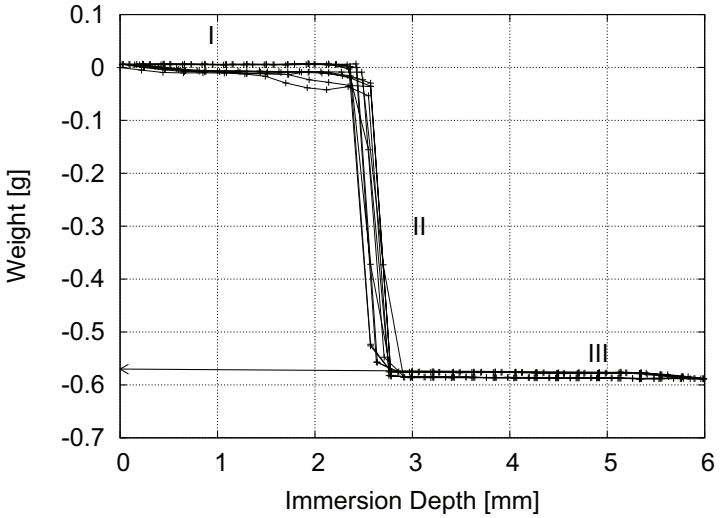

Figure 2.3: Raw data of buoyancy measurement of partially saturated DM to calculate the saturation according to Equation 2.2 on page 60.

The wire, connecting the sample and the load cell, intersects the water surface. This results in additional force on the wire caused by the meniscus. The shape of the meniscus is different for the submerging and the emerging section of the measurement cycle and, therefore, the force on the balance is different. This is a source of a significant error for the buoyancy measurement. The error can be reduced by using a thin wire for the connection since the force of the meniscus is proportional to the circumference of the wire. The motion dependent part of the meniscus force can be eliminated if the data analysis is limited consistently to the submerging or the emerging branch. Experiments showed that the emerging branch gives the smaller variation and, hence, the emerging branch is used exclusively. The buoyancy of the wire depends linearly on the position of the stage and this would cause an error if the mass difference is calculated at different immersion depth from saturation to saturation. This effect can be taken into account by linear extrapolation of the data points in 'horizontal' regions (see I and III in Figure 2.3) to zero immersion depth.

The accuracy of the pressure control for the saturation procedure was $\pm$ 0.5 kPa, the surface balance is accurate to 0.001 g. For the saturation measurement, the systematic error is about $\pm$ 1 %. But, as it will be shown in the next section, the random errors are in the order of $\pm$ 5 %, mainly caused by the forces of the meniscus at the wire connecting the sample with the load cell. Since the multiple wetting of the wire surface causes contact angle hysteresis, the force at the meniscus varies randomly from one test cycle to the next.

2.2.2 Result

The DM samples used in the saturation measurement had a pentagonal shape with an edge length of 20 mm. The pentagonal shape is preferred since it represents a good trade-off between the utilisation of the round cross section of the beaker (maximising the sample-size) and the necessity to have a gap between the sample and the rim of the beaker to free trapped gas bubbles which might accumulate below the sample during the saturation procedure.

In a first step, the buoyancy and, therefore, the porosity is determined for the unsaturated sample as a baseline. The sample appears silvery since there is a thin gas cushion between the water and the sample. This is caused by the hydrophobic fibres that do not

allow the water to penetrate the outermost fibre layer. Subsequently, the same sample is saturated with water at increasing saturation pressure. At each saturation step the buoyancy is measured three times. Since the saturation is subject to hysteresis [Bea88], the pressure was reduced for a few points to environmental pressure after measuring the saturation at higher water pressure. One reason for the hysteresis is the difference of contact angles between water and fibre for the advancing meniscus and the receding meniscus. The difference of the surface shape, just before touching a fibre and just after touching a fibre in the advancing case, causes a pressure discontinuity, the same is true in the receding case between just before detachment and after detachment. Yet, the liquid volumes at the transitions are different in the two cases. This is a second reason for the pressure-saturation hysteresis (see also Section 3.3.4 on page 103).

Figure 2.4 shows the pressure-saturation relationship for Toray 060 containing 10 % PTFE and 7 % PTFE, obtained from five different samples with the technique previously described, including some hysteresis points.

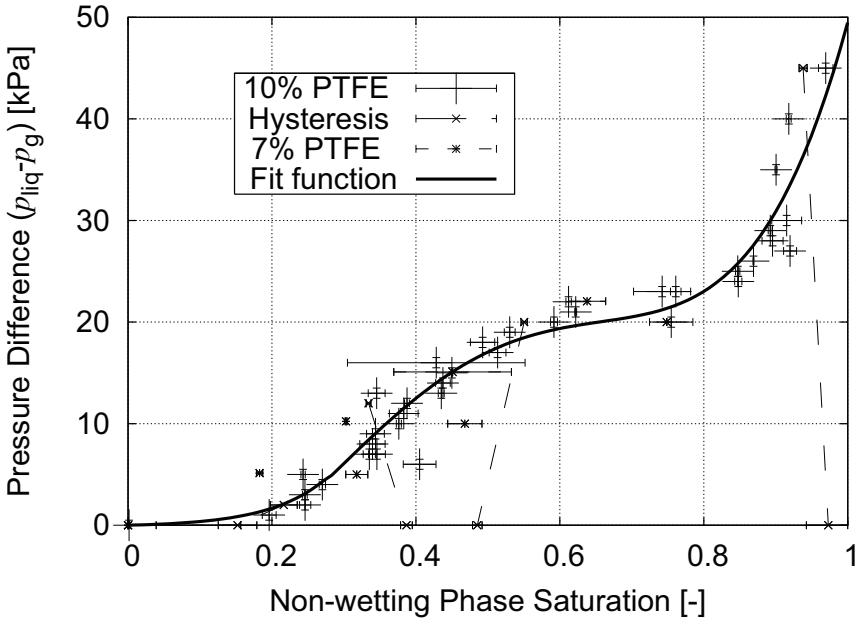

Figure 2.4: Pressure-saturation relationship for Toray 060 (five different samples) with 10 % PTFE and 7 % PTFE at room temperature ($\sigma_{H_2O} = 71.392 \pm 1.23$ mN/m). The fit function is defined stepwise: $s_{nw} < 0.28$: $p_{liq} = 0.144$ kPa $[\exp(12.685\ s_{nw}) - 1]$ and $s_{nw} \geq 0.28$: $p_{liq} = (606.386\ s_{nw}^4 - 1155.570\ s_{nw}^3 + 705.716\ s_{nw}^2 - 108.437\ s_{nw} + 1.387)$ kPa.

Due to the accidental errors of the measurement the saturation data of the different individual samples form a range rather than a single line. The x-error bars represent one standard deviation of three measurements. The fairly large standard deviation is caused by the fact that small weight differences (0.1 mg) are measured with a transient method. The sensitivity of saturation to the level of hydrophobic impregnation of 7 % and 10 % PTFE is minor compared to the sample-to-sample variance. The hysteresis is significant; the saturation under ambient condition keeps at the same level as it was at the water pressure previously exposed.

In order to parametrise the relationship for further calculations, a stepwise fit to the experimental data for the increasing pressure is suggested:

$$\begin{aligned} s_{\mathrm{nw}} < 0.28 : p_{\mathrm{liq}} &= 0.144 \text{ kPa } [\exp\,(12.685\ s_{\mathrm{nw}}) - 1] \qquad (2.3) \\ s_{\mathrm{nw}} \geq 0.28 : p_{\mathrm{liq}} &= \left(606.386\ s_{\mathrm{nw}}^4 - 1155.570\ s_{\mathrm{nw}}^3 + 705.716\ s_{\mathrm{nw}}^2 - 108.437\ s_{\mathrm{nw}} + 1.387\right) \text{ kPa} \end{aligned}$$

Strictly speaking, the abscissa and the ordinate in Figure 2.4 had to be interchanged since the pressure is the independent variable. But historically, the pressure-saturation relationship is plotted as presented here.

The pressure-saturation relationship suggests that 20 % pores are less hydrophobic or fairly large. This can be seen at very low pressures. The smallest pressure applied was 1 kPa, and according to Young-Laplace this corresponds to an apparent pore radius of r = -145.6 µm$\cdot \cos\theta$ (since $\cos\theta < 0$ while $\theta > 90°$). A plateau can be found between 40 % and 80 % saturation, corresponding to a pressure of 18 kPa − 22 kPa and a pore radius r = -7 µm$\cdot \cos\theta$ to r = -8 µm$\cdot \cos\theta$. The steep increase in saturation beyond 22 kPa indicates that only a small portion of the total volume has an apparent pore size smaller than r = -7 µm$\cdot \cos\theta$. The contact angle θ is unknown, therefore the radius is not stated as a simple number. The shape of the function suggests that a bi-modal distribution is underlying.

A comparison between the formulation of the capillary pressure by Brooks and Corey [BC64], Van Genuchten [VG80] and the third-order polynomial discussed in Section 1.3.2 on page 30ff. and the measured data is plotted in Figure 2.5. Even qualitatively, the proposed relationships and the measured data deviate significantly.

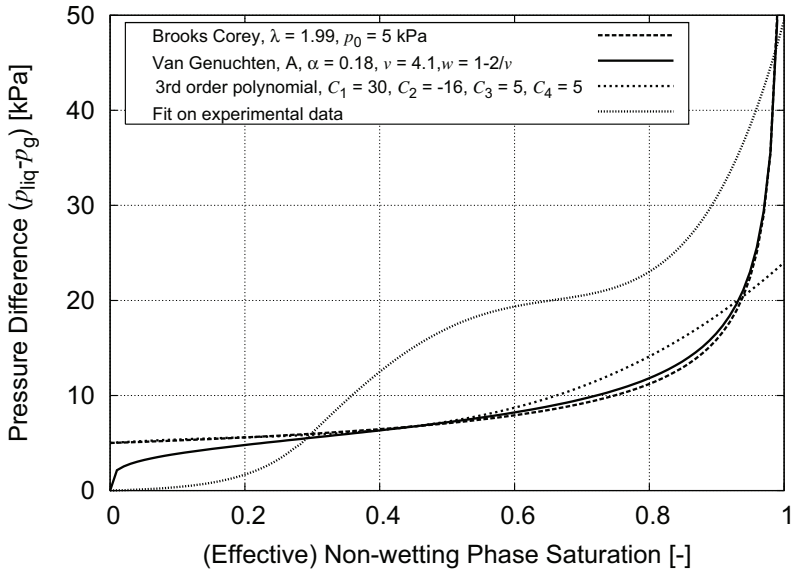

Figure 2.5: Comparison between pressure-saturation relationships used in literature and measurement fit (Equation 2.3).

From permeability experiments (see Section 2.3 on page 69ff.), it is observed that the water flux is only possible if the pressure difference across the sample exceeds the breakthrough pressure. Pressure differences below the breakthrough pressure lead to a saturation that does not effect the permeability of the sample. The concept of residual saturation, explained also in Section 1.3.2 on page 31, can be applied to link the saturation-pressure relationship with the pressure dependent permeability. In the light of the observation discussed previously, the residual saturation can be defined as the saturation at which hydraulic permeability is just established. There is also a residual saturation for the gas phase, yet there was no experiment conducted during the course of this work to measure it. The residual saturation for the gas phase is ignored here, because the focus is on the low water saturation. The permeability experiment (see Section 2.3.3 on page 72ff.) suggests that the permeability that establishes at 5 kPa pressure difference is sufficient to transport all the water produced at a current density in the order of 10 A/cm^2 to 20 A/cm^2. Since there is a pressure threshold to overcome in order to establish water permeability of the sample, the pressure-saturation relationship can be based on an effective saturation. This rescales the plot and artificially introduces a pressure offset at an effective saturation of zero ('residual saturation'). The effective saturation is the reduced

real saturation, normalised by the residual saturation

$$s_{\mathrm{e,nw}} = \frac{s_{\mathrm{nw}} - s_{\mathrm{r,nw}}}{1 - s_{\mathrm{r,nw}}}. \tag{2.4}$$

The effective saturation depends on the level where the residual saturation is assumed (based on the pressure-permeability experiment). If a residual saturation of 15 % is assumed, the first part of Udell's equation agrees with the saturation corrected experimentally determined pressure-saturation relationship for the range of 0 % up to 10 % saturation (depicted in Figure 2.6). More realistic, because experimentally supported, the residual saturation is between 20 % and 30 % if the breakthrough pressure is chosen as criterion (see Section 2.3.3 on page 72ff.).

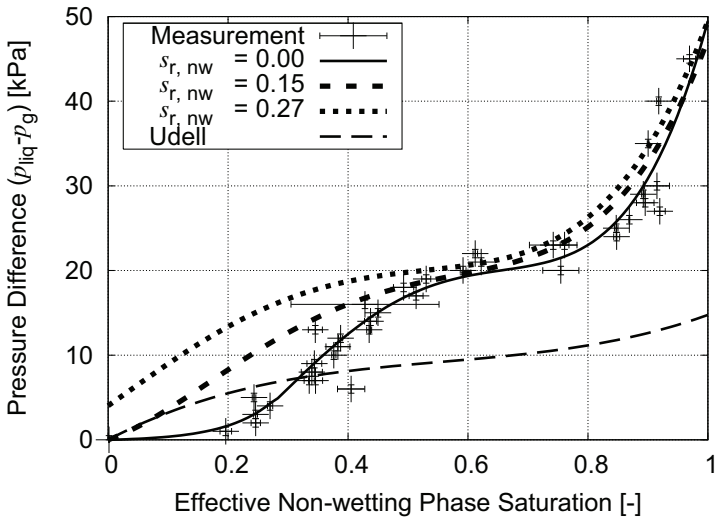

Figure 2.6: Effect of different assumed residual saturations on the measured pressure-saturation relationship (the parameter of Udell can be found on page 33).

The pressure-saturation relationship based on the residual saturation of 27 % is used exemplary. It corresponds to a pressure of 4 kPa which is the upper end of entry pressures observed experimentally. The fit function to the experimental data, based on the effective saturation of 27 %, is

$$p_{\mathrm{liq}} = \left(172.2\ s_{\mathrm{e,nw}}^4 - 194.8\ s_{\mathrm{e,nw}}^3 + 18.6\ s_{\mathrm{e,nw}}^2 + 49.4\ s_{\mathrm{e,nw}} + 4.0\right) \mathrm{kPa}. \tag{2.5}$$

2.3 Water Permeability

2.3.1 Setup

The most direct approach to investigate the convective transport of liquid water through DM is to perform a flow experiment. Benziger et al. [BNB+05] suggested a gravity driven flow experiment. In their experiment, the pressure is set by a water column which was not held constant during the outflow, measured gravimetrically. In the experiment suggested here, the combination of pressure and flow rate of liquid water is measured. The boundary conditions of such an experiment are important, since the flow pattern depends upon the local velocity even in much simpler cases like the flow inside tubes (e.g. laminar and turbulent flow). The flow velocities inside the DM in an operating fuel cell are certainly extremely low and this represents an experimental challenge. Regular flow meters fail to measure the flow rates of ~ 0.1 µL/s which is the water production rate at 1 A/cm^2 for 16 cm^2 (sample size used in this experiment).

Instead of measuring and controlling flow rates, a pressure-controlled experiment was developed and it turned out that the same approach had been used previously for measuring the permeability of rocks [HKPV96]. The experimental setup is based on a pressurised water column which is in connection with the sample (see Pos. 4 in Figure 2.7). At a defined entry pressure (p_{in}, relative to the environmental pressure), air fills the space above the water (Pos. 3). This leads to the following results:

1. The pressure inside the gas volume (Pos. 3) increases until the pressure corresponds to the capillary pressure of the largest passage between the two surfaces of the DM (defined by its widest opening).

2. Then, water flows through the sample leading to an increased gas volume above the water.

The two steps represent both a dynamic and a stationary part regarding its pressure characteristics, discussed analytically in the next section.

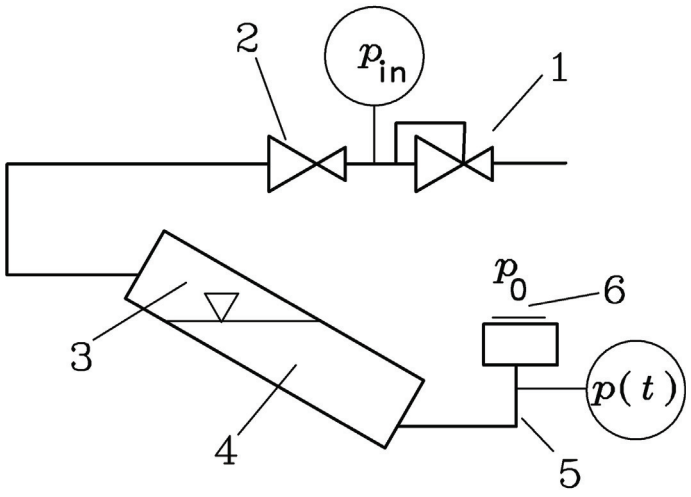

Figure 2.7: Setup for the permeation experiment. 1: Pressure regulator, 2: Throttle valve, 3: Gas volume, 4: Water reservoir, 5: Water pipe to sample, 6: Sample.

2.3.2 Analytical Description

The analytical description starts with a mass balance around the experimental setup. For the throttle valve (Pos. 2 in Figure 2.7), it was experimentally found that the flow rate can be approximated with a second order polynomial with regard to the pressure:

$$\frac{dV_{\text{in}}}{dt} = C_7 \ [p_{\text{in}} - p(t)]^2 + C_8 \ [p_{\text{in}} - p(t)] \tag{2.6}$$

$\frac{dV_{\text{in}}}{dt}$ denotes the volumetric incoming gas flux, $C_7 = 9.81 \cdot 10^{-8}$ L/s/kPa^2 and $C_8 = 2.05 \cdot 10^{-6}$ L/s/kPa are the polynomial coefficients, p_{in} is the entry pressure difference, and $p(t)$ is the gas pressure difference inside the water column (Pos. 3 in Figure 2.7), both relative to the environmental pressure. The experiment for characterising the valve was done for small pressure differences against atmospheric pressure on the outlet side at room temperature. Therefore the molar flux through the valve in Pos. 2 can be written as (2.7):

$$\frac{dn_{\text{in}}}{dt} = \frac{\left[C_7 \ [p_{\text{in}} - p(t)]^2 + C_8 \ [p_{\text{in}} - p(t)]\right] \ p_0}{\Re \ T} \tag{2.7}$$

For the water flow through the sample (Pos. 6 in Figure 2.7) Darcy's law for incompressible media is used:

$$\frac{dV}{dt} = \frac{A\ k_{\mathrm{DM}}}{l\ \mu_{\mathrm{H_2O}}}\left[p(t) - p_0\right] \tag{2.8}$$

A is the sample area, l the thickness of the sample, k_{DM} the permeability of the diffusion medium (treated as scalar, for the 1D model), and $\mu_{\mathrm{H_2O}}$ the viscosity of the water.

The constitutive equation for the water reservoir can be expressed by the isothermal total derivative of the ideal gas law:

$$\frac{dn}{dt}\ \Re\ T = \frac{dp}{dt}\ V(t) + \frac{dV}{dt}\ p(t) \tag{2.9}$$

The left part of the equation describes the incoming flux, while the right part describes the pressure change and the change in volume due to the water displacement. The expected change in gas volume is small compared to the initial gas volume ($V_0 \approx 10^{-3}$ m^3) due to low permeability. It is assumed constant as a first approximation, which allows for an analytical solution. By combining Equations 2.7, 2.8, and 2.9, the following equation is obtained:

$$\Big[C_7\ \left[p_{\mathrm{in}} - p(t)\right]^2 + C_8\ \left[p_{\mathrm{in}} - p(t)\right]\Big]\ p_0 = V_0\ \frac{dp}{dt} + \frac{A\ k_{\mathrm{DM}}}{l\ \mu_{\mathrm{H_2O}}}\ \left[p(t) - p_0\right]\ p(t) \tag{2.10}$$

Rearranged for the pressure change:

$$\frac{dp}{dt} = \Big[C_7\ \left[p_{\mathrm{in}} - p(t)\right]^2 + C_8\ \left[p_{\mathrm{in}} - p(t)\right]\Big]\ \frac{p_0}{V_0} - \frac{A\ k_{\mathrm{DM}}}{l\ \mu_{\mathrm{H_2O}}}\ \left[p(t) - p_0\right]\ \frac{p(t)}{V_0} \tag{2.11}$$

Since the development of pressure above the water over time represents the experimentally measured property, further rearrangement is required. This leads to the differential equation

$$dt = \frac{dp}{C_9\ p(t)^2 + C_{10}\ p(t) + C_{11}} \tag{2.12}$$

with:

$$\begin{aligned} C_9 &= C_7\ \frac{p_0}{V_0} - \frac{k_{\mathrm{DM}}\ A}{\mu\ l\ V_0} \\ C_{10} &= \left(\frac{k_{\mathrm{DM}}\ A}{\mu\ l} - C_8 - 2\ C_7\ p_{\mathrm{in}}\right)\ \frac{p_0}{V_0} \\ C_{11} &= \left(C_7\ p_{\mathrm{in}}^2 + C_8\ p_{\mathrm{in}}\right)\ \frac{p_0}{V_0} \end{aligned}$$

A solution for this integral can be found in [BS89]. Within the boundaries from p_0 to $p(t)$ and rearranged for $p(t)$ the final equation for the dynamic part is obtained:

$$p(t) = \frac{C_{12} - C_{10} + (C_{12} + C_{10})\ C_{13}\ \exp\left[C_{12}\ t\right]}{2\ C_9\ (1 - C_{13}\ \exp\left[C_{12}\ t\right])} \tag{2.13}$$

with

$$\begin{aligned} C_{12} &= \sqrt{-(4\ C_{11}\ C_9 - {C_{10}}^2)} \\ C_{13} &= \frac{2\ C_9\ p_0 + C_{10} - C_{12}}{2\ C_9\ p_0 + C_{10} + C_{12}} \end{aligned}$$

The experiment can be done with different boundary conditions like flow rate, as well as dry and wet outlet configurations on the low-pressure side of the sample. This boundary is represented by the flow field structure in the fuel cell. Depending on whether the location of interest is located in the channel or the land region, a wet or a dry spot in the channel, the boundary is either wet or dry. In the light of this consideration, different possible configurations are tested experimentally in the following section.

2.3.3 Boundary Conditions

Wet boundary as well as dry boundary conditions had been applied to the permeability measurements on Toray 060 carbon paper, impregnated with 7 % PTFE on the low-pressure side of the sample.

The wet boundary was set by covering the surface of the sample at the low-pressure side with water before the gas flow through the throttle valve (Pos. 2 in Figure 2.7) was allowed. The entry pressure was set to 6 kPa relative to the environment. The chamber pressure raises steadily under these conditions until a stationary pressure is established. The water permeability at the given saturation can be determined with the aid of Equation 2.13 by adjusting k_{DM} (C_9 and C_{10}). The disk-shaped samples allowed for a circular flow cross section of 4.5 cm diameter. Figure 2.8 shows the measured data, as well as two calculated curves for different permeability values.

The thin solid line represents the gas flow rate into the setup (throttle valve, Pos. 2 in Figure 2.7), calculated based on Equation 2.6. The incoming gas flow rate is equal

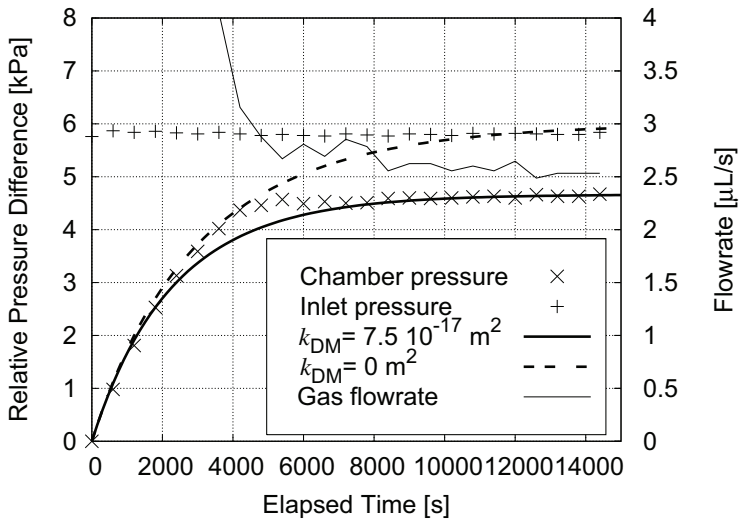

Figure 2.8: Pressure response of water covered sample at 6 kPa inlet pressure in comparison with calculated results for impermeable DM ($k_{\mathrm{DM}} = 0$ m^2) and permeable DM ($k_{\mathrm{DM}} = 7.5 \cdot 10^{-17}$ m^2).

to the water flow rate through the sample at equilibrium. The thick solid line assumes a permeability of $7.5{\cdot}10^{-17}$ m^2 and underestimates the experimentally found pressure in the beginning, but meets the measurement at $t \geq 8000$ s and beyond. The dotted line represents the pressure development for an impermeable sample and agrees with the measurement in the beginning, but deviates after $t \geq 4000 - 5000$ s.
This is a clear indication that the sample has too few or none hydrophilic domains to provide a connected pore network with zero or negative entry pressure. A liquid pressure of 4.5 kPa is required to establish a connected pore network across the sample thickness.

Dry boundary conditions are desired in the channel region of the DM in the fuel cell in order to keep the reaction going. To set the dry boundary condition in the experiment, the water was pushed through the sample parallel to the gravity vector (top-down). This ensures that the low-pressure side remains dry since the water repels from the sample and falls off once the drops have a specific size. Thereby, a defined removal of the droplets formed on the low-pressure side is guaranteed. This is similar to the fuel cell when the gas stream in the channel shears off the droplets. The pressure response during the course of the experiment at the dry boundary condition is depicted in Figure 2.9. In

the beginning, the pressure characteristic of the wet boundary experiment and the dry boundary experiment agree well, but at a certain pressure (breakthrough) the rise stops for the dry boundary and a rapid pressure decrease is observed due to a sudden water permeability of the sample. The line pressure between the pressure regulator and the throttle valve is constant in the setup, but the flow rate through the valve is not. The flow rate is determined by the pressure gradient across the valve which decreases as the pressure in the reservoir increases and thus, the flow rate decreases, too. At the point where the water permeability suddenly establishes at a high level, the gas above the water surfaces expands and the pressure drops. Simultaneously, the pressure drop across the inlet valve increases, causing an increase of the incoming flow rate. Figure 2.9 shows the pressure response at an entry pressure of 5 kPa, the gas pressure inside the water column, the gas flow rate through the inlet valve, as well as the calculated case for an impermeable sample by applying Equation 2.13.

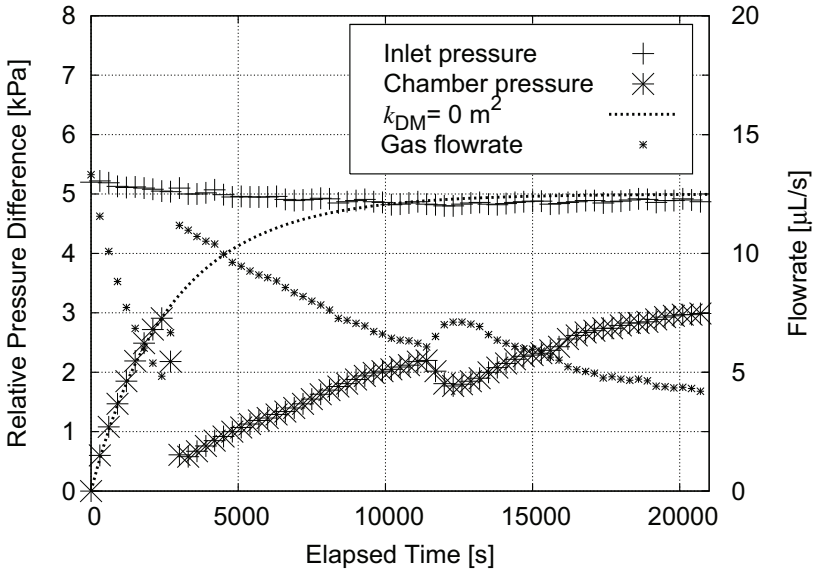

Figure 2.9: Pressure response of a sample with air at the low-pressure side in comparison with calculated result for impermeable DM ($k_{\mathrm{DM}} = 0$ m^2).

The pressure development for the dry boundary condition deviates significantly from the wet boundary condition and different model hypothesis will be tested against the measurement in the following. 'Octave' version 2.1.73 was chosen as the code to solve the equations numerically.

It is assumed in the first model (Model 1) that there are two discontinuities in the permeability. The first discontinuity is hypothesised at breakthrough, and the second at low pressure. The second is motivated by the consideration that the pressure might become insufficient to keep the water in the sample connected. The permeabilities had been chosen to ensure that the calculated pressure meets the experimentally determined pressure at the end. This assumption is applied for Model 1 in Figure 2.10, resulting in an over prediction of the pressure increase beyond the second discontinuity at 3000 s.

The second model (Model 2) is based on pure empiricism. This model contains one discontinuity in permeability at breakthrough, but also a second term which is not physically justified. Equation 2.8 (page 71) is extended by a new term

$$\frac{dV}{dt} = \frac{A\ k_{\mathrm{DM}}}{l\ \mu_{\mathrm{H_2O}}}\left[p(t) - p_0\right] + \frac{Y\ \frac{dp}{dt}}{p(t)}, \tag{2.14}$$

Where Y is the subject of discontinuity in the new term. The new term affects the mass balance of the experimental setup like an extra gas volume; it provides compressibility to the system. The assumption that the additional gas volume in the water reservoir due to draining during the experiment is proofed wrong, since it turns out that the additional volume Y is in the order of 4 L, while the gas volume V_0 is in the order of 0.7 L and the water level in the reservoir decreased only little. With the extension by Y Equation 2.10 becomes:

$$\Big[C_7\ \left[p_{\mathrm{in}} - p(t)\right]^2 + C_8\ \left[p_{\mathrm{in}} - p(t)\right]\Big]\ p_0 = \left[V_0 + Y\right]\ \frac{dp}{dt} + \frac{A\ k_{\mathrm{DM}}}{l\ \mu_{\mathrm{H_2O}}}\ \left[p(t) - p_0\right]\ p(t) \tag{2.15}$$

Although extremely empiric and arbitrary, the calculation based on Equation 2.15 allows to model the experimentally found pressure development up to 1150 s (see Model 2 in Figure 2.10). The drop in pressure, seen in the measurement at 1200 s might come from a spontaneous permeability increase, like the one seen at the initial breakthrough pressure. This second pressure drop is not represented in the results computed with the empirical model (Model 2).

The third model (Mualem) is physically the most justified. Here, one discontinuity in permeability is assumed at the breakthrough as well – not to a new constant value,

but to a saturation dependent permeability. The pressure-saturation relationship was determined experimentally (see Section 2.2 on page 59ff.) and Mualem's model for relative permeability is used (see Section 1.3.4 on page 45). The residual saturation was adjusted here to be 24 % rather than 27 %. The reason is that the entry pressure for this individual sample is lower than the average, measured on PTFE coated Toray 060. The resulting pressure development over time is depicted in Figure 2.10. This model is representative for all models with saturation dependent permeability with respect to the shape of the pressure plot. Once the sample becomes permeable at the breakthrough pressure, the saturation and the permeability seek for equilibrium. The pressure at equilibrium is always lower than the breakthrough pressure and falls monotonically. The experimentally found pressure increase cannot be reflected by Mualem's model. The detailed parameters of the models are given in Appendix C on page 177ff.

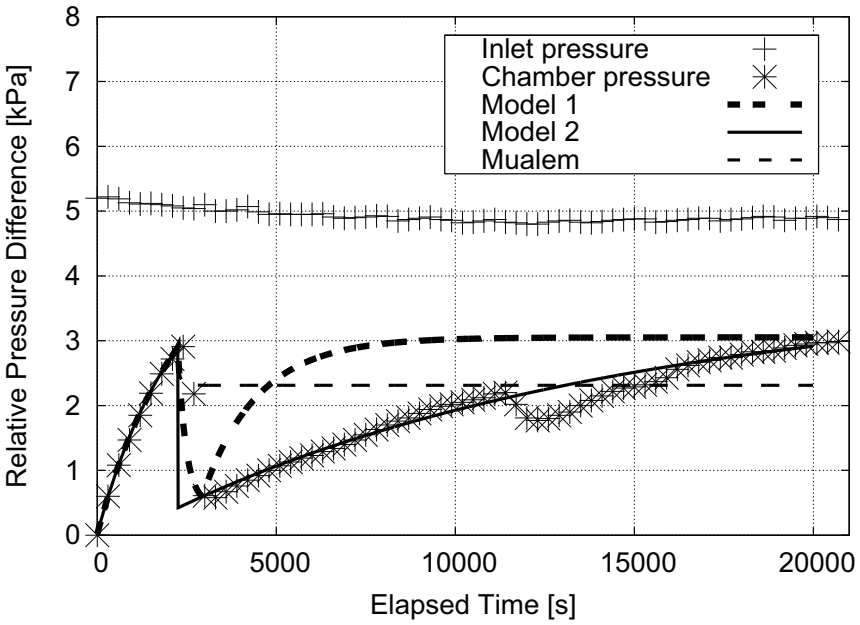

Figure 2.10: Different attempts to model the pressure response of a sample with air at the low-pressure side. Model 1 assumes two discontinuities in permeability. Model 2 does so as well, but with an additional compression term. Mualem considers saturation dependency once the water flow sets in.

The dry boundary condition has a strong influence on the permeability of the DM. The processes involved in equilibrating material saturation and permeability are associated

with time constants in the order of several hours and are not covered by the concept of relative permeability used in hydrology. The major difference between the materials described in hydrology and here is the thickness of the material. Here, the material consists only of 10 to 20 layers of 7 µm thick fibres. In hydrology, the problems often deal with formation thicknesses of several meters consisting of particles in the 10^{-3} m length scale. The study revealed that the boundary condition at the low-pressure side has a strong influence on the permeability. Furthermore, the experiment shows that the water permeability of DM is subject to hysteresis.

In a nutshell, the used method for determining the liquid permeability in partially saturated media is based on a slow displacement of air and it can be assumed that the processes are near equilibrium. The volume fluxes, applied in the experiment are in the range of µL/s. This flux appears high in terms of fuel cell operation since it corresponds to a water production rate in the order of 10 A/cm^2. This raises the question whether the surface tension is still the dominant force in relation to wall friction (viscosity). The capillary number Ca (see Section 1.3.6 on page 52) sets the two effects into relation. In the fuel cell operation, this ratio was found to be in the order of 10^{-12}, while the experiment gives 10^{-5}. This discrepancy is caused by the viscosity difference due to temperature assumptions in Section 1.3.6 on page 52ff. and the difference in current density. But, even if the capillary numbers from fuel cell operation and the experiment differ by seven orders of magnitude, the surface tension is still the dominating factor in the experiment (since $\mathrm{Ca} \ll 1$).

Also, it was found that the hydrophobic diffusion medium has no hydrophilic pore network (no pores with positive capillary pressure).

Further it can be concluded, that the permeability is not constant but a function of the pressure history and surface boundary condition. Based on the later finding, it is not meaningful to extract a constant relative permeability for a dry boundary condition from the measurement since the traditional concept of a time-independent relative permeability does not seem to apply. In case of the wet boundary no contradiction to the conventional relative permeability concept was found and the relative permeability can be determined by the described method (see the next section).

2.4 Saturation Dependent Relative Permeability

The stationary part of the permeation experiment at wet boundary conditions is the base for obtaining relative permeability data. In combination with the pressure-saturation relationship it is possible to test different theoretical models, found in literature, against the experimentally found permeability.

The permeability as a function of pressure is determined experimentally by the following test sequences. One for the draining of the wetting fluid and the other for the imbibing of the same. The permeability as a function of pressure for drainage of the wetting fluid (air) is measured as follows. A sheet of Toray 060 with 10 % PTFE in the dimension of about 5 cm by 5 cm is mounted in the setup depicted in Figure 2.7 on page 70 and covered with water on the low-pressure (upper) surface (wet boundary). The inlet pressure is set to 4 to 5 kPa. The pressure in the water column, as well as the pressure difference across the throttle valve are measured during the course of the experiment. The inlet pressure is held constant till the equilibrium pressure across the sample is well established (about 1 hr) and the permeability is calculated. Then the next higher inlet pressure is applied.

For the case where the inlet pressure is decreased, the inlet pressure into the setup is set to 10 kPa. Once the stationary part of the curve is reached, the permeability is calculated. The inlet pressure is decreased to a new set point in the next step and data at the new plateau are taken to calculate the permeability. This is done several times. The obtained permeablitiy is normalised by the dry gas permeability of the material, which was measured seperately to be about $4{\cdot}10^{-12}$ m^2 (4 Darcy).

The result of this experiment on four different samples of Toray 060 with 10 % PTFE is compared with the relative permeability calculated from

- Mualem's model,
- Burdine's models (see Section 1.3.4 on page 43ff.) with the measured pressure-saturation relationship,
- third power relation ($k_{rel} = s^3$) with Udell's function used in fuel cell modelling [WWC01],
- third power relation ($k_{rel} = s^3$) with the measured pressure-saturation relationship.

The computation of the model data was done with the aid of 'Octave', version 2.1.73. The result of this experiment, as well as the calculated data from the various models are plotted in Figure 2.11.

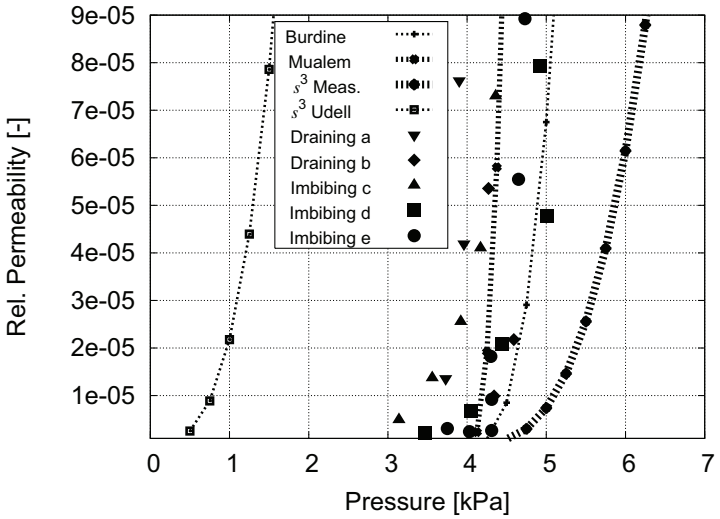

Figure 2.11: Relative permeability for T060 with 10 % PTFE measured for the non-wetting fluid (water) draining and imbibing the sample with a wet boundary on the low-pressure side (points) and commonly used models (lines and points). The measurements had been done on different individual samples.

The comparison indicates that the experimental data scatter to a large extent, based upon the nature of the randomly laid and thin fibre papers. Nevertheless, all samples have in common that the relative permeability increases steeply as the pressure increases.
The draining and imbibing experiment indicates that any hysteresis effect on the relative permeability is within the sample-to-sample variance.

The third power model, in combination with the pressure-saturation function of Udell, overestimates the relative permeability by several orders of magnitude at comparable non-wetting fluid pressure. This is due to the shape of Udell's function at low saturation. Burdine's model, as well as Mualem's model, in combination with the measured pressure-saturation function predicts a relative permeability within the cloud of measured points. The best agreement is found for Mualem's and Burdine's model with the measured pressure-saturation function. Theoretically, the two models have the biggest difference for the non-wetting phase saturation (see Figure 1.16 on page 49 in Section 1.3.4). Yet, the

sample-to-sample variance exceeds this difference.

The third power approach underestimates the relative permeability if the measured pressure-saturation function is used.

The ex-situ experiments suggest that the pressure-saturation function, used in fuel cell literature, and the commonly used model to calculate the relative permeability is not able to describe the relative permeability quantitatively. The relative permeability is over-predicted by orders of magnitudes since the pressure required to establish water permeability is not included.

This statement is true for the case of the water-covered boundary condition. The common saturation dependent Darcy-type approach does not describe the permeability behaviour of DM with a dry boundary on the low-pressure side (channel region in fuel cell).

In the fuel cell, the two different boundary conditions are found in the gas channels (dry) or under the land (wet), as well as in the channel where a water slug is pinned on the DM. Both phenomena are important, which implies the need to create a deeper understanding of the underlying physics. In order to gain deeper insights into the water transport through DM, analytical and numerical free surface calculations were conducted and will be presented in the next section. This can serve as a stepping stone towards a better founded theoretical base for the description of multi-phase flow in DM and allows for advanced material design in the end.

Chapter 3

The Free Surface Model

3.1 Analytical 2D Model of Water in Fibrous Substrates

In order to understand the experimental findings and to provide tools to help on material design other than by trial and error, structure resolving models are needed. An analytical free surface model will be presented and compared with a numerical free surface model. The physics represented in the models described in this section are dominated by surface tension effects as indicated by the dimensionless numbers. In the domain of the DM the water flow rates, represented in the Weber number (We = 10^{-17}), the length scales represented in the Bond number (Bo = 10^{-7}), and the viscosity represented in the Capillary number (Ca = 10^{-12}), are negligible compared to the surface tension, and therefore ignored (see Section 1.3.6 on page 52ff.).

The first approach to investigate the liquid water behaviour in the DM is based on simple two dimensional geometrical considerations. The traditional approach to represent the fluid-dynamic properties of a porous system by a bundle of straight capillaries does not seem to be appropriate for the fibrous system investigated here. Microscopically, the DM consists of hydrophobic fibres with a volume fraction of only 20 %. A simple 2D impression with regular spaced fibres is given in Figure 3.1.

This makes clear that a system with a solid pore wall is not a good model. The "walls of the pores" filled with water are primarily formed by gas and the fibres just provide a kind of support structure. For the gas the "walls of the pores" mainly consist of water.

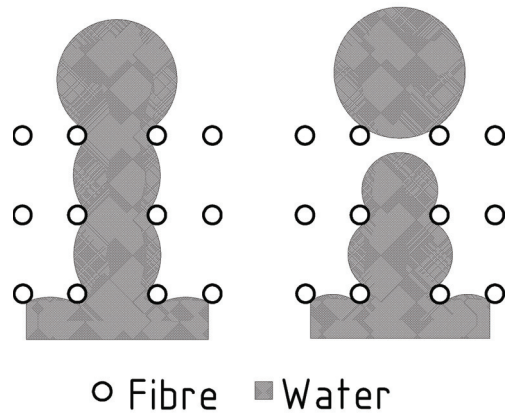

Figure 3.1: Cross-sectional view through an idealised diffusion medium with a continuous (left) and a discontinuous water filament (right).

The proposed model focuses on the water-gas interface and not so much on solid pore walls. In order to estimate the importance of the interaction of the liquid with the fibre on the one hand and the gas on the other hand, the surface energy ratio

$$\frac{\Gamma_{\mathrm{sol}}}{\Gamma_{\mathrm{g}}} = \frac{|A_{\mathrm{sol}}\ \gamma_{\mathrm{sol}}|}{A_{\mathrm{g}}\ \sigma} = \frac{|A_{\mathrm{sol}}\ \sigma\ \cos\theta|}{A_{\mathrm{g}}\ \sigma} \tag{3.1}$$

of the wetted fibre Γ_{sol} and the liqid-gas interface Γ_{g} is used. With A_{g} and A_{sol} as area of the interface between gas phase and solid phase respectively, θ as the contact angle between the liquid and the solid phase. σ and γ_{sol} as the interfacial tension of the corresponding liquid-gas or liquid-solid interface. To determine the surface area of the interface solid-liquid and gas-liquid, it is necessary to make some assumptions on geometrical boundary conditions like fibre (torus) spacing and fibre (torus) radius. The geometrical arrangement is sketched in Figure 3.2. The parameters assumed for the pressure calculation are listed in Table 3.1.

Table 3.1: Model parameter

Vertical fibre distance	a	30	µm
Horizontal fibre distance	b	40	µm
Fibre radius	r_1	3.5	µm
Surface tension	σ	72.8	mN/m
Contact angle solid-liquid	θ	90 - 180	°

Since the shapes of the interfaces depend on the liquid volume, it is helpful to limit the study to the case of a minimum curvature (maximum pressure). This is fulfilled when the angle α in Figure 3.2 is 90 °. Thereby, the inner half of the fibre surface is in contact with water. The wetted fibre area is constant, while the surface energy at the solid-liquid interface scales with the cosine of the contact angle. In contrast to that, the surface energy at the liquid-gas interface varies due to surface area changes with the variation of the vertical fibre spacing a.

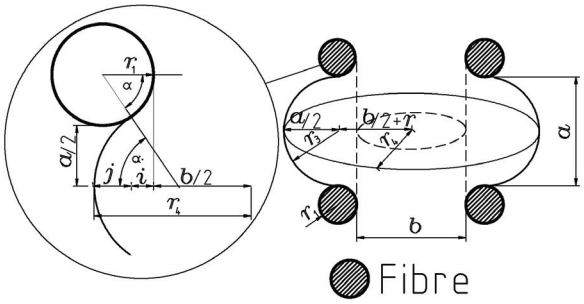

Figure 3.2: Geometrical arrangement of fibre, liquid and gas interfaces in the model system. The limiting radii of curvature in a pore of the DM for the two extremes (right). And the focus on the radius r_4 (left).

For this geometrical configuration, the inner half of the torus area has to be compared with the wrap area of a barrel side (the derivation of the area formulae can be found in Appendix D on page 183ff.). The ratio of the two areas, scaled by the cosine of the contact angle is described as follows:

$$\frac{\Gamma_{\text{sol}}}{\Gamma_{\text{g}}} = \frac{-\pi \left[2\pi \ \left(\frac{b}{2} + r_1\right) \ r_1 - 4 \ r_1^2\right] \ \cos\theta}{4\pi \frac{\frac{a}{2}}{\cos\theta} \left[(\theta - \frac{\pi}{2}) \left(-\frac{\frac{a}{2}}{\cos\theta} \sin\theta - r_1 - \frac{b}{2}\right) - \frac{a}{2}\right]} \tag{3.2}$$

Here, a represents the vertical fibre distance, b the horizontal fibre distance, r_1 the fibre radius. The plot of this equation as a function of the contact angle θ is depicted in Figure 3.3. The vertical fibre spacing was varied relative to the fibre diameter and it was found that the closer the layers (the bigger the fibres) are, the more influence the fibres have.

At contact angles of 90 °, the ratio vanishes since the fibre surface behaves neutral to

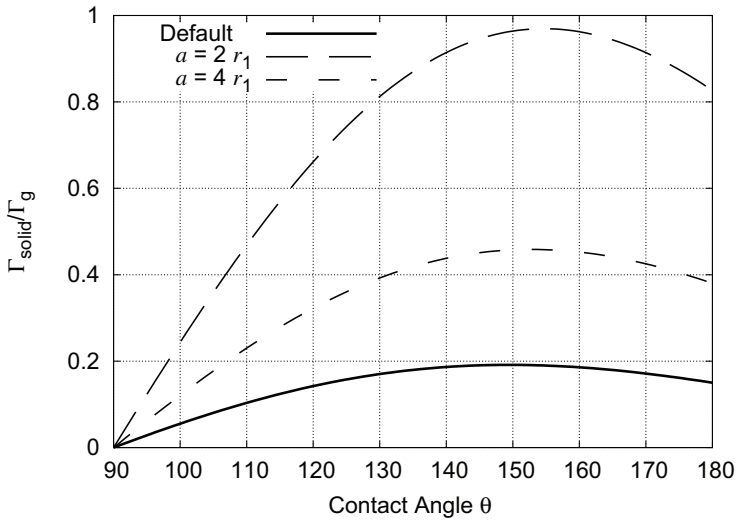

Figure 3.3: Ratio of surface energy components on fibres (torus) and gas-water interface for water-fibre contact angles between 90 ° and 180 ° at different vertical fibre spacing (a). The default parameters are: Vertical fibre spacing $a = 30$ µm, fibre radius $r_1 = 3.5$ µm.

the water (same energy as in the bulk water). As the contact angle increases, the fibre surface becomes more important. At a contact angle of $\sim 150\,^\circ - 160\,^\circ$ the fibre surface has the largest influence on the system. The angle increases with decreasing fibre distance. The contribution of the fibres is 20 % of the contribution of the gas phase to the surface energy for the geometrical assumptions based on hydrophobic Toray 060 material.

The contact area between liquid and fibre is overestimated here. The fibres do not have contact all along the circumference of the 'bottleneck' in the DM. It turns out that the liquid-fibre interaction is less relevant than the liquid-gas interaction. The validity of the assumption that the liquid-fibre interaction is negligible depends strongly on the geometrical assumptions.

If water penetrates the fibrous matrix it might behave like single water filaments providing hydraulic conductivity (depicted in Figure 3.1 on page 82). At this point it is unclear whether the filaments penetrate the medium continuously or with interruptions along the way of least resistance. The pressure gradient, associated with a continuous water transport mode, can be estimated to be in the order of 2 kPa based on the law of Hagen-Poiseuille (Equation 1.31 on page 37) and the following assumptions: 3 filaments/cm^2, 25 µm pore diameter, 1 A/cm^2 current density, 200 µm filament length, no-slip. The

no-slip boundary condition is assumed, although the slip flow at the water-gas interface is possible but neglected for the estimations done here due to the low transport rate. The pressure for reconnection of the filament has to be built up periodically in case of discontinuous filaments.

To assess the stability of such filaments in non-wetting environment, the Plateau-Rayleigh instability [DGBWQ03] was used as an analogy. This instability is observed at free water jets, which fall apart into droplets along their way with a certain frequency (see Figure 3.4) caused by small perturbations. The theory from Plateau and Rayleigh predicts the stability of the jet in dependence on the local diameter of the water jet. This way of thinking to d for estimating the stability

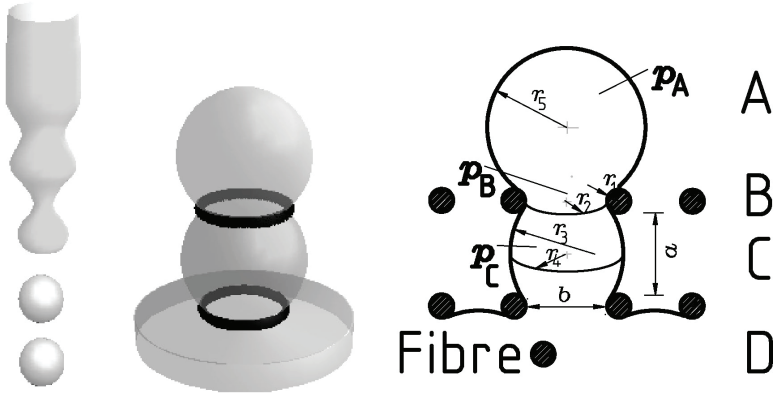

Figure 3.4: Plateau-Rayleigh instability (left), simplified model situation in the DM (centre) and cross-section through the simplified model (right). With radii of curvature r_i and fibre distances (a and b).

The analysis of the Plateau-Rayleigh instability begins with the study of the local pressure in a transient situation. The pressure inside the water jet varies locally since the curvature of the free surface of the water varies locally, too. The pressure differences determine the stability of the jet. The area with the smallest radius holds the largest pressure and since water flows from higher pressure towards lower pressure, the locations with a small radius will lose water and the radius gets even smaller. The result is the formation of single droplets. In order to apply this reasoning to the DM, the filament (right side of Figure 3.4) will be discussed based on four sections. Part 'A' is outside the

DM or within a large free space inside the DM. The pressure inside of 'A' is called p_A. The centre section 'B' has the smallest distance between the fibres, here the pressure is called p_B. Section 'C' represents the volume between fibre layers (p_C). The lowest section 'D' is the space either in the bulk water outside or the pore space on the high-pressure side of the DM. In similarity with Plateau-Rayleigh, the filament is expected to be stable as long as the pressure in all three locations is equal or greater than the pressure in 'B'. If p_B exceeds p_A or p_C, then the water will flow into 'A' or 'C' causing the filament to rupture. The criterion of stability can be expressed as:

$$p_D \geq p_C \geq p_B \leq p_A \tag{3.3}$$

Yet, this criterion is too restrictive for the geometry depicted in Figure 3.4, as will be discussed next. Furthermore, since the filament shall enable water transport from the membrane towards the channels, a pressure gradient from 'D' to 'A' is necessary and p_B can exceed p_A if enough liquid is flowing from underneath to keep the radii of curvature in 'B' constant. The Young-Laplace equation (Equation 1.21 on page 32) is inappropriate to calculate the local pressure in section 'B', because of its limitation to three phase boundaries. If the equation were used anyhow, the radius of curvature r_1 would have a negative sign because of its concave curvature. The consequence thereof, would be a negative pressure in section 'B', since $|r_1| < |\frac{b}{2}|$. A negative pressure means wetting behaviour which is not considered here. The pressure in the bottleneck between the fibres (section 'B') is independent from the geometrical parameters, which is shown by an experiment of thoughts. One imagines a non-wetting torus (made of PTFE). The torus clasps around a drop of water in such a way, that the volume of the drop above and below the torus is equally distributed (Figure 3.5). This system is in unstable equilibrium, the radii of curvatures are equal, therefore, the liquid pressure on both sides of and inside the torus are equal, too. This statement is independent from the size of the two volumes and the inner diameter of the torus as long as the bulge diameters exceed the inner torus diameter. In case of non-equally distributed liquid volumes, the radii and also the liquid pressures on the two sides are different. In consequence, the liquid will flow from the smaller volume (higher pressure) to the larger volume and all the water will end up on

one side of the torus.

Figure 3.5: Model for experiment of thoughts to describe the dependency of geometry and pressure in the 'bottleneck' between the fibres (section 'B').

Now the focus will be set on the geometry above and below the bottleneck (sections 'A' and 'C'). Since the pressure p_{B} is not relevant as explained, Equation 3.3 for stable filaments reduces to

$$p_{\mathrm{C}} = p_{\mathrm{A}} = p_{\mathrm{D}}. \tag{3.4}$$

This is true for the static situation (represented by the torous model in Figure 3.5). To allow for stable flux in the filament between the fibers, as sketched on the left in Figure 3.1 on page 82, the condition changes to

$$p_{\mathrm{D}} > p_{\mathrm{C}} \geq p_{\mathrm{A}}. \tag{3.5}$$

To assess the filament stability under the premises sketched in Figure 3.4 (right) on page 85 and the pressure boundary given in Equation 3.5, the radii of curvature of the liquid-gas interface are fathomed. At the fibre surface (section 'A', Figure 3.4, right) and between the fibres (section 'C', Figure 3.4, right), a completely non-wetting situation between the fibre and liquid is assumed for simplification ($\theta = 180\,^{\circ}$). The pressure in section 'A' is given by

$$p_A = -\sigma \left(\frac{2}{r_5} \right), \tag{3.6}$$

and for section 'C' by

$$p_C = -\sigma \left(\frac{1}{r_4} + \frac{1}{r_3} \right). \tag{3.7}$$

The two radii r_3 and r_4 are relevant for the pressure in 'C' and depend on each other, as well

as on the distance of the fibres and their diameter. The geometry is illustrated in Figure 3.2 on page 83. The extreme of the radius r_3 is infinite at maximum (shape of a straight cylinder) and half of the vertical fibre distance $a/2$ at minimum (most spheroidal shape). Whether the lower boundary of r_3 becomes relevant depends strongly on the horizontal fibre spacing of the layers above. In case of a regular horizontal spacing throughout all layers, the radius r_3 is $b/2$ at the lower boundary. In case of a varying horizontal spacing, the lower boundary is $b/2$ of the following layer or $a/2$ at the most extreme case if $a/2$ equals $b/2$ of the following layer. Otherwise, the filament will pass horizontally, not vertically between the fibres since the growing filament seeks the widest passage.

It is also possible that the curvature changes from convex ($\lim_{r_3 \to +\infty}$) to concave ($\lim_{r_3 \to -\infty}$) which alters the sign of the radius (discussed in Section 3.2 on page 90ff.). But at first, the convex case will be highlighted. The boundaries for the radius are:

$$\infty \geq r_3 \geq \left\{ \frac{a}{2}, r_3 \right\} \geq 0 \tag{3.8}$$

The radius r_4 is limited between half of the horizontal distance of the fibres $b/2$ and the sum of half the vertical fibre distance $a/2$ plus half of the horizontal fibre distance $b/2$ plus the radius of the fibre r_1, if the sign of r_3 is positive. The radius r_4 lies within the following boundaries:

$$\left[\frac{a}{2} + \frac{b}{2} + r_1 \right] \geq r_4 \geq \frac{b}{2} \tag{3.9}$$

The upper boundary represents the extreme and depends also on the horizontal spacing of the following layers. To describe the dependency of the radii from each other, the angle α is introduced (see Figure 3.2 (left) on page 83). It is possible to express r_3 and r_4 as a function of α:

$$r_3 = \frac{\frac{a}{2} + r_1}{\sin \alpha} - r_1. \tag{3.10}$$

and

$$r_4 = C_{14} + C_{15} + \frac{b}{2} \tag{3.11}$$

with

$$C_{14} = r_3 \ (1 - \cos \alpha) \tag{3.12}$$

and

$$C_{15} = r_1\ (1 - \cos\alpha). \tag{3.13}$$

The equation for r_4 in dependence of the geometrical parameters is obtained by combining Equation 3.10 to Equation 3.13:

$$r_4 = \frac{b}{2} + \left(\frac{a}{2} + r_1\right)\sqrt{\frac{1-\cos\alpha}{1+\cos\alpha}} \tag{3.14}$$

The dependence of liquid pressure and r_4 on r_3 in the bulk (between the fibres, section 'C') is shown in Figure 3.6.

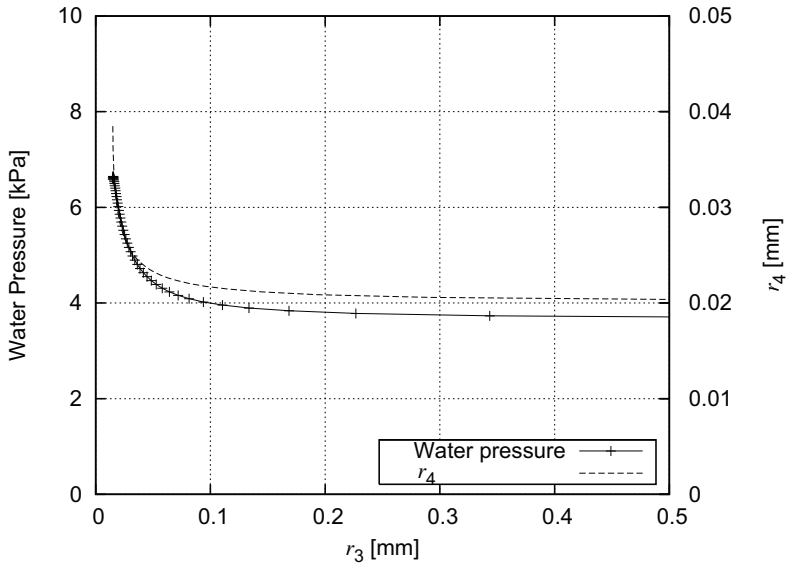

Figure 3.6: Dependence of liquid pressure and bulge radius r_4 on bulge radius r_3. Parameters: Vertical fibre spacing $a = 30$ µm, horizontal fibre spacing $b = 40$ µm and fibre radius $r_1 = 3.5$ µm.

The smallest pressure in the bulk (section 'C') is about 3.8 kPa, this value is in the order of the lower permeation pressure, found experimentally (see Section 2.4 on page 78ff.). Below this pressure the tested sample became impermeable for water, indicating unstable water filaments.

As already mentioned, it is also possible that the curvature of the free water surface in the bulk (section 'C') becomes concave. The consequences of this case will be analysed in the next section.

3.2 Simplified 3D Stability Study

In order to further discuss the subject, it is helpful to turn from analytical towards numerical methods for the sake of feasibility.

If the water filament in a DM connects two areas that have flat free surfaces, like two surfaces covered with water, the surface of the connecting filament can detach from the surrounding fibres 'supporting' the filament in the middle. The shape formed by the filament is called catenoid (Figure 3.7). The contact zone at the fibres is ignored which corresponds to a fibre contact angle of 180 °.

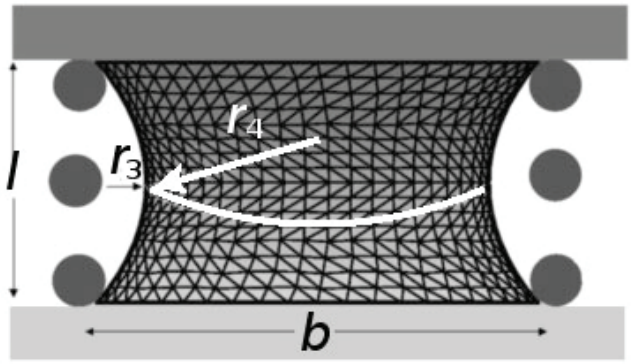

Figure 3.7: Shape of a liquid connection between two completely wetting surfaces. The grid lines represent the computational mesh used by the 'Surface Evolver' code.

Along with the detachment from the centre fibres a change of curvature takes place. According to the usual convention the sign of r_3 has to be taken negative in order to calculate the pressure with the Young-Laplace equation. The radius r_4 in this case gets smaller than indicated in Equation 3.9 on page 88. The catenoidal shape is stable, as long as the absolute values of the radii r_3 and r_4 are equal at each location, but with opposite sign. In this case, the sum $\frac{1}{r_3} + \frac{1}{r_4} = 0$; thus, the pressure inside the filament is uniform. The stability is granted as long as the ratio of the horizontal distance of the surrounding fibres (pore diameter) b and the vertical distance of the two water films l stays below 1.51.

$$b = 1.51 \cdot l \tag{3.15}$$

This ratio can be calculated analytically (see "The Science of Soap Films and Soap Bubbles" [Ise92]) or, e.g. by 'Surface Evolver', a numerical solver to find surface geometries

with the lowest energy [Bra92] (further information is given in Section 3.3.1 on page 93ff.). This value is valid for a circular shape of the limiting matrix, although the real boundary has a polygonal shape.

Since the thickness of the DM in question is 200 µm, the radius of the opening has to be 300 µm at least, in order to stabilise the filament. Such a geometry is also beneficial due to the entry pressure of such a pore. This pressure would be 0.242 kPa under idealised conditions, which is one order of magnitude smaller than the measured breakthrough pressure with the conventional material.

Since the boundary of a filament in the DM is not circular, but some kind of polygon, the next step is the calculation of the stability criterion for non-circular filament boundaries. 'Surface Evolver' was used to calculate the stability criterion for triangular boundaries. In this study it is distinguished between rectangular and regular triangles. Triangles where chosen because they are the simplest polygon and most different from circles. In these cases, the contact angle between water and fibre is still assumed to be 180 °. The solution is expressed by the ratio between the radius $b/2$ of a circle, surrounding the triangular boundary and the distance between the triangular planes l. The ratio for the regular triangle is 1.32, for the rectangular triangle 1.56 and for the boundary of circular planes 0.76. The resulting shapes for the triangular boundary cases are shown in Figure 3.8. To explore the quality of the computation, the command sequence used for the development of the triangular shapes was applied to the example with the circular shape. The stability limit b/l for the catenoidal shape was found to be 1.512. Compared to the theoretical value of 1.5088 the difference is 0.2 %.

In case of the triangular boundaries, the two wetting planes have to move even closer to form a stable filament. This puts some question marks on the boundary conditions, like the assumption that the wetting surface is really planar and the fibre is represented by a line, rather than a three-dimensional rod.

For further clarification a more detailed model is required. The next section has the smallest repeating unit inside the DM in focus to address this question, to test the simplified pseudo 3D model. Further, the results from the permeation experiments (Section 2.3 on page 69) are compared to free surface model approaches in Section 3.4 on page 107.

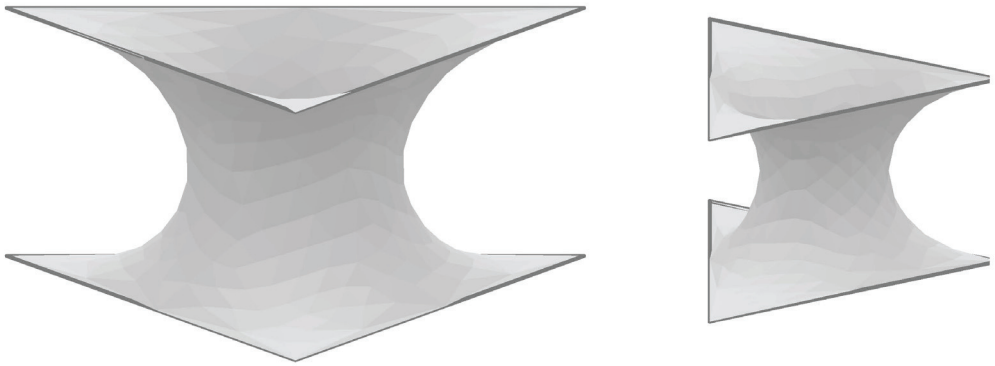

$\frac{b}{2l} = 1.56$ $\frac{b}{2l} = 1.32$

Figure 3.8: Shape of a liquid connection between two water-wetting surfaces constrained by triangular geometry and the ratio of the radius of the surrounding cycle to the height of the geometry. Rectangular configuration on the left, regular configuration on the right side.

3.3 Detailed 3D Study

3.3.1 Model Geometry and Procedure

The geometry of the model DM consists of a 'cage' of six fibres forming two triangles in two layers. This is a dramatic simplification, but since the DM consists of numerous randomly laid fibres, the effort to study a real-size sample of DM by numeric methods would be tremendous. The idea behind this very simple approach is to take a close look at the smallest unit a DM consists of, to study the liquid behaviour on this unit, and to project the findings on the DM.

The model domain consists of two layers and a bottom plane, each composed of three fibres in triangular configuration (see Figure 3.9). The fibres of the real DM are bonded

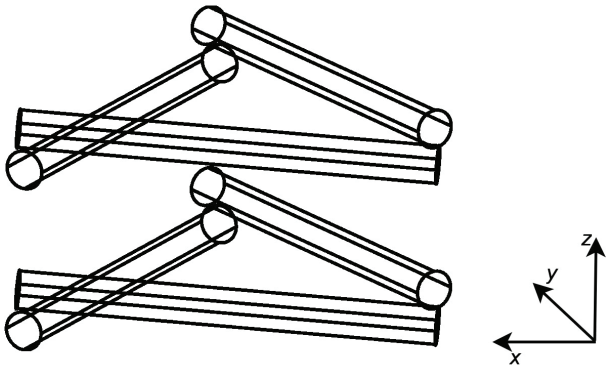

Figure 3.9: Basic geometrical fibre arrangement for microscopic numerical investigation.

by phenolic resin, which concentrates at the intersections. In the model, this additional material was neglected due to the practical difficulties to generate the mesh and boundary constraints. The binder concentrates in areas of fibre intersection in the DM, but as it will be seen, this region is not in contact with the liquid phase in the simulation (at least if the binder content is not too high). If the water is in contact with the binder, additional support for the water filaments will be provided.

The varied parameter space in the simulation encompasses the contact angle between water and fibre, and imbibition as well as drainage. The parameters of the base case can be found in Table 3.2. The output parameter of this study is the pressure inside the liquid phase as a function of volume. This reveals the required pressure to transport water in the fibrous substrate. The influence of gravity is ignored unless otherwise stated.

Table 3.2: 3D model parameters

Vertical fibre layer distance	a	30	µm
Fibre length (intersection)	l	71.2	µm
Fibre angle	α	60	°
Fibre radius	r_1	3.5	µm
Contact angle at base plane	θ_0	90	°
Contact angle at fibres	θ	120; 180	°
Base plane distance to fibre plane	a_0	15	µm
Surface tension	σ	72.8	mN/m

The procedure of modelling is based on minimising the surface energy of a surface mesh. The code used is 'Surface Evolver', written by Kenneth Brakke [Bra92]. This code is based on a surface mesh consisting of vertexes, lines and facets, representing the liquid-gas, liquid-solid and solid-gas interfaces. The aim is to find the shape with the lowest surface energy. This is done by translating the vertex coordinates in directions that give a lower total surface energy. Associated with the translation is a scaling factor that gets smaller as energy differences between one shape and the next are getting smaller. The scaling factor is used as a criterion for convergence. The code is initialised with a coarse mesh, approximated to the expected result (see Figure 3.10), and a preset volume. The mesh is refined during the calculation depending on the convergence progress for each individual preset volume. The typical area of an average facet at the end of the calculation is 0.1 µm^2 which translates to a total number of $\sim 10^5$ facets depending on the water volume used in the model. The scaling factor at the end of the calculation has to be smaller than 10^{-5}. Thereby, a static solution for the pressure and the shape of a given volume is obtained. Since a static solution is generated, any dynamic forces like the viscous or inertia forces are ignored. This simplification is justified since the surface tension dominates the shape of the liquid (see Section 1.3.6 on page 52ff.).

This procedure is repeated with a slightly increased or decreased volume, depending on the imbibing or draining case. In order to set the boundary conditions correctly, it is necessary to modify the surface mesh, depending on the volume. This is the case

when the liquid surface approaches a fibre that has not been in contact at the previous volume. Other occasions arise where such a modification is necessary when the calculated shape is not meaningful to the problem since the interface intersects a region forbidden for geometrical reasons. The liquid surface is represented by a number of facets, defined by vertexes and vectors. To represent the fibre surface, the translation of the mesh vertexes is constrained in their movement to ensure that the surface of the individual fibre stays at the specified location during the simulation. The vertexes very close to the fibre surface, but still on the liquid-gas interface are not constrained in such a way and are, therefore, free to translate into the 'forbidden' zone, beyond the fibre boundary into the interior of the fibre during iteration. To avoid such unphysical situations, the initial mesh has to be modified. The surface of the cylinders in Figure 3.10 (right) represents the area of spatial constraints for vertex movement.

The run begins with a small volume on the bottom plane and ends with the rupture of the filament due to a large radius of curvature of the drop sitting on the upper fibre layer. This takes about one week of computation on a 1.2 MHz PC.

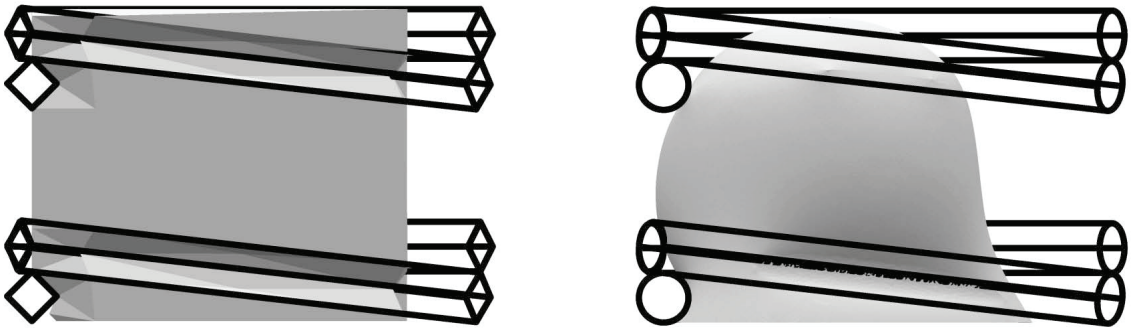

Figure 3.10: Geometry at initialisation (left) and at the end of the computation and refinement (right).

3.3.2 Effect of Gravity

It was assumed that the effect of gravity can be ignored in the model domain, based on the assessment of the Bond number and the dimensionless pressure (see Section 1.3.6 on page 52ff.). This assumption is tested by computing the pressure for a water volume of 8 nL in the fibre cage geometry at identical boundary conditions, beside of the gravity setting.

The contact angle on the fibres was set to 120 °. This volume is selected because the fibre interaction is not as dominant as in the case of smaller volumes (< 1 nL) where the drop is completely located between the two fibre layers. Also, the likelihood of filament rupture, as to expect at larger volumes (> 10 nL) is small at a droplet volume of 8 nL.

The visual comparison of the results does not reveal any difference between the computation with gravity or without (see Figure 3.11).

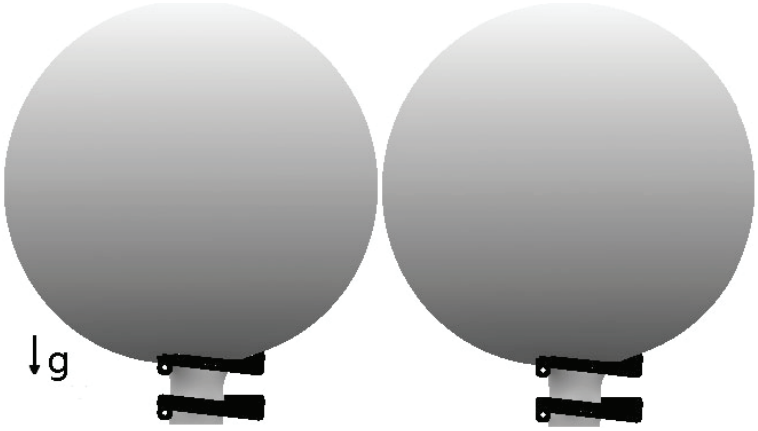

Figure 3.11: Gravity influence: Water shapes with (left) and without gravity (right) for a volume of 8 nL.

The pressure difference between the two cases is 0.15 Pa and is not significant enough to invalidate any observations made ignoring the gravity. The numerical details of the two cases are given in Table 3.3.

Table 3.3: Numerical results for water shape calculation with and without gravity for a volume of 8 nL.

Parameter	Case 1	Case 2	Unit
g	9.81	0	m/s^2
Facets	1393978	1392758	-
p	1.178268	1.178414	kPa
Δp	0.15		Pa

The assumption that the effect of gravity can be neglected, based on the assessment of the dimensionless numbers is proven to be correct. The shape and the pressure of the liquid are not affected by gravity in the considered geometry.

3.3.3 Boundary Conditions

As seen in the permeability experiment (Section 2.3.3 on page 72ff.), the boundary conditions at the low-pressure side impact the water transport fundamentally. For deeper understanding, the boundary conditions are emulated in the free surface model. The 'dry' boundary condition assumes a completely hydrophobic system, while the 'wet' boundary condition could be considered as a partly hydrophilic system. A drop of liquid is initialised on the upper fibre plane, yet the fibres are hydrophobic. To be consistent with the experiments, this section is categorised as 'dry' and 'wet'.

The dry boundary condition serves as the base case. The general setup for this study is the following: The liquid forms a 90 ° angle with the base plane and the liquid volume is placed in the centre of the lower fibre layer; the fibre-water contact angle is set to 120 °. The simulation is carried out beginning with a small volume (15 pL), just touching the fibres of the lower plane, up to a large volume (40 nL) where the water is mostly located on the upper fibre plane till the connection to the bottom plane snaps off. When the water volume increases, the pressure fluctuates around (6 ± 2) kPa till the volume exceeds 0.1 nL (see Figure 3.12). Beyond this volume, the pressure decreases until the water connection between the two layers breaks off. Since the volume of interest covers three orders of magnitude, the volume is represented in logarithmic scale on the abscissa in Figure 3.12. Three different regions can be identified along the volume-pressure curve. A typical shape, corresponding to each region, is depicted in Figure 3.13.

The first region (I) is characterised by a strong pressure dependence on the water-fibre interaction. At each volume where the liquid touches a fibre for the first time, the pressure changes discontinuously. Furthermore, strong hysteresis effects are expected in this region which are subject of the next section (see Section 3.3.4 on page 103ff.). The starting volume for the plots was chosen in such a way that the fibres of the lower plane are just in contact with the liquid. A slightly smaller volume would result in a mound, sitting on the base layer. The second region (II) is characterised by a dominating gas-liquid interaction and the pressure decreases with $p \sim \frac{1}{\sqrt[3]{V}}$. The influence of the water volume in contact with and between the fibres is negligible in comparison to the volume on top of the layer. This is supported by the possibility to describe the volume-pressure function in this section

by the Young-Laplace equation in a volume-dependent formulation:

$$\begin{aligned} p &= \frac{2\,\sigma}{r} \\ V &\approx \frac{4\,\pi}{3}\,r^3 \\ p &\approx \frac{2\,\sigma}{\sqrt[3]{\frac{3\,(V-V_0)}{4\pi}}} \end{aligned} \tag{3.16}$$

r denotes as the radius of the drop on top of the fibres, V as the water volume and V_0 as a water volume between the base plane and the upper fibre layer. This result is important for the description of the water saturation at the interface as one required boundary condition in constitutive fuel cell models [NN03, PW04].

The water pressure becomes so low in the third section (III) that the water filament between the fibres changes from convex to concave (see right image in Figure 3.13), similar to the catenoid described in Section 3.2 on page 90. As the pressure decreases due to the large radius of curvature of the volume above the upper fibre layer, the neck shrinks down to a point and finally the volume splits. The pressure associated with this event gives the lower threshold for the pressure difference that has to be maintained across the water filament in order to keep it stable and allow for transport.

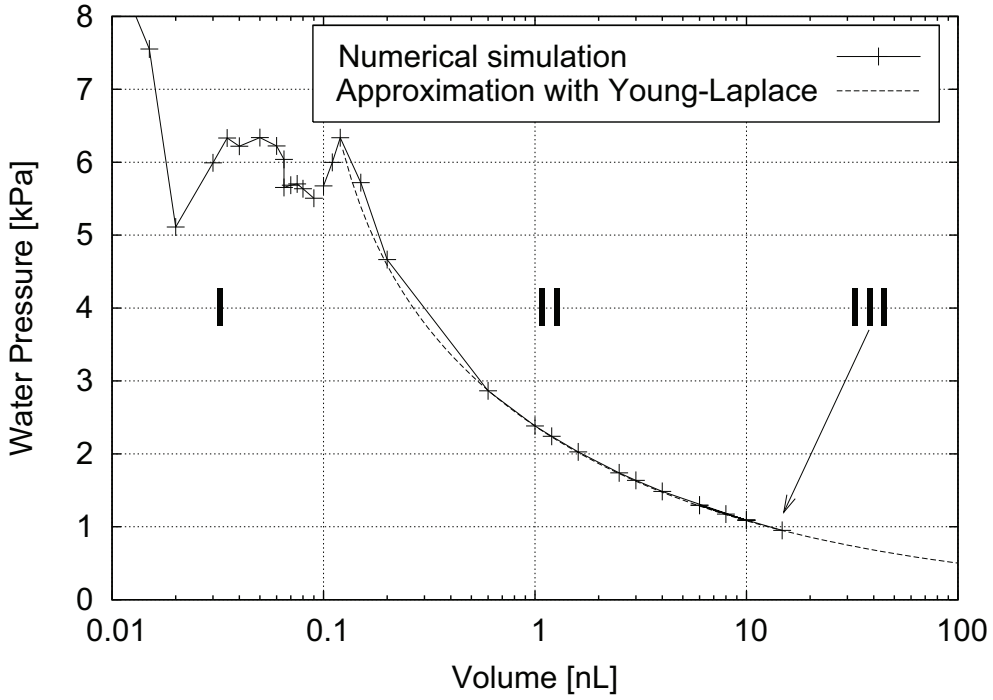

Figure 3.12: Volume-pressure plot for water in a configuration of six fibres and a semi-empirical fit. Section I is dominated by fibre interaction. Liquid-gas interaction dominates in section II. In section III the fibre interaction becomes important again. The fibre-water contact angle is set to 120 °.

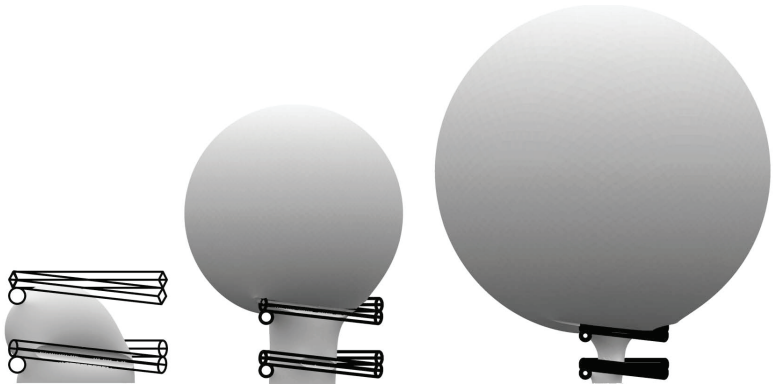

Figure 3.13: Typical geometrical shape for the sections I - III and the corresponding volumes ($\theta = 120\,°$).

The wet boundary condition applies when the filament splits off, as described previously, and the water forms a sphere on the top of the upper layer (depicted in Figure 3.14).

Figure 3.14: Computational setup for the wet boundary case.

If the drop on the surface is large, the radius of curvature is large too, thus the liquid pressure is small. This argument is used to extrapolate the model to hydrophilic boundary conditions, like in cases where the gas flow rate in the flow channel is not sufficient to move a pinning drop, or the filament develops under a hydrophilic boundary like a flow field land in the real environment of a fuel cell.

In the wet boundary situations, the water volume below the drop starts to grow again, until the growing volumes from below and on the top touch each other, causing the pressure to drop. The volume on top of the fibres will increase further, while the water pressure at the lower fibre level becomes large again when a new droplet begins to form and grow. This leads to a periodic pressure oscillation in the region of the lower fibre plane. For the given geometry the lower volume was found by simulation to be 62 pL. This corresponds to a pressure of 5.5 kPa (see Figure 3.12). The actual volume in this case is less important compared to the pressure, since in the real situation more than one fibre plane is present and the water volume of the filament is larger. The pressure, however, might be of a

similar magnitude, since the characteristic length scale of the fibre cage is comparable. When the volumes have merged, the pressure drops below 1 kPa, and the major part of the water between the fibre layer is adsorbed by the water volume above.

If a current density is assumed, the dynamics of water transport can be assessed in a qualitative manner. The limitation to a qualitative statement is due to the fact that only a 50 µm thick pack of six fibres is modelled here. The pressure versus time, plotted in Figure 3.15 (top), for a dry top layer and an already wet top layer (Figure 3.15, bottom) corresponds to a water production rate of 1.65 pL/s. This flow rate corresponds to 1 A/cm^2 on the base plane of the model domain. The calculation is based on the area confined by the three fibres (0.177 pm^2) and projected onto the base plane. The latter has a liquid volume of 15 nL sitting on the upper fibre plane.

In case of the water-covered situation, the pressure oscillates with a period of 40 s between the highest and the lowest pressure, while in the dry case it would take 160 min under the same flow condition to reach the same low pressure. The drop on top of the DM grows extremely slowly, compared to the filling of the space between the two fibre planes.

In a real DM, the volume of the filament is many times larger, therefore, it is to expect that the pulse period in the water-covered situation is increased by that factor. This leads to time constants in the order of several minutes, but depends also on the location of the snapp-off relative to the distance to the boundary. This model assumes that only the water produced on the area confined by the fibre arrangement is conducted through the geometry. The time constants scale with the inverse proportion of number of transport sites. In the wet case, the time constants are small enough to experience an averaging phenomenon if many sites of transport are present. This makes it possible to describe the transport macroscopically, as confirmed experimentally (see Section 2.4 on page 78ff.) and discussed in Section 3.4 on page 107ff. For the dry boundary condition, the periodicity is two orders of magnitude larger; that reduces the likelihood of averaging phenomena significantly.

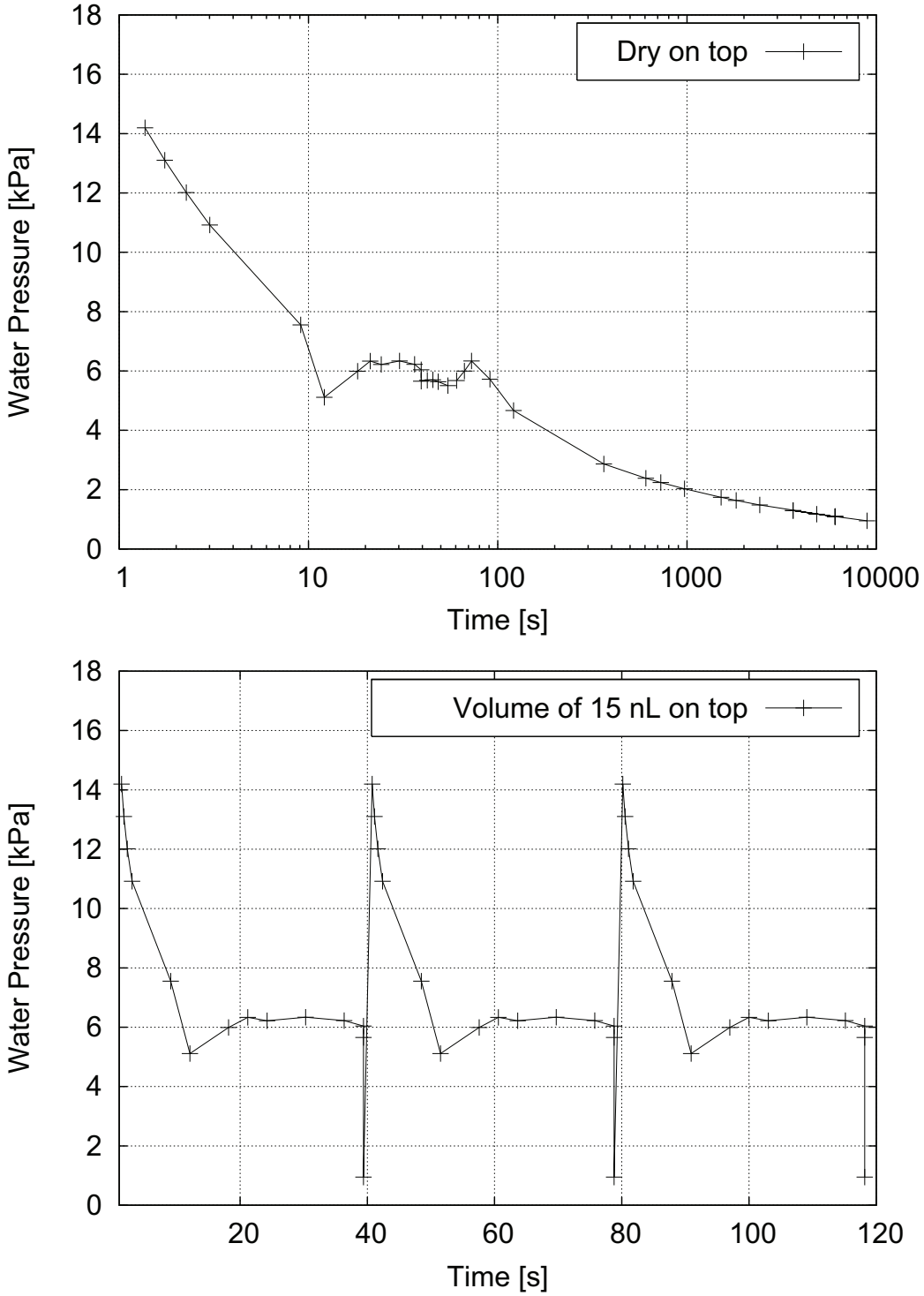

Figure 3.15: Development of pressure over time for a fibre contact angle $\theta = 120\,^\circ$ at an assumed current density of 1 A/cm^2 (1.5 pL/s) with dry upper layer (top) and a liquid volume of 15 nL on the upper fibre plane (bottom).

3.3.4 Hysteresis Effects

As observed, for sufficiently small volumes, the pressure fluctuates with increasing volume. These fluctuations are caused by the liquid fibre interaction and will be investigated more closely. The boundary conditions are identical with the previously described dry boundary case, the fibre-water contact angle is set to 120 °. Figure 3.16 shows the result of the pressure-volume calculation for the imbibing (circles) and the draining (triangles) case up to a water volume of 0.11 nL. Because all fibres are in contact with the liquid at a volume of 0.1 nL, no matter whether the water imbibes or drains, the pressure-volume relation is independent from the direction the volume changes for larger volumes. The hysteresis is caused by the fact that invading water suddenly gets in contact with a fibre and the pressure decreases because the average radius of curvature increases. The liquid volume is still the same, but the pressure differs (see Figure 3.17). If the liquid retreats from the fibres, the interface area between fibre and water will become zero at one point and the shape and the pressure changes suddenly (see Figure 3.18). The hysteresis becomes the larger the more the contact angle deviates from 180 °. The hysteresis disappears at 180 °, since there is no gain in energy when the fibres are becoming wet. The angle of 120 ° is chosen to get close to the properties of the actual DM. For this contact angle, the pressure hysteresis is in the order of 2 kPa to 2.5 kPa. The hysteresis for the real situation is probably larger since the contact angle depends on velocity and direction of the water front line [DGBWQ03].

Being conservative, five contact angles can be specified, which are the static, the wet advancing, the dry advancing, the wet receding, and the dry receding angles. In this case only one contact angle was selected to calculate the results. From an experimental point of view it is difficult to determine the five angles. The wet receding angle of PTFE-treated DM surface was measured with the plate technique (developed by Wilhelmy [Wil63]) to be slightly below 90 ° and the pressure hysteresis for the actual material is much larger than for this idealised assumption. The estimate of 120 ° is based on entry pressure measurements for water and pore size data. The important point here is, that even at an immeasurably small contact angle hysteresis, the volume-pressure function depends upon the situation of imbibing or draining.

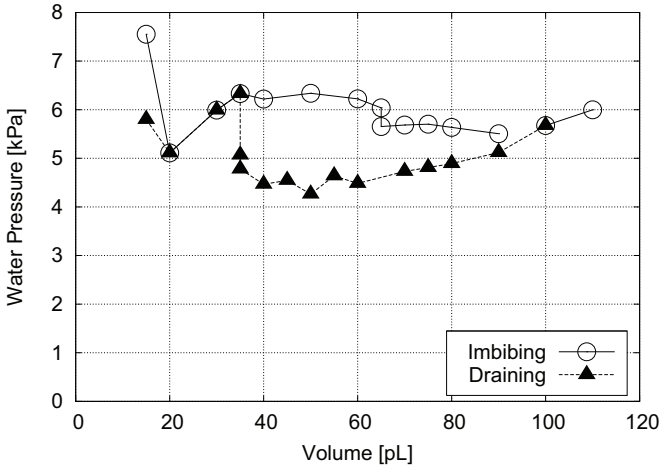

Figure 3.16: Imbibing-draining hysteresis of water volume-pressure relationship. The water volumes are filling the space between two fibre layers only. The water-fibre contact angle is 120 °.

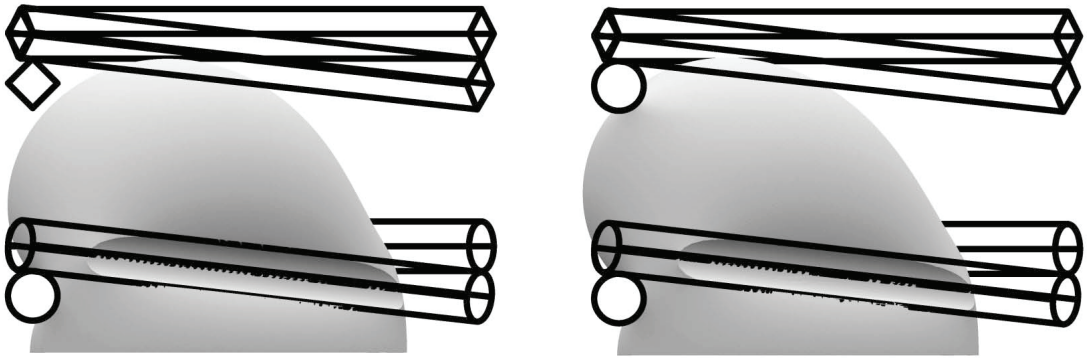

Figure 3.17: Geometry at 65 pL water volume for the imbibing cases before (left) and after fibre contact (right). The squared cross sections of the fibres indicate that they were not active as boundary.

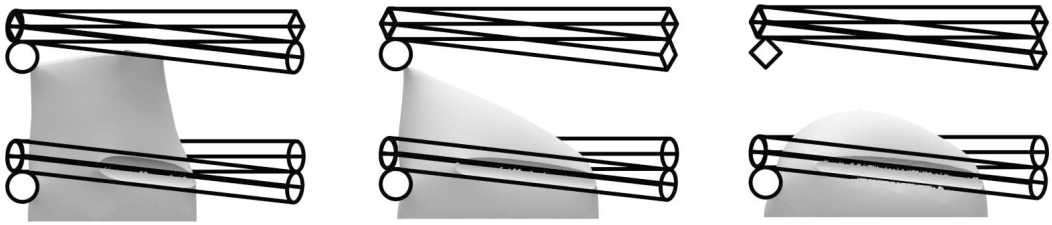

Figure 3.18: Draining discontinuity, detachment process at ≈ 35 pL water volume. The squared cross sections of the fibres indicate that they were not active as boundary.

3.3.5 Variation of Fibre Contact Angle

Two extreme cases with regard to the contact angle between fibre and water will be presented and discussed here. The contact angle on the bottom plane was held constant, while the contact angle on the fibres was 120 ° in one and 180 ° in the other case. The lower angle was chosen since this is the appearing contact angle on PTFE-treated DM, and the upper limit was chosen to look at the extremes.

The same boundary conditions (beside of the contact angle) as in the base case study of 120 ° are chosen. The biggest differences between the two cases appear if the volume is small, filling parts of the space between the two fibre planes (see Figure 3.19), and close to snap-off of the filament at large volumes. For the latter case, the pressure difference between the two contact angle cases is less interesting, since the pressure-volume characteristic becomes equal as the liquid volume exceeds 0.15 nL (see insertion in Figure 3.19). Yet, the shape of the liquid-gas interface of the water volume between the two fibre layers is more interesting, since it represents the stability of the liquid connection between the bottom and the water volume on the top. Figure 3.20 depicts the shape of the liquid between the fibre layers.

The pressure difference between the two contact angles at small liquid volumes is 1 kPa at maximum. To evaluate the stability of the structure at large volumes, it is more meaningful to study the effects of the contact angles on the shape of the filament. The structure appears stable at a contact angle of $\theta = 120\,^\circ$ and a volume of 15 nL, while the shape of the liquid at $\theta = 180\,^\circ$ fibre contact angle has an extremely narrow section and a snap-off is likely to happen close to that volume.

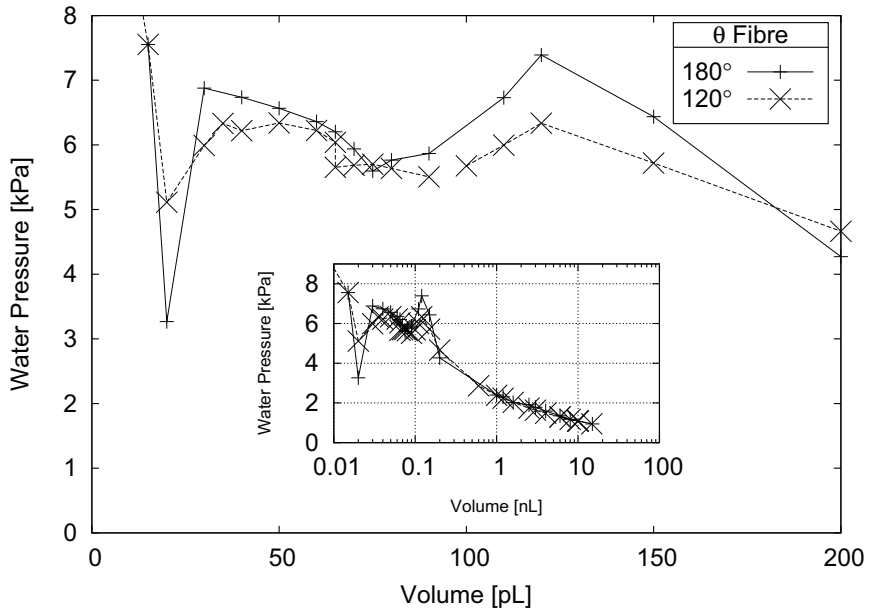

Figure 3.19: Volume-pressure plot for water in a six-fibre configuration comparing different water-fibre contact angles. The base plane contact angle is set to 90 °.

$\theta = 120\,°$
stable

$\theta = 180\,°$
not stable

Figure 3.20: Liquid shape at a volume of 15 nL (0.9 kPa) at a fibre contact angle of $\theta = 120\,°$ (left) and $\theta = 180\,°$ (right) focusing on the volume between the fibre layers. Fibres and base plane are adumbrated only to illustrate the shape of the liquid more clearly.

3.4 Discussion of the Simulation and the Experiments

A comparison between the different models and the experimental findings is given in this section, followed by an interpretation of the experimental agreement between Darcy's law in combination with Mualem's and Burdine's two-phase description (see Section 2.4 on page 78ff.).

Analytical contemplation reveals the water pressure in dependence of the radius of curvature for the water surface in a simplified, pseudo 3D geometry. The maximum water pressure, required to push the water through the space between the fibres is found analytically to be 6.4 kPa (see Figure 3.6 on page 89). The numerical 3D calculation, gives a pressure of 7.4 kPa for a contact angle between water and fibre of 180 ° and 6.5 kPa for a contact angle of 120 ° (see Figure 3.19 on page 106 at 120 pL) for the similar situation. The pressure, required to establish permeability, experimentally is found to be 3 kPa to 5 kPa (see Section 2.3.3 on page 72ff.). The results are summarised in Table 3.4 for comparison.

Table 3.4: Breakthrough Pressure – Model and Experiment

	Model			Experiment
	Analytical	Numerical		
		$\theta = 120\,^\circ$	$\theta = 180\,^\circ$	
Pressure [kPa]	6.4	6.5	7.4	3 – 5

Following conclusions can be drawn:

- Both models overestimate the required breakthrough pressure by 20 % - 50 % compared to the experiment. Yet, the geometry is extremely simplified in the models and the accuracy is sufficient to investigate trends and fundamental mechanisms.
- The strength of the analytical pseudo 3D model is fast estimation of the required maximum liquid pressure to establish a penetration through the gas diffusion medium based on fibre spacing

The second parameter that allows for comparison between the analytical and numerical approach is the limiting pressure when the liquid filament gets cylinder-shaped in the analytical case (Section 3.1 on page 89). This is the transition point between the convex

and concave surface curvature for the analytical 2D model. The limiting pressure at the transtion point in the analytical model is 3.46 kPa (radius of curvature: 20 µm, see Figure 3.6 on page 89). This pressure corresponds to a volume of about 380 pL. The shape found by the numerical simulation for this volume, is shown in Figure 3.21 and is fairly cylindrical in the section between the two fibre layers. The two models are in agreement in that regard.

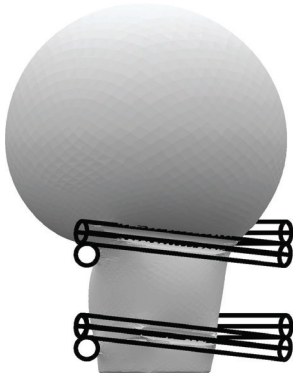

Figure 3.21: Shape of a water volume of 380 pL with a pressure of 3.46 kPa with 180 ° fibre contact angle.

The stability of the filament, determined by the simplified numerical 3D stability study (Section 3.2 on page 90ff.) is compared with the detailed 3D modelling at large volumes. The geometrical ratio of the radius of the surrounding circle of the regular triangle to the distance between the two triangles (r/h) for the stable connection was calculated to be 1.32 for the regular triangle. If this is applied to the fibre arrangement assumed for the DM, the total thickness of the DM will be 31 µm, one order of magnitude less than the real material. The detailed 3D model did not show the detachment behaviour, assumed for the simplified model. Even in the hydrophobic situation ($\theta = 120\,^\circ$) the connection stays stable down to a pressure of 1 kPa in the 3D study (see Figure 3.12 on page 99). This indicates that the stacked fibre arrangement and the rod-like shape of the fibres have a stabilising effect. In the simple 3D model, the fibre layers were reduced to planes and the rod-like shape to simple lines, which turns out to be an improper assumption for the pore sizes and geometries considered here.

For extended layer distances or much larger pore sizes, where these simplifications might be appropriate, the probability that a polygonal or even circular-shaped border exists is much higher than triangular-shaped configurations of the pinning planes. The

application of the stability criterion for the catenoid is more appropriate. The key message here is:

- The effort to compute the volume-pressure characteristic numerically with 'Surface Evolver' requires several days but allows the investigation of various boundary conditions, geometrically, as well as interface related. This model is advised if the filament stability at low pressures is of interest, the simplified 3D model is not sufficient for this case.

Experimentally it was found that the boundary conditions at the low-pressure side of the DM make a difference, as seen in Section 2.3.3 on page 72ff. Similar was seen in the detailed numerical study (see Section 3.3.3 on page 97). This has implications on the macroscopic transport description. The pore diameter in the experimentally investigated DM is 30 µm to 40 µm and one order of magnitude smaller than the one theoretically necessary for stable filaments based on the catenoid criterion. It is likely that the water filaments inside the DM are not stable. The detailed simulation shows stability down to 1 kPa. Further down, rupture is likely to occur, especially if gas flow induced perturbations are taken into consideration. The consequences for the macroscopic water transport will be discussed as follows.

Macroscopic water transport seems to depend on the boundary conditions, as found experimentally. The analytically derived stability condition for the gas-exposed DM is stated in Equations 3.4 and 3.5 on page 87. The water-covered sample has to fulfil a different criterion. The water film on top of the sample has a negligible curvature, therefore $r = \infty$ and $p_{\mathrm{cap,end}} = 0$. Since the geometrical condition (Equation 3.15 on page 90) is not fulfilled, the filament is not stable in a water covered case. Figure 3.22 illustrates the two different cases.

In case of a water-covered DM, the water flow through the DM is discontinuous because of the discontinuous path (Figure 3.22, right). The water flow can be expressed as

$$\frac{dV}{dt} = \Delta V \cdot \nu. \tag{3.17}$$

ν denotes as the frequency of the path build-up to push the water volume ΔV into the upper water film. The frequency is inversely proportional to ΔV and proportional to the

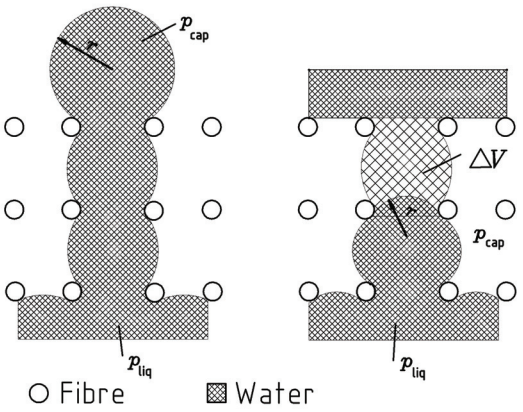

Figure 3.22: Comparison of a continuous filament (left) with a discontinuous filament in case of a water covered DM (right).

average volumetric flow rate. On a macroscopic scale, the flowrate is

$$\frac{dV}{dt} = k_{\text{fil,e}}\ \bar{p}_{\text{liq}} \tag{3.18}$$

with $k_{\text{fil,e}}$ as effective permeability (saturation dependent) and $\bar{p}_{\text{liq}}$ as average liquid pressure. This might be an explanation for the good agreement between the experimentally found relative permeability and Mualem's or Burdine's model.

The water transport is closely related to the filament. A continuous filament provides continuous flow. The flow rate might obey the law of Hagen-Poiseuille (Equation 1.31 on page 37) in a first approximation, or in a more macroscopic point of view, Darcy's law:

$$\frac{dV}{dt} = \mathbf{K}\ \nabla p \approx k_{\text{fil}}\ p_{\text{liq}} \tag{3.19}$$

k_{fil} denotes as the permeability constant, valid for the existing lateral connected filaments at the given liquid pressure p_{liq} inside the water below the DM; it depends on the fibre geometry. In extreme cases it might be only one filament and a Hagen-Poiseuille-like description might apply.

Both cases can be described by Darcy's law. Yet in the discontinuous case, the permeability constant is not analytically accessible but the result of a long-time average observation. This means that predictions for transient situations are not allowed if Equation 3.18 is employed.

Chapter 4

Assessment of In-Situ Visualisation of Liquid Water in Fuel Cells by NMR Imaging

4.1 Fuel Cells and NMR

In the previous sections, the water transport in DM was approached by ex-situ experiments and free surface modelling. From an practical point of view and to verify the findings made previously, an experiment to study both the water saturation and the behaviour in a running fuel cell is of interest. Certain phenomena like voltage fluctuations and limiting-current phenomena are believed to have their root cause in liquid water flooding but direct experimental evidence is missing. A visualisation of water within the fuel cell under operation provides guidance to understand and avoid situations where too much or too little water compromises the performance or durability. A set of different constraints has to be considered in order to enable fuel cells for transient power output operation.

In detail, the following situations are of special interest for fuel cell operation since they affect reliability, durability and cost.

- At low-power operation the fuel cell runs at low gas flow rates to reduce parasitic load in the system. In connection with the reduced heat production under these operating conditions voltage instabilities due to flooding might occur.

- At medium-power operation of the fuel cell operates at its design point. This requires an optimised water management to keep the number of cells in the fuel cell stack and, thus, the cost as low as possible. Also the parasitic system load, mainly driven by the cathode feed rate, can be minimised.

- Voltage instabilities can occur also at high-power operation at which some cells of a fuel cell stack or parts of cells operate at limiting current. This can either be caused by liquid water clogging the gas transport, or by protonical or electrical transport limitation in dry ionomer.

These three operation modes provide guidance to choose the experimental boundary conditions for the visualisation work. Different methods to measure the water distribution inside opaque structures like neutron radiography (NR), synchrotron radiography (SR), or nuclear magnetic resonance (NMR) are known. All the different methods have different strengths and weaknesses since they are based on very different physical principles. A discussion of the different methods is given by St. Pierre [SP07]. The NMR technique is explored here because it has the potential to resolve the DM's structure in the order of 20 µm depending on the sample size and due to the high sensitivity for water.

NMR is widely used in medical diagnostics and material science. In 2000, Martin Ise [Ise00] used NMR to characterise water transport in Nafion® and sulfonated poly-ether-ether-ketone (PEEK) membranes by studying diffusion coefficients within an electrolyser arrangement. This was one of the first fuel cell related applications of NMR. Others followed, in 2004 Kirk Feindel et al. [FLS$^+$04] performed a 3D tomography taken from an operating fuel cell. Their study was time-consuming, so they needed up to 13 hours to get the data for one set of 3D images of their cell. The images had a spatial resolution of 15 µm x 234 µm, the voxel extension in the third dimension is not stated in their paper. This group presented water distribution images from flow fields and membranes but not from the DM. In 2005 a Japanese group [TTH05] and [TTH06] reported also in-situ images of water distribution inside the membrane and studied the dynamic change in water concentration. Their work is based on 2D images which can be taken within 10 s to 30 s. In-situ measurements, focusing on the membrane and the flow field had been performed by Minard et al. [MVM$^+$06] and Dunbar et al. [DM07, DM08]. Porous

materials had been also under investigation, e.g. by Manz et al. [MCG99]. NMR is also applied in the context of ex-situ measurements to characterise diffusion of various liquids like by Gong et al. [GBT01] or Zhang et al. [ZGWJ05]. So far, the investigation of water transport in the diffusion medium was only touched briefly by Dunbar et al. [DM07], but not investigated systematically.

Since the NMR is based on interaction of electromagnetic fields at the wavelength of radio frequencies with, e.g. protons, there are open questions to be answered in order to assess the NMR as a diagnostic tool for in-situ fuel cell studies. The current collector and the DM are electrically conductive and conduct electricity during the in-situ experiment. This rises three questions:

- Is the water visible inside electrically conductive porous structures (electromagnetic shielding)?
- What happens if an electric current is produced inside the NMR (field distortion)?
- How does the operating temperature affect the NMR experiment (signal decay due to diffusion)?

None of the researchers, who applied NMR on fuel cells before, has discussed these subjects in the light of DM characterisation. Only the requirements on the material of the flow field had been addressed so far.

In the next section, the test equipment like the fuel cell and the test stand will be introduced, followed by an excursion into the fundamentals of NMR. This is necessary to prepare the ground for discussing the different aspects of the fuel cell experiment in the NMR, like the material selection, operating conditions and further more.

4.2 The Fuel Cell and Test Stand

The laboratory environment for NMR experiments is characterised by strong magnetic fields and a sensitivity for electromagnetic radiation. Therefore, special fuel cell and test stand equipment is required to account for these facts. To accommodate the fuel cell to the requirements of NMR, the fuel cell body has to be proton free and electrically insulating, therefore, PTFE was used. The current collectors were made from gold-plated copper

(to reduce the corrosion). The flow field had ten straight channels with 2 mm pitch and a depth of 1.2 mm (see Figure 4.1). The rational behind the material selection will be discussed in detail in Section 4.3.1 on page 120ff. The cell temperature was controlled by deionised (DI) water which was pumped with a Haake thermostat at high velocity through extra channels below the active area (see the cross section in the left part of Figure 4.1).

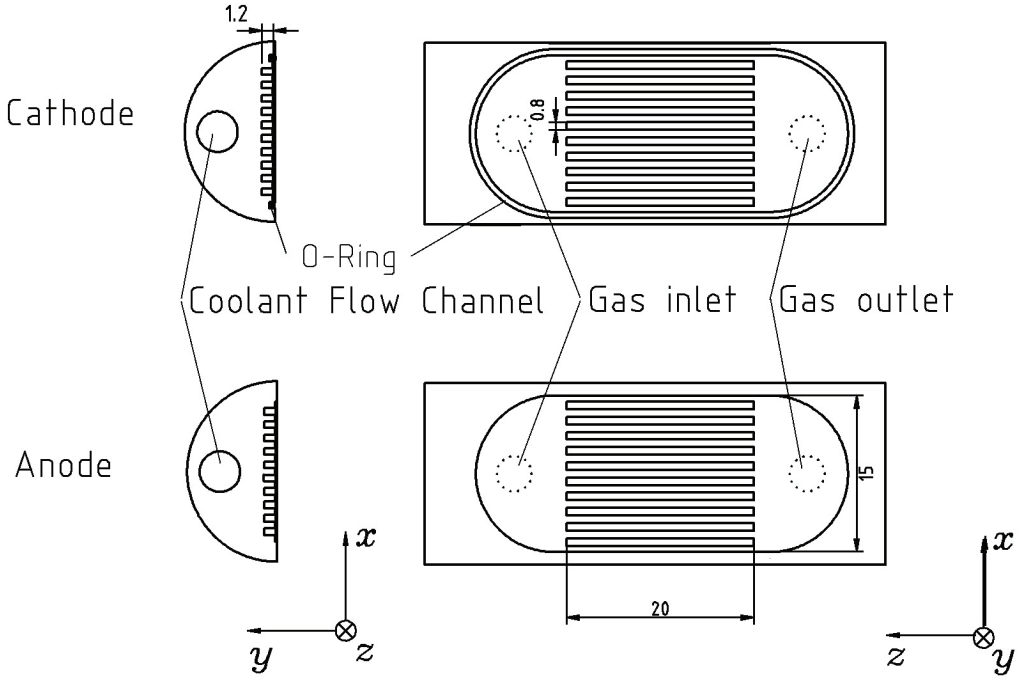

Figure 4.1: Layout of the fuel cell for the NMR experiment.

Motionless deionised water gives a large proton signal in the NMR experiment which would disturb the observation significantly. This issue was solved with the high water flow rate which causes a fast magnetisation decay of the DI water inside the coolant channels (the magnetisation disappears faster than the instrument can measure). The cell was oriented in the spectrometer in such a way that the gravity vector ran parallel with the membrane plane (z-vector) and co-current with the gas streams. The fuel cell operation is not affected by the orientation because of the small length scales, the surface tension dominates the physics and gravity effects are only secondary (for details see also discussion in Section 1.3.6 on page 52ff.). The NMR instrument has the highest resolution along the y-axis, thus, the used orientation optimises resolution inside the DM and the membrane

without increasing the measurement time. If the membrane were placed horizontally, the test time would be four times longer for similar spatial resolution. The imaging probe head used for this work was 100 mm long and had an inner diameter of 25 mm. This size was chosen since the spatial resolution decreases with increasing probe head size. The active area of the fuel cell was 3 cm^2. The hardware-specific data are summarised in Table 4.1.

Table 4.1: Characteristic data of the experiment

Fuel cell	Active area	3 cm^2
	№ of channels in flow field	10
	Channel depth	1.2 mm
	Pitch	2 mm
Imaging probe head	Length	100 mm
	Inner diameter	25 mm
Image data	Spatial resolution x	313 µm/pix
	Spatial resolution y	20 µm/pix
	Spatial resolution z	625 µm/pix
	Magnetisation signal	8 bit
	Temporal resolution 3D	2 h
	Temporal resolution 2D	30 s

The cell layout in relation to the proton density images is pictured in Figure 4.2. The left part shows the cathode flow field and the x-z-cross section through the membrane parallel to the current collectors. The right part of Figure 4.2 depicts a cross-sectional view perpendicular to the current collectors.

The orientation of the cell is defined such that the membrane plane is in the x-z-plane, the z-direction points along the channel, parallel to the gravity vector during the test. The y-direction points normal to the membrane plane. Due to the different spatial resolution along the three dimensions, the corresponding images appear distorted since the aspect ratio is not 1 to 1. The horizontal bright yellow stripes show flooded flow channels, the magenta area in the middle section shows the location of DM and membrane. The images have a depth of 256 colours and the lighter the colour the higher is the water concentration. Quantitative statements require calibration specific to material and temperature, which will be explained in Section 4.3.4 on page 131ff. The test stand was operated manually and consisted of a bank of two rotameters for hydrogen and two for oxygen to allow a wide range of flow, pressure gauges, a thermostatic bath for cooling the fuel cell, an

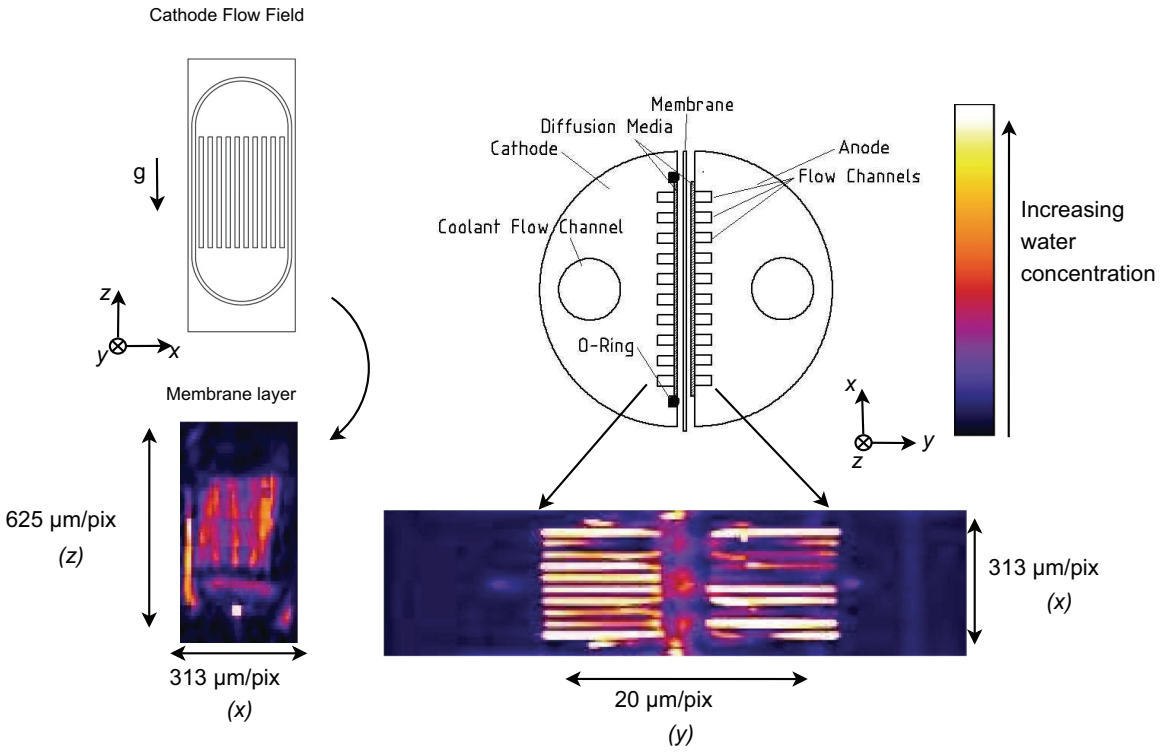

Figure 4.2: Relation between the fuel cell layout and proton density images. Left part: Layout of the active area in x-z-plane and the resolution in x-z-plane exemplary on the membrane. Right part: x-y-cross section through the fuel cell and the proton density image resolution for the x-y-cross section.

electric load, and a multi-channel plotter. Initially, a vapour-fed humidification system was implemented but not used due to reasons later to be explained (see Section 4.3.3 on page 125ff.). The gas was supplied to the fuel cell by a "tube-in-a-pipe" system. The inner tube was used for gas supply, while the surrounding pipe contained the water for cooling the cell. The anode and the cathode feed had co-current flow to each other. The cathode gas ran co-currently with the coolant flow, while the anode gas ran counter-currently. This was done in order to avoid condensation in humidified cathode streams. To validate the design, the performance of the cell was characterised outside the spectrometer. The potential-current characteristic is depicted in Figure 4.3.

The cell was operated inside a Bruker Avance 400 MRI scanner. For the imaging, a pulse sequence for 3D Imaging called 'Spin Warp' was applied, as described by Edelstein et al. [EHJR80].

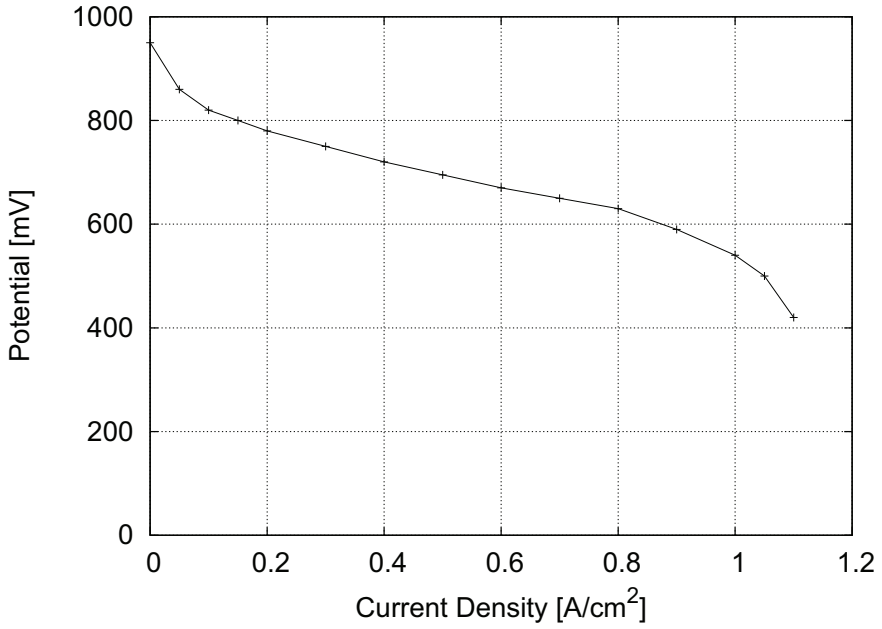

Figure 4.3: Performance of the fuel cell designed for NMR tests at 353 K and constant gas flows, sufficient for 2 A/cm^2 (stoichiometry 1). The anode humidity is 80 % RH and cathode humidity 7 % RH.

4.3 Fundamentals of NMR

The following excursion into the details of NMR is necessary to discuss the different aspects which have to be considered in order to use NMR as in-situ diagnostics for fuel cells. It is limited to the information required to select the material and define the operating conditions. The following details can be found in textbooks like Eiichi Fukushima and Stephen B.W. Roeder [FR81].

NMR takes advantage of the magnetic properties of protons and neutrons which pose a rotating magnetic moment, called nuclear spin. In certain elements like ^{1}H and ^{13}C, an unpaired spin configuration exists and NMR experiments can be performed. The nuclear spin can be interpreted as a rotating rod magnet. This property becomes important if certain chemical elements like hydrogen are exposed to strong magnetic fields. Since this work deals with water, the following explanations will use protons as the example. In a magnetic field, the protons separate into two groups, one is energetically favourable and the spins are aligned parallel with the external field. The other one is aligned anti-parallel. The two different configurations are defined $+\frac{1}{2}$ and $-\frac{1}{2}$. At room temperature, the spin distribution is such, that slightly more protons are in the energetically favourable orientation. The difference in energy between the two stages depends linearly upon the intensity of the external magnetic field. The imaging experiment is done with a series of electromagnetic pulses which alter the spin orientation of the protons in the control volume. If the impulse energy changes the ratio of spins $+\frac{1}{2}$ and $-\frac{1}{2}$ to become 1:1, the net magnetisation of the protons in the z-direction (parallel to the static field) will disappear; this is called a 90 ° pulse. Once the spin ratio is changed, the protons re-establish their original spin distribution (Boltzmann). The time law for this rearrangement is exponential and the time constant is called T_1. Due to the fact that not only a magnetic moment, but also an angular momentum is present, a second effect is observed. When a rotating axis is exposed to a force trying to tilt it, the axis starts to precess. A 90 ° pulse causes such a rotation of the spins toward the x-y-plane. At this moment all the spins are in phase. With progressing time, the spins start to fan out since the individual spins rotate with slightly different frequencies due to local field inhomogeneities. This results in a decay of

the magnetisation $\mathcal{M}$ in the x-y-plane

$$\mathcal{M}(t) \quad = \quad \mathcal{M}_0 \, e^{-\frac{t}{T_2^*}}. \tag{4.1}$$

The spin-spin relaxation time constant T_2 or T_2^* is associated with this phenomenon. The time constant T_2^* is an effective time constant and relates to the same effect as T_2 but includes artificially induced field inhomogeneity used to encode the spatial information required for the imaging:

$$\frac{1}{T_2^*} \approx \frac{1}{T_2} + \gamma^* \Delta H \tag{4.2}$$

With T_2 as the undisturbed time constant, γ^* as gyromagnetic ratio (species property) and ΔH as the difference of strength between homogeneous magnetic field and the local contribution of the imposed gradient. The time constant T_2 is influenced by the interaction of the proton containing molecules with each other or the surrounding environment. The more the molecules interact with the environment, the more momentum exchanges and the signal decays faster. In imaging, a spacial field gradient is superimposed on the homogeneous main field, causing a location-dependent T_2^*. With the pulse technique, the time constant T_2^* can be measured. From the exponential time law of signal decay, the original magnetisation is calculated. Derived from Curie's law, the magnetisation depends linearly upon the water mass in the control volume:

$$\mathcal{M}_0 \quad = \quad <n> \frac{(\gamma^* \hbar)^2 \mathcal{I}(\mathcal{I}+1)}{3 k_\mathrm{B} T} H \tag{4.3}$$

$\mathcal{M}_0$ denotes the magnitude of magnetisation, $<n>$ as the number of spins (proportional to species concentration), $\mathcal{I}$ represents the spin quantum number (species property), $\hbar$ the Planck constant, k_B the Boltzmann constant, T the temperature and H as the strength of the magnetic field. This means that any property of the fuel cell experiment affecting the magnetic field, interferes with the measurement. This has to be considered in order to draw meaningful conclusions from the experiment. The following section deals with the material aspects.

4.3.1 Material Effects

The requirement for the cell to be made of materials being electrical insulators, arises from the fact that any alternating magnetic field introduces current in electrically conductive material. This current disturbs the local magnetic field then by generating a counter field. Thus, the proton signal in the vicinity of the electrical conductor is compromised. Furthermore, the electromagnetic radiation is reflected and partially adsorbed by electrically conductive material. The electrical and magnetic properties of carbon fibres have the potential to act as an electromagnetic shield [Chu01]. The shielding effect is mostly based on reflection due to the free electrons in the shield. The shielding effectiveness of a carbon fibre material depends upon the fibre geometry and conductivity of the bulk material, the connectivity of the fibres, and the frequency of the electromagnetic radiation. Li and Chung [LC94] reported a shielding effectiveness of 44 dB for a polyethersulphone composite containing 20 % vol. carbon fibres of 10 µm diameter, with a length of 3 mm, and 2.7 mm thickness at a frequency of 1 GHz, while a fibre length of 0.4 mm results in a shielding effectiveness of 17 dB. The similarity to the DM lies in the fibre diameter, length, and fill ratio, but the frequencies for the NMR experiment is around 400 MHz. The thickness of the DM is only a tenth of composite samples described by Li and Chung, which means that the shielding is less effective.

The rate of shielding as a function of frequency can be estimated by the skin effect, responsible for the attenuation of high-frequency radiation [FLS89]. Alternating current is conducted mainly on the surface of a conductor. The higher the frequency, the thinner is the conducting layer called skin thickness δ. A material of a skin thickness of one reduces the intensity of high-frequency radiation by 37 %. The skin thickness can be calculated by

$$\delta = \sqrt{\frac{\epsilon_0 c^{*2}}{\sigma^* 2\pi\nu}}. \tag{4.4}$$

ϵ_0 denotes as electric field constant, c^* as speed of light, σ^* as specific conductivity and ν as frequency of electromagnetic radiation. Equation 4.4 applies as long as

$$2\pi\nu \leq \frac{\sigma^*}{\epsilon_0} \tag{4.5}$$

which is the case for carbon with $\frac{\sigma^*}{\epsilon_0} = 10^{17}$ Hz, this is way beyond 2.5 GHz (= $2\pi \cdot 400$ MHz, Equation 4.5). If the conductivity of carbon is assumed as 10^4A/V/m [Kin88], the skin depth at 400 MHz calculates to $\delta_{400\ \mathrm{MHz}} =$ 25 µm and for 1 GHz to $\delta_{1\ \mathrm{GHz}} = 16$ µm. For both cases, the skin depth is larger than the fibre thickness, this means that the DM weakens the NMR signal but does not shield it completely. Faint signals might be attenuated to such an extent that they cannot be detected. Based on pure theory it is not possible to calculate the shielding effect for the DM precisely and the experiment will reveal to what extent the protons can be detected inside the DM.

Not only the conductivity of carbon fibre based DM has some effect on the sensitivity, but also the conductive current collectors, as will be shown next. Thus, the geometry of the current collectors is important to obtain good signal intensities from the water inside gas diffusion media. The following ex-situ experiments were done with Toray 060 DM and Gore 5510 membrane, while the in-situ work was done with SGL21AA coated with 10 % PTFE by weight. The reason is that the Toray DM shields the water signal more effectively than the SGL material, which was discovered later. The water saturation under fuel cell operation turned out to be below the detection threshold for water inside the Toray DM. Two reasons can be suggested to explain this finding: firstly, the electrical conductivity of SGL21AA is several times smaller than the conductivity of Toray, and secondly the pore structure is less dense. The shielding issue was explored by ex-situ work (with Toray 060) with modified current collector geometries in a PTFE housing without flow channels. Two pieces of DM had been saturated to a high extent outside the fuel cell and and placed between the current collectors, sandwiching the membrane in the PTFE housing. The proton density distribution of this arrangement was measured by NMR. During the measurement the cell represented a closed system. This test was repeated with different current collector designs. Figure 4.4 shows the tested modifications as well as the finally used geometry.

The upper left side (Pos. 1) in Figure 4.4 displays the original geometry. Below, a x-z-cross sectional 400 µm thick slice (1a to 4a) of the water concentration in membrane (parallel to the collector) is shown. The x-y-cross sectional images (1b to 4b) show a 2D projection of the proton signal in the x-y-plane. The light vertical line represents the membrane, the magenta area on the left and the right side from the membrane represent

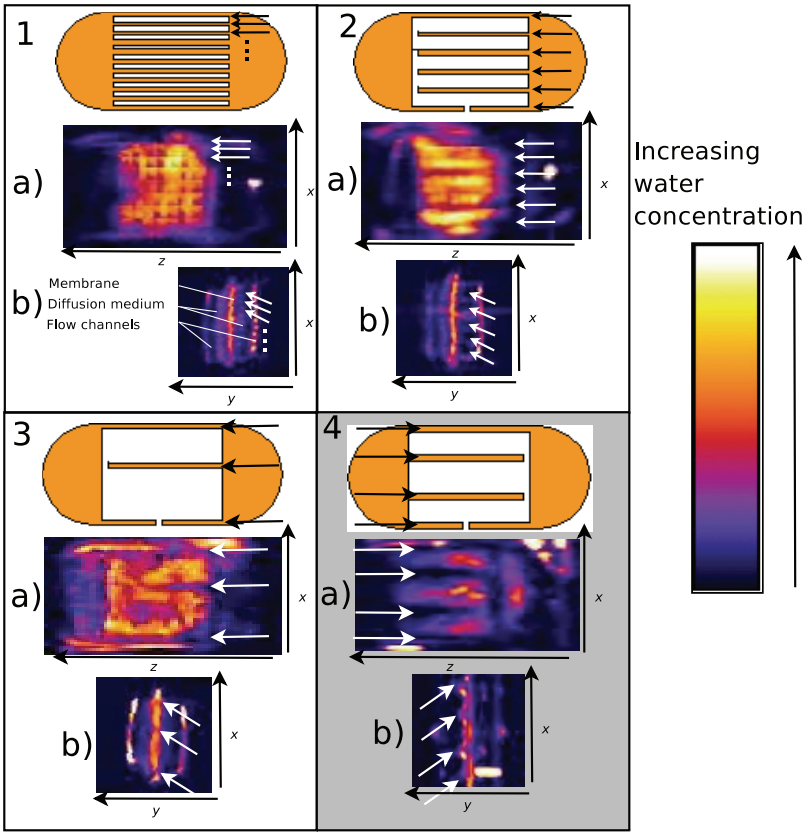

Figure 4.4: Different current collector modifications 1 to 4 and the resulting images of membrane and diffusion media. Modification 4 was finally used. Images 1a) to 4a) show the membrane in the x-z-plane and images 1b) to 4b) show the x-y-cross section through the test cell. The cell was not in operation, the diffusion media had been saturated ex-situ. The arrows indicate regions of shielding.

the anode DM (left), and the cathode DM (right). The outer area on the left and the right side show the slits in the current collector. The white arrows indicate areas of reduced signal intensity and these correspond well with the location of the black arrows pointing at the ligaments of the current collectors. The y-z-cross sectional image 1a) depicts a striped pattern where a more uniform distribution is expected. The x-y-cross section 1b) shows a dot-pattern in the location of the DM, aligning well with the ligaments of the current collector. The upper right part 2) in Figure 4.4 shows a configuration where every second ligament was removed. This causes a change in the pattern, the shielding is reduced. Further reduction of shielding is found when only one ligament remained (image 3 lower

left part). This modification would be most favourable from an imaging standpoint, while the fuel cell operation would be compromised severely. Such a modification causes large ohmic losses since the produced current has to travel a long way in the DM to get to the current collector. Finally, the modification 4), used for the in-situ work, was a trade-off between ohmic losses and image signal losses and is shown in the lower right part in Figure 4.4. In contrary to the resolution stated above, the x-y-cross sectional images in Figure 4.4 have a resolution of 40 µm/pixel in y-direction.

Since the collector geometry has a strong impact on the result, it can be concluded that the reason for the shielding is the disturbance of the local magnetic field due to magnetically induced eddy currents in the current collectors [FLS89]. The signal loss due to eddy currents and the shielding from the DM add up. Tests in an ex-situ arrangement with current collectors and wet membrane, but without DM, had an increased signal intensity of the wet membrane in comparison to the configuration with DM.

4.3.2 Current Production

The local magnetic field in the domain of the membrane and the DM is not only influenced by eddy currents induced by the electromagnetic radiation, but also by the electromagnetic field caused by the current flowing in an operating fuel cell. In this section, the field disturbance due to the produced current in the fuel cell will be estimated. The fibre structure of the DM represents a complex conductive network which will be replaced by a simplified model to estimate the effects (see Figure 4.5). In the model, a regular mesh of fibres and a homogeneous current density is assumed. The current travels through the intersections normal to the fibre plane. The distance between the conductive paths can be estimated from the porosity of the DM. If a homogeneous porosity of 80 % and a fibre diameter of 7 µm is assumed, the distance between the paths is $b = 28$ µm.

The magnetic field strengh H surrounding a straight wire is a function of the distance from the wire r and the current I running through the wire [Kuc95]:

$$H = \frac{I}{2\pi r} \tag{4.6}$$

The diameter of the model conductor is assumed to be identical to the fibre diameter of

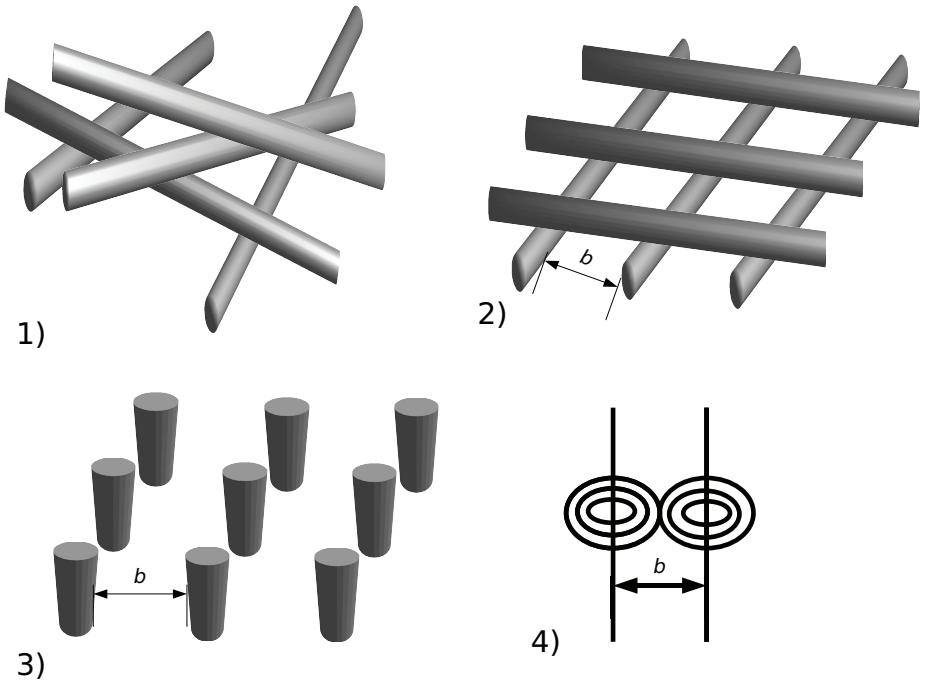

Figure 4.5: Steps of simplification to estimate influence of current flow through the DM on the magnetic field. 1) Real fibre structure. 2) Simplified fibre grid. 3) Path of current through simplified grid. 4) Magnetic field lines around two straight conductors.

7 µm and the current is estimated from the current density and the fibre density. In the simplified model, the current runs in the same direction through the parallel conductors and the sense of rotation of the field lines is the same. This means that between the fibres the magnetic field strength changes sign along the distance b and the resulting magnetic field strength between the two conductors is the sum of the magnetic field of each conductor. In Figure 4.6 the spatial variation of the current-induced magnetic field between two conductors is calculated for three different current densities.

The model strongly simplifies the real situation but it becomes clear that at higher current density the field becomes distorted. The ratio between the additional field and the main field of 9 Tesla comes in the range of 10^{-7} for the simplified model. The distortion becomes relevant if the ratio is $\geq 10^{-6}$. It is not unlikely that the simplified model is off by one order of magnitude and additional loss of accuracy might be seen at higher current densities. To determine the field distortion more accurately, extensive numerical modelling

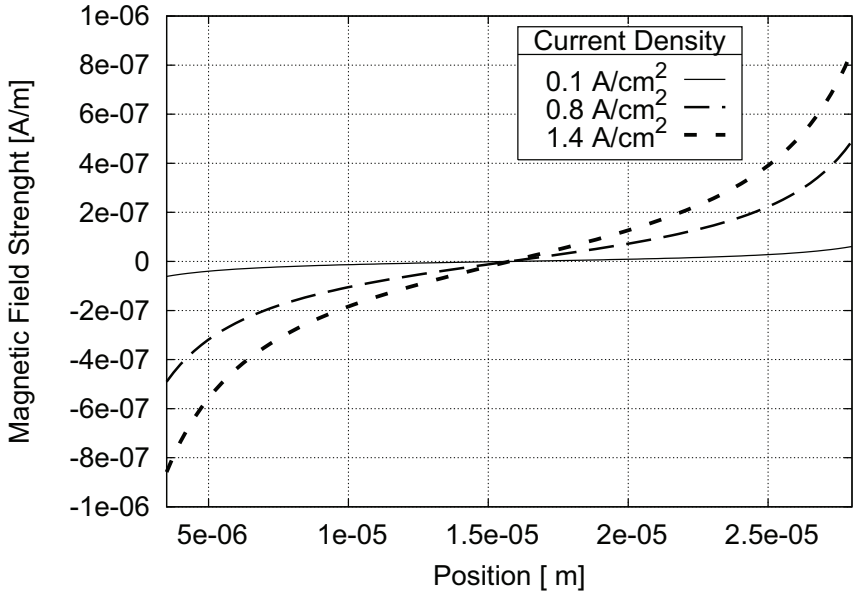

Figure 4.6: Magnetic field strength between to straight conductors as a function of position at different current densities.

is necessary and beyond the scope of this work. The possibility that the measurement is influenced by the current production at high current densities cannot be excluded and has to be kept in mind when the results are interpreted.

4.3.3 Temperature Effects

The influence of the temperature on the measurement is twofold. First, the magnetisation is proportional to $1/T$ according to Equation 4.3 on page 119 and secondly the decay time T_2 depends on temperature since the molecular interaction, i.e. the spin-spin exchange increases with rising temperature. The more a molecule interacts with the environment, the more momentum exchange takes place and the signal decays faster. At higher temperatures, the number of collisions of the water molecules with the walls of the pores and with each other increases. This accelerates the spin-spin relaxation rate $1/T_2^*$. Also the pore size matters in that regard, that if the pores are small, the more interaction between water and the pore walls take place. A linear relation between T_2 and the pore size in the range between 50 µm and 1 mm is reported by V. Leon and H. Diaz [LD86]. In addition to that, the dead time of the NMR instrument, when no signal can be measured due to

the time constants of the spectrometer, is 1 ms and any signal lost during this time is not detected. This is the reason why the DI water in the cooling channels does not interfere with the image acquisition.

To estimate the probability of impacts between DM substrate and water and, thereby the signal loss, the mean travel distance of the water molecules within 1 ms in dependence of temperature is calculated. According to Einstein-Smoluchowski equation (Equation 4.7) [Atk94], the travel distance $<r^2>$ in dependence of time t calculates to

$$<r^2>= 2\ D(T)\ t \tag{4.7}$$

with $D(T)$ as the temperature-dependent self diffusion coefficient. The self diffusion coefficient for liquids itself is estimated by the Stokes-Einstein equation [Atk94]:

$$D(T) = \frac{k_\mathrm{B}\ T}{2\pi\ \mu(T)} \left(\frac{N_\mathrm{A}}{V_\mathrm{mol}(T)} \right) \tag{4.8}$$

with

$$V_\mathrm{mol}(T) = \frac{M_\mathrm{H_20}}{\rho(T)} \tag{4.9}$$

k_B represents the Boltzmann constant, $\mu(T)$ the viscosity, N_A the Avogadro constant, $V_\mathrm{mol}(T)$ the molecular volume, $M_\mathrm{H_2O}$ the molar mass of water and $\rho(T)$ its density.

The calculation of the self diffusion coefficient of water at 298 K with Equation 4.8 results in $2.23 \cdot 10^{-9}$ m^2/s, while the measured self diffusion coefficient for free water is reported as $2.27 \cdot 10^{-9}$ m^2/s [EEW84]. The temperature variation of the self diffusion coefficient covers one order of magnitude between 273 K and 373 K. This means that the range of values for the self diffusion coefficient is much larger than the difference between the calculated and the measured value at 298 K, thus, the accuracy of the calculated value is sufficient to assess the consequences of temperature variation.

The dependence of the viscosity and the molecular volume (density) upon temperature can be represented by an exponential (viscosity) and binomial (density) fit to data reported in literature [Lin96]. The diffusion length $<l>= \sqrt{<r^2>}$, the viscosity, and the density between 273 K and 373 K are shown in Figure 4.7. The density variation with temperature is only minor, but for completion it is also considered. The diffusion length increases

significantly between 273 K and 373 K due to the temperature dependence of the viscosity and gets in the order of several µm. At higher temperatures, the probability of wall contact and, therefore an increasing spin-spin interaction is to expect. This results in a faster signal decay making it difficult to measure if the decay takes place within milliseconds.

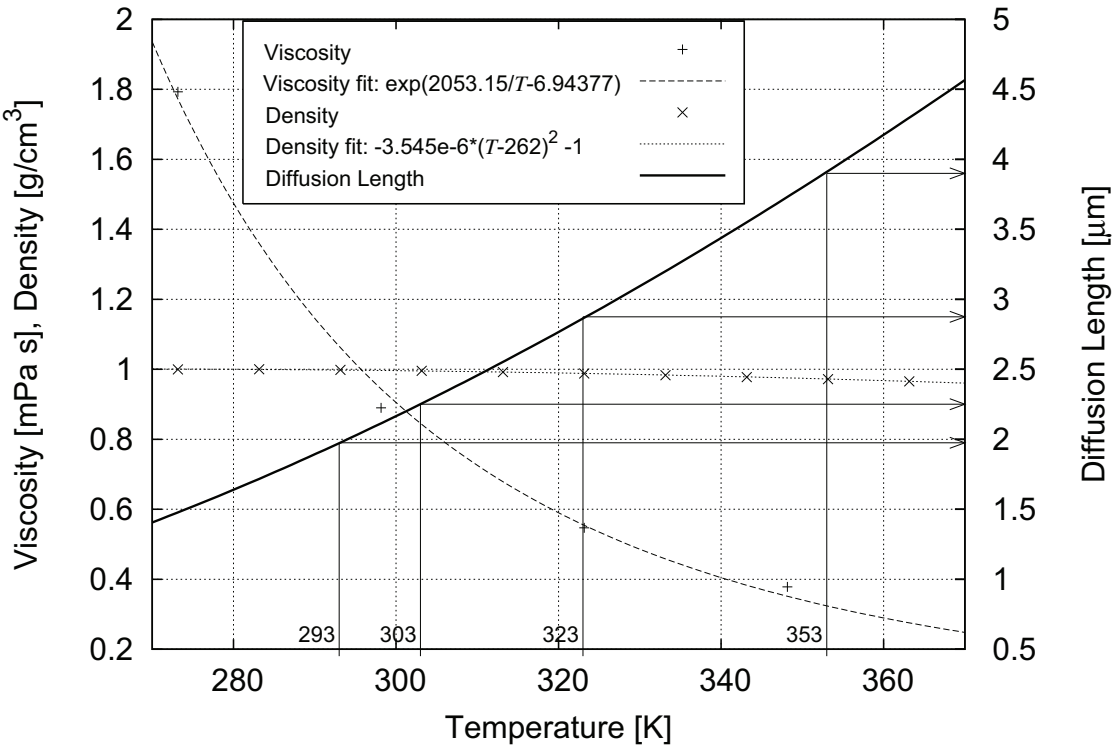

Figure 4.7: The temperature-induced variation of viscosity, density, and diffusion length of water within 1 ms.

The attempt to estimate the signal loss as a function of the pore size or the temperature will be made with a simple model. The signal intensity is directly proportional to the number of protons in a volume element and, hence, proportional to the mass of free water or, if the temperature dependency of the density is ignored, to the volume of water.

In the experiment it is observed that less signal from a water-filled volume V is obtained at elevated temperatures. This might be caused by the spin relaxation effect at the walls, a water layer near the wall and, therefore, a part of the water volume being invisible V_{inv}. The width of that layer can be estimated to be in the order of the diffusion length $<l>$. This is used to express a relative magnetisation $\mathcal{M}_{\mathrm{rel}}$ by introducing a reference volume

at the reference temperature T_0:

$$\mathcal{M}_{\text{rel}} = \frac{V - V_{\text{inv}}(T)}{V - V_{\text{inv}}(T_0)} \tag{4.10}$$

For further analysis, an assumption on the geometry of the open space has to be made and in this case, a cylindrical pore model will be used. The geometry is illustrated in Figure 4.8.

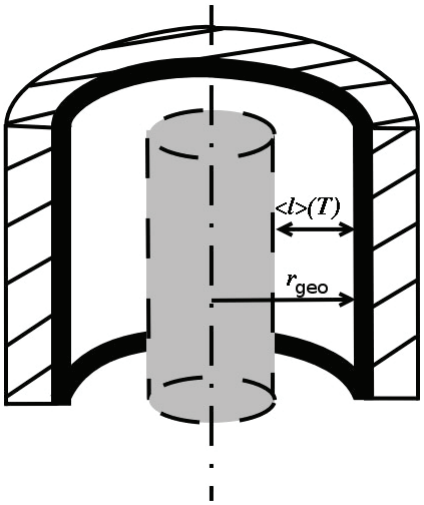

Figure 4.8: Cylindrical pore model to explain the temperature-dependent NMR signal. r_{geo} is the geometrical radius of the pore, and $<l>\,(T)$ the temperature-dependent diffusion length.

For the cylindrical pore, the volume in Equation 4.10 can be replaced by the area. This is, because the 'invisible length' of the cylinder is independent from temperature. The grey cylinder in Figure 4.8 represents the volume visible by NMR imaging and the ratio of the cross sectional area can be used to estimate the relative signal intensity according to

$$\begin{aligned} \mathcal{M}_{\text{rel}} &= \frac{V - V_{\text{inv}}(T)}{V - V_{\text{inv}}(T_0)} \\ &= \frac{l\,[A - A_{\text{inv}}(T)]}{l\,[A - A_{\text{inv}}(T_0)]} \\ &= \frac{\left[r_{\text{geo}} - \sqrt{<l^2>\,(T)}\right]^2}{\left[r_{\text{geo}} - \sqrt{<l^2>\,(T_0)}\right]^2} \end{aligned} \tag{4.11}$$

The quadratic exponent in Equation 4.11 is a consequence of the cylindrical assumption;

in the real DM where the pores are not cylindrical, the exponent can be anywhere between 1 (two flat plates) and 3 (closed sphere); any pre-factors (like π) will cancel out. Since Equation 4.11 only considers pore size effects, the temperature dependence of Curie's law (Equation 4.3 on page 119) has to be included in Equation 4.11 for completion:

$$\mathcal{M}_{\mathrm{rel}} = \frac{\left[r_{\mathrm{geo}} - \sqrt{<l^2>(T)}\right]^2}{\left[r_{\mathrm{geo}} - \sqrt{<l^2>(T_0)}\right]^2} \frac{T_0}{T} \tag{4.12}$$

The development of the signal intensity with temperature due to pore interaction and Curie's law is calculated according to Equation 4.12 for a reference temperature of 293 K for three different pore radii and compared to the measurement described in the following. The comparison is plotted in Figure 4.9.

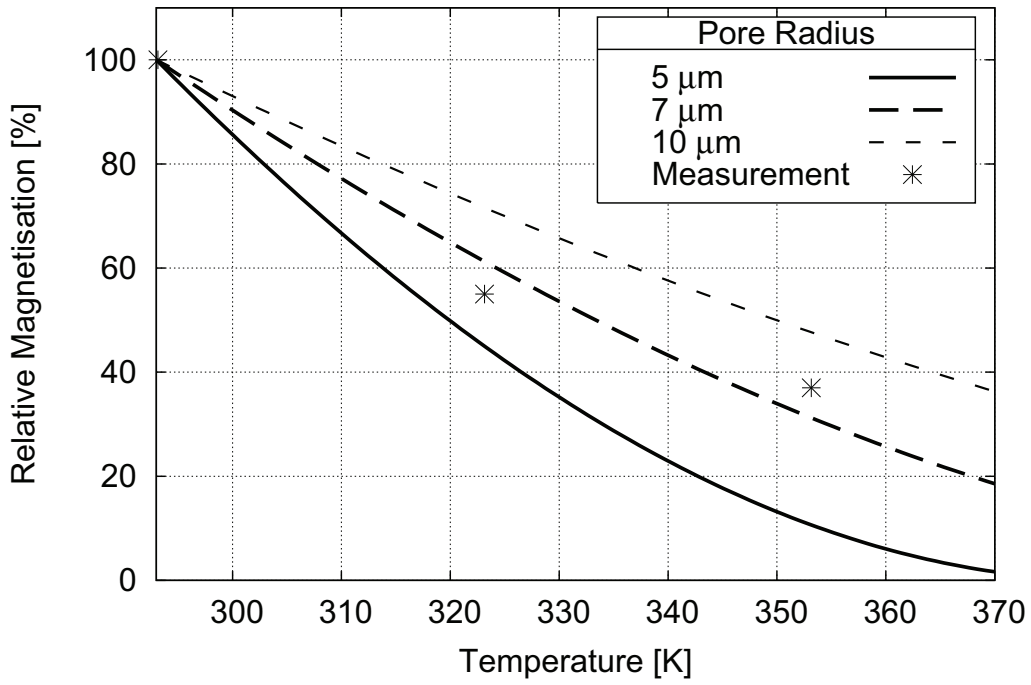

Figure 4.9: Relative magnetisation as a function of temperature for three different pore radii including the temperature dependence of Curie's law. Reference temperature is 293 K.

From Figure 4.9 it becomes clear how strongly the water signal depends upon the temperature and the pore radii of the substrate. Both parameters, pore size and temper-

ature have to be considered in order to get NMR imaging information. To get as close as possible to application-relevant operating conditions, higher test temperatures are desirable. In order to make a trade-off between non-ambient operating temperature and signal intensity, tests without operation were done at room temperature 293 K (20 °C), 323 K (50 °C), and 353 K (80 °C). It was found that the signal intensity weakened significantly between 323 K and 353 K operating temperature (see Figure 4.9 and Figure 4.10). The measured data points in Figure 4.9 are based on the average magnetisation of the centre part of the cathode DM, in relation to the value, measured at 293 K.

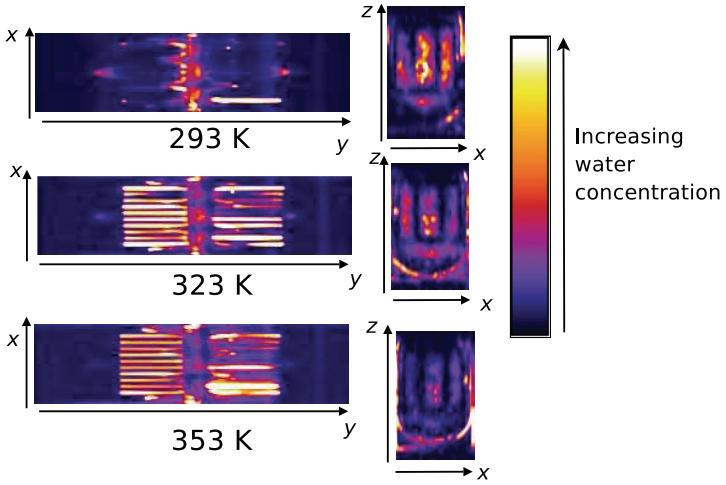

Figure 4.10: Centre layer in the x-y and the x-z-plane of the non-operating fuel cell with pre-saturated DM (Toray 060) at different temperatures.

The images in the centre of Figure 4.10 show the cross section perpendicular to the current collector. With increasing temperature (top to bottom) the signal intensity in the DM/membrane area decreases, while the water signal in the channels increases from 293 K to 323 K. The cell was built with pre-saturated diffusion media and the gas ports were sealed. The elevated temperature seems to cause a migration of water from the DM into the flow channels within two hours of testing. Since the channels at 323 K and 353 K seem to be equally filled with water and the initial saturation of the DM was similar, it can be concluded that DM and membrane are in a similar state of saturation. Thus, the signal intensity of the two pictures can be used for comparing the DM-membrane signal.

The signal intensity from the central slice of the membrane on the right side in Figure 4.10 clearly shows a decrease with increasing temperature. At 293 K the DM-membrane area might contain significantly more water than the other two and a comparison is not possible. Based on this consideration, all the fuel cell testing is done at 303 K (30 °C) in order to get sufficient signal intensity.

4.3.4 Calibration

Following variables of the fuel cell experiment have been identified to be also relevant variables for the water visualisation by NMR:

- Electrical conductivity of DM
- Current density
- Temperature

Thus, the values of these variables have to be similar in the fuel cell and the calibration experiment. If this is not possible because the calibration experiment does not allow to control a specific property, e.g. the current density, care has to be taken by interpreting the results.

The shielding effect, explained in Section 4.3.1 on page 120ff. causes that a similar proton density in the channel and the DM result in a different magnetisation signal for the channel and the DM. This intensifies the difficulties for absolute quantitative statements. The attempt to find a calibration curve for the DM was done as follows: The DM (SGL 21AA) was saturated ex-situ with water and images were taken over two hours. The water saturation in the DM was measured gravimetrically before and after the imaging. This was done for three different saturation levels of SGL21AA material, the kind of material used for the further testing. The DM was mounted in a dummy cell (same cell the shielding experiments had been done with). The major difference between the dummy and the actual cell is the absence of flow channels, coolant flow channels, the membrane electrode assembly (MEA), and the disability to apply electrical potential or run electrical current through the materials because of unwanted electrolysis. The current

collectors were situated in pockets next to the DM in order to establish identical shielding environment as in the fuel cell. The cell was held at a constant temperature of 303 K by an air blower during the imaging and the water mass inside the cell was constant.

To obtain a calibration line, the signal intensity information of each voxel from the centre region with the two DM in each 3D image series (boxes in Figure 4.11), is summarised and represented by one virtual voxel containing all the information. The noise (average signal of water-free voxels multiplied by the number of voxels in the region of interest) is subtracted from the signal of the virtual voxel containing all water. This signal then was correlated with the mass of water in the two DM obtained by weighing.

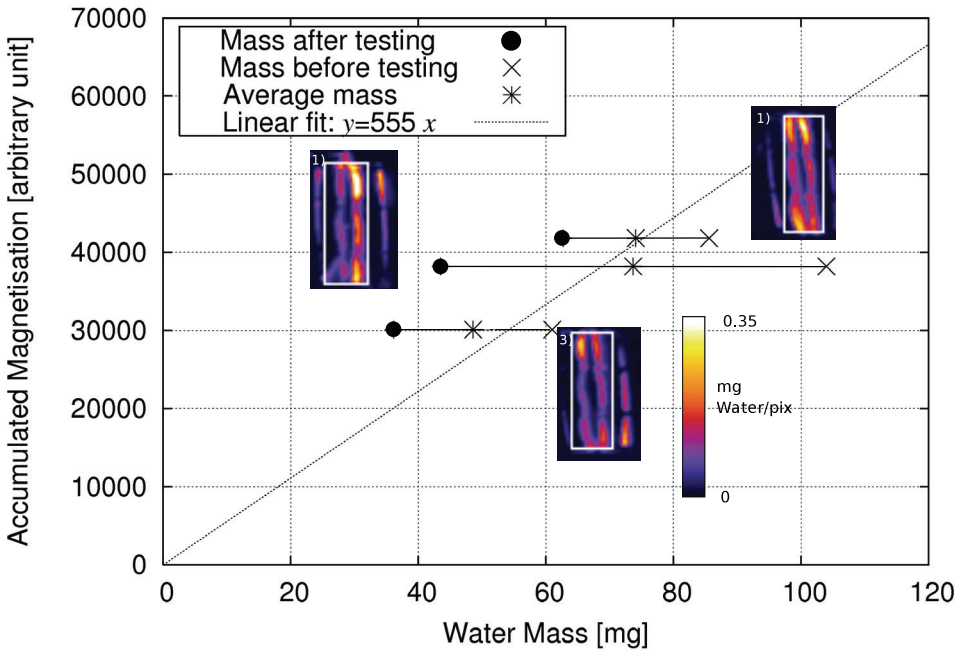

Figure 4.11: Calibration plot for SGL 21AA DM. The inserts represent the integrated x-y-projection of the calibration cell. Colours indicate signal intensity integrated along z-direction. The area inside the white rectangles is used for calibration.

Since one complete 3D scan takes two hours, the water content in the diffusion media changes, and water was found outside the DM-membrane area. The dynamics of the water redistribution is unknown. Therefore, it is not clear whether the water mass in the two DM in the beginning, or in the end of the experiment, or the average of the two shall be used. For the calibration, all three different combinations were tested and the correlation with

average mass was found to have the best linear trend (see Figure 4.11). The correlation between magnetisation intensity ($\mathcal{M}$) and the water mass ($m_{\mathrm{H_2O}}$) is found to be:

$$\mathcal{M} = 555 \left[\frac{\text{nmr cts.}}{\text{mg}} \right] m_{\mathrm{H_2O}}. \tag{4.13}$$

The unit 'nmr cts.' represents the intensity information of the voxel in the images. The individual masses of the two DM in the calibration tests are known and this gives the opportunity to cross-check the calibration.

From the calibration images shown in Figure 4.11 the two different DM in each picture are analysed separately and the average water mass before and after taking the image can be compared with the calculated mass from the NMR signal. It turned out that four of the six test points are within the 10 % error. Figure 4.12 shows the result together with ± 10 % lines.

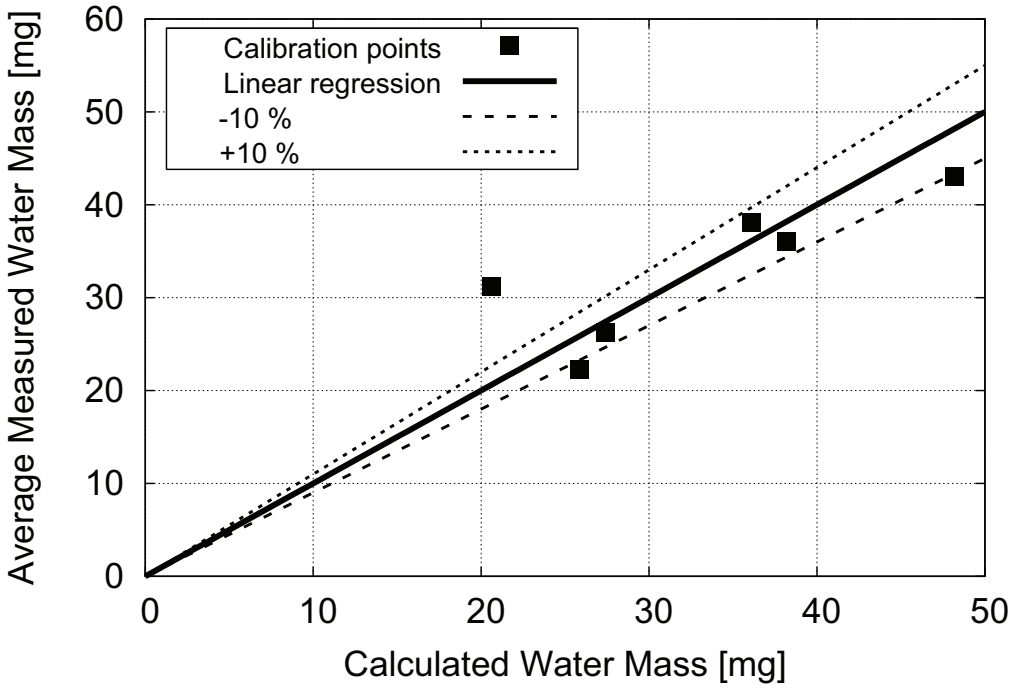

Figure 4.12: Comparison between measured water mass in DM and the water mass obtained with NMR signal by the calibration.

The weak spots in the calibration are:

- The uncertainty of the water distribution dynamics.
- The fact that only three points were measured.
- The effect of flowing electrical current through the cell is not considered.

The error in water mass of the DM caused by the dynamics of water distribution is already covered by the ± 10 % error estimation due to the averaging procedure between initial and final water mass. The shielding limits the calibration to the DM. For the reasons stated here, the NMR test shall be considered as semi-quantitative.
In order to use the calibration to calculate the saturation 's' of the DM, the water volume has to be calculated from the water mass and normalised by the volume of each voxel:

$$s = \frac{m_{\mathrm{H_2O}}}{\rho_{\mathrm{H_2O}}\ \varepsilon\ V_{\mathrm{xyz}}} \tag{4.14}$$

With Equation 4.13, the saturation is expressed as a function of magnetisation by:

$$\begin{aligned} s &= \frac{\mathcal{M}\,[\text{nmr cts.}]}{555\left[\frac{\text{nmr cts.}}{\text{mg}}\right]\ 0.99610^{-9}\left[\frac{\text{mg}}{\mu\text{m}^3}\right]\ 0.9\cdot 20\,[\mu\text{m}]\ \ 313\,[\mu\text{m}]\ \ 625\,[\mu\text{m}]} \\ s &= \frac{\mathcal{M}\,[\text{nmr cts.}]}{1.947\ \ [\text{nmr cts.}]} \end{aligned} \tag{4.15}$$

The lower saturation limit detectable by this NMR experiment is set by the noise intensity. The noise is determined from the images used for calibration at locations where no water can be seen. It was found that the noise magnitude is 0.158 counts per voxel, which corresponds to a saturation of (8 ± 1) % or a water mass of 28 µg. This is in the order of 10 % of the saturation used in the calibration experiment (see scale in Figure 4.11).

4.3.5 Data Generation and Processing

3D data sets need a pre-processing to analyse the water distribution quantitatively. Water profiles across the thickness of the DM on the channel and on the land area, as well as water profiles in the DM along the channel are extracted from the 3D data sets. For general orientation, two 3D data sets are discussed. Two data sets of the fuel cell built

with PTFE-coated DM (SGL21AA), operated at 0.1 A/cm^2 and 0.8 A/cm^2 with air at a stoichiometry of four and hydrogen at a stoichiometry of two at 303 K and 270 kPa absolute are presented in Figure 4.13.

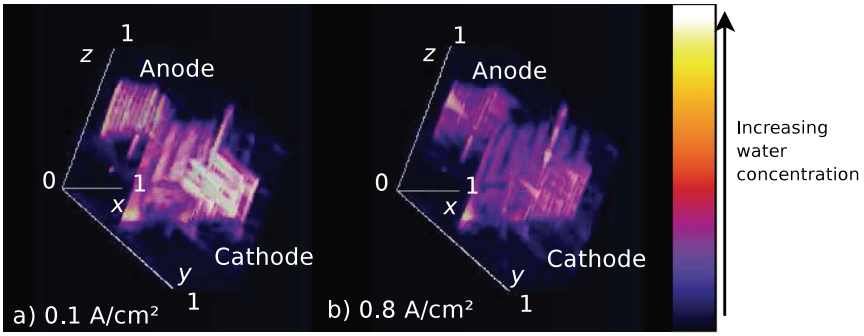

Figure 4.13: 3D tomography images of operating fuel cells a) at 0.1 A/cm^2 and b) 0.8 A/cm^2 with air at a stoichiometry of four and hydrogen at a stoichiometry of two at 303 K and 270 kPa absolute. The normal of the membrane plane is parallel to y and the channels run along the z-axis.

The x-axis in Figure 4.13 runs in the paper-plane, while z- and y-axis point to the background. The y-direction appears to be stretched due to the anisotropic resolution. The membrane is located in the x-z-plane at the half of the y-axis. The space, bounded by $0 \leq x \leq 1$, $0 \leq z \leq 1$ and $0 \leq y \leq 0.5$, represents the anode compartment with flow channels and DM. The cathode compartment is bounded by $0 \leq x \leq 1$, $0 \leq z \leq 1$ and $0.5 \leq y \leq 1$. It can be seen that image a) (0.1 A/cm^2) contains more water than image b) (0.8 A/cm^2).

The procedure to extract water profiles across the thickness of the DM on the channel and on the land area is illustrated in Figure 4.14. The procedure starts with averaging the intensity of the voxels in z-direction (in channel direction), represented by a 2D image. Thereby, the land and channel region can be isolated, and the average intensity of the voxels in the x-direction can be calculated. This reduces the information to 1D. Due to the coarse resolution in x-direction, the boundaries of the channels do not align with the boundaries between the pixels in one slice. For this reason, only five slices can be attributed clearly to contain only land or only channel information. The other slices contain both channel and land information and are abolished.

The isolated 1D layer again is transformed into a 2D intensity-y-position line plot, that allows for quantitative comparison between conditions and cell setups. This procedure is illustrated in Figure 4.14. Since the axes of the fuel cell do not necessarily align with the axes of the NMR instrument, the raw images might appear tilted and an angular correction for all three axes is necessary. The rotating procedure causes errors which result in edge-blurring since the pixel boundaries in the rotated frame intersect with the pixels of the original frame and averaging is required. The land cross sections show peaks at the outermost positions (lower-right graph in Figure 4.14); these result from blurring of the water filled channels and are artefacts.

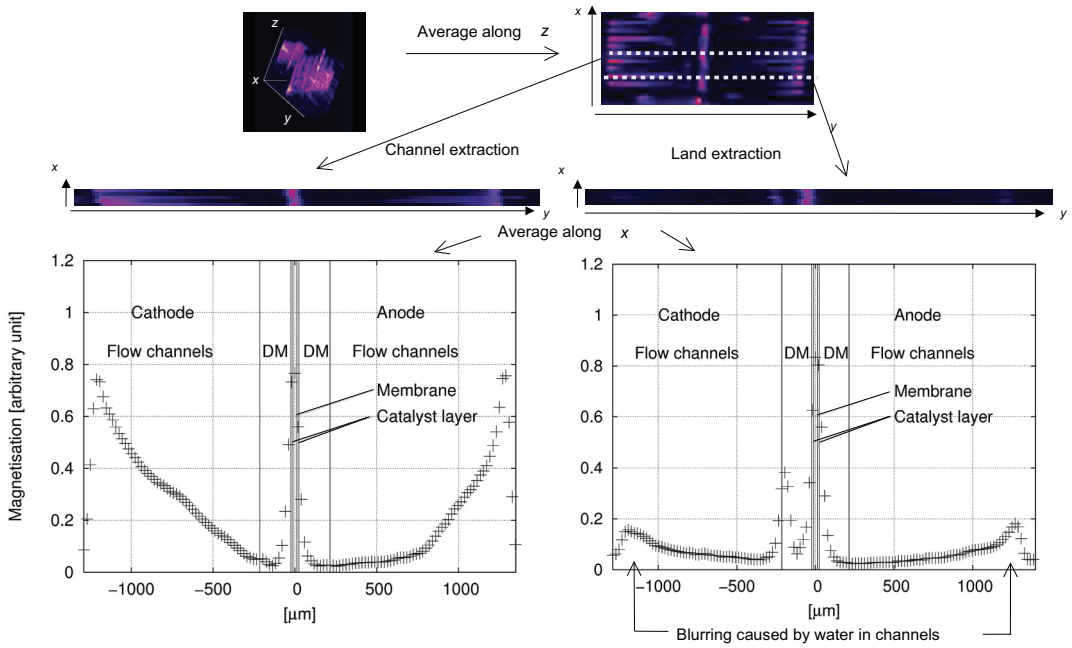

Figure 4.14: Transformation scheme of 3D image to 2D line plot (section in y-direction) for quantitative comparison.

A similar technique was used to extract the profile plots in the z-direction, illustrated in Figure 4.15. The z-direction contains information about the region where liquid water starts to accumulate relative to the inlets and outlet of the cells. In the channel region, the whole thickness of the DM was averaged in the x-direction. In the land area, a bi-modal water distribution along the y-direction was found and treated differently. The information of five voxels in the y-direction was averaged near the interface to the land, and five voxels near the membrane. This allows to study the water on top of the land independently from the water near the membrane.

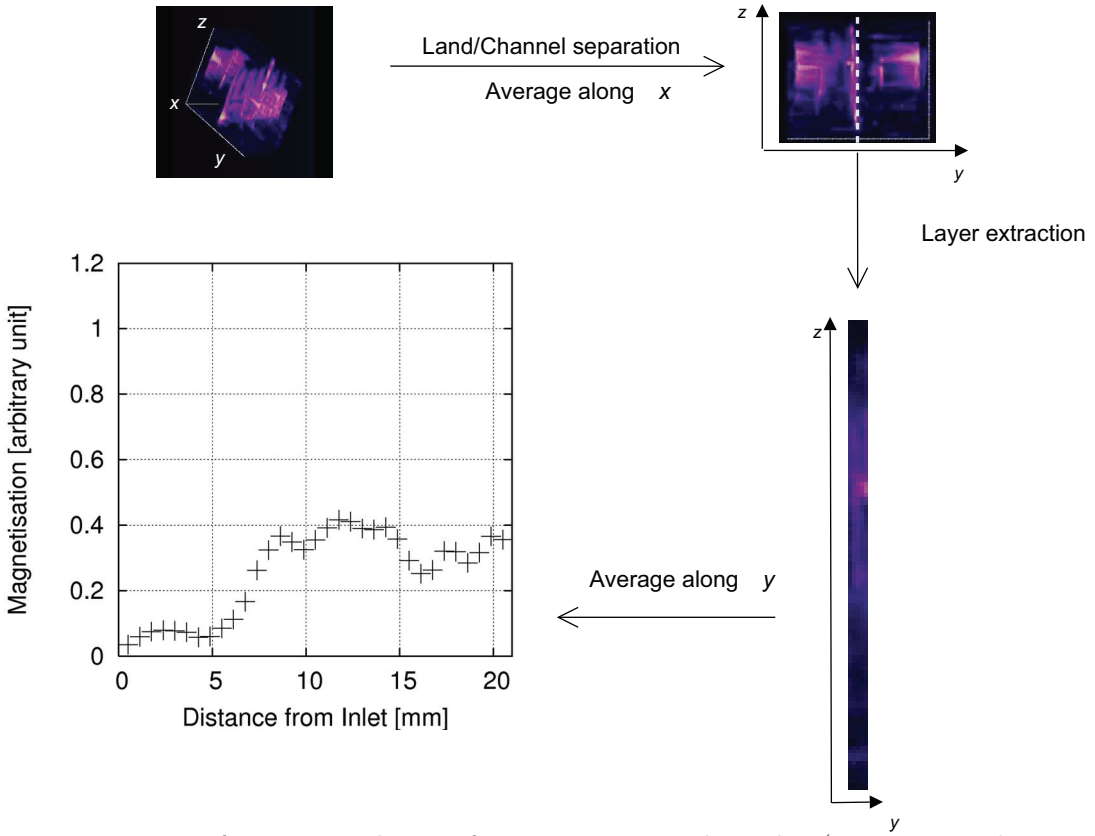

Figure 4.15: Transformation scheme of 3D image to 2D line plot (section in z-direction) for quantitative comparisons.

2D data sets had also been taken since the 3D tomography has the disadvantage of poor temporal resolution. The 2D data sets can be taken within 30 s to 60 s and allow to study dynamic effects with time constants in the order of minutes. The 2D images are projections of the x-y-plane and automatically summed up along the z-dimension during the data acquisition. For the dynamic effects, the change in water content is more of interest than the absolute amount, therefore, a picture of the average magnetisation distribution within the test time is calculated and then subtracted from the individual pictures to make the changes in water content visible. The change in magnetisation for the individual locations is compared with the normalised change in cell potential or current, depending on test condition. The normalisation of potential and current is done according to Equation 4.16, while ϖ is the respective temporal average over the test duration.

$$\varpi_{\mathrm{rel}}(t) = \frac{\varpi(t) - \bar{\varpi}}{\bar{\varpi}} \tag{4.16}$$

Since the domains of interest (flow channel, DM, membrane) are different in size, the contribution of noise is different. For each domain a reference noise level for corresponding domain sizes from image regions without water is calculated and plotted with the other data for comparison. This procedure is illustrated in Figure 4.16 (a detailed discussion of the plot in this figure is given in Section 4.4.3 on page 157ff.). The noise intensity is about ± 5 % in the example, while the temporal signal fluctuation is about ± 20 %. The noise level is important to decide whether a dynamic signal change is significant or not.

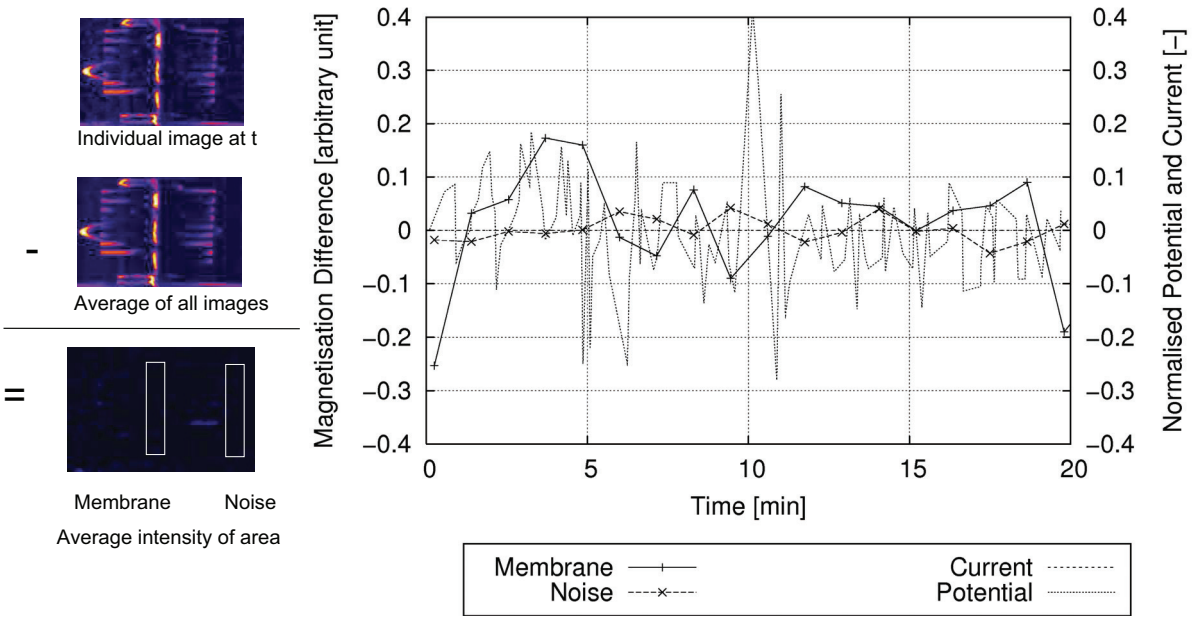

Figure 4.16: Transformation scheme of 2D images to a line plot for comparing dynamic response of local magnetisation to relative changes in current and voltage (for detailed discussion see Section 4.4.3 on page 157ff.).

4.3.6 Samples and Operating Conditions

As explained previously (Section 4.3.1 on page 120ff. and Section 4.3.3 on page 125ff.), the sample selection is constraint by the shielding and the temperature-dependent signal loss. Since this effect depends upon the pore size in the DM, only DM with large pores

are suitable for NMR saturation studies. SGL21AA was chosen as the baseline material since it allows the observation of liquid water inside its structure despite all the constraints previously mentioned. Following material combinations are tested:

- SGL21AA plain on anode and cathode
- SGL21AA with 10 % wt. PTFE on anode and cathode
- SGL21AA with 10 % wt. PTFE on anode and SGL21AA with 10 % wt. PTFE plus Gore Carbel Z30® on cathode

The fuel cell is tested in operation at four different operating conditions. The choice of these test points is done in order to cover low-power as well as high-power conditions. All tests are done at a cell temperature of 303 K with dry air and hydrogen in co-flow at a pressure of 270 kPa at the inlet. The stoichiometries on the cathode vary between four and eight. The anode is fed with a stoichiometry of two. The reason for the high stoichiometries is the removal of the significant amount of liquid water in the channels caused by the low operating temperature (a detailed discussion follows on page 142ff.). The anode stoichiometry is difficult to control and varies significantly from the point of design at the low-current test point. The test points (TP) for the four operating conditions are shown in Table 4.2.

Table 4.2: Fuel Cell Test Points

Test Point	Current Density [A/cm^2]	Stoichiometry Hydrogen	Stoichiometry Air
1	0.1	2	4
2	0.8	2	4
3	0.8	2	8
4	1.4	2	8

The data acquisition time for one complete 3D scan is 2 hours with the stated resolution. To exclude any transient start-up effects from the 3D scanning, the test conditions are applied for 20 minutes before the 3D scan is initiated. Following on the 3D scan a series of 2D images is taken in order to study slow dynamic behaviour.

Since the cell body is made of PTFE with low thermal conductivity, the temperature at the DM can be higher than the coolant temperature. This depends strongly on the current density and influences the quantitative measurement of the water saturation. In order to

address this point, the cell was equipped with a thermocouple on the land area in contact with the DM after the NMR tests were finished. The introduction of the thermocouple during the NMR experiments would have increased the amount of conducting material in the system and was omitted to avoid further disturbance. TP 1 to TP 4 are tested with this cell modification outside the NMR spectrometer. To explore the largest temperature deviations from the set point, the cell setup with the largest thermal resistance is tested. The DM in this case is SGL21AA with 10 %wt. PTFE on anode and cathode and a Carbel® layer only at the cathode side. The cell with the Carbel® layer at the cathode side performs fairly at TP 1, but at TP 2 the cell runs in limiting current mode. At TP 3 the performance is fair again. Under condition TP 4 the cell performs extremely well. The temperatures of the cathode DM/current collector interface is elevated. Potential, current density and stoichiometries are plotted in the upper part of Figure 4.17 and the measured temperatures are shown in the lower part.

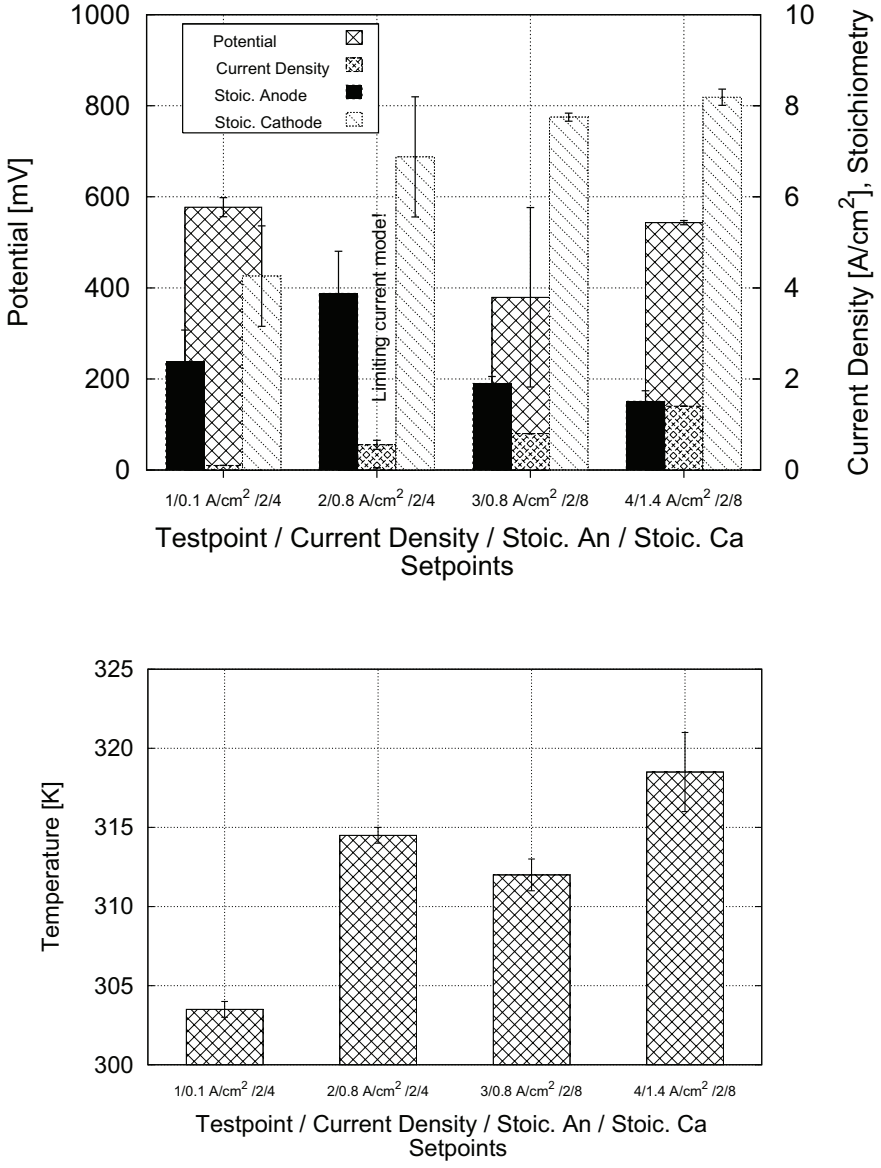

Figure 4.17: Fuel cell performance (top) and temperature at the cathode DM-current collector interface (bottom) at TP 1 to TP 4. Conditions: Coolant temperature: 303 K; Cathode DM: SGL21AA 10 % wt. PTFE & Carbel® layer on cathode; Anode DM: SGL21AA 10 % wt. PTFE; Membrane: Gore 5510.

The temperature at the DM is highest under condition of TP 4 (1.4 A/cm^2) at around 316 K to 321 K and lowest under condition of TP 1 (0.1 A/cm^2) with 303 K to 304 K. At test conditions TP 2 and TP 3 temperatures of 314 K to 315 K and 311 K to 313 K are measured respectively. This impacts the quantitative statements since the signal intensity is a function of temperature, and the calibration is done for 303 K. Strictly speaking, the quantitative statements hold true only under condition TP 1. For the other test points the saturation might be higher than indicated. At the membrane or catalyst layer, the temperature is even higher and the humidity reduced, but at these layers no measurement was done and the further analysis is based on the measured temperatures.

To show the influence of operating temperature and stoichiometry on the relative humidity (RH) in the channel, a simple sensitivity test was done. Following assumptions enter into the model:

Table 4.3: Model parameters for RH sensitivity

Property		Value	Unit
Pressures	Air in	270	kPa
	H_2 in	270	kPa
	Outlet	250	kPa
Temperatures	Air Dew Point in	293	K
	H_2 Dew Point in	293	K
	Channel	303 to 323	K
Stoichiometry	Anode	2	-
	Cathode	4 to 8	-

The RH calculation is based on the assumption that anode and cathode outlet streams are mixed, any differences between anode and cathode are homogenised mathematically by averaging (further details of the model can be found in Appendix E on page 187ff.). For TP 1 the cell is about eight times over-saturated (8 to 8.4), related to 100 % saturation at outlet conditions. Due to the higher temperatures under the condition of TP 2, the humidity is half of the expected at 303 K, but still over-saturated (4.5 to 4.7 times). The doubling of the cathode stoichiometry reduces RH down to 2.3 to 2.5 times. The condition of TP 4 (cathode stoichiometry of 8 at 1.4 A/cm^2) is the driest, but also over-saturated (1.5 to 2 times) as depicted in Figure 4.18.

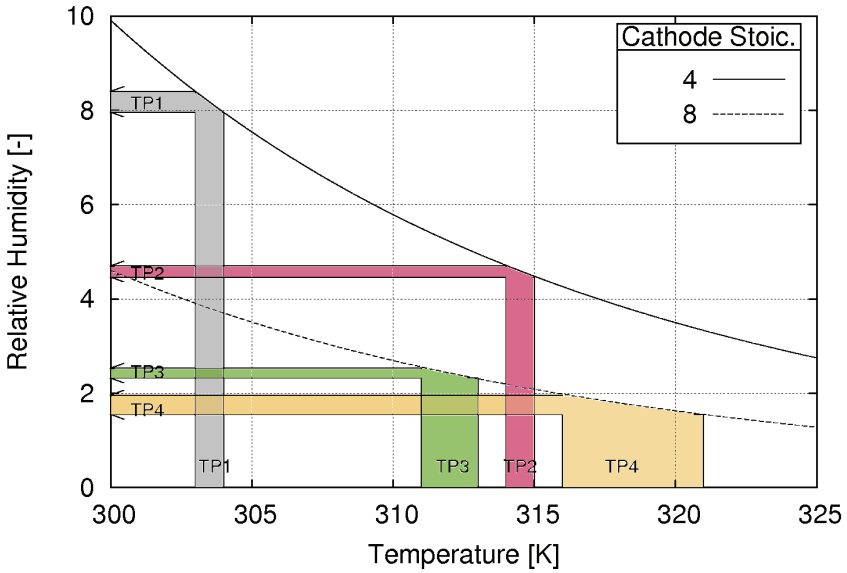

Figure 4.18: Calculated relative humidity (average) in the outlet streams of the fuel cell. The temperature and humidity range for the test points are indicated. RH of '1' indicates saturated conditions.

To relate the relative signal intensity to the change in temperature, the pore radii of the DM have to be known. Since the measured pore radii depend upon the specific measurement techniques, it is not possible to use the number from mercury porosimetry or any other method directly as a quantitative value. The only way to find the right value would be an NMR experiment with different spin echo times to get the limiting diffusion length $<l>$ at constant temperature, as suggested by [LD86]. Since this experiment was not done, two extreme values for the pore radii (5 µm and 10 µm) are used in this evaluation. The details of estimating the temperature effect can be found in Section 4.3.3 on page 125ff. Figure 4.19 illustrates the results graphically. For TP 1 the signal loss is 3 % if a pore radius of 5 µm is assumed, therefore, at TP 1 the effect is only minor. Due to the high temperature at TP 2, the loss is around 9 % for 10 µm pore radius and 25 % for 5 µm radius. TP 3 has a calculated loss of 7 % for 10 µm pore radius and 20 % for 5 µm radius. Even in the 5 µm case, the relative difference between TP 2 and TP 3 is only 7 %. Since TP 4 is the hottest, the losses are between 10 % for 10 µm and 35 % for 5 µm radius. The assumption of a 10 µm radius is conservative, based on the pore size distribution of common DM [MRFL03], thus, the signal loss might be in the order of

15 % at the maximum. The measured temperature-dependent signal decay presented in Section 4.3.3, Figure 4.9 on page 129 suggests a pore radius around 7 µm.

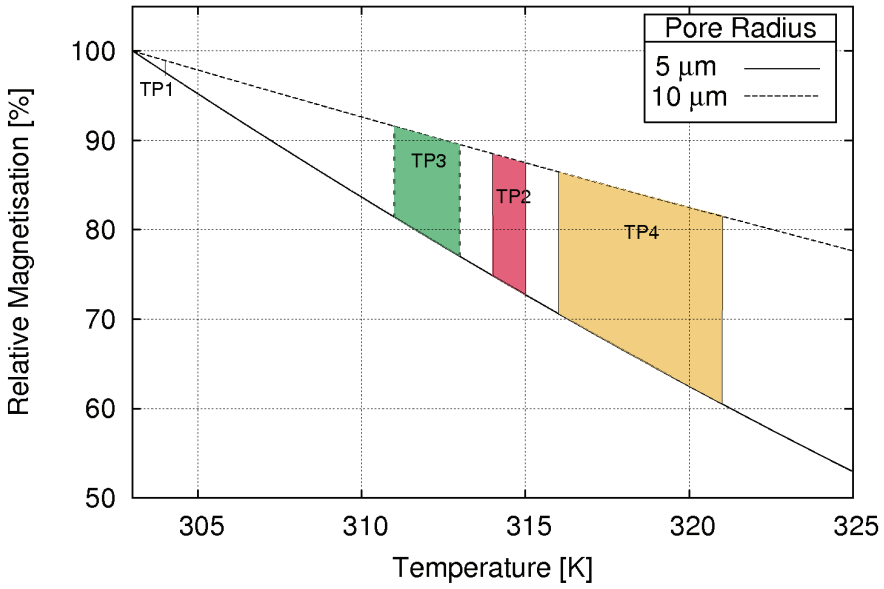

Figure 4.19: Relative magnetisation for TP 1 to TP 4 related to the calibration temperature (303 K).

With that, the theoretic discussion on the fundamental constraints will be concluded. In the next section experimental findings on the operating fuel cell under NMR visualisation will be presented.

4.4 Experimental Results of Fuel Cell NMR Imaging

4.4.1 Effects of Operating Conditions

In this section, the different test points and cell configurations will be discussed in the light of the magnetisation originated by protons, measured by NMR. The performance of this cell configuration was decent under all operating conditions. Potential, current density, and stoichiometric average of two hours of operation are plotted in Figure 4.20.

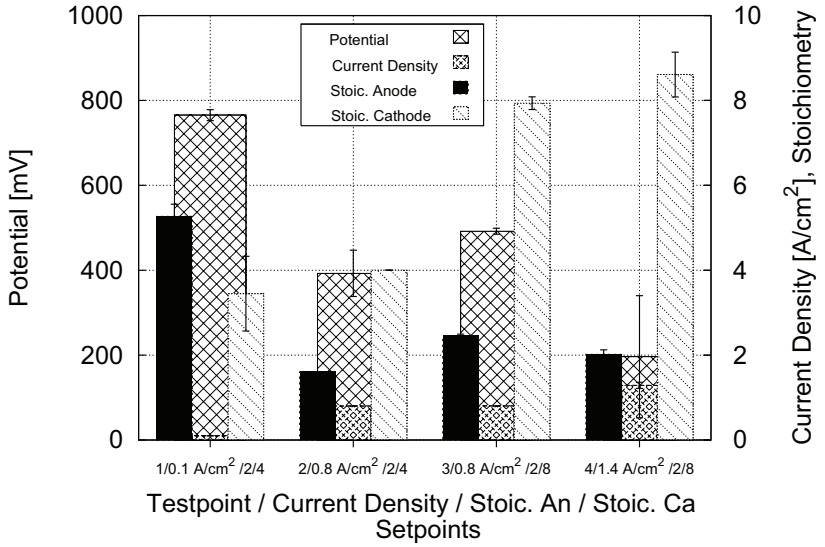

Figure 4.20: Fuel cell performance at TP 1 to TP 4. Conditions: Cathode DM: PTFE-treated DM SGL21AA (10 % wt.); Coolant temperature: 303 K; DM: PTFE-treated SGL21AA; Membrane: Gore 5510.

The cell potential stabilises and increases when the cathode stoichiometry at 0.8 A/cm^2 is increased from 4 to 8. The potential level is low and fluctuation is large at TP 4. This indicates a severe limitation and the additional information from the NMR experiment may help to shade light on the mechanisms.

The correlation with saturation is not done in this context due to the fact that the calibration is influenced by the actual temperature in the DM. Here, the total proton signal from the cell is in focus, including the membrane where no calibration is available. The proton signal of all voxels within the active DM and MEA volume are averaged for each test point and compared against the current density of the cells with various

configurations. Figure 4.21 shows the average proton signal intensity in an arbitrary unit versus the current density. The lines represent the original data, while the shaded areas indicate the range of temperature-corrected magnetisation. The correction is based on the estimations shown in Figure 4.19 on page 144. In order to demonstrate the general trends, the three different modifications (plain, PTFE-treated and with MPL) are shown. The focus is on the cell with the PTFE-treated cathode DM only in the further part.

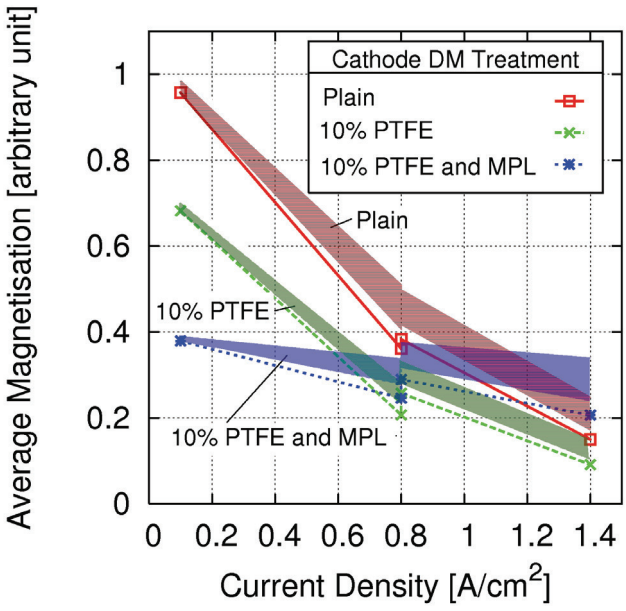

Figure 4.21: Average magnetisation of the whole cell in arbitrary unit versus the current density for the different cell configurations and the conditions TP 1 to TP 4 (see Section 4.2 on page 139). The shaded areas indicate the range of temperature-corrected magnetisation. Conditions: Cell temperature: 303 K – 323 K; DM: SGL21AA, DM treatment at anode: PTFE-coated; At cathode: see legend; Membrane: Gore 5510.

Three observations can be made:

- The average magnetisation decreases with increasing current.
- The average magnetisation decreases from plain to PTFE-treated to MPL configuration.
- The two test points at 0.8 A/cm^2 differ in water content in all three configurations.

The decrease of the magnetisation with increasing current is either an experimental

artefact or a real effect of the water transport. The two possibilities will be discussed here. The magnetisation might be sensitive to the current production and to the temperature in the fuel cell. The temperature also effects the balance between water in liquid and in vapour phase, as already discussed on page 142.

The temperature in the active area increases due to the increased power and the decreased efficiency. The observed magnetisation loss between TP 1 (0.1 A/cm^2) and TP 2 (0.8 A/cm^2) is more than 50 %, while the estimated signal loss due to temperature elevation is in the order of 20 % (see Figure 4.9 on page 129).

Under ideal circumstances, the relative humidity at TP 1 and TP 2 is equal since the stoichiometry is constant (proportional increased gas flow at higher current density). At TP 1 condition the water flux is sufficient to saturate the gas stream 8 times. The molar water flux in liquid phase is 11-fold the molar water flux in the gas phase. Under TP 2 conditions this ratio becomes 6 due to the increased temperature (the vapour pressure is doubled). Though, the current density at TP 2 is 8 times the current density of TP 1, thus the total water flux at TP 2 is 8 times the total water flux at TP 1. If the ratio liquid-to-vapour is considered, the molar liquid water flux is about 4 times higher at TP 2 compared to TP 1.

The magnetisation is a measure of average liquid water saturation rather than of liquid water flux. Therefore, it seems that either the magnetisation intensity is strongly influenced by the electrical current, or the average saturation decreases because the water transport becomes more effective under the conditions of TP 2.

The increase in proton signal intensity between cathode stoichiometry of four and eight (TP 2 and TP 3) is small, but against the expected trend. Theoretically, the channel RH at stoichiometry of eight at TP 3 is half of the RH at TP 2 (stoichiometry of four) but still over-saturated by a factor of two. The temperatures at TP 2 and TP 3 might be key to this question. The temperature at TP 2 is higher than at TP 3, the magnetisation is likely to be reduced due to the increased signal decay at TP 2 (see Section 4.3.6 on page 142ff.). This reduction is in the order of 5 % to 20 % (based on the signal of TP 3) which is sufficient to explain this finding. The cell configuration with the plain material supports this hypothesis since the temperature correction for the magnetisation reverses the trend (see the area labelled with 'Plain' (red) in Figure 4.21). Thus, the differences in

magnetisation between stoichiometry two and four at TP 2 and TP 3 are likely to be an experimental artefact.

To shed more light on that topic, the differences in local magnetisation between the two stoichiometries and current densities are explored in detail on the example of the cell configuration with SGL21AA DM with a PTFE loading of 10 % by weight. By comparing the spatial details of the magnetisation magnitude, it is found that the magnetisation inside the flow channels and the DM/membrane decreases with increasing current densities at all locations as depicted in Figure 4.22 (for details of the data processing and cross sections Figure 4.14 on page 136 is referred). At 0.1 A/cm^2 the cathode flow channels show a large magnetisation, indicating a large water volume even at the channel DM interface. The channel proton signal at 0.8 A/cm^2 for stoichiometry of four and eight appear almost identical. Here, differences in the magnetisation at the membrane area are observed. At 1.4 A/cm^2 the flow channels appear completely dry.

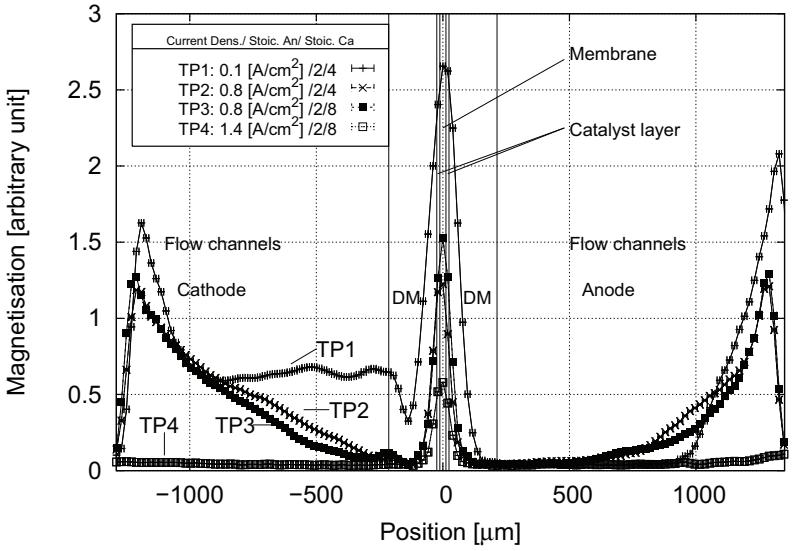

Figure 4.22: In-situ magnetisation magnitude in arbitrary unit along the y-axis at TP 1 to TP 4 in channel only. Conditions: see Figure 4.20; Current density and stoichiometries see legend. Details of the data processing and cross sections can be found in Figure 4.14, page 136.

By focusing on the DM/membrane section more details can be found. This analysis differentiates between channel and land area. The magnetisation in DM and membrane,

facing the flow channels, is depicted on the left side of Figure 4.23. The right side shows the magnetisation parallel to the flow. The x-axis error bars are based on a pixel size of ± 10 µm. The saturation is not calculated for the following plots since the calibration holds only true for test condition TP 1 at small current densities and low temperature (more details on this test at TP 1 can be found in Section 4.4.2 on page 152ff.). The cross section perpendicular to the flow at 0.1 A/cm^2 (left plot in Figure 4.23) revealed that the membrane and the cathode DM have a large magnetisation magnitude, indicating a high water saturation. The DM shows a minimum magnetisation, 150 µm away from the membrane, while at increased current densities the DM magnetisation falls down to noise level within the first 80 µm. This applies also to the anode side. The increase in cathode stoichiometry at 0.8 A/cm^2 affects more the magnetisation in the membrane than in the cathode DM. The lowest magnetisation and, thus, the driest membrane is observed at 1.4 A/cm^2.

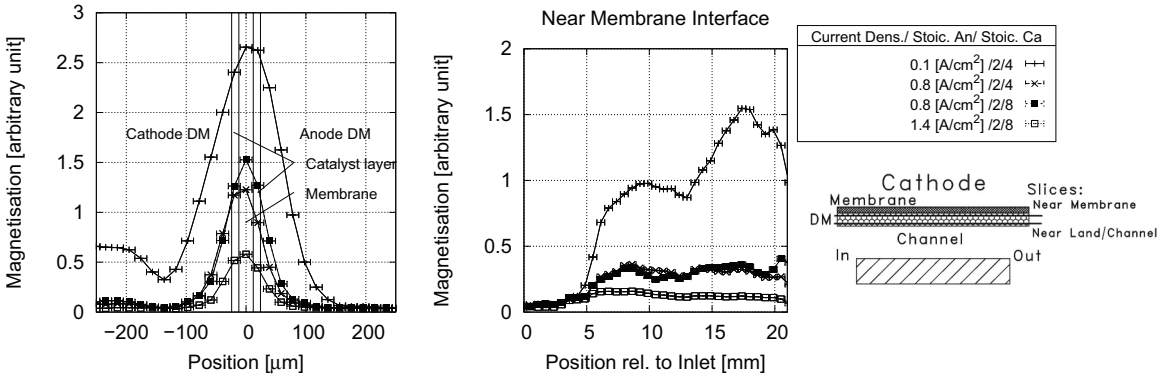

Figure 4.23: Integrated in-situ magnetisation magnitude along the y-axis perpendicular to the flow, focusing on the DM/membrane location facing the channel (left) and in the cathode DM on top of the channels along the z-axis, parallel to the flow (right), at TP 1 to TP 4. The error bars (± 10 µm) are based on one pixel size. Conditions: see Figure 4.20; Current density and stoichiometries see legend. Details of the data processing and cross sections can be found in Figure 4.14 and Figure 4.15 on pages 136 and 137.

Parallel to the flow channel (inlet is at position 0 mm) in the z-direction (see right side in Figure 4.23), a strong magnetisation increase in the cathode DM near the outlet from 40 % to 70 % is found for the low current density case. The stoichiometry increase from four to eight at 0.8 A/cm^2 does not influence the magnetisation along the flow channels.

In all three cases a stable magnetisation level is reached 8 mm from the inlet. In the 1.4 A/cm^2 case the magnetisation is close to noise level.

The integrated magnetisation along the y-axis in the DM/membrane region on top of the land area, perpendicular to the flow, is shown in the upper plot of Figure 4.24. A similar situation as in the flow channels is found above the land region. At 0.1 A/cm^2 the DM and the membrane has the highest magnetisation, while the magnetisation in general decreases as the current density increases. It is to notice that the DM on top of the land shows a large magnetisation, indicating a large amount of water in all cases except for the 1.4 A/cm^2 case. The magnetisation in the cathode DM is high near the land area and the membrane but low in the centre. Especially the centre part of the DM has an extremely low magnetisation at 0.8 A/cm^2 condition. The region with low magnetisation in the centre expands and the height of the magnetisation peak at the interfaces increases as the stoichiometry increases from 4 to 8. The lowest magnetisation is, again, found at 1.4 A/cm^2. The magnetisation parallel to the flow on top of the land on the cathode side near the land is depicted in the lower-left graph in Figure 4.24 and near the membrane in the lower-right graph in Figure 4.24.

The magnetisation at the cathode DM near the land increases slower than near the membrane. At 0.1 A/cm^2 the magnetisation near the land reaches a plateau 13 mm behind the inlet, while the magnetisation near the membrane keeps increasing towards the outlet. At 0.8 A/cm^2 a stoichiometry sensitivity is observed at the membrane interface, while the land interface is less sensitive. The magnetisation in the land area stays low at 1.4 A/cm^2, probably due to temperature effects.

The detailed analysis of the origin of magnetisation reveals that the major difference between the two current densities 0.1 A/cm^2 and 0.8 A/cm^2 is caused by the magnetisation in the cathode flow channel. A high channel water content at TP 1 causes also a high saturation in the cathode DM.

At 0.8 A/cm^2 and cathode stoichiometry of eight, a reproducible increase in magnetisation is found compared to the cathode stoichiometry of four (TP 2 vs. TP 3). The origin of the difference is localised around the membrane plane. Only temperature or gas-water interaction in the flow field can provoke this effect as discussed previously on page 148.

At 1.4 A/cm^2 the water content in flow channels, averaged over two hours, stays below

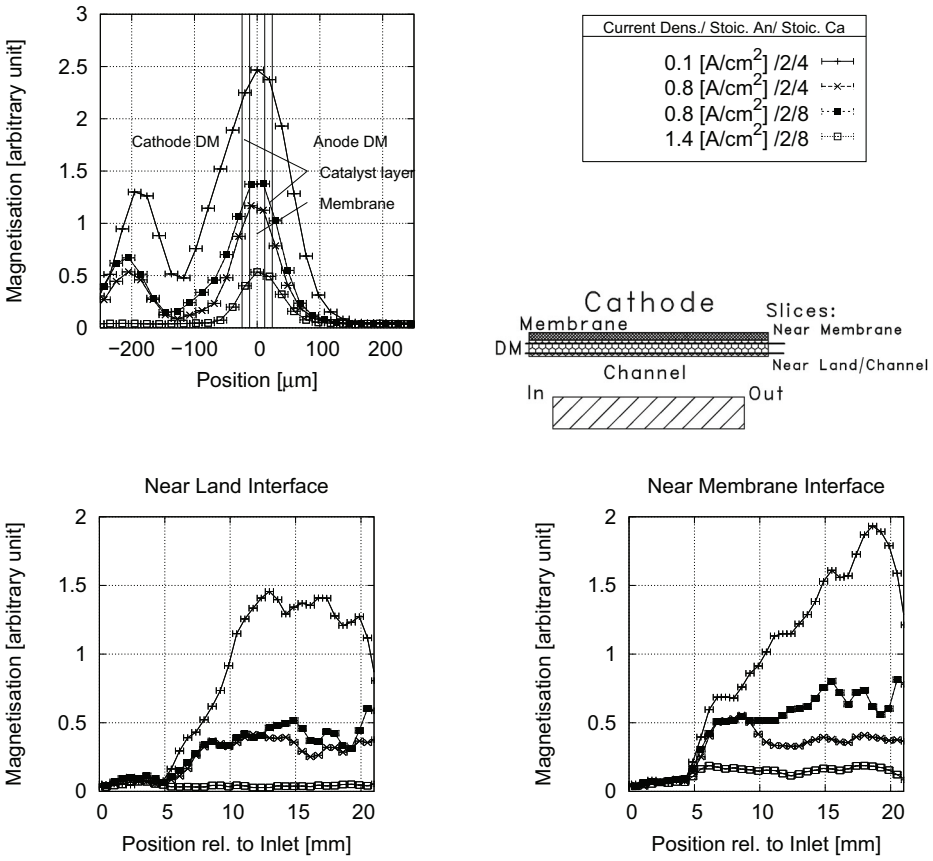

Figure 4.24: Magnetisation magnitude on top of the lands in the cathode DM (y-axis) perpendicular to the flow (upper graph), parallel to the flow channels (z-axis) on top of the land, near to the land (lower left graph) and near the membrane (lower right graph) at TP 1 to TP 4. The inlet is at position 0 mm. Conditions: see Figure 4.20. Details of the data processing and cross sections can be found in Figure 4.14 and Figure 4.15 on pages 136 and 137.

the detection limit of NMR, so does the concentration in the DM. The increased gas shear in combination with the increased temperature is probably the root cause for the relatively dry conditions.

Further, it is found that the magnetisation in the cathode DM has two maxima of water saturation near the interfaces of the DM with the land and with the catalyst layer. In all cases where liquid water is found in the DM, the water distribution in the DM is not uniform. The temporal average saturation over 2 hours at the DM/membrane interface is high and decreases towards the centre of the DM. In most of the tested cases, the magnetisation drops below the detection limit and increases at the DM/land or DM/filled

channel interface. Hickner et al. [HSC+08] explored the water management by means of 2D neutron radiography. They observed similar trends with regard to water concentration in the cathode DM at low and high current densities at an operating temperature of 343 K (60 °C). They also found a similar bi-modal water distribution pattern across the DM (high saturation towards the flow field and the membrane, but low in the centre). The 2D synchrotron experiments done by Hartnig et al. [HMK+08], focusing on through-plane visualisation, also confirm such a pattern. In summary, the trends of saturation in dependence of location, measured by NMR, appear to be realistic. Yet, the quantification of saturation is not very accurate if the magnetic field is distorted by electric currents and strongly influenced by the local temperature. Thus, the measurement temperature needs to be the same as the temperature during the calibration in order to get quantitatively reliable results.

4.4.2 Effects of Diffusion Media Treatment

Fuel cells with different cathode DM configurations will be compared in this section. It was found in the previous section that the magnetisation decreases with increasing current, either due to real drying or disturbance of the magnetisation signal caused by magnetic fields, created by the produced current at higher current densities. In consequence of this finding, the effect of DM configuration on liquid water handling is discussed under the condition of TP 1 where the current is low and the temperature stays low, too. This has the advantage that the calibration can be applied and semi-quantitative statements are possible. TP 1 is characterised by a current density of 0.1 A/cm^2 and moderate stoichiometries of 2 at the anode and 4 at the cathode. The large errors of the anode stoichiometry are caused by the difficulties to control the small flow rates. But since the anode reaction is much more robust due to better kinetics and the diffusion of hydrogen is fast, this can be tolerated. The cathode stoichiometry is easier to control due to larger flow rates. At a current density of 0.1 A/cm^2 the cells have a potential between 580 mV and 760 mV. The poorest performance is shown by the cell with the MPL attached to the cathode DM (see Figure 4.25). The error bars represent one standard deviation calculated from data taken at intervals of 1 min during the imaging process of 120 minutes.

The average magnetisation inside the fuel cell reveals significant differences in the flow

channels within the 120 minutes of testing. Figure 4.26 shows the magnetisation along the y-axis of the fuel cell (perpendicular to the flow channels). The magnetisation is not converted into saturation since the calibration is not valid for the flow channels and the membrane (see Section 4.3.4 on page 131).

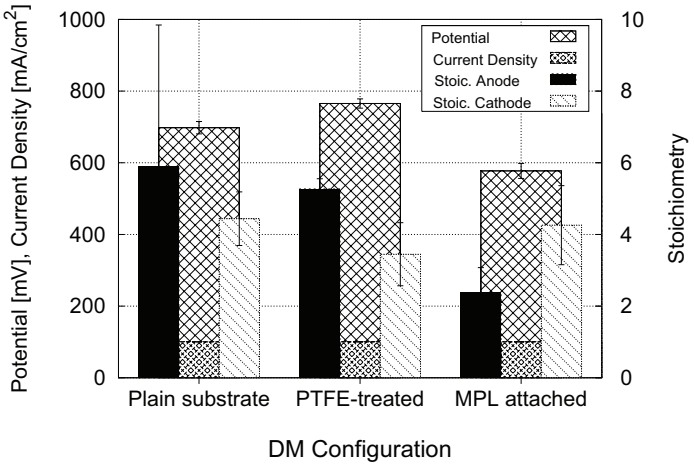

Figure 4.25: Fuel cell performance data with different DM configurations at low-power conditions (TP 1). Conditions: Coolant temperature: 303 K; Anode DM: PTFE-treated SGL21AA; Membrane: Gore 5510.

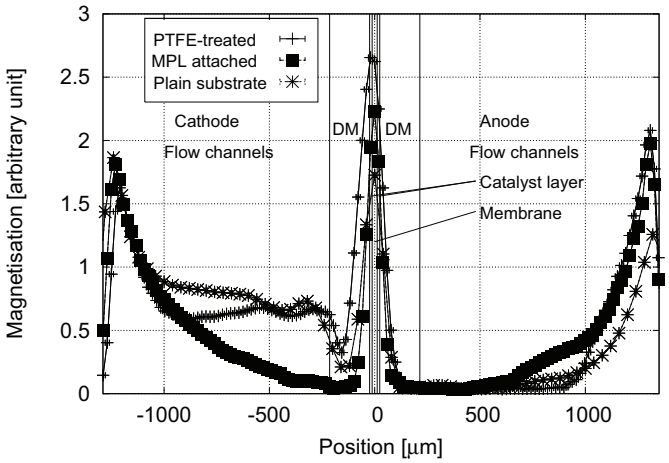

Figure 4.26: Magnetisation along the y-axis on the channel section at TP 1 for different fuel cell configurations (see legend). Conditions: see Figure 4.25. Details of the data processing and cross sections can be found in Figure 4.14, page 136.

The centre part (DM/membrane section) of the cells in the channel area is represented on the left plot in Figure 4.27 and the one of the land area (on the right). The different magnetisation of the membrane is noticeable.

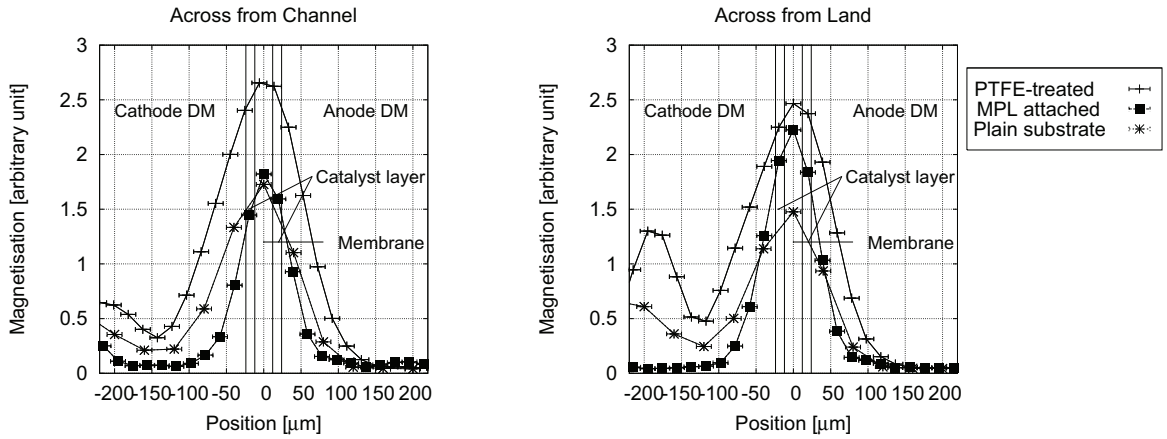

Figure 4.27: Magnetisation along the y-axis perpendicular to the flow, focusing on the DM/membrane location facing the channel (left) and the land (right) at TP 1. The error bars (± 10 µm) are based on one pixel size. Conditions: see Figure 4.25. Details of the data processing and cross sections can be found in Figure 4.14, page 136.

Since the anode side does not hold liquid water and the saturation calibration is not valid for the membrane, the focus is set on the cathode DM in Figure 4.28. The saturation is calculated from the calibration (see Section 4.3.4 on page 131) and shall be used for orientation purposes only.

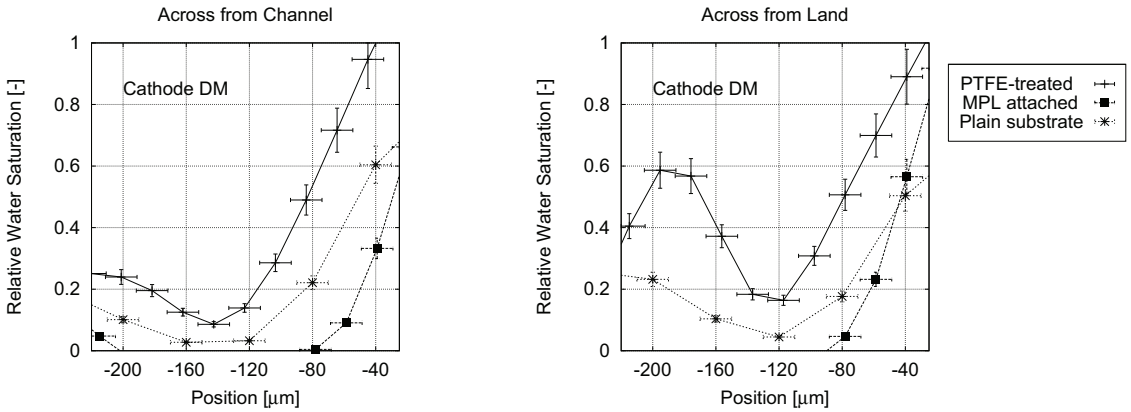

Figure 4.28: In-situ saturation along the y-axis perpendicular to the flow, focusing on the cathode DM location facing the channel (left) and the land (right) at TP 1. The error bars (± 10 µm) are based on one pixel size. Conditions: see Figure 4.25. Details of the data processing and cross sections can be found in Figure 4.14, page 136.

The three tested cell configurations have in common that the proton signal intensity is extremely low on the anode side, indicating that the vast amount of liquid water is handled by the cathode side. This supports the assumption that the variation in the anode stoichiometries for the different tests can be tolerated.

The local proton signals on the cathode side, taken from the cell configuration with MPL, differs significantly form the plain and the PTFE-treated configuration. This cell appears to be dry, only the membrane shows high proton intensity (see Figures 4.26 and 4.27). In fact, the magnetisation in the centre of the cell configuration with the MPL (location of the membrane) shows a different trend than the other configurations (higher magnetisation across from the channel). The magnetisation magnitude across from the flow channels is similar to the configuration with the plain substrate, while across from the land, the magnetisation increases and becomes similar to the PTFE-coated configuration. The performance of the configuration with MPL is the poorest of the three tested cells. This leads to the hypothesis that the water transport mechanism is different from the configurations without MPL. This is probably due to the different thermal conditions induced by the thermal resistance of the MPL.

The fuel cell configurations with the plain material and the PTFE-treated material have in common that there is a proton signal accounted to the cathode flow field, indicating liquid water in the gas channels near the DM surface (see Figures 4.26), the intensities differ only slightly. Another commonality of the configurations with plain and PTFE-treated cathode DM is the signal distribution accounted to the cathode DM. There is a strong signal near the membrane, as well near the interface between flow field and cathode DM. The centre section of the cathode DM shows a local signal minimum (see Figure 4.28). Yet, the intensities differs between the two configurations. The PTFE-treated DM accumulates more liquid water under the land than the plain DM. The trend of magnetisation magnitude between land and channel area in the membrane is similar in cases of the PTFE-treated and MPL layered DM, but, the configuration with PTFE-treated DM shows a stronger membrane signal.

The differences between the plain and the PTFE-treated configuration are significant with respect to the potential ($\Delta U = 68$ mV). The PTFE-treated cell seems to hold the most liquid water especially in the land area and performs best, even in the situation that the

cathode stoichiometry was the lowest in this series of tests (see Figure 4.25). This implies that the lower performance of the cell with the plain configuration and the one with the MPL is unlikely to be caused by mass transport limitation in the channel or the DM. But, since this test is done at low current density, the reaction transfer kinetics (Butler-Volmer) seems to be affected. In the next section (see 4.4.3, page 156ff.) further evidence for a performance-limiting mechanism in the membrane-catalyst layer region will be presented.

4.4.3 Dynamic Phenomena

Low-Frequent Voltage Oscillations are observed during the testing for some cell configurations. This is explored by 2D images with a temporal resolution of 1 min. The 2D images resolve the x-y-plane of the cell with the spatial resolution 313 µm/pix times 20 µm/pix, while the signal of the z-direction is integrated over the whole length. To remind of the orientation, the lower part of Figure 4.2 on page 116 is referred. The cell, built with the MPL on the cathode side, shows various instabilities at 0.1 A/cm^2 and at 0.8 A/cm^2 at high cathode stoichiometry (TP 1 and TP 3).

At the lowest current density the voltage drops from 700 mV to 500 mV after 2 min. from starting the 2D testing and stays low for the rest of the testing. The previous 2 hours of the test, the cell had performed at a voltage level of 600 mV – 700 mV with a low-frequent instability pattern (alternation periods in the order of 1/2 hrs). A comparison with the proton signals in all compartments, like the anode and cathode flow fields, the two DM, and the membrane is made. The only obvious temporal agreement between the potential drop and change in magnetisation is found for the proton signal in the membrane. In Figure 4.29, left, the relative changes over time for magnetisation of the cell with MPL at membrane level at TP 1 and normalised average voltage and current is shown (details on the normalisation and general data processing are given in Section 4.3.5 on page 138). Further, the noise level is shown for comparison to give an impression of the magnitude of statistical signal scatter in the tested area. The qualitative change of the proton signal between min. 2 and 3 is represented on the right images in Figure 4.29. To allow better orientation, the channel layout is superimposed on the images.

The voltage drop is not caused by mass transport limitations in channels or DM since only the signal from the membrane-catalyst area changes simultaneously to the voltage

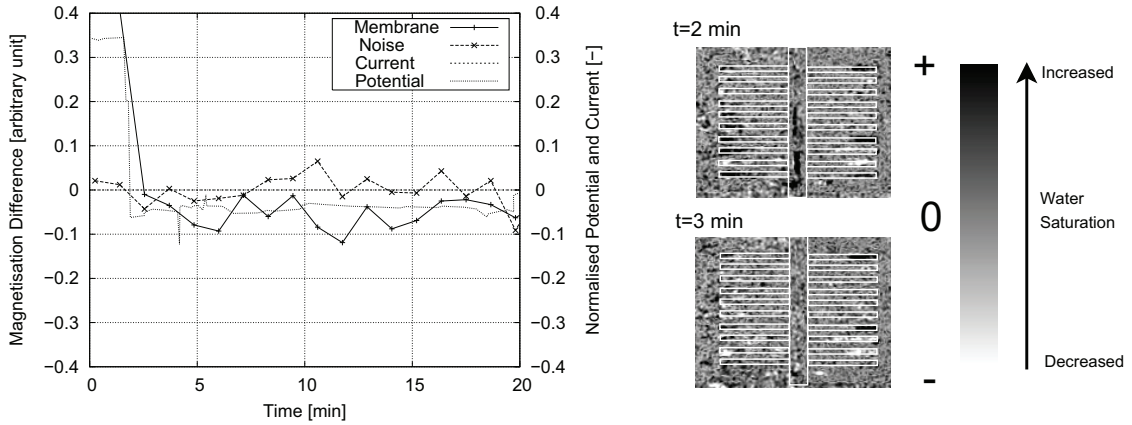

Figure 4.29: Left: Relative change over time of average voltage, current, and magnetisation of the cell with MPL at membrane level at TP 1. Right: 2D differential images of cell with MPL at TP 1 at $t = 2$ min and at $t = 3$ min. The images show the differences in proton signal from the average image calculated from 20 images over the test period. The superimposed lines represent the layout of the flow channels and the DM/membrane area. Conditions: Coolant temperature: 303 K; DM: PTFE-treated SGL21AA; Membrane: Gore 5510.

signal. The spontaneous dry-out of the membrane is a direct result of the thermal conditions, set by the heat generation at the catalyst layer. This assumption is supported by the 3D result.

High-frequent voltage oscillations are observed at a current density of 0.8 A/cm^2 and high stoichiometries (TP 3) for the cell with the MPL. Not a sudden drop as described previously, but an oscillation with a period in the order of 30 seconds. The NMR 2D analysis reveals a similar oscillation of the magnetisation in the membrane (upper plot in Figure 4.30) and some fluctuations of the magnetisation in the cathode DM (lower plot in Figure 4.30). The conclusions to be drawn in this case are limited by the temporal resolution of the 2D imaging. The oscillating frequency of the voltage is too high to allow for unequivocal statements based only on the frequency. The fluctuation magnitude of the magnetisation in the cathode DM and the membrane is large compared to the fluctuation in the noise. This indicates that the humidification state and the water saturation in the cathode DM is related to the voltage oscillation. The other locations in the cell have a magnetisation variation at noise level only.

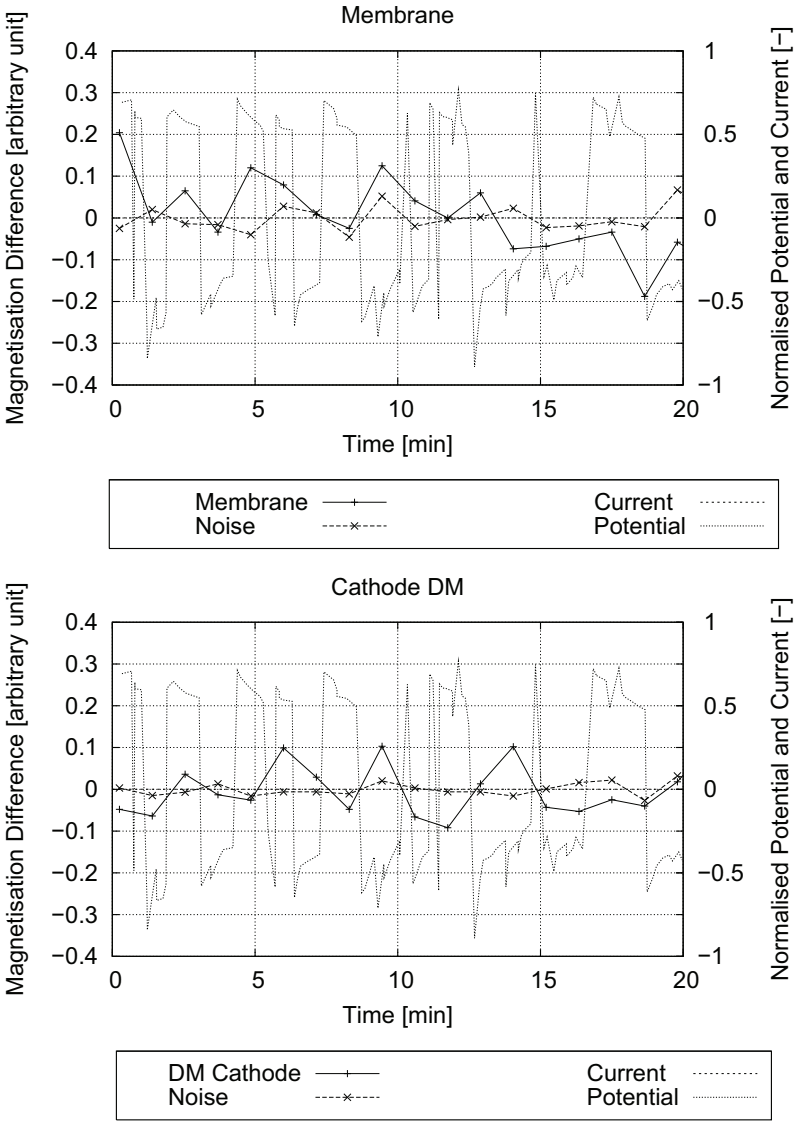

Figure 4.30: Relative change of average voltage, current, and magnetisation in the membrane (top) and the cathode DM (bottom) of the cell with MPL at cathode DM at TP 3. Conditions: Coolant temperature: 303 K; DM: PTFE-treated SGL21AA; Membrane: Gore 5510.

The kind of voltage oscillation as just described is also found at TP 2 for the cell with the PTFE-treated DM. In this case, the oscillating frequency is even higher. The 2D analysis shows oscillating characteristics for the proton density in the membrane (Figure 4.31).

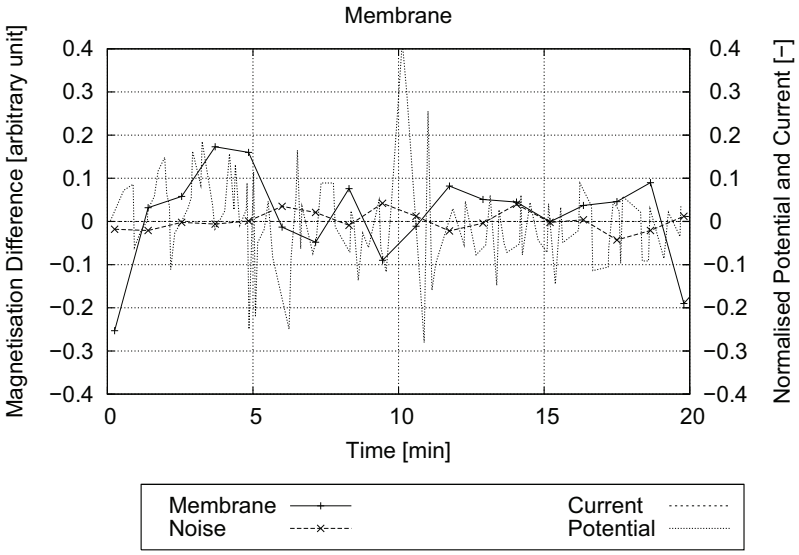

Figure 4.31: Relative change over time of average voltage, current, and magnetisation of the membrane of the cell with PTFE-treated DM at TP 2. Conditions: Coolant temperature: 303 K; DM: PTFE-treated SGL21AA; Membrane: Gore 5510.

The highest oscillation magnitude of magnetisation is found in the membrane, the other locations in the fuel cell have magnetisation variations comparable to the noise and behave totally inconspicuously. The stationary 3D investigation of this cell under this condition indicates a low state of humidification at membrane level, thus, the water transport rate from the membrane to the channels is too high.

If the potential is sensitive on the liquid water content in or close to the membrane, as indicated by the sudden potential drop, the oscillating voltage indicates a non-continuous, pulsating water transport. The oscillation period of this pulsation is in the order of 10 s to 20 s.

Microscopically resolved water transport in DM is studied in 2D.

The macroscopic approach, as presented in Section 4.4.1 (page 145ff.), was done to find a correlation between cell performance and water rearrangement in the different parts of the fuel cell. Details of local water rearrangement can be studied by focusing on details

within the DM. This approach pushes the method to its limit in resolution and the analysis is done very close to, or even within the noise limit. Therefore, the data in this chapter are presented in a different way than in the previous sections. A small part of the cathode DM is taken out of the 2D image and transformed into an intensity-2D image, while the x-y-plane represents the spatial coordinates and the z-axis the signal intensity. The resulting image looks like parts of a mountain range. As previously described, the cell is built with a Gore 5510 membrane and the SGL21AA gas diffusion media, which are rendered hydrophobic by in-house treatments with PTFE. The fuel cell is operated current-controlled at 0.1 A/cm^2 with air and hydrogen at a stoichiometry of four (TP 1). The gases are dry when fed to the cell which has a temperature of 303 K. The potential is about 630 mV. Under these conditions a 2D image sequence with a frequency of one image per minute is taken. The analysis of the images is done as stated above and the resulting images are shown in Figure 4.32. The peaks on the left side of each individual intensity-2D image represents the flow field and the right side represents the membrane side.

The images in Figure 4.32 show the cross section perpendicular to the current collector. On the left, the cross section of the whole cell is shown (black and white), while the focus is on a 18 x 8 pixel area in the upper part of the cathode diffusion medium (magnifications). The 3D surface plots display the signal intensity (colour and z-axis) versus the x-y-orientation. The interface of cathode DM and membrane is shown on the right side of the surface plots, while the left side represents the interface between DM and flow channels. The water content inside the cathode DM changes over time in the order of minutes. At 't' two connections between membrane and DM are shown, while at 't+1' the water concentration starts to decrease and at 't+2' only one connection remains. At 't+4' no connection between membrane and flow channels exists.

Caution is advised with this finding, since the temporal fluctuations in the area between the membrane and the DM are close to the magnitude of the temporal fluctuations of the background noise. The probability that the dynamic observation by NMR is an artefact is reduced by findings of Hartnig et al. [HMK$^+$09]. Recently they studied water transport by in-situ synchrotron radiography and reported pulsing water transport with a period of 1.5 min.

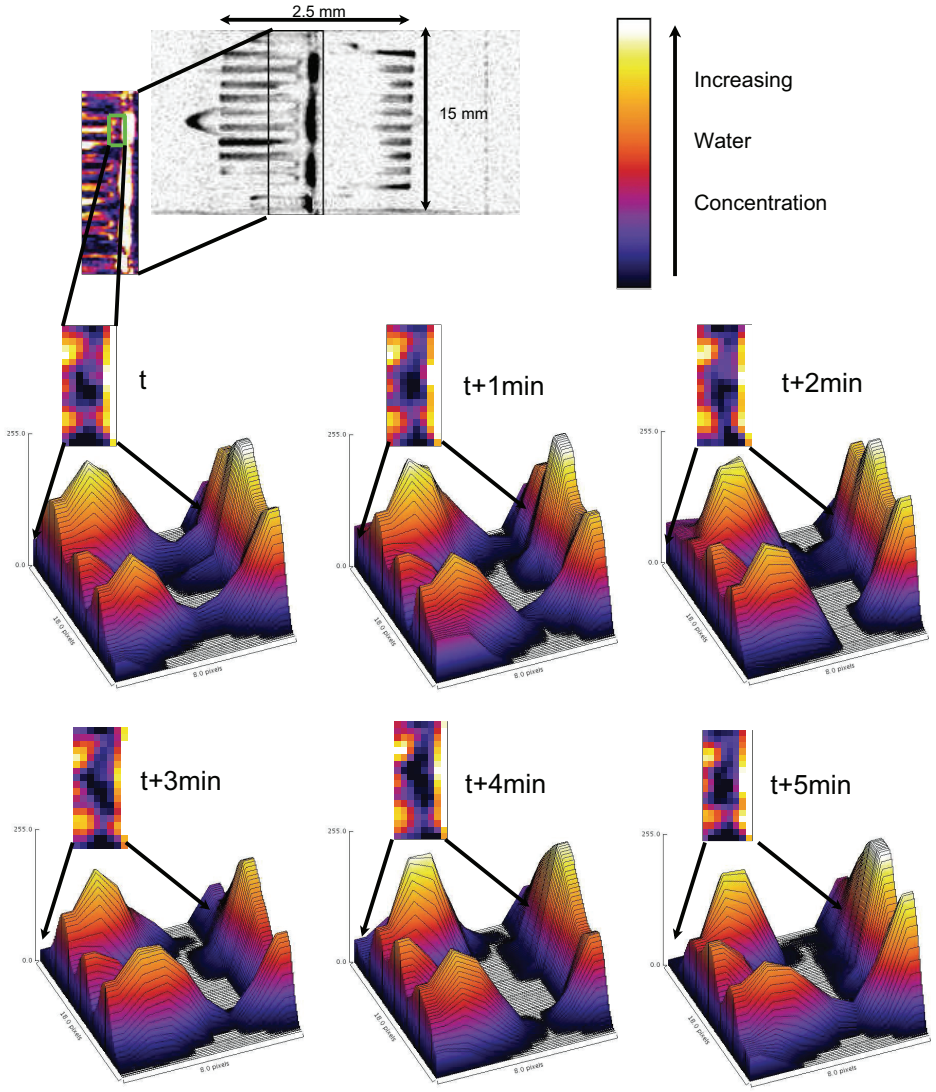

Figure 4.32: 2D and intensity-2D image sequence of the fuel cell at 0.1 A/cm^2 (630 mV) with air and hydrogen at a stoichiometry of four at 303 K. The DM is PTFE-treated.

4.5 Concluding Remarks

The applicability of state-of-the-art nuclear magnetic resonance imaging for fuel cell diagnostics is investigated. Thereby, special attention is drawn on the visualisation of water inside the gas diffusion medium. The fundamental considerations, based on first-order approximation of the relevant physics, indicate that following variables of the fuel cell experiment are also variables in the NMR imaging process:

- Temperature
- Current density
- Electrical conductivity
- Poresizes

The theoretical consideration does not allow to assess the sensitivity of these variables with regard to the imaging of water in DM. Yet, the experimental assessment proves that the sensitivity of the listed variables is high for the NMR imaging process. This constraints the applicability of NMR imaging for fuel cell diagnostics to low temperature, low current density applications with low conductive DM with large pores, channel, or membrane investigations. Only if the NMR instrument can handle much faster T_2^* time constants (see Section 4.3.3 on page 125), or the magnetisation is done at much stronger fields, the NMR imaging can overcome its current limitations.

Within the identified constraints, it is demonstrated that the NMR technique is capable of visualising liquid water inside the DM of a running fuel cell in 3D with a 20 µm resolution. The temporal resolution for a 3D image is 2 hrs. and 1 min for 2D. It is shown that the saturation profile within the DM is bi-modal and there are hints that the saturation is less dependent on the water flux in the DM.

The recent advances in neutron radiography increased the resolution to pixel sizes of 20 µm. The water profiles measured by Hickner et al. [HSC$^+$08] and Boillot et al. [BDL05] are in qualitative agreement with the profiles found by NMR. The quantitative deviation is caused by the application of different DM materials (cloth vs. randomly laid fibres) and operating conditions, like temperature.

Another high-resolving and fast alternative is the synchrotron radiation imaging. This method was recently applied for in-situ studies by Manke and Hartnig et al. [MHG+97, HMK+08, HMK+09], Mukaide et al. [MMY+08] and others. Hartnig et al. found similar water profiles in the DM as seen by NMR in experiments presented in this thesis. Yet, the synchrotron radiation used for imaging fuel cell components might interfere with the materials used in the fuel cell in an undesirable way. Synchrotron radiation is known for its ability to damage and decompose polymers like poly-methyl-metacrylate (PMMA) or even PTFE. Henry et al. [HMD+98] investigated the impact of synchrotron radiation on PMMA with beam energies in the order of 4 keV. They found structural changes like swelling. Others, like Nishi et al. [NKS02], used synchrotron radiation in the energy range between 1 keV and 10 keV for PTFE etching. In the energy range below 1 keV a change in wetting behaviour of radiation exposed PTFE was reported by Kanda et al. [KIH+03]. The beam energy used for fuel cell visualisation experiments is in the order of 13 keV [MHG+97], which is beyond the harmful 10 keV. But due to the presence of transition metal elements in the fuel cell (Fe, Pt), x-ray fluorescence is likely to occur and fluorescence radiation in the energy range below 10 keV can be emitted and can damage the fuel cell components in the visualised area. Thus, it cannot be excluded that the measurement technique interferes with the experiment. But this has not yet been studied systematically.

Chapter 5

Final Conclusions

The results of the different parts of this work have already been discussed at the end of the individual chapters. A summary of the key findings and the interplay of the different parts will be presented here.

Hydrological formulations are often used when dealing with porous flow systems in fuel cells. The accuracy (or even applicability) of the description of such systems might be debatable since the morphological difference and the scales in focus between porous flow systems in fuel cells and their counterparts in soil science or hydrology differ significantly. In order to assess the state-of-the-art description of two-phase flow in porous media, the pressure-saturation characteristic of Toray 060 carbon fibre paper with 7 % and 10 % PTFE is measured by the buoyancy-based technique, specifically developed during the course of this work. It is found that the difference of the pressure-saturation characteristic for the PTFE of 7 % or 10 % is too small to be detected by the applied method or the difference is not significant compared to the effects of randomness in the material. The measured characteristic can be described best by the empirical representation of a fourth-order polynomial

$$p = \left(172.2\ s_{\mathrm{e,nw}}^4 - 194.8\ s_{\mathrm{e,nw}}^3 + 18.6\ s_{\mathrm{e,nw}}^2 + 49.4\ s_{\mathrm{e,nw}} + 4.0\right) \mathrm{kPa}. \tag{5.1}$$

Equation 5.1 is obtained for the case of invading water and considers the breakthrough pressure in contrast to the frequently used third-order polynomial function suggested by Udell [Ude85].

The validity limitation of Equation 5.1 to situations for imbibing water is set by the strong saturation hysteresis, found for decreasing liquid pressure. If the water pressure is set to environmental pressure - after invasion - the saturation stays almost constant.

An experiment to measure the water permeability as a function of pressure for extremely low flow rates was presented. The measured pressure-permeability data are used to assess common descriptions of relative permeability. The measured pressure-saturation characteristic is taken as input for Burdine's, Mualem's and the s^3 model. It is found that Mualem's and Burdine's model applied with the measured pressure-saturation characteristic gives the closest representation of the measured values at low pressures (or saturation). The sample appeared impermeable till a liquid pressure of 3.5 kPa to 5.5 kPa is applied. Once the required pressure is reached, a sudden flow with a fairly high flow rate sets in. This indicates that the hydrophobic diffusion medium has no hydrophilic pore network (no interconnected pores with positive capillary pressure).

Yet, this statement holds only true in those cases of water coverage on both surfaces of the DM (wet boundary condition). In cases of air exposure on the low-pressure side of the DM (dry boundary condition), a completely different permeation pattern is found. The permeation sets in, similar to the case of the wet boundary condition but at a much higher apparent permeability. Due to the setup of the experiment, pressure and flow are coupled and it is observed that the permeability decreases over time even if every other controlled parameter is constant. The observed flow rate is not linearly dependent on the pressure, as Darcy's law suggests. Thus, it can be concluded, that the permeability is not constant but a function of the liquid pressure applied before (history dependent) and the surface boundary conditions. Also, the time constants for the equilibration of saturation and permeability are in the order of hours and not negligible. Based on the latter finding, it is not meaningful to measure the relative permeability for a dry boundary condition since the concept of relative permeability as a function of saturation only does not seem to apply. The long time constants would require the implementation of time dependency.

The wet and the dry boundary condition exist in fuel cell applications. The dry boundary is located where the DM faces the gas channels, the wet boundary applies under the land as well as in the channel where a water slug is pinned on the DM. Both phenomena are important, which implies the need to create a deeper understanding of the underlying

physics. In order to gain deeper insights into the water transport through DM, analytical and numerical free surface calculations were conducted. This will serve as a stepping stone towards a better founded theoretical base for the description of multi-phase flow in DM and allows for advanced material design in the end.

The free surface modelling is based on neglecting gravity effects, which was suggested by the assessment of dimensionless numbers and confirmed by the calculation of a typical model case with and without gravity. The water redistribution for the imbibing and receding situation into a geometry of six fibres is investigated at a contact angle of 120°. The calculation reveals that even at constant contact angle the pressure-volume characteristic is subject to hysteresis, based on geometrical reasons only. The magnitude of hysteresis is in the order of 2 kPa to 2.5 kPa for the geometry investigated here.

The numerical investigation of water pressure relative to water distribution at contact angles of 120° and 180° in the fibre geometry shows a breakthrough pressure difference in the order of 1 kPa. Also the filament stability is affected by the contact angle. The higher the contact angle is, the less stable is the filament.

The calculated breakthrough pressure is in the range between 6.5 kPa and 7.4 kPa, depending on the contact angle. The breakthrough pressure calculated with the simpler analytical pseudo 3D model is found to be 7.5 kPa for 180° contact angle. The calculated results for the breakthrough pressure by the numerical 3D calculation and the much simpler pseudo 3D analytical model agree well with each other.

The experimentally found breakthrough pressures are in the range of 3 kPa to 5 kPa and lower by 1.5 kPa to 4.5 kPa in comparison to the calculated breakthrough pressures. The difference probably occurs due to the simplifications of the free surface model, like, e.g. neglecting the binder, the triangular arrangement of the fibres and the static contact angle. Furthermore, the exact contact angle of the experimentally tested material is not known. Keeping the simplicity of the analytical pseudo 3D model in mind, the agreement with the numerical 3D model is good enough to use the fast 2D approach for assessing the breakthrough pressure trends of different fibre geometries.

Experimentally it was found that the boundary condition with regard to saturation at the low-pressure side of the DM makes a difference; similar behaviour was seen by a study with the free surface model. Based on a simple geometry of six fibres the effect of boundary

conditions was explored. The simulation of pressure versus water volume showed that in case of the water-covered case, the pressure oscillates with a period of 40 s between the highest and the lowest pressure during the filament development, while in the dry case it would take 160 min under the same flow condition (water production rate corresponding to 1 A/cm^2) to reach the same low pressure as in the water-covered case. The hypothesis to connect the experimental result with the simulation assumes that the water network for the water transport is not constant in time, but disconnects and reconnects according to the liquid water pressure. The detailed simulation shows filament stability down to 1 kPa water pressure. Further down, filament rupture is likely to occur, especially at large contact angles between fibre and water, and if gas flow induced perturbations are taken into consideration.

The attempt to confirm this hypothesis by in-situ observation of water dynamics and water distribution in the fuel cell by nuclear magnetic resonance imaging lead to an assessment of the methodology with regard to fuel cell in-situ testing. First fundamental considerations, based on first-order approximation of the relevant physics, indicated that following variables of the fuel cell experiment are also variables in the NMR imaging process:

- Temperature
- Current density
- Electrical conductivity
- Pore sizes

The experimental assessment proved that the sensitivity of the listed variables is high for the NMR imaging process. This limits the applicability of NMR imaging for fuel cell diagnostics to low temperature and low current density applications with low-conductive DM with large pores, channel, or membrane investigations.

Within the identified constraints, it has been demonstrated that the NMR technique is capable of visualising liquid water inside the DM of a running fuel cell in 3D with a 20 µm resolution. It was shown that the saturation profile within the DM is bi-modal and different at land or channel regions. The dynamic aspects of the NMR experiment

gave indications that the water-filled pore space is subject to temporal changes even under stationary conditions. This gives strong support to the pulsing hypothesis erected on the results of the free surface simulation.

The aim of this work was the assessment of two-phase transport models based on Darcy's law. It was found that the Darcy-type approach is not able to describe the two-phase water transport in the thin fibrous matrix of gas diffusion media in the fuel cell for the dry boundary condition. The interface between the DM and the catalyst or micro-porous layer on one side and the gas channel on the other side influences the liquid water transport much stronger than the bulk properties of the DM. For the wet boundary condition, the two-phase Darcy approach in conjunction with Mualem's model and an experimentally determined pressure-saturation relation is in agreement with the permeation experiment.

Further work is necessary to replace the traditional Darcy-type two-phase flow description by a new constitutive model that is able to predict distribution and pressure loss correctly in cases where the interfaces dominate the transport phenomena like at the dry boundary condition. With regard to the second aim, the linkage between mathematical mass transport description and material design, the first steps had been taken by numerical free surface modelling. With increasing computational power the replacement of the empirical design of porous layers for fuel cells by math-based design comes within reach.

Appendix A

Derivation of Burdine's Equation

Although it is called 'Burdine's equation' a useful derivation of this equation can be found by Wyllie and Gardner [WG58]. They took the main concepts of several researchers like Burdine, Purcell, Scheidegger, Spangler, and others and a relative permeability equation was achieved by analytical methods. The derivation starts with laminar flow in a tube (Hagen-Poiseuille's law, see Equation 1.31 on page 37).

The assumptions made for describing the radius of the tube are based on a probability approach, explained as follows: Beginning with a bundle of straight capillaries with different diameters and a saturation s (Figure A.1a). The phases are distributed in the bundle in such a way, that the small capillaries are filled with the wetting fluid, while the large capillaries are filled with the non-wetting fluid. The radius of a filled capillary is described by the Young-Laplace equation (Equation 1.21 on page 32). The bundle is sliced (Figure A.1b) and the individual pieces of tubes in each slice are randomly rearranged (Figure A.1c). In the next steps, the slices are grouped together to get the initial sample volume in Figure A.1d. The illustrations in Figure A.1a – d are idealised with respect to the position of the centres of the capillaries; just for illustration, the spatial distribution is regularly. In Wyllie and Gardner's work, the capillaries are moved arround (Figure A.1e). This procedure maintains the porosity and the saturation. Yet, this does not account for the fact that small capillaries filled in the original geometry, might not be filled in the real situation due to connections with large pores only.

The description of the saturation is based on effective saturation, the residual wetting-

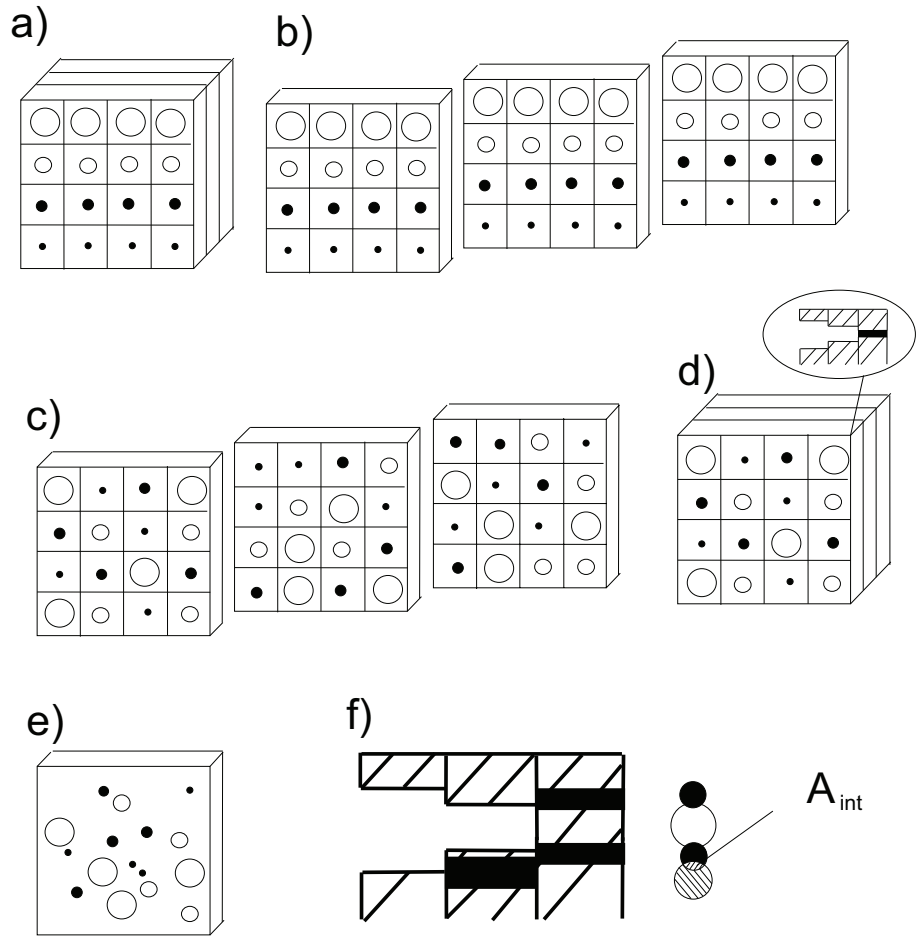

Figure A.1: Model for deriving Burdine's equation. a) Bundle of capillaries with different diameters and filling. b) Sliced bundle. c) Rearranged capillaries in each slice. d) Grouping the slices. e) More realistic situation, capillaries moved randomly within the slice. f) Branching at interface and overlapping area A_{int}.

fluid content is added to the solid-phase content of the matrix (see Section 1.3.2 on page 31). The gas saturation (wetting phase) is defined by

$$s_{\text{e,g}} = \frac{V_{\text{g}}}{V} = \frac{\int_{r_{\min}}^{r} \pi r^2 \omega(r) dr}{\int_{r_{\min}}^{r_{\max}} \pi r^2 \omega(r) dr} \tag{A.1}$$

in this model with $\omega(r)$ as the pore radii distribution function. The differential saturation

$$ds_{\mathrm{e,g}} = \frac{r^2\omega(r)dr}{\int_{r_{\min}}^{r_{\max}} r^2\omega(r)dr} \tag{A.2}$$

is required later. In the employed pore model, there are flow restrictions at the interface between the slices (see Figure A.1f) and an estimation of this restriction is made with a probability analysis. The gas-filled area of each slice cross section is

$$A_{\mathrm{g}} = s_{\mathrm{e,g}}\varepsilon A. \tag{A.3}$$

When a filled pore with radius r is considered at the interface, the probability that this pore faces another pore filled with the same fluid on the other side of the interface is $s_{\mathrm{e,g}} \cdot \varepsilon$. Based on this consideration it is possible to express the interface area A_{int} for the fluid between the two slices:

$$A_{\mathrm{int}} = \pi <r>^2 q = s_{\mathrm{e,g}}\varepsilon\pi <r>^2 \tag{A.4}$$

While r is the equivalent radius of the new model pore and q is a factor to account for branching if the pore connects with more than one other pore (Figure A.1f). Resolved for the equivalent radius, Equation A.4 becomes

$$r = \sqrt{\frac{s_{\mathrm{e,g}}\varepsilon}{q}} <r> . \tag{A.5}$$

The flow through the model matrix can be described by Equation A.6 by using Equation 1.33 (page 38) and Equation A.5. Since the pressure drop in the model capillaries is not only restricted by the smaller radius r, but also due to vortices near the interfaces, a pressure drop factor β is introduced.

$$\frac{dV}{dt} = -\frac{\pi\beta q\left(\frac{s_{\mathrm{e,g}}\varepsilon}{q}\right)^2}{8\mu}\nabla p \sum_{i=0}^{j} {r_i}^4 <n_i> \tag{A.6}$$

With $<n_i>$ being the number of pores with diameter i. The summation is replaced by

the integral, resulting in

$$\frac{dV}{dt} = -\frac{\pi\beta q \left(\frac{s_{\mathrm{e,g}}\varepsilon}{q}\right)^2}{8\mu}\nabla p \int_{r_{\min}}^{r} r^4\omega(r)dr. \tag{A.7}$$

By rearranging Equation A.2, one obtains

$$r^2\omega(r)dr = ds_{\mathrm{e,g}} \int_{r_{\min}}^{r_{\max}} r^2\omega(r)dr. \tag{A.8}$$

Equation A.8 is multiplied by $r^2 = \left(\frac{2\sigma\cos\theta}{p}\right)^2$:

$$r^2 \cdot r^2\omega(r)dr = \left(\frac{2\sigma\cos\theta}{p}\right)^2 \cdot ds_{\mathrm{e,g}} \int_{r_{\min}}^{r_{\max}} r^2\omega(r)dr \tag{A.9}$$

and Equation A.7 is rewritten as:

$$\frac{dV}{dt} = -\frac{\pi\beta q \left(\frac{s_{\mathrm{e,g}}\varepsilon}{q}\right)^2}{8\mu}\nabla p \int_0^{s_{\mathrm{e,g}}} \left(\frac{2\sigma\cos\theta}{p}\right)^2 ds_{\mathrm{e,g}} \int_{r_{\min}}^{r_{\max}} r^2\omega(r)dr \tag{A.10}$$

Based on Equation A.10, the flow velocity

$$u = \frac{1}{A}\frac{dV}{dt} \tag{A.11}$$

with

$$A = \frac{1}{\varepsilon}\int_{r_{\min}}^{r_{\max}} \pi r^2\omega r dr \tag{A.12}$$

is obtained:

$$u(s_{\mathrm{e,g}}) = -\frac{\beta\sigma^2\cos^2\theta s_{\mathrm{e,g}}^2\varepsilon^3}{2\mu q}\nabla p \int_0^{s_{\mathrm{e,g}}} \frac{ds_{\mathrm{e,g}}}{p^2}. \tag{A.13}$$

By forming the quotient of the saturation-dependent velocities of the partial saturated case and the fully saturated case, the relative permeability and Burdine's equation is obtained:

$$k_{\mathrm{rel,g}}(s_{\mathrm{e,g}}) = (s_{\mathrm{e,g}})^2 \frac{\int_0^{s_{\mathrm{e,g}}} \frac{ds_{\mathrm{e,g}}}{p^2}}{\int_0^1 \frac{ds_{\mathrm{e,g}}}{p^2}} \tag{A.14}$$

Appendix B

The Details of the Multi-phase Mixture Model

The derivation of the multi-phase mixture model (see Section 1.3.5 on page 50ff.) involves a transition step which is not very intuitive and details of transition is given here. In order to get from Equation 1.61 to Equation 1.62 (page 51), the following steps are required. The detailed formulation of Equation 1.61 is

$$2\varepsilon\frac{ds_{\mathrm{nw}}}{dt} - \nabla\cdot\left[k\left(\frac{k_{\mathrm{rel,nw}}}{\mu_{\mathrm{nw}}}\nabla p_{\mathrm{nw}}\right)\right] + \nabla\cdot\left[k\left(\frac{k_{\mathrm{rel,w}}}{\mu_{\mathrm{w}}}\nabla p_{\mathrm{w}}\right)\right] = 0. \tag{B.1}$$

This is reduced to higher terms with the global mobility Q (see Equation 1.57 on page 51) for more effective notation.

$$2\varepsilon\frac{ds_{\mathrm{nw}}}{dt} - \nabla\cdot\left[kQ\left(\frac{k_{\mathrm{rel,nw}}}{Q\mu_{\mathrm{nw}}}\nabla p_{\mathrm{nw}}\right)\right] + \nabla\cdot\left[kQ\left(\frac{k_{\mathrm{rel,w}}}{Q\mu_{\mathrm{w}}}\nabla p_{\mathrm{w}}\right)\right] = 0 \tag{B.2}$$

$$\frac{k_{\mathrm{rel,nw}}}{Q\mu_{\mathrm{nw}}} + \frac{k_{\mathrm{rel,w}}}{Q\mu_{\mathrm{w}}} = 1 \tag{B.3}$$

With Equation B.3, Equation B.2 can be further reduced to higher terms:

$$2\varepsilon\frac{ds_{\mathrm{nw}}}{dt} - \nabla\cdot\left[kQ\left[\left(\frac{k_{\mathrm{rel,nw}}}{Q\mu_{\mathrm{nw}}} + \frac{k_{\mathrm{rel,w}}}{Q\mu_{\mathrm{w}}}\right)\frac{k_{\mathrm{rel,nw}}}{Q\mu_{\mathrm{nw}}}\nabla p_{\mathrm{nw}} + \left(\frac{k_{\mathrm{rel,nw}}}{Q\mu_{\mathrm{nw}}} + \frac{k_{\mathrm{rel,w}}}{Q\mu_{\mathrm{w}}}\right)\left(\frac{k_{\mathrm{rel,w}}}{Q\mu_{\mathrm{w}}}\nabla p_{\mathrm{w}}\right)\right]\right] = 0 \tag{B.4}$$

Equation B.4 is expanded and even further reduced to higher terms by

$$+\frac{k_{\mathrm{rel,nw}}k_{\mathrm{rel,w}}}{Q^2\mu_{\mathrm{w}}\mu_{\mathrm{nw}}}\nabla p_{\mathrm{nw}} - \frac{k_{\mathrm{rel,nw}}k_{\mathrm{rel,w}}}{Q^2\mu_{\mathrm{nw}}\mu_{\mathrm{w}}}\nabla p_{\mathrm{nw}} \tag{B.5}$$

and

$$+\frac{k_{\mathrm{rel,nw}}k_{\mathrm{rel,w}}}{Q^2\mu_{\mathrm{w}}\mu_{\mathrm{nw}}}\nabla p_{\mathrm{w}} - \frac{k_{\mathrm{rel,nw}}k_{\mathrm{rel,w}}}{Q^2\mu_{\mathrm{nw}}\mu_{\mathrm{w}}}\nabla p_{\mathrm{w}} \tag{B.6}$$

allowing for the following rearrangement:

$$2\varepsilon\frac{ds_{\mathrm{nw}}}{dt} - \nabla\cdot\left[kQ\left[2\frac{k_{\mathrm{rel,nw}}}{Q\mu_{\mathrm{nw}}}\frac{k_{\mathrm{rel,w}}}{Q\mu_{\mathrm{w}}}\nabla\left(p_{\mathrm{nw}}-p_{\mathrm{w}}\right)\right.\right.$$
$$\left.\left.+\left(\frac{k_{\mathrm{rel,nw}}}{Q\mu_{\mathrm{nw}}}-\frac{k_{\mathrm{rel,w}}}{Q\mu_{\mathrm{w}}}\right)\left(\frac{k_{\mathrm{rel,nw}}}{Q\mu_{\mathrm{nw}}}\nabla p_{\mathrm{nw}}+\frac{k_{\mathrm{rel,w}}}{Q\mu_{\mathrm{w}}}\nabla p_{\mathrm{w}}\right)\right]\right]=0 \tag{B.7}$$

The last step, required to arrive at Equation B.10, is the application of the definition of the capillary pressure (Equation 1.22, page 32) and its total derivative (Equation B.8), as well as Equation B.9.

$$\nabla p_{\mathrm{cap}} = \nabla\left(p_{\mathrm{nw}}-p_{\mathrm{w}}\right) = \frac{\partial p_{\mathrm{cap}}}{\partial s}\nabla s \tag{B.8}$$

$$\frac{k_{\mathrm{rel,nw}}(s)}{\mu_{\mathrm{nw}}}\nabla p_{\mathrm{nw}} + \frac{k_{\mathrm{rel,w}}(s)}{\mu_{\mathrm{w}}}\nabla p_{\mathrm{w}} \equiv Q\nabla p \tag{B.9}$$

$$\varepsilon\frac{ds_{\mathrm{nw}}}{dt} - \nabla\cdot\left[k\frac{k_{\mathrm{rel,nw}}k_{\mathrm{rel,w}}}{\mu_{\mathrm{nw}}\mu_{\mathrm{w}}Q}\frac{dp_{\mathrm{cap}}}{ds_{\mathrm{nw}}}\nabla s_{\mathrm{nw}}\right] - \nabla\cdot\left[\left(\frac{k_{\mathrm{rel,nw}}}{\mu_{\mathrm{nw}}}-\frac{k_{\mathrm{rel,w}}}{\mu_{\mathrm{w}}}\right)\frac{k}{2}\nabla p\right] = 0 \tag{B.10}$$

Appendix C

Time-Dependent Pressure Calculation

The model details related to the permeability experiment (see Section 2.3.3 on page 73ff.) are presented in this section. The model parameters and the operational sequences to calculate the pressure as a function of time are given for the three different model approaches. All the calculations are based on the mass balance of the experiment. This results in the governing equation (Equation C.1) (for details see Section 2.3.2 and Section 2.3.3 on page 70ff. and page 73ff.).

$$\Big[C_7\,[p_{\mathrm{in}}-p(t)]^2+C_8\,[p_{\mathrm{in}}-p(t)]\Big]\,p_0=[V_0+Y]\,\frac{dp}{dt}+\frac{A\;k_{\mathrm{DM}}}{l\;\mu_{\mathrm{H_2O}}}\,[p(t)-p_0]\,p(t) \qquad \text{(C.1)}$$

In order to investigate the experimentally found pressure-dependent water flux characteristic, three different models are employed.

- In the first model, it is assumed that there are two discontinuities in the permeability, dependent on the pressure.
- The second model contains one discontinuity in permeability at breakthrough, but also a second pressure-dependent term Y which is not physically justified.
- The third model contains one discontinuity in permeability at the breakthrough as well – not to a new constant value, but to a saturation-dependent permeability.

The programme flow charts for the models 1 and 2 are depicted in Figure C.1 to C.3. The parameters applying to all three models are listed in Table C.1, while the specific parameters, unique to the individual model are shown in Table C.2.

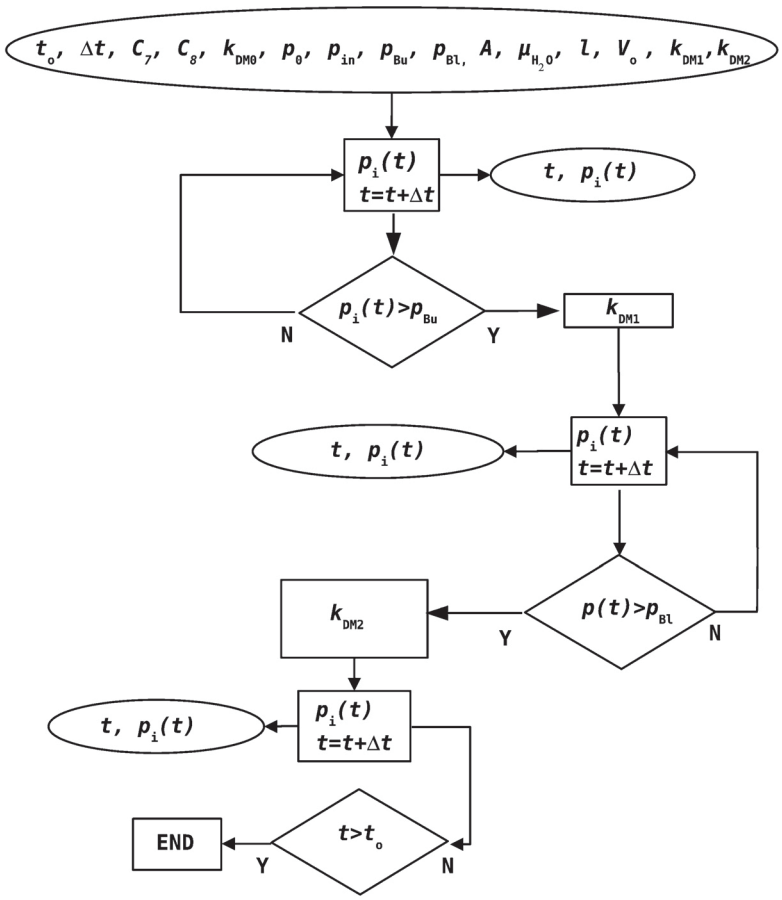

Figure C.1: Programme flow chart to calculate the pressure as a function of experimental time. Model 1 with two different permeability values.

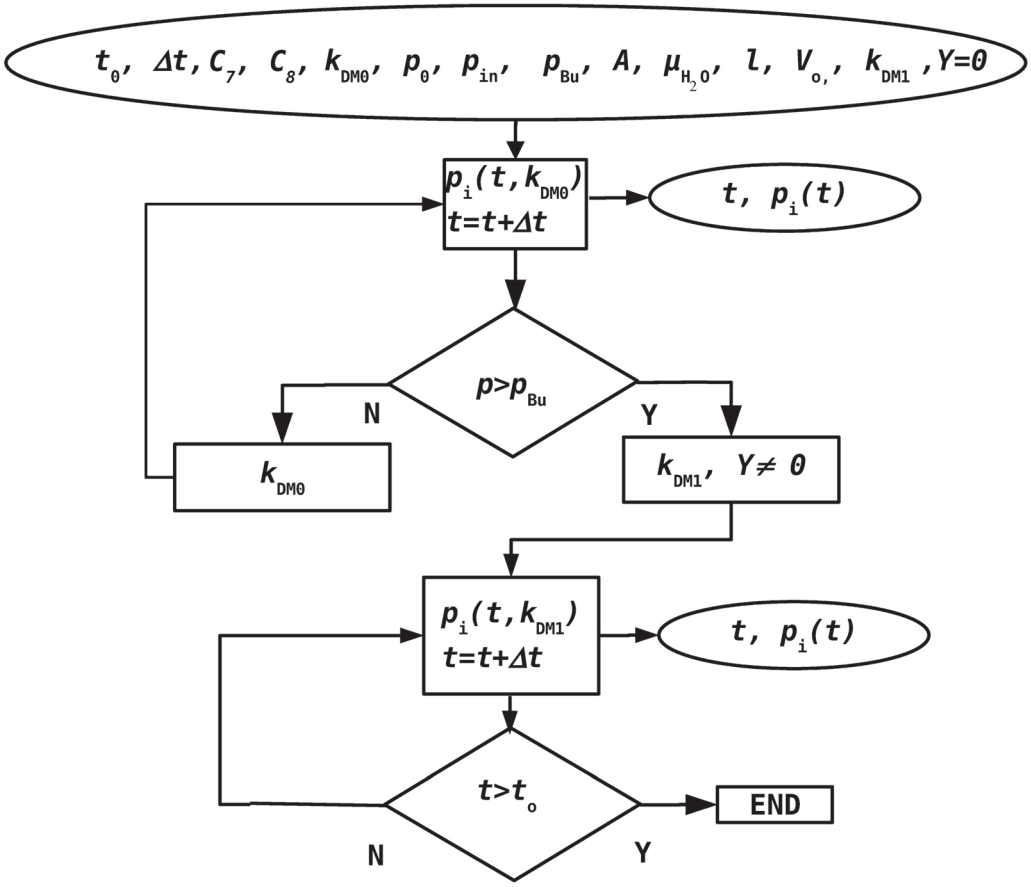

Figure C.2: Programme flow chart to calculate the pressure as a function of experimental time. Model 2 with additional compressibility term Y.

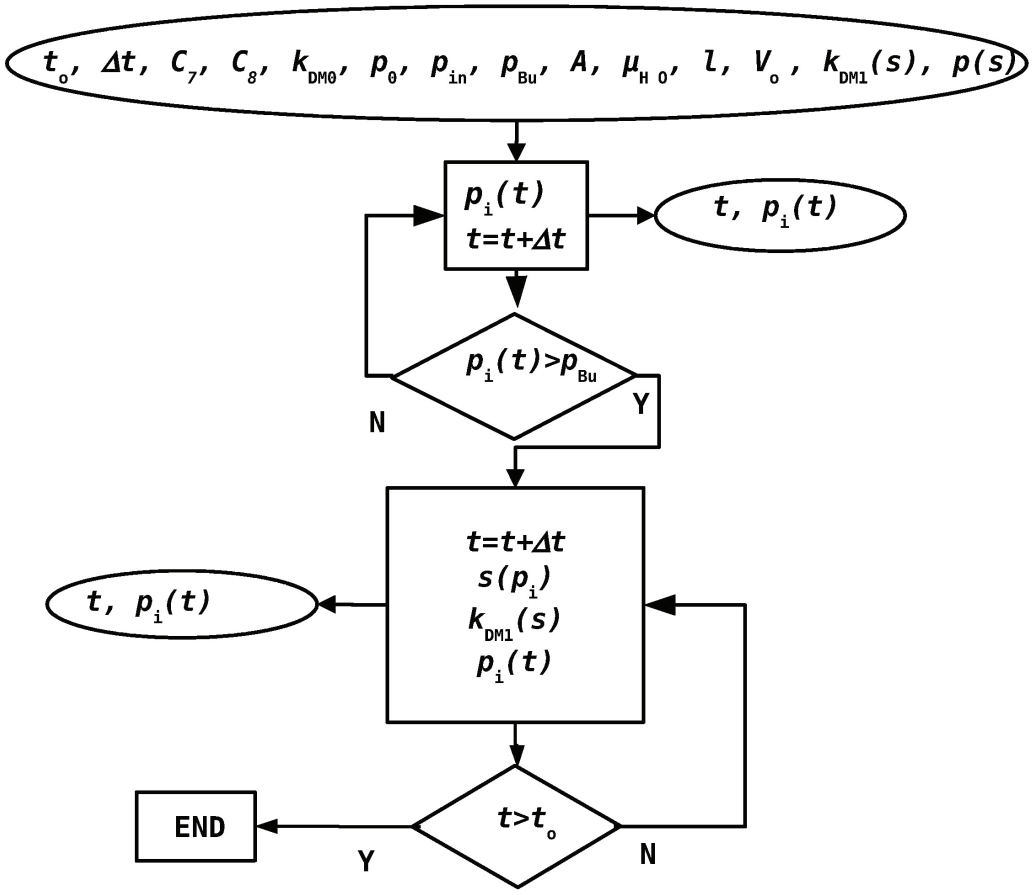

Figure C.3: Programme flow chart to calculate the pressure as a function of experimental time. The saturation-dependent Mualem model.

Table C.1: Global model parameters

t_0	Δt	C_7	C_8	$k_{\mathrm{DM},0}$	p_0	p_{in}	p_{Bu}	A	$\mu_{\mathrm{H_2O}}$	l	V_0
s	s	L/s/kPa^2	L/s/kPa	m^2	kPa	kPa	kPa	m^2	Pa s	m	m^3
20000	10	$9.81{\cdot}10^{-8}$	$2.05{\cdot}10^{-6}$	0	101.3	106.3	104.19	$15.9{\cdot}10^{-4}$	$1.005{\cdot}10^{-3}$	$2.00{\cdot}10^{-4}$	$0.66{\cdot}10^{-3}$

Table C.2: Model dependent parameters

Type	p_{Bl}	$k_{\mathrm{DM,\,1}}$	$k_{\mathrm{DM,\,2}}$	Y	$p(s)$[kPa] ♠ for $s_{\mathrm{r}} = 0.24$				
	kPa	m^2	m^2	m^3	C_1	C_2	C_3	C_4	C_5
Model 1	101.9	$3{\cdot}10^{-15}$	$1.8{\cdot}10^{-16}$	-	-	-	-	-	-
Model 2	-	$8{\cdot}10^{-17}$	-	$3.87{\cdot}10^{-3}$	-	-	-	-	-
Mualem	-	$4{\cdot}10^{-12} \cdot {s_{\mathrm{e,g}}}^{1/2} \left[\frac{\int_0^{s_{\mathrm{e,g}}} \frac{ds_{\mathrm{e,g}}}{p}}{\int_0^1 \frac{ds_{\mathrm{e,g}}}{p}} \right]^2$	-	-	202.3	251.7	48.1	48.8	2.1

♠ $\mathrm{p(s)}=C_1\ (1\text{-}s_{\mathrm{e,g}})^4\text{-}C_2\ (1\text{-}s_{\mathrm{e,g}})^3+C_3\ (1\text{-}s_{\mathrm{e,g}})^2+C_4\ (1\text{-}s_{\mathrm{e,g}})+C_5$

Appendix D

Interface Area Calculation

The assessment of the area ratio for the free surface area calculation is based on the interface area between fibre and water, as well as water and gas. In Section 3.1 on page 83 this ratio is employed. Here, the geometric assumption, leading to Equation 3.2 on page 83, is explained.

The area of the interface between fibre and water does not depend upon the contact angle, since the consideration is under the premises that volume and pressure are set to a volume, that the fibre (inner area of the torus) is half wet. This is the most conservative assumption for the hydrophobic case. The geometrical assumption is sketched in Figure D.1. The inner area of the torus is described by Equation D.1

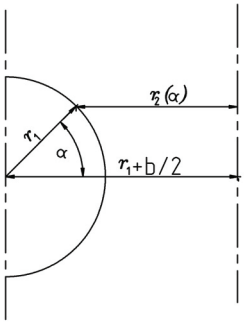

Figure D.1: Geometrical configuration to calculate interfacial area between water and fibre.

$$A = 2 \int_0^{\pi/2} 2\pi r_2(\alpha) r_1 d\alpha \tag{D.1}$$

According to the given geometry, the radius r_2 depends on the parameter angle α by

$$r_2(\alpha) = r_1 + b/2 - r_1 \cos\alpha = b/2 + r_1 \left[1 - \cos\alpha\right]. \tag{D.2}$$

Thus, Equation D.1 becomes

$$A = 4\pi \int_0^{\pi/2} (b/2 + r_1 \left[1 - \cos\alpha\right]) r_1 \; d\alpha. \tag{D.3}$$

The final equation for the wet area of the torus is:

$$A = \pi \left[2\pi \left(\frac{b}{2} + r_1 \right) r_1 - 4r_1^2 \right] \tag{D.4}$$

The interface between the interface gas-water is idealised as depicted in Figure D.2. The detail covers the location between two vertically spaced fibres, with a horizontally rotation-symmetric boundary condition.

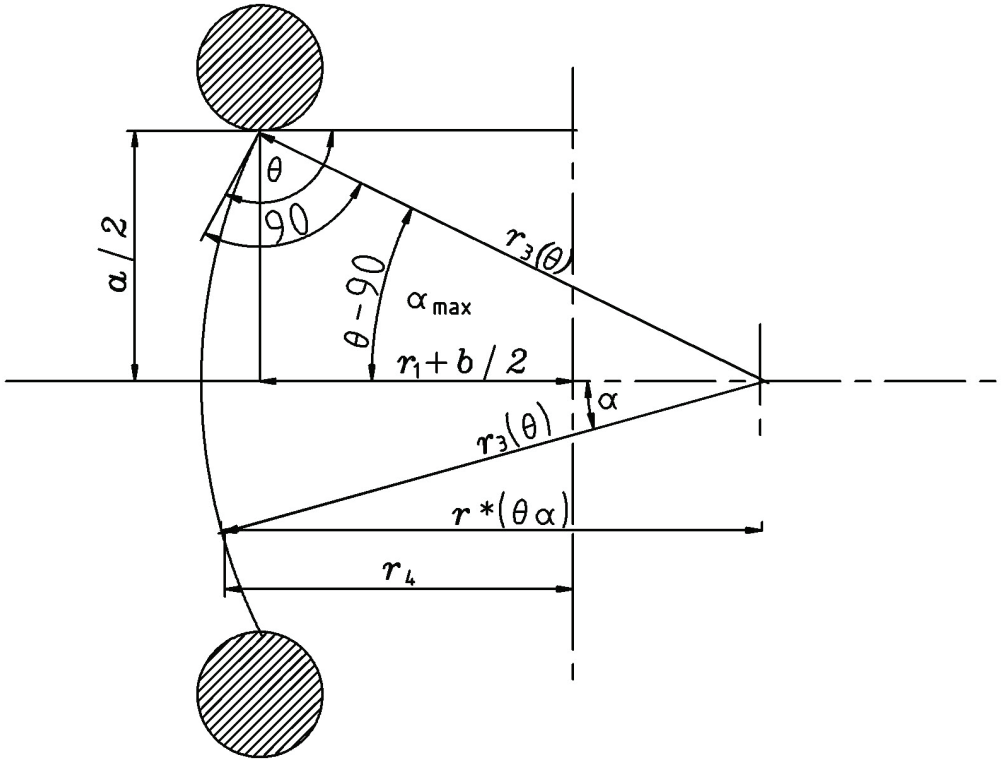

Figure D.2: Geometrical configuration to calculate interfacial area between water and gas.

The wrap area of a barrel-shaped geometry is calculated by

$$A = 2\int_0^{\alpha_{\max}} 2\pi r_4(\alpha,\theta) r_3(\theta) d\alpha \tag{D.5}$$

[BS89]. With r_4 as the apparent cylinder radius dependent on the contact angle θ and the parameter angle α. r_3 denotes as the radius of curvature, depending upon the contact angle. For a known contact angle and vertical fibre spacing, the radius of curvature is defined by

$$r_3(\theta) = \frac{a/2}{\sin\alpha_{\max}}. \tag{D.6}$$

The radius r^* is related to the radius of curvature:

$$r^*(\alpha,\theta) = r_3(\theta)\cos\alpha \tag{D.7}$$

And the radius r_4 is the distance between the centre symmetry line and the location of the interface and calculated by

$$r_4(\alpha,\theta) = r^*(\alpha,\theta) - \left[r_3(\theta)\cos\alpha_{\max} - (r_1 + b/2)\right]. \tag{D.8}$$

By combining Equations D.5 to D.8, one obtains:

$$A = 4\pi\int_0^{\alpha_{\max}} \left[\frac{a/2}{\sin\alpha_{\max}}\cos\alpha - \frac{a/2}{\sin\alpha_{\max}}\cos\alpha_{\max} + r_1 + b/2\right]\frac{a/2}{\sin\alpha_{\max}} d\alpha \tag{D.9}$$

Since $\alpha_{\max} = \theta - \pi/2$ and $\sin(\theta - \pi/2) = -\cos\theta$, $\cos(\theta - \pi/2) = \sin\theta$, Equation D.10 for the interface area gas/water is obtained by integration.

$$A = 4\pi\frac{\frac{a}{2}}{\cos\theta}\left[\left(\theta - \frac{\pi}{2}\right)\left(-\frac{\frac{a}{2}}{\cos\theta}\sin\theta - r_1 - \frac{b}{2}\right) - \frac{a}{2}\right] \tag{D.10}$$

Appendix E

The Simple Humidity Model

The relative humidity (RH) as a function of operating temperature is required to estimate the effects of temperature on the NMR study in Section 4.3.6 on page 142. The relative humidity is defined as the ratio of the existing partial pressure of water $p_{\mathrm{H_2O}}$ divided by the highest vapour pressure possible at the given temperature $p_{\mathrm{H_2O,max}}(T)$:

$$\mathrm{RH} = \frac{p_{H_2O}}{p_{\mathrm{H_2O,max}}(T)} \tag{E.1}$$

The vapour pressure at a given temperature can be calculated by the Clausius-Clapeyron equation

$$p_{\mathrm{H_2O,max}}(T) = p_{\mathrm{H_2O,max}}(T_0) \exp\left(\frac{-\Delta\mathcal{H}}{\Re T} + \frac{\Delta\mathcal{H}}{\Re T_0}\right). \tag{E.2}$$

In Equation E.2 $\Delta\mathcal{H}$ represents the enthalpy of evaporization, $\Re$ the ideal gas constant, and T_0 the reference temperature. The partial pressure is defined by the molar ratio of the component of interest κ_i multiplied by the total pressure p_0:

$$p_i = p_0\kappa_i = p_0 \frac{n_i}{\sum_{i=1}^{n} n_i} \tag{E.3}$$

The next step is the mass balance for all components. The product water, calculated according to Faraday's law (Equation E.4), as well as the air flow (Equation E.5) and hydrogen flow (Equation E.6), and also the water in the incoming air stream has to be

considered.

$$\frac{dn_{\mathrm{H_2O,prod}}}{dt} = \frac{i}{2F} \tag{E.4}$$

$$\frac{dn_{\mathrm{air}}}{dt} = \frac{i}{4F}\frac{\lambda_{\mathrm{O_2}}}{0.21} \tag{E.5}$$

$$\frac{dn_{\mathrm{H_2}}}{dt} = \frac{i}{2F}\lambda_{\mathrm{H_2}} \tag{E.6}$$

i represents the current density, F the Faraday constant, λ_i the stoichiometry of the component i, and the factor in Equation E.5 accounts for the oxygen concentration in the air. Since the hydrogen is provided with a purity of 5.0 ($\kappa_{\mathrm{H_2}} \geq 99.999\,\%$), it contains no water. The water content in the air stream is calculated with Equation E.7 which is obtained by rearranging Equation E.3 and Equation E.5.

$$\frac{dn_{\mathrm{H_2O,in}}}{dt} = \frac{p_{\mathrm{H_2O}}(T_{\mathrm{air}})\lambda_{\mathrm{O_2}}}{(p_0 - p_{\mathrm{H_2O}}(T_{\mathrm{air}}))0.21 \cdot 4F}\; i \tag{E.7}$$

Since the water distribution between the two sides of the membrane is unknown, it will not be considered and the average humidity of the gas streams is calculated by mixing the two flows virtually. The total channel humidity can be calculated with Equation E.8 which is obtained by combining Equation E.1 and Equation E.3 to E.7.

$$\mathrm{RH} = \frac{p_0}{p_{\mathrm{H_2O}}(T)} \frac{\frac{\lambda_{\mathrm{air}} p_{\mathrm{H_2O}}(T_{\mathrm{air}})}{2\cdot 0.21\left(p_{0,\mathrm{air}} - p_{\mathrm{H_2O}}(T_{\mathrm{air}})\right)} + 1}{\frac{\lambda_{\mathrm{air}}-1}{2\cdot 0.21} + \lambda_{\mathrm{H_2}} + \frac{\lambda_{\mathrm{air}} p_{\mathrm{H_2O}}(T_{\mathrm{air}})}{2\cdot 0.21\left(p_{0,\mathrm{air}} - p_{\mathrm{H_2O}}(T_{\mathrm{air}})\right)}} \tag{E.8}$$

Bibliography

[AKP+07] Hasan K. Atiyeh, Kunal Kanran, Brant Peppley, Aaron Phoenix, Ela Hlliop, and Jon Pharoah. Experimental investigation of the role of a microporous layer on the water transport and performance of a PEM fuel cell. *Journal of Power Sources*, 170:111–121, 2007.

[Ant03] A. Antolini. Review Formation, microstructural characteristics and stability of carbon supported platinum catalysts for low temperature fuel cells. *Journal of Materials Science*, 38:2995–3005, 2003.

[Arc42] Gustav E. Archie. The electrical resistivity log as an aid in determining some reservoirs characteristics. *Trans. AIME*, 146:54–67, 1942.

[AS03] Svante Arrhenius and J.W. Sandstroem. *Lehrbuch der kosmischen Physik*. S. Hirzel, Leipzig, 1903.

[ASC+03] J.R. Atkins, C.R. Sides, S.E. Creager, J.L. Harris, W.T. Pennington, B.H. Thomas, and D.D. DesMarteau. Effect of Equivalent Weight on Water Sorption, PTFE-Like Crystallinity, and Ionic Conductivity in Bis[(Perflouroalkyl)Sulfonyl] Imide Perfluorinated Ionomers. *Journal of New Materials for Electrochemical Systems*, 6:9–15, 2003.

[Atk94] Peter W. Atkins. *Physical Chemistry*. Oxford University Press, 5 edition, 1994.

[BA59] D.F. Boucher and E.I. Alves. Dimensionless numbers. *Chemical Engineering Progress*, 55(9):55 – 64, September 1959.

[BA63] D.F. Boucher and E.I. Alves. Dimensionless numbers - 2. *Chemical Engineering Progress*, 59(8):75–83, August 1963.

[BC64] R.H. Brooks and A.T. Corey. HYDRAULIC PROPERTIES OF POROUS MEDIA. Hydrology Papers Colorado State University Fort Collins, Colorado, March 1964.

[BD01a] Daniel R. Baker and Robert M. Darling. A Model of Diffusion and Convection of Gases from a Serpentine Flow Field to the Cathode of a PEM Fuel Cell. *International Journal of Transport Phenomena*, 3:231–256, 2001.

[BD01b] Torsten Berning and Ned Djilali. TRANSPORT PHENOMENA IN A PEM FUEL CELL. In *Proceedings of the 11th Canadian Hydrogen Conference*, pages 699–707, 2001.

[BDL05] Mathieu Boillot, Sophie Didierjean, and Francçois Lapicque. Residence time distributions of gases in lab-scale polymer electrolyte membrane fuel cells (PEMFC). *Chemical Engineering Science*, 60:1187–1192, 2005.

[Bea88] Jacob Bear. *Dynamics of Fluids in Porous Media*. Dover Publications Inc., 1988.

[Ber02] Torsten Berning. *Three-Dimensional Computational Analysis of Transport Phenomena in a PEM Fuel Cell*. PhD thesis, Department of Mechanical Engineering, University of Victoria, 19th April 2002.

[BIS+06] J. Becker, O. Iliev, V.P. Schulz, K. Steiner, and A. Wiegemann. Determination of Material Parameters of Gas Diffusion Layers by Combining Pore-Morphology Method and Single-Phase Simulations. In *Workshop Modelling and Simulation of PEM Fuel Cells, Berlin 2006*, September 2006.

[BNB+05] Jay Benziger, James Nehlsen, David Blackwell, Tom Brennan, and Johannah Itescu. Water flow in the gas diffusion layer of PEM fuel cells. *Journal of Membrane Science*, 261:98–106, 2005.

[BR73] John O'M. Bockris and Amulya K.N. Reddy. *Modern Electrochemistry: An Introduction to an Interdisciplinary Area: 2*, page 994 ff. Kluwer Academic / Plenum Publishers, 2. edition, June 1973.

[Bra92] Kenneth A. Brakke. The Surface Evolver. *Experimental Mathematics*, 1:141–165, 13th May 1992.

[Bru35] D.A. Bruggeman. Berechnung verschiedener physikalischer Konstanten von heterogenen Substanzen, 1. Dielektrizitätskonstanten und Leitfähigkeiten der Mischkörper aus isotropen Substanzen. *Annalen der Physik*, 5(24):636–664, 1935.

[BS89] Bronstein and Semendjajew. *Taschenbuch der Mathematik*. Harri Deutsch, Frakfurt/Main, 1989.

[Buc01] Isidor Buchmann. *Batteries in a Portable World: A Handbook on Rechargeable Batteries for Non-Engineers*. Cadex Electronics Inc, http://www.buchmann.ca/Chap4-page8.asp, 2 edition, 2001.

[Bur53] N.T Burdine. Relative permeability calculations from pore size distribution data. *Petroleum Transactions, AIME*, 198:71–77, 1953.

[Cal38] G.S. Callendar. The artificial production of carbon dioxide and its influence on temperature. *Quarterly Journal of the Royal Meteorological Society*, 64:223–240, 1938.

[CD98] Shiyi Chen and Gary D. Doolen. LATTICE BOLTZMANN METHOD FOR FLUID FLOWS. *Annual Reviews of Fluid Mechanics*, (30):329–364, 1998.

[CF69] Paul Concus and Robert Finn. ON THE BEHAVIOR OF A CAPILLARY SURFACE IN A WEDGE. *Applied Mathematical Sciences*, 63:292–299, 1969.

[Cha76] G. Chavent. *Applications of Methods of Functional Analysis to Problems in Mechanics*, volume 503 of *Lecture Notes in Mathematics*, chapter A NEW

FORMULATION OF DIPHASIC INCOMPRESSIBLE FLOW, pages 258–270. Springer Berlin/Heidelberg, 1st edition, 1976.

[Chu01] D.D.L. Chung. Electromagnetic interference shielding effectiveness of carbon materials. *Carbon*, 39:279–285, 2001.

[CJTD06] Pyoungho Choi, Hikhil H. Jalani, Tony M. Thampan, and Ravindra Datta. Consideration of Thermodynamic, Transport, and Mechanical Properties in the Design of Polymer Electrolyte Membranes for Higher Temperature Fuel Cell Operation. *Journal of Polymer Science: Part B: Polymer Physics*, 44:2183–2200, 2006.

[CK03] M. Cifrain and K. Kordesch. *Handbook of Fuel Cells: Fundamentals, Technology, Applications*, volume 1, chapter 14 Hydrogen/oxygen (Air) fuel cells with alkaline electrolytes, pages 267–280. Wiley, 1st edition, March 2003.

[Dar56] Henry Darcy. Les Fontaines Publiques de la Ville de Dijon. Technical report, Libraire des corps impériaux des ponts et chausses des mines, http://biosystems.okstate.edu/darcy/French/index.htm, 1856.

[DG06] C. J. T. De Grotthuss. Sur la décomposition de l'eau et des corps qu'elle tient en dissolution à l'aide de l'éctricité galvanique. *Annales de Chemie*, pages 54–74, 30 April 1806.

[DGBWQ03] Pierre Gilles De Gennes, Françoise Brochard Wyart, and David Quéré. *Capillarity and wetting phenomena*. Springer, 2003.

[DLRT59] Robert De La Rue and Charles W. Tobias. On the Conductivity of Dispersions. *Journal of Electrochemical Society*, 106(9):827–833, September 1959.

[DM07] Zachary W. Dunbar and Richard I. Masel. Quantitative MRI study of water distribution during operation of a PEM fuel cell using Teflon flow fields. *Journal of Power Sources*, 171:678–687, 2007.

[DM08] Zachary W. Dunbar and Richard I. Masel. Magnetic resonance imaging investigation of water accumulation and transport in graphite flow fields in

a polymer electrolyte fuel cell: Do defects control transport? *Journal of Power Sources*, 182:76–82, 2008.

[DR03] M. Doyle and G. Rajendran. *Handbook of Fuel Cells: Fundamentals, Technology, Applications*, volume 3, chapter 30 Perfluorinated membranes, pages 351–395. Wiley, 1st edition, March 2003.

[EEW84] Allan J. Easteal, A. Vernon J. Edge, and Lawrence A. Woolf. Isotope Effects in Water Tracer Diffusion Coefficients for H_2 ^{18}O in Ordinary Water. *Journal of Physical Chemistry*, 88:6060–6063, 1984.

[EHJR80] W. A. Edelstein, J. M. S. Hutchinson, G. Johnson, and T. Redpath. Spin wrap NMR imaging and applications to human whole-body imaging. *Physics in Medicine and Biology*, 4(25):751–756, 1980.

[EIA07] EIA. Annual Energy Review 2007. Report DOE/EIA-0384(2007), Energy Information Administration, 2007.

[EIA08] EIA. International Energy Outlook 2008. Report DOE/EIA-0484(2008), Energy Information Administration, 2008.

[Eik06] M. Eikerling. Water Management in Cathode Catalyst Layers of PEM Fuel Cells. *Journal of The Electrochemical Society*, 153(3):E58–E70, 2006.

[Eps89] Norman Epstein. On tortuosity and the tortuosity factor in flow and diffusion through porous media. *Chemical Engineering Science*, 44(3):777–779, 1989.

[FG08] Alejandro A. Franco and Mathias Gerard. Multiscale Model of Carbon Corrosion in a PEFC: Coupling with Electrocatalysis and Impact on Performance Degradation. *Journal of The Electrochemical Society*, 155(4):B367–B384, 2008.

[FLS89] Richard P. Feynman, Robert B. Leighton, and Metthew L. Sands. *The Feynman Lectures on Physics*, volume 2. Allan M. Wylde, 1989.

[FLS+04] Kirk.W. Feindel, P.A. LaRocque, Logan, Dieter Starke, Steven H. Bergens, and Roderick E. Wasylishen. In-Situ Observations of Water Production and Distribution in an Operating H_2O_2 PEM Fuel Cell Assembly Using ^{1}H NMR Microscopy. *Journal of American Chemical Society*, 126(37):11436–11437, 2004.

[FR81] Eiichi Fukushima and Stephen B.W. Roeder. *Experimental Pulse NMR*. Addison Wesley, 1981.

[FS02] Daan Frenkel and Berend Smit. *Understanding Molecular Simulation*, volume 1. Academia Press, San Diego, San Fransisco, New York, Boston, London, Sydney, Tokyo, 2 edition, 2002.

[GBT01] X. Gong, A. Bandis, and A. Tao. Self-diffusion of water, ethanol and decafluoropentane in perfluorosulfonate ionomer by pulse field gradient NMR. *Polymer*, 42:6458–6492, 2001.

[GFI06] Jeffrey T. Gostick, Michael W. Fowler, and Marios A. Ioannidis. Capillary pressure and hydrophilic porosity in gas diffusion layers for polymer electrolyte fuel cells. *Journal of Power Sources*, 156(2):375–387, 2006.

[GIFP08] Jeffrey T. Gostick, Marios A. Ioannidis, Michael W. Fowler, and Mark D. Pritzker. Direct Measurement of the Capillary Pressure Characteristics of Water-Air-Gas Diffusion Layer Systems for PEM Fuel Cells. *Electrochemistry Communications*, 10:1520–1523, 2008.

[Goe09] Steven G. Goebel. Nested bipolar plate for fuel cell and method. Patent US 7 601 452, GM GLOBAL TECHNOLOGY OPERATIONS, INC., 2009.

[Gro39] W. R. Grove. On Voltaic Series and the Combination of Gases by Platinum. *Philosophical Magazine and Journal of Science*, 14:127–130, 1839.

[Gro72] Walter Gustav Grot. Surface-activated fluorocarbon objects. Patent US 3 692 569, du Pont, 1972.

[Hal24] J. B. S. Haldane. *DAEDALUS or Science and the Future*. E.P. Dutton, http://www.cscs.umich.edu/∼crshalizi/Daedalus.html, 1924.

[HKPV96] D. Häfner, A. Kornjaef, A. Pohl, and H.D. Voigt. Permeabilitäts-und Porositätsmessungen an Gesteinsproben mit dem instationären Zweikammerverfahren. *Erdöl Erdgas Kohle*, 112:401–404, 10 1996.

[HMD+98] A.C. Henry, R.L. McCarley, S. Das, C. Kahn, and D.S. Poche. Structural changes in PMMA under hard X-ray irradiation. *Microsystem Technologies*, 4:104–109, 1998.

[HMK+08] Christoph Hartnig, Ingo Manke, Robert Kuhn, Nicolay Kardjiilov, John Banhart, and Werner Lehnert. Cross-sectional insight in the water evolution and transport in polymer electrolyte fuel cells. *Applied Physical Letters*, 92:134106.1–3, 2008.

[HMK+09] Christioph Hartnig, Ingo Manke, Robert Kuhn, Sebastian Kleinau, Jürgen Goebbels, and John Banhart. High-resolution in-plane investigation of the water evolution and transport in PEM fuel cells. *Journal of Power Sources*, 188:468–474, 2009.

[Hoa85] James P. Hoare. *Standard Potentials in aqueous solution*, chapter 4 Oxygen, pages 49–58. CRC Press, 1985.

[HR98] Gerold Hübner and Emil Roduner. EPR investigation of OH· radical initiated degradation reactions of sulfonated aromatics as model compounds for fuel cell proton conducting membranes. *Journal of Materials Chemistry*, 9:409–418, 1998.

[HS03] Holtappels, P. and Stimming, U. *Handbook of Fuel Cells: Fundamentals, Technology, Applications*, volume 1, chapter 20 Solid oxide fuel cells (SOFC), pages 335–354. Wiley, 1st edition, March 2003.

[HSC+08] M.A. Hickner, N.P. Siegel, K.S. Chen, D.S. Hussey, D.L. Jacobson, and M. Arif. In Situ High-Resolution Neutron Radiography of Cross-Sectional Liquid Water Profiles in Proton Exchange Membrane Fuel Cells. *Journal of The Electrochemical Society*, 155(4):B427–B434, 2008.

[HT78] Walter Hengartner and Radu Theodorescu. *Einführung in die Monte-Carlo-Methode*, volume 1. Hanser, 1978.

[Hub49] King Hubbert. Energy from Fossil Fuels. *Science*, 109:103–109, 1949.

[HV81] C.H. Hamann and Vielstich, W. *Elektrochemie II*, volume 2. VCH, Weinheim, 1981.

[IEA08] IEA. Key World Energy Statistics. Report, INTERNATIONAL ENERGY AGENCY, 9, rue de la Fédération, 75739 Paris Cedex 15, www.iea.org, 2008.

[IPC07] IPCC. Climate Change 2007: Synthesis Report. Technical report, Intergovernmental Panel on Climate Change, 2007.

[Ise92] Cyril Isenberg. *The science of soap films and soap bubbles*. Dover Publications, 1992.

[Ise00] Martin Ise. *Polymer-Elektrolyt-Membranen: Untersuchungen zur Mikrostruktur und zu den Transporteigenschaften für Protonen und Wasser*. PhD thesis, Fakultät für Physik der Universität Stuttgart, Max-Planck-Institut für Festkörperforschung, Stuttgart, 2000.

[JG07] Seung Soon Jang and A. III Goddard. Structures and Transport Properties of Hydrated Water-Soluble Dendrimer-Grafted Polymer Membranes for Application to Polymer Electrolyte Membrane Fuel Cells: Classical Molecular Dynamics Approach. *Journal of Physical Chemistry*, 111:2759–2769, 2007.

[JZQ06a] Kui Jiao, Biao Zhou, and Peng Quan. Liquid water transport in parallel serpentine channels with manifolds in cathode side of a PEM fuel cell stack. *Journal of Power Sources*, 154:124–137, 2006.

[JZQ06b] Kui Jiao, Biao Zhou, and Peng Quan. Liquid water transport in straight micro-parallel-channels with manifolds for PEM fuel cell cathode. *Journal of Power Sources*, 157:226–243, 2006.

[KC09] Byoungwoo Kang and Gerbrand Ceder. Battery materials for ultrafast charging and discharging. *Nature*, 458:190–193, March 2009.

[KFF+08] Denis Kramer, Stefan A. Freunberger, Reto Flückiger, Ingo A. Schneider, Alexander Wokaun, Felix Büchi, and Günther G. Scherer. Electrochemical diffusimetry of fuel cell gas diffusion layers. *Journal of Electroanalytical Chemistry*, 612:63–77, 2008.

[KFMT06] Tetsuya Koido, Toru Furusawa, Koji Moriyama, and Keiichiro Takato. Two-phase Transport Properties and Transport Simulation of the Gas Diffusion Layer of a PEFC. In *ECS Transactions*, volume 3, pages 425–434, 2006.

[KIH+03] Kazuhiro Kanda, Tomoya Ideta, Yuichi Haruyama, Hiroyuki Ishigaki, and Shinji Matsui. Surface Modification of Fluorocarbon Polymers by Synchrotron Radiation. *Japan Journal of Applied Physics*, 42:3983–3985, 2003.

[Kin88] Kim Kinoshita. *Carbon*. John Wiley, 1st edition, 1st January 1988.

[KK03] J.M. King and H.R. Kunz. *Handbook of Fuel Cells: Fundamentals, Technology, Applications*, volume 1, chapter 16 Phosphoric acid electrolyte fuel cells, pages 287–300. Wiley, 1st edition, March 2003.

[KKL+02] Chang Sun Kong, Do-Young Kim, Han-Kyu Lee, Yong-Gun Shul, and Tae-Hee Lee. Influence of pore-size distribution of diffusion layer on mass-transport problems of proton exchange membrane fuel cells. *Journal of Power Sources*, 108:158–191, 2002.

[KPSS04] Klaus-Dieter Kreuer, Stephen J. Paddison, Eckhard Spohr, and Michael Schuster. Transport in Proton Conductors for Fuel-Cell Applications: Simulations, Elementary Reactions, and Phenomenology. *Chemical Reviews*, 104:4637–4678, 2004.

[KSM07] E.C. Kumbur, K.V. Sharp, and M.M. Mench. Capillary Pressure-Saturation Behavior of Carbon Paper Fuels Cell Diffusion Media: A Validated Approach. In Fuller T., H.A. Gasteiger, S. Cleghorn, and Ramani et al., V., editors, *ECS Transactions*, volume 11, pages 683–692, 2007.

[Kuc95] Horst Kuchling. *Taschenbuch der Physik*. Fachbuchverlag Köln, 15th edition, 1995.

[LC94] L. Li and D.D.L. Chung. Electrical and mechanical properties of electrically conductive polyethersulfone composite. *Composites*, 25(3):215–224, 1994.

[LD86] V. Leon and H. Diaz. Surface Effects Measured by Additional Echo Decay in the T_2 Spin-Echo Experiment. *Applied Spectroscopy*, 40(3):416, 1986.

[Leg06] Jeremy Legget. *Peak Oil*. Kiepenheuer & Witsch, 1st edition, 2006.

[Lev41] M.C. Leverett. Capillary behavior of porous media. *Trans A.I.M.E*, 142:341–358, 1941.

[Lin96] David R. Linde, editor. *HANDBOOK of CHEMISTRY and PHYSICS*. CRC Press, 76th edition, 1996.

[Lin09] Linde. Hydrogen cars can be fueled in as little as three minutes with Linde technology. Technical report, http://hydrogendiscoveries.wordpress.com/category/hydrogen-fueling-time/, 23 March 2009.

[LS04] Xiangou Li and Imran Sabir. Review of bipolar plates in PEM fuel cells: Flow-field designs. *International Journal of Hydrogen Energy*, 30:359–371, 2004.

[LTZ88] Roland Lenormand, Eric Touboul, and Cesar Zarcone. Numerical models and experiments on immiscible displacements in porous media. *Journal of Fluid Mechanics*, 189:165–187, 1988.

[Mar99] N.S. Martys. Diffusion in partially-saturated porous materials. *Materials and Structures*, 32:555–562, October 1999.

[MBK+86] A.D. Myshkis, V.G. Babskii, N. D. Kopachevskii, L.A. Slobozhanin, and A. D. Tyuptsov. *Low-Gravity Fluid Mechanics*. Springer, Berlin, Heidelberg, New York, 1st edition, 1986.

[MCG99] Bertram Manz, P.S. Chow, and Glassen L.F. Echo-Planar Imaging of Porous Media with a Spatial Resolution below 100 µm. *Journal of Magnetic Resonance*, 136(2):226–230, February 1999.

[MHG+97] Ingo Manke, Christoph Hartnig, M. Grünerbel, Werner Lehnert, N. Kardjilov, A. Haibel, A. Hilger, J. Banhart, and H. Riesemeiner. Investigation of water evolution and transport in fuel cells with high resolution synchrotron x-ray radiography. *Applied Physical Letters*, 90:174105–1–174105–3, 1997.

[MKM02] Minas M. Mezedur, Massoud Kaviany, and Wayne Moore. Effect of Pore Structure, Randomness and Size on Effective Mass Diffusivity. *AIChE Journal*, 48(1):15–24, January 2002.

[MLE01] L.B. McCusker, B. Liebau, and G. Engelhardt. NOMENCLATURE OF STRUCTURAL AND COMPOSITIONAL CHARACTERISTICS OF ORDERED MICROPOROUS AND MESOPOROUS MATERIALS WITH INORGANIC HOSTS. *Pure Applied Chemistry*, 73:381–394, 2001.

[MMY+08] Thaihei Mukaide, Satoshi Mogi, Jun Yamamoto, Akira Morita, Shinnosuke Koji, Kazuhiro Takada, Kentaro Uesugi, Kantaro Kajiwara, and Takashi Noma. In situ observation of water distribution and behaviour in a polymer electrolyte fuel cell by synchrotron X-ray imaging. *Journal of Synchrotron Radiation*, 15:329–334, 2008.

[MRFL03] Mark Mathias, Joerg Roth, Jerry Fleming, and Werner Lehnert. *Handbook of Fuel Cells: Fundamentals, Technology, Applications*, volume 3, chapter 46 Diffusion media materials and characterisation, pages 517–537. Wiley, 1st edition, March 2003.

[Mua76] Yechezkel Mualem. A new model for predicting the hydraulic conductivity of unsaturated porous media. *Water Resources Research*, 12(3):513–532, 1976.

[Mug03] Y. Mugikura. *Handbook of Fuel Cells: Fundamentals, Technology, Applications*, volume 4.2, chapter 66 Stack material and Stack design (MCFC), pages 907–941. Wiley, 1st edition, March 2003.

[MVM+06] Kevin R. Minard, Vilayanur V. Viswanathan, Pail D. Majors, Li-Qiong Wang, and Peter C. Rieke. Magnetic resonance imaging (MRI) of PEM

dehydration and gas manifold flooding during continuous fuel cell operation. *Journal of Power Sources*, 161:856–863, 2006.

[Nit08] Iwao Nitta. *Inhomogeneous compression of PEMFC gas diffusion layers*. PhD thesis, Helsinki University of Technology, 2008.

[NK03] Jin Hyun Nam and Massoud Kaviany. Effective Diffusivity and Water-Saturation Distribution in Single-and Two-Layer PEMFC Diffusion Medium. *International Journal of Heat and Mass Transfer*, 46:4595–4611, February 2003.

[NKS02] N. Nishi, T. Katoh, and S. Sugiyama. Study on three-dimensional micromachining using synchrotron radiation etching. *Microsystem Technologies*, 9:1–4, 2002.

[NLOW06] T.V. Nguyen, G. Lin, H. Ohn, and X. Wang. MEASUREMENTS OF TWO-PHASE FLOW PROPERTIES OF THE POROUS MEDIA USED IN FUEL CELLS. In T. Fuller, T.V. Nguyen, T.D. Jarvi, V. Ramani, Stuve, E.M., Bock, C., M. F. Mathias, H.A. Gasteiger, Chleghorn, S., and Zawodinski, T., editors, *Proton Exchange Membrane Fuel Cells 6*, volume 3, pages 415–423, 2006.

[NN76] G. Neale and W.K. Nader. Prediction of Transport Processes Within Porous Media: Diffusive Transport Processes Within Anisotropic or Isotropic Swarms of Nonspherical Particles. *AIChE Journal*, 22(1):182–188, January 1976.

[NN03] D. Natarajan and T.V. Nguyen. Three-dimensional effects of liquid water flooding in the cathode of a PEM fuel cell. *Journal of Power Sources*, 115:66–80, 2003.

[PD06] Timothy W. Patterson and Robert M. Darling. Damage of the Cathode Catalyst of a PEM Fuel Cell Caused by Localized Fuel Starvation. *Electrochemical and Solid State Letters*, 9(4):A183–A185, 2006.

[Pha05] J. G. Pharoah. Fluid mechanics of serpentine flow fields on a porous media. *Journal of Green Energy*, 2:421–438, 2005.

[Pla73] Joseph Plateau. *Statique expérimentale et théorique des liquides soumis aux seules forces moléculaires*. Gauthier - Villars, Paris, 1873.

[PRJ62] D.W. Peaceman and H.H. Rachford Jr. Numerical Calculation of Multidimensional Miscible Displacement. *SPE Journal*, 2(4):327–339, December 1962.

[PSL+01] E. Passalacqua, G. Squadrito, A. Lufrano, A. Patti, and L. Giorgi. Effects of the diffusion layer characteristics on the performance of polymer electrolyte fuel cells. *Journal of Applied Electrochemistry*, 31:449–454, 2001.

[PW04] Ugur Passaogullari and C.Y. Wang. Liquid Water Transport in Gas Diffusion Layer of Polymer Electrolyte Fuel Cells. *Journal of the Electrochemical Society*, 151:A399–A406, 2004.

[Rif02] Jeremy Rifkin. *The Hydrogen Economy*. Tarcher Putnam, 1st edition, 2002.

[RRF08] Dirk Rensink, Jörg Roth, and Stephan Fell. LIQUID WATER TRANSPORT AND DISTRIBUTION ON FIBROUS POROUS MEDIA AND GAS CHANNELS. In *Proceedings of the Sixth International ASME Conference on Nanochannels, Microchannels and Minichannels Darmstadt*, 23 June 2008.

[RS57] Roger Revelle and Hans E. Suess. Carbon Dioxid Exchange Between Atmosphere and Ocean and the Question of an Increase of Atmospheric CO_2 during the Past Decades. *Tellus*, 9:18–27, 1957.

[SA03] Lev A. Slobozahanin and J. Iwan D. Alexander. Stability diagrams for disconnected capillary surfaces. *Physics of Fluids*, 15(11):3532–3545, November 2003.

[SACG06] Lev. A. Slobozhanin, J. Iwan D. Alexander, Steven H. Collicott, and S. Roberto Gonzales. Capillary pressure of a liquid in a layer of close-packed uniform spheres. *Physics of Fluids*, 18(8):2104–2119, August 2006.

[SAP02] Lev. A. Slobozhanin, J. Iwan D. Alexander, and D. Viral Patel. The stability margin for stable weightless liquid bridges. *Physics of Fluids*, 14(1):209–224, January 2002.

[Sch39] Christian Friedrich Schoenbein. Lecture of 13 March 1839. *Berichte der Verhandlungen der naturforschenden Gesellschaft in Basel*, 4:52–55, 1839.

[Sch03] Paul von Schröder. Über Erstarrungs- und Quellungserscheinungen von Gelatine. *Zeitschrift für Physikalische Chemie*, 45:75–117, 1903.

[SH01] Brian C. Steele and Angelika Heinzel. Materials for fuel-cell technologies. *Nature*, 414:345–352, 15 November 2001.

[SKWS05] V. Schulz, D. Kehrwald, A. Wiegemann, and K. Steiner. Flow, heat conductivity, and gas diffusion in partly saturated microstructures. In *NAFEMS Seminar:"Simulation of Complex Flows (CFD)" Niedernhausen/Wiesbaden*, 25 April 2005.

[SMB+06] V.P. Schulz, P. P. Mukherjee, J. Becker, A. Wiegemann, and C. Y. Wang. Numerical Evaluation of Effective Gas Diffusivity Saturation Dependence of Uncompressed and Compressed Gas Diffusion Media in PEFCs. In T. Fuller and C. Bock and S. Cleghorn and H. Gasteiger et al., editor, *Proceedings of the 20th ECS Meeting*, volume 3 of *1069-1076*. Electrochemical Society, 2006.

[SP07] Jean St-Pierre. PEMFC in situ liquid-water-content monitoring status. *Journal of The Electrochemical Society*, 154(7):B724–B731, 2007.

[SW08] Puneet K. Sinha and Chao-Yang Wang. Liquid water transport in a mixed-wet gas diffusion layer of a polymer electrolyte fuel cell. *Chemical Engineering Science*, 63:1081–1091, 2008.

[SZG91] T. E. Springer, T. A. Zawodzinski, and S. Gottesfeld. Polymer Electrolyte Fuel Cell Model. *Journal of the Electrochemical Society*, 138:2334–2342, 1991.

[SZS99] Ruben Scardovelli, Zaleski, and Stéphane. DIRECT NUMERICAL SIMULATION OF FREE SURFACE AND INTERFACIAL FLOW. *Annual Reviews of Fluid Mechanics*, 31:567–603, 1999.

[Tho03] Thompsett, D. *Handbook of Fuel Cells: Fundamentals, Technology, Applications*, volume 3, chapter 37 Pt alloys as oxygen reduction catalysts, pages 467–480. Wiley, 1st edition, March 2003.

[TS91] Manolis M. Tomadakis and Stratis V. Sotirchos. Effective Knudsen Diffusivities in Structures of Randomly Overlapping Fibers. *AIChE Journal*, 37(1):74–85, January 1991.

[TS93] Manolis M. Tomadakis and Stratis V. Sotirchos. Ordinary and Transition Regime Diffusion in Random Fiber Structures. *AIChE Journal*, 39(3):397–412, March 1993.

[TTH05] S. Tsushima, K. Teranishi, and S. Hirai. Water diffusion measurement in fuel-cell SPE membrane by NMR. *Energy*, 30(2 - 4):235–245, 2005.

[TTH06] Kazuhiro Teranishi, Shohji Tsushima, and Shuichiro Hirai. Analyis of Water Transport in PEFCs by Magnetic Resonance Imaging Measurement. *Journal of The Electrochemical Society*, 153(4):A664–A668, 2006.

[Ude85] Kent S. Udell. Heat transfer in porous media considering phase change and capillarity-the heat pipe effect. *International Journal of Heat and Mass Transfer*, 28:485–495, February 1985.

[Ver75] Jules Verne. *L' ÎLE MYSTÉRIEUSE*. J. Hetzel, 1875.

[VG80] M.Th. Van Genuchten. A Closed-form Equation for Predicting the Hydraulic Conductivity of Unsaturated Soils. *Soil Science Society of America Journal*, 44:892–898, 1980.

[VLG03] Wolf Vielstich, Arnold Lamm, and Hubert Gasteiger, editors. *Handbook of Fuel Cells: Fundamentals, Technology, Applications*, volume 1. Wiley, March 2003.

[Wag01] Walter Wagner. *Strömung und Druckverlust*. Vogel Verlag, 5 edition, 2001.

[WB93] Chao Yang Wang and C. Beckermann. A two - phase mixture model of liquid - gas flow and heat transfer in capillary porous media - I. Formulation. *International Journal of Heat Mass Transfer*, 36(11):2747–2757, 1993.

[WG58] M.R.J. Wyllie and G.H.F. Gardner. The generalized Kozeney-Carman equation. *World Oil*, pages 210–228, April 1958.

[Wie01] Christian Wieser. *Stromdichteverteilung und Leistungsverhalten der Polymerelektrolyt-Brennstoffzelle*. PhD thesis, University of Stuttgart, 2001.

[Wil63] Ludwig Wilhelmy. Über die Abhängigkeit der Capillaritäts-Constanten des Alkohols von Substanz und Gestallt des benetzten festen Körpers. *Annalen der Physik und Chemie*, 6:177–217, March 1863.

[WN03] Adam Z. Weber and John Newman. Modelling Transport in Polymer - Electrolyte Membranes I Physical Model. *Journal of The Electrochemical Society*, 150(7):A1008–A1015, 2003.

[WN04] Adam Z. Weber and John Newman. Modelling Transport in Polymer - Electrolyte Fuel Cells. *Chemical Review*, 104:4679–4726, 2004.

[WSKB02] J. Wind, R. Späh, W. Kaiser, and G. Böhm. Metallic bipolar plates for PEM fuel cells. *Journal of Power Sources*, 105:256–260, 2002.

[WV03] Wilkinson, D.P. and Vanderleeden, O. *Handbook of Fuel Cells: Fundamentals, Technology, Applications*, volume 3, chapter 27 Serpentine flow field design, pages 315–324. Wiley, 1st edition, March 2003.

[WWC01] Z.H. Wang, C.Y. Wang, and K.S. Chen. Two-phase flow and transport in the air cathode of proton exchange membrane fuel cells. *Journal of Power Sources*, 94:40–50, 2001.

[WWW+95] J.S. Wainright, J.-T. Wang, D. Weng, R.F. Savinell, and M. Litt. Acid-Doped Polybenzimidazoles: A New Polymer Electrolyte. *Journal of Electrochemical Society*, 142(7):L121–L123, 1995.

[YGM+06] Paul T. Yu, Wenbin Gu, Rohit Makharia, Frederick T. Wagner, and Hubert A. Gasteiger. The Impact of Carbon Stability on PEM Fuel Cell Startup and Shutdown Voltage Degradation. In *Electrochemical Society Transactions*, volume 3 of *PEM Fuel Cell 6*, page 797, 2006.

[YTA+06] Kazuaki Yasuda, Aktira Taniguchi, Tomoki Akita, Tsutomu Ioroi, and Zyun Siroma. Platinum dissolution and deposition in the polymer electrolyte membrane of a PEM fuel cell as studied by potential cycling. *Physical Chemistry Chemical Physics*, 8:746–752, 2006.

[YYX+02] Jingrong Yu, Baolian Yi, Danmin Xing, Fuqiang Liu, Zhigang Shao, Yongzhu Fu, and Huamin Zahng. Degradation mechanism of polystyrene sulfonic acid membrane and application of its composite membranes in fuel cells. *Physical Chemistry Chemical Physics*, 5:611–615, 2002.

[ZGWJ05] Jinghui Zhang, Marcus V. Giotto, Wen Yang Wen, and Alan A. Jones. An NMR study of the state of ions and diffusion in perfluorosulfonate ionomer. *Journal of Membrane Science*, 269(1 - 2):118–125, 2005.